2022

Rational Design of Flexible and Stretchable Electronics based on 3D Printing

Yuanhang Yang

Rational Design of Flexible and Stretchable Electronics based on 3D Printing

A dissertation submitted in partial fulfillment of the requirements for the degree of Doctor of Philosophy at Virginia Commonwealth University

By

Yuanhang Yang

M.S., Mechanical Engineering, Beijing Institute of Petrochemical Technology, China, 2018

B.S., Mechanical Engineering, Qingdao University, China, 2015

Advisor: Dr. Hong Zhao

Associate Professor

Department of Mechanical and Nuclear Engineering

Virginia Commonwealth University

Richmond, Virginia

July 2022

Acknowledgment

First of all, I would like to thank my advisor Dr. Hong Zhao. She has provided me with continuous support, careful guidance, constructing advices, and encouragement during my Ph.D. program. Under her assistance, I get a conspicuous promotion in my academic research. Besides, she also shares me with her life experience. When I am lost and helpless, Dr. Zhao always patiently try to understand my confusion, and give me family-like care. It is her assistance rendering me the encourage to face all difficulties with an optimistic and positive attitude in the foreign land.

Apart from my advisor, I would like to thank my dissertation committee members Dr. Xuewei Wang, Dr. Wei-Ning Wang, Dr. Ravi Hadimani, and Dr. Tse Nga (Tina) Ng for their insightful suggestions and informative discussions that broaden my research horizontal from various perspective. I believe these comments is useful for my research, and will have a positive effect on my future investigation.

My sincere thanks also go to Prof. Dmitry Pestov and Prof. Carl Mayer for giving me the training in material characterization in the VCU facility center. Their technical support is crucial in my research. Also, I thank graduate program director Prof. Karla Mossi for her careful explanation when I request any assistance in my Ph.D. program. The assistance from Prof. Duan Shun is appreciated. He teaches me a lot including enthusiasm and motivation to life and academic research.

I would also like to thank everyone who helped me in my life and research during my Ph.D. program. The favor from you, Dr. Zan Zhu, Dr. Peng Wang, Dr. Karam Nashwan Al-Milaji, Dr. Zheng Li, Dr. Qijin Huang, Dr. Xiang He, Dr. Christina Tang, Jianping Chen, Jie Zhang, Hao Tu, Tianyuan Zhang, Wuwei Li, and Kashmingder Singh Mehta are really appreciated. Your accompany make my life abroad colorful.

Finally, I am deeply thankful to my family members, my grandfather, Zhichun Yang, and grandmother, Yuxiu Chen, for blessing me in heaven. I grateful for my father, Huping Yang, mother, Feng'e Tao, brother, Yuanzheng Yang, for being with me throughout. Your love and understanding encourage me to overcome all troubles in my life. There is no doubt that your love must be a great treasure in my life.

Tables of Contents

List of Figures

List of Tables

Abstract

Rational Design of Flexible and Stretchable Electronics based on 3D Printing

By Yuanhang Yang

A dissertation submitted in partial fulfillment of the requirements for the degree of Doctor of Philosophy at Virginia Commonwealth University

Virginia Commonwealth University, 2022

Advisor: Dr. Hong Zhao

Associate professor, Department of Mechanical and Nuclear Engineering

Flexible and stretchable electronics have been considered as the key component for the next generation of flexible devices. There are many approaches to prepare the devices, such as dip coating, spin coating, Mayer bar coating, filtration and transfer, and printing, etc. The effectiveness of these methods has been proven, but some drawbacks cannot be ignored, such as lacking pattern control, labor consuming, requiring complex pretreatment, wasting conductive materials, etc.

In this investigation, we propose to adopt 3D printing technology to design flexible and stretchable electronics. The objective is to rationally design flexible and stretchable sensors, simplify the preparation process, form the sample with the complex desirable patterns, and promote the performance of the samples. The dissertation comprises of three major parts: water-induced polymer swelling and its application in soft electronics, utilizing 3D printing to transfer conductive layer into elastomer for building soft electronics, and 3D printing of functional devices.

In the first part, we developed the soft electronics with wrinkled structure via 3D printing and water-induced polymer swelling, which can avoid some disadvantages in conventional method, e.g., pre-stretching and organic solvent-induced polymer swelling, including mechanical loss,

negative effect to human health, and unidirectionally response to external deformation. Water-induced polymer swelling was achieved by introducing soluble particles into silicone matrixes and soaking the polymer composites in aqueous solution. We have investigated the characteristics and mechanisms of water-induced polymer swelling. Then, the conductive materials were deposited on the swollen sample to form the desired wrinkled structures for stretchable sensors. Furthermore, a dopamine layer was adopted to enhance the adhesion of matrix and conductive layer. The improvement was a key enabler to achieve superior electrical properties of 3D printed stretchable sensors for long-term cyclic stretching. We have demonstrated a series of human motion detection by using these stretchable strain sensors.

Another part is designing flexible electrodes with desirable complex pattern by transferring a conductive layer into soft substrates during a 3D printing process. Taking advantage of extrusion pressure and polymer adhesion, the thin conductive layers were embedded into the printed polymer patterns, which can achieve conductive flexible electronics with desirable complex patterns. High-quality transfer has been achieved through adjusting conductive layer thickness, nozzle-to-substrate distance, and printing parameters, etc. Moreover, various printing patterns were created, and their properties were exhibited. The stretchable sensors showed an outstanding stress-strain relationship and electrical response to external deformations.

The third part is about 3D printing of functional devices. In the collaborated study, the drug particles were introduced into silicone matrix to prepare the drug-eluting devices. When water molecules transported into the silicone matrix, the loaded drug particles decomposed and released nitric oxide (NO) enabling antibacterial properties. It is noted that 3D printing is creatively employed to form the desirable patterns. We also observed a self-wiring effect in the printing process, i.e., the printed device is covered by a drug-free layer due to the diffusion of a low viscosity silicone component during printing, which can be utilized to prevent drug release bursts and to form a gradient drug-loaded device. The printed samples showed a sustainable NO release and good antibacterial property. Furthermore, the water-induced polymer swelling was possible to be used as actuator in humidity environment.

There are some highlights deserving emphasis in the dissertation. Firstly, the water-induced polymer swelling is proposed to develop the flexible and stretchable electronics. The findings have

a wide potential application. Additionally, a drug-eluting polymer device with a drug-loaded bulk and a drug-free coating is prepared via leveraging self-wiring effect in 3D printing. The structure can regulate the drug release rate. On the other hand, the additive manufacturing platform offers unique opportunities to produce drug-eluting silicone devices in a customized manner. Finally, 3D printing is employed to encapsulate the conductive layers to achieve the flexible electronics with patterned structure and high performances. The facile and effective approach provides a distinctive view in advancing the development of stretchable electronics.

CHAPTER 1 Introduction

Soft electronics have received tremendous attention due to their potential applications in many fields, such as human motion detection, personal healthcare monitoring, human-machine interactions, soft robotics, wearable devices, energy storage devices, light emitting devices, and thin film transistor. To now, soft electronics have exhibited many good performances, such as excellent ductility, fatigue durability, ultra-sensitivity, and short response time, etc. These advantages bring forth huge economic benefits and drastically improve the quality of human life.

To obtain soft electronics with desirable performance, researchers have paid a lots efforts, including synthesis of conductive materials, fabrication of conductive network, encapsulating conductive layer into elastomer, and many others. The common conductive materials comprise of graphene,[1-2] reduced graphene oxide (rGO),[3-4] carbon nanotube (CNT),[5-6] metal nanoparticles/wires/flakes,[7-9] etc. To form conductive network, drop casting,[10] spin coating,[11] spray coating,[12] Meyer rod,[13] printing,[14] etc. have been proposed. Printing transfer is widely adopted to encapsulate the formed conductive network into polymer substrate. Based on these advances, various soft electronics have been successfully fabricated. They are able to deform while maintaining their designed functionalities.

It is noticed that designing soft electronics with wrinkled structure has many merits [15-16]. Compared with smooth films, the wrinkled structure provides a larger surface area to attach more conductive materials so that the conductive pathway with higher density can be formed. Furthermore, the wrinkled flexible substrates are more deformable thanks to the out of plane wrinkles, rendering less permanent damage in the conductive network when subjected to an external deformation. Recently, several methods have been demonstrated to fabricate stretchable conductors with wrinkled conductive structures.

Unidirectionally pre-stretching method has been widely adopted to fabricate wrinkled conductive structures in view of its low cost and simple process [17]. Conductive nanomaterials are applied to deposit on the pre-strained elastomer substrate. The wrinkled structure has been

achieved upon removal of the strain due to mechanical instability between the polymer substrate and the conductive layer. The size, distance, and density of the wrinkles can be tailored by implementing various pre-strains [18]. Yang *et al.*[19] adhered conductive fibrous mat of MXene onto the pre-strained elastomer tapes. Wrinkled structures with various wavelengths have been obtained where the wrinkle wavelength has a negative correlation with the amount of pre-strain. Lee *et al.*[20] sprayed carbon nanotube (CNT) suspension on the acrylic rubber and silicone rubber substrate with different pre-strains. Similar trends were identified regarding the negative correlation of wrinkle wavelength and pre-strain level. Furthermore, the wrinkle amplitude is positively related with the amount of pre-strains up to 100%, and drops thereafter due to plastic deformation in the elastomer layer. Although pre-stretching method provides a simple process to fabricate stretchable devices, unfortunately, the sensors prepared by this unidirectional pre-stretching are invalid in detecting the deformation perpendicular to the pre-stretching direction.

To overcome the limitations, the biaxial pre-stretching method has been developed. Liu *et al.*[21] systematically investigated the morphologies and electrical properties of AgNW networks on polydimethylsiloxane (PDMS) with different pre-stretching conditions (i.e., no stretching, uniaxially, and biaxially stretching). Despite the initial uniform AgNW deposition on the un-stretched sample, cracks and gaps in AgNW networks were easily created when a slight external deformation (10%) was applied. The AgNW networks on uniaxially pre-stretched PDMS film displayed a nearly periodical wrinkle structure. The conductive pathway keeps intact and continuous in the pre-stretched direction even when the sample was stretched by 80%, whereas the samples exhibited a poor stretching capacity in any other direction. As for the samples biaxially pre-stretched, a wavy mountain-like structure was obtained which enables better electrical conductivity and ultra-reliability when compared with un-stretched and uniaxially pre-stretched samples. Chu *et al.*[22] stretched an acrylic film to the direction of x-axis and y-axis with different amounts of strains, followed by deposition of reduced graphene oxide layer, creating unique gradient wrinkle structures. The prepared sample exhibited high sensitivity, broad strain range, robust response, and fast response which have been demonstrated in human body motion detection.

In addition to pre-stretching, other methods (such as heat treatment and templating) have been employed to create wrinkled substrates with conductive materials. Sahoo *et al.*[23] adopted reactive-ion etching (RIE) technology and post-heat treatment of thermoplastic polystyrene (PS) films. 3D wrinkles with different sizes were created as templates by regulating the RIE time. A wrinkled PDMS film was obtained by casting liquid PDMS onto the PS mold. Finally, this wrinkled PDMS film was treated with oxygen plasma and sprayed with CNT suspension to construct the wrinkled conductors. Chen *et al.*[24] utilized thermal annealing to treat the MXene-deposited biaxially oriented polystyrene (BOPS) film. Owing to the modulus mismatch, BOPS shrinks leading to a formation of wrinkled polystyrene/MXene film. Subsequently, PDMS was coated on the wrinkled structure and the hierarchical PDMS/MXene film was obtained upon removal of the BOPS film. Some flexible sensors with excellent properties have been constructed, but the complex process limits the application.

Among these methods, the mechanical stretching may cause strain localization and micro-cracks, and yield an anisotropic matrix deformation and a residual stress after the releasing process. These characteristics have an adverse effect on the fatigue life and stability of the devices which impair their applications in electrodes [25]. On the other hand, molding on a wrinkled template may fail to replicate the wrinkles at nanoscale. In this situation, the solvent induced polymer swelling was proposed due to its uniform volume expansion. Gao *et al.*[26] soaked PDMS film in chloroform followed by electroless deposition of silver nanoparticles. By regulating the metal deposition time, the conductive wrinkles with different wavelength and amplitude were obtained after removal of residual solvent. Zhang *et al.*[27] noticed significant swelling when the cross-linked PDMS was immersed in toluene which results in the expansion of a polymer chain network. Accompanied with subsequent carbon nanotube deposition, a wrinkled conductive layer was prepared after the matrix recovered its original size. However, the majority of these organic solvents are volatile and toxic. There is no doubt that the organic solvent induced polymer swelling produces a negative effect on human health and the environment.

Therefore, we put forward to utilize a water-induced polymer swelling to create wrinkled conductive layers replacing the toxic organic solvents [28]. Swelling behaviors of the elastomer

composite with soluble additives was systematically studied in chapter 3. The conductive layers, including in-situ synthesized silver nanoparticles (AgNPs), graphene, gold (Au), and silver nanowires (AgNWs), were separately deposited on the swollen elastomer. Thus, the wrinkled conductive layers were formed by removing the residual water (in chapter 4). To enhance the adhesion between conductive layer and polymer matrix, the dopamine was concurrently coated onto the swollen elastomer substrate during the immersion process. Both films and 3D printed sensors were fabricated, and their electrical properties are characterized.

Apart from preparing the wrinkled soft electronics, a novel printing transfer technique is introduced to encapsulate the conductive materials into polymer matrix in the project. It is reported that the integration of conductive materials and elastomer is vital to obtain the flexible electronics with ultra-performance. The conventional methods generally include three steps: (1) spreading liquid polymer on conductive layer, (2) self-encapsulating conductive layer into flexible matrix, and (3) peeling off the cured polymer where conductive layer embedded [29]. Guided by the process, researchers have obtained many results. Yun *et al.* used indium-doped zinc oxide (IZO) to decorate AgNW network, which not only enhances the interconnection between wires, but also reduces the surface roughness of AgNW film. The improvement can broaden their application in organic light-emitting diodes (OLEDs) [30]. Chen *et al.* applied a reactive ink on AgNW film, and used a chemical reaction to weld AgNWs connection. The sinter process can promote the mechanical strength and the conductivity of AgNW film [31]. Unfortunately, these attempts only can be used to construct simple film structure. It damages the electrodes mechanical stability and electrical sensitivity. On the other hand, it limits the application range of flexible electrode. Thus, it is necessary to prepare a flexible electronic with desirable patterns.

To realize above purpose, researchers have proposed to transfer the patterned conductive layer into polymer matrix. Jung *et al.* obtained a patterned MoS2/rGO conductive layer via a soft lithographic patterning approach. Subsequently, it was transferred onto PET film, and form a highly sensitive gas sensor [32]. Jeong *et al.* formed a AgNW layer with channel shape by attaching polymide (PI) masking film on bottom PDMS before pouring AgNW solution. Then, the patterned conductive layer was transferred into top PDMS film, and constructed a gas

sensor. By selecting a suitable channel length, a sample with high sensitivity, superior durability, repeatability, and hysteresis, etc. can be realized [33]. Furthermore, preparing a replica mold to shape the conductive layer is gradually adopted. Liu *et al.* obtained a flexible matrix structure by pouring liquid polymer into a designed solid mold. Next, graphene suspension was dropped into the flexible structure. After a thermal treatment, the flexible sensor can be formed. The fabricated device illustrated a high sensitivity, deformation limits, and repeatability, etc. [34] However, aforementioned methods generally require the polymers with a low viscosity, because it is necessary for polymer to evenly spread on the surface of conductive layer, and seep into interior of conductive layer to achieve encapsulation. Therefore, there are limited available polymer in the transfer process, which narrow the application. Meantime, designing special mold, using laser scribing, and patterning conductive layer complicate the transfer process, surge the cost, and hinder the large-scale applications, etc.

In the project, we bring forward to utilize 3D printing to fabricate a flexible electrode with complex patterns. In chapter 5, graphene conductive layer was transferred into elastomer with different patterns. We confirmed that the 3D printing is valid to encapsulate the organic material into polymer matrix, and the structure patterns have an important effect on the performance of the fabricated samples. Chapter 6 displayed that the inorganic conductive material, AgNW, was transferred into polymer matrix. Considering the excellent performances, the formed sample was possible to be used as wearable sensor. In these sections, the polymer with high viscosity have been demonstrated enabling encapsulate the conductive layer. For another thing, it can simplify the step to construct the samples, which can be used to replace multiple treatment in previous reports. Thence, it broadens the application, achieve a simple process, and reduces the cost, etc. The advances can provide a novel idea to construct a stable flexible electronic.

To summarize, the dissertation introduces some novel and facile strategies to construct flexible and stretchable sensor via 3D printing technology. The fabricated samples exhibit a large range of electrical response with outstanding repeatability and accurately fast dynamic responses. Human motion detections exemplify the potential applications of these formed stretchable sensors in wearable electronics, which demonstrates the research value to a certain extent.

CHAPTER 2 Review of Fabrication of Flexible and Stretchable Electronics

Over the past few years, flexible and stretchable electrodes have attracted intensive attention due to the increasing demand of electronics market [35-40]. They have been widely explored in diverse fields, such as wearable electronics, display and lighting devices, and energy storage devices, which have a profound influence on the current society and human living. For instance, organic light emitting devices (OLEDs) have enabled curved displays, contemporary lighting panels, and electronic books given the flexibility of the substrate. Thus, conventional paper may be replaced in the future, saving the natural resources and providing a better vision experience to customer. Wearable sensors can monitor human health conditions in real time, which greatly relieves the workload of doctors, facilitates telediagnosis, and develops self-awareness and self-monitoring for patients. Thus, there is no doubt that our daily life is being comprehensively changed with the invention of flexible and stretchable electrodes.

As the core component, the quality of flexible and stretchable electrodes largely determines the device performance. Thus, preparing a reliable electrode is one of the most important steps to form a high-performance device. However, it is challenging for the conventional approaches of fabricating flexible electrodes to meet the requirements of electrical and mechanical properties for large-scale applications, owing to the limitations of materials and manufacturing methods.

It is known that indium tin oxide (ITO) is widely applied as the basic material of conventional flexible electrodes because of its conductivity and optical transparency in past years [41]. But the main ingredient of ITO, indium, is very expensive and scarce, which means that ITO is hard to be widely used in engineering fields [42-44]. Furthermore, an ITO film is very brittle and can strongly absorb UV light [45]. Therefore, it is not suitable to integrate the ITO component into flexible electrodes in certain situations [41]. In addition, the traditional manufacturing process for ITO-based flexible electrodes is sophisticated. It not only has to proceed in a vacuum environment, but also requires high processing temperatures. All of these means that it is prohibitively costly and challenging to produce the flexible devices in a large scale [46]. Thus, it is crucial to develop innovative materials and processes for flexible and stretchable electrodes to cater for the increasing demand.

In this review, we systematically introduce several strategies and approaches to fabricate conductive electrodes for flexible and/or stretchable electronics. First of all, suitable conductive materials for those electrodes are briefly summarized with an emphasis on silver-based nanomaterials. Secondly, different strategies are surveyed to construct the conductive network for stretchable devices, e.g., the unidirectional and multidirectional stretchable devices. This review also highlights the recent research efforts in promoting the performance of conductive networks through physical and chemical routes. Finally, we showcase some representative applications of flexible/stretchable conductors and provide our perspective in this field. This review does not focus on the synthesis and preparation of the conductive materials, rather we thoroughly review various strategies in enhancing the conductive pathways with a purpose of inspiring researches in utilizing these strategies or their combination in various fabrication processes for flexible and stretchable electronics.

2.1 Nano-conductive Materials for Flexible and Stretchable Electronics

Nano-conductive materials play an important role in many fields involving soft-wearable devices, displays, and flexible medical devices, etc. The electric pathways can be formed by percolation network through contacting joints of nano-conductive materials. Suitable materials not only guarantee ultra-conductivity, but also provide an excellent flexibility and stretchability. Up to date, commonly used conductive materials comprise of graphene, reduced graphene oxide (rGO), carbon nanotubes (CNTs), copper/silver nanoparticles (CuNPs and AgNPs), copper/silver nanowires (CuNWs and AgNWs), silver flakes (AgFs), and so on (Table 2.1). Among them, graphene has attracted a lot of attention, due to its low electrical resistivity, excellent thermal stability, and superior mechanical properties [47]. However, pure single layer or a few layers of graphene are very challenging to prepare, which is a limiting factor in implementing them in a large scale. Therefore, majority of the graphene-based conductors involved graphene nanoplatelets and graphene derivatives, such as reduced graphene oxides [47-49]. rGO possess cost-efficiency, but harmful substances are inevitably involved in the conventional synthesis process [50-51]. Additionally, the conductivity of the obtained rGO usually is inferior to its counterparts. CNTs have outstanding mechanical property that is partially attributed to their hexagonal honeycomb skeleton [52]. However, the rough surface and the insufficient sheet resistance limit

their application potential in advanced flexible electrodes [53]. Copper-based materials show a great cost advantage. Unfortunately, toxic chemicals are involved and/or complex technologies and advanced equipment are required in the synthesis process [54-56]. On the other hand, copper possesses high reactivity and is easily oxidized when exposed in air, which results in a high sheet resistance [57]. Due to its superior conductivity, high transmittance, and excellent flexibility, silver-based materials have been explored as a suitable alternative candidate for the next generation flexible electrodes [58-60]. Various morphology of silver nanomaterials, such as 0-D silver nanoparticles (AgNPs) [61-63], 1-D silver nanowire (AgNWs) [64-66], and 2-D silver flakes (AgFs) [67-69], have been employed in the flexible/stretchable devices.

2.1.1 AgNPs

As the 0-D silver nanomaterials, AgNPs in general are not a good candidate for stretchable electrodes because of their high percolation threshold, and large particle-particle contact resistance. They have been used in flexible electronics where minimum deformation would not damage the electrical conductivity [70-72]. However, for large bending and stretching deformations, AgNPs tend to form cracks and electrical conductivity is significantly deteriorated [73]. As a result, they are usually employed as a decoration material to enhance the performance of electrodes [74-78]. It not only can increase the electron transfer rate, but also offer an ultra-catalytic activity [74, 79].When they were deposited as a conductive coating layer on a stretchable polymer substrate, the metal nanoparticles could experience the stress-induced nanoparticle reorganization upon deformation maintaining high electrical conductivity [80]. Conventional methods to synthesize AgNPs include electrical arc discharge [81-83], photo reduction [84-85], and chemical reduction [86-89], etc. Among them, chemical reduction method is the most common way in which silver nitrate generally is used as the metal precursor, and reducing agent of glucose, trisodium citrate, hydroxylamine hydrochloride, and hydrazine hydrate are selected [90-92]. By redox reactions, AgNPs are generated. In the past few years, various green synthetic methods have been proposed, such as polysaccharide, Tollens, irradiation, and biological routes, etc. [93] Silver nanoparticles have been used to decorate GO and/or rGO nanocomposites, facilitate nanowire sintering, and prepare conductive inks, etc. [94-98] The progress in the AgNPs synthesis encourages the exploration in expanding the application of AgNPs. For example, in addition to the electrical

property, another benefit of silver nanomaterials is their antibacterial property which is very attractive for wearable electronics [99-101].

2.1.2 AgNWs

AgNWs are one of the most widely used silver-based materials by virtue of high optical transmittance, superior electrical conductivity, and excellent mechanical property. To synthesize AgNWs with high quality, various approaches have been employed involving polyol method [102-103], modified-polyol method [104-105], and single-pot synthesis method [106], etc. The growth of AgNWs are generally achieved by reducing silver nitrate ($AgNO_3$) in the presence of polyvinylpyrrolidone (PVP) in ethylene glycol (EG). Key parameters to regulate the synthesis process include reaction temperature, $AgNO_3$ concentration, PVP molecular weight, and salt mediator type, etc. [107-108] Sonntag *et al.* investigated the effect of reaction temperature between 135 ℃ and 150 ℃ on the growth of silver nanowires, and proved that longer AgNWs are easier to form when the process is proceeded at higher temperatures [109]. Hemmati *et al.* summarized that low $AgNO_3$ concentration is prone to produce AgNPs, and too high concentration may produce complex nanostructures rather than 1D AgNWs due to the high concentration of seeds [108]. Recent reports have revealed that ultra-thin and long AgNWs with large aspect ratios were successfully prepared [110-112]. With these advances, AgNWs has been widely used to fabricate functional flexible/stretchable devices, such as electronic skin, solar cell, touch screen, and optoelectronic devices [113-116].

2.1.3 AgFs

AgFs has been adopted in fabricating flexible and/or stretchable conductive electrodes even though its application is not as wide as other silver-based materials. To date, there are several methods to prepare AgFs, including electrochemical synthesis [117], PVP-mediated galvanic replacement synthesis [118], and biosynthesis [119], etc. Generally, the dimension of synthesized AgF is within tens of micro-meters. Given the size scale and good conductivity, AgFs are considered as a good candidate forming conductive composites for screening printing and 3D printing processes. Matsuhisa *et al.* developed an elastic conductor ink comprised of AgFs, a fluorine rubber and a fluorine surfactant, which directs the formation of surface-localized conductive networks leading to high conductivity and stretchability in the screen-printed conductors [120]. Lei

et al. proposed to adopt AgFs as the conductive filler to prepare 3D-printed circuit. The thermal stability, excellent volume resistance, and strong adhesion of the printed sample have been demonstrated by a series of comparison experiments [121]. Yoon *et al.* provided a threshold of mass ratio between AgF and different polymers to improve electrical conductivity. Furthermore, self-wiring effect is identified during this printing process because of the phase separation of conductive ink, leading to concentrated AgFs in the core of the printed threads [122]. Recently, some researchers attempted to apply AgFs in other fields. For example, Lee *et al.* adopted AgFs in screen printing process, and proved that addition of AgF can improve the mechanical stability of the printed sample [123]. Ding *et al.* mixed AgFs and hydrogel to prepare conductors, and the obtained samples showed large stretchability and good cyclic durability [124].

Table 2.1 Characteristics of different conductive materials

Name	Description	Performance			Application	Ref.
		Electrical performance	Optical Transmittance	Mechanical Behavior		
ITO	0.12 μm thickness	11 Ω/sq;	90 %	Brittle	Flat Flexible electrodes	125
	Conventional ITO	50.5 Ω/sq				126
Graphene	30 nm thickness	460 Ω/sq		Flexible	Solar cells	127
	Printing film <20 nm in thickness	5 KΩ/sq~1 MΩ/sq	>80 %		Organic PV cells	128
rGO	rGO/metal film	18 Ω/sq	80 %	Flexible	Optoelectronic devices	129
	PPy/cellulose	1.7 Ω/sq		Stable	Paper-based devices	130
CNT	0.0% Nitrogen doped CNT 7.4% Nitrogen doped CNT	3.6×10^{-3} Ω/sq 5.5×10^{-3} Ω/sq			Possibly in Energy storage	131
CuNP	Inkjet printing, sintered at 250 ℃	0.88 Ω.cm			LED	132
CuNW	Purified CuNW	35 Ω/sq	81 %	Stable	Electrode	133
AgNP	Direct writing, annealing, AgNP ink with 71 wt.% solids	1.22×10^{-4}~ 3.64×10^{-5} Ω.cm	94.1 %		Large-area electronics	134
	Screen printing, AgNP on PU	1.64–2.85 Ω/sq		Flexible & stretchable	Wearable sensors	135
AgNW	AgNW/MM/PET	0.668 Ω/sq	91.25 %	Reliable	Electrodes	136
	AgNW/Metal	0.754 Ω/sq	90.3 %	Stable	Electrodes	137
	AgNW/ZnO	11 Ω/sq	90 %		Solar cell	138
	AgNW/ATO	18 Ω/sq	76–82 %	Flexible	Solar cell	139
AgNF	PEDOT: PSS/AgNFs/NOA 63 hybrid	2.12 Ω/sq	84.65%	Ultra-flexible	Supercapacitor device	140
	PANI/AgF/TPU	1.26×10^{-5} Ω.m		Flexible	Flexible heater	141

2.2 Strategies of Constructing Conductive Pathways in Flexible and Stretchable Electronics

The silver-based materials form conductive pathways during the deposition process, which is essential in the functional devices including but not limited to electrodes, interconnects, and sensors. When external deformation is applied (e.g., stretching, bending or twisting), the conductive pathway changes. For sensors, it leads to a varying sheet resistance thereby converting mechanical deformations into electrical signals. To date, a wide spectrum of Ag nanomaterial-based devices has been developed. According to the stretch direction the devices are capable of, they can be divided into unidirectional and multidirectional devices.

2.2.1 Unidirectionally Stretchable Devices

The unidirectionally stretchable devices show an excellent stretching capacity in a certain direction. They are usually composed of 1D fibers or pre-stretched flat-substrate combined with silver-based conductive material as shown in Figure 2.1a and 2.1b [142-143]. The 1D fibers include threads made of conductive nanocomposites or natural nonconductive fibers treated with conductive coatings. The fiber electrodes, as a fundamental building block, can be directly integrated into clothes and textiles for textile-based electronics, considering their light-weight, flexible, and weavable characteristics [144-146]. The pre-stretched devices display a periodical wrinkled structure, which endows the AgNW network with high conductivity, reliability, and mechanically tunable properties under different strain conditions. When the electrodes are stretched along the pre-strained direction or longitude direction of the meandering patterns, the resultant deformation tends to “straighten” the tortuous paths while the local conductive network remains intact, leading to minimal impact on electrical conductivity [21]. Because of these characteristics, the unidirectionally stretched devices are viewed having a great potential as a component of practical wearable electrodes where deformation in one specific direction is dominant [147-150].

Researchers have demonstrated several techniques to fabricate 1D fiber electrodes, such as direct spinning method, dip coating method, physical deposition, and chemical reduction, etc. In direct spinning method, AgNWs were simply mixed with elastomeric matrix to form electronic yarns; rearrangement of AgNWs towards the fiber surface due to the interaction between the AgNWs and coagulation solvents leads to high electrical conductivity of the fiber [151]. Based on

the processing environment, direct spinning method can be furtherly divided into wet spinning method, dry spinning method, and thermal drawing method. In the wet spinning method, the polymeric solution was injected into a coagulation bath at a suitable rate. Subsequently, AgNW-based conductive fibers can be prepared by directly pulling out of the bath as shown in Figure 2.1c. As a scalable production technique in industry, the wet spinning method has been widely adopted in research laboratories as well [152-158]. In the dry spinning method, polymer in a volatile solvent is spun in the air ambient condition to directly form fibers (Figure 2.1d) [159], where no additional solvent is involved to coagulate the polymer solution, and no electrical field is needed compared with the traditional electrospinning technique [160]. The spun fibers have been stitched into gloves to realize a smooth human-machine operation [151]. In the thermal drawing method, a preform is fed into furnace where materials soften or melt, and an external force is applied to extract functional filaments. A fast-drawing process can be realized (Figure 2.1e) [161-162], which features with low cost and large scalability. As a matter of fact, hundreds of kilometers of optical fibers are typically produced by the thermal drawing process. Up to now, thermal drawing have been employed to produce flexible electronic fibers using various metals and nanocomposite materials, elastomers and liquid metals, [163] with potential applications in smart textiles, robotics, and medical implants, etc.

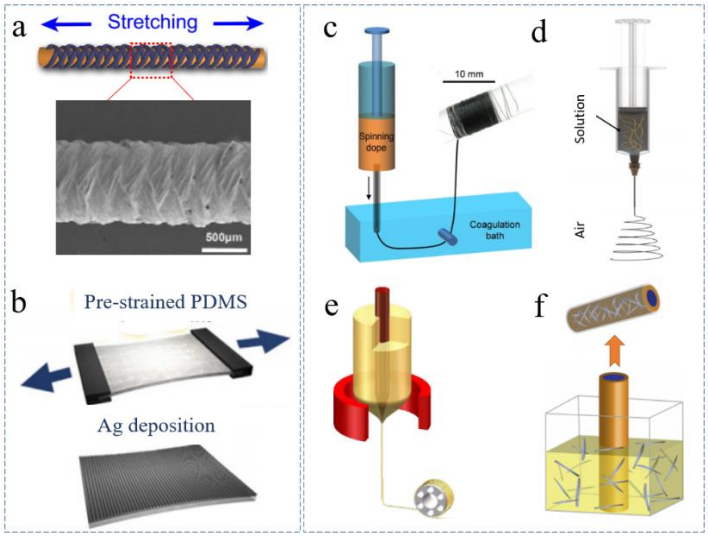

Figure 2.1 (a) A conductive fiber during a stretching process [148]. (b) A pre-stretched flat-substrate combined with Ag conductive material [164]. (c) Illustration of wet-spinning process [151]; (d) illustration of dry-spinning process [165]. (e) Illustration of thermal drawing process [161]. (f) Illustration of dip coating process [166].

Dip coating method is also widely adopted to fabricate a unidirectional stretched-devices due to its simple process, and being a cost-efficient and mature technique [167]. The process contains immersing an elastic yarn into AgNW solution and adhering the AgNWs onto the yarn (Figure 2.1f) [166]. Several factors determine the structure and performance of AgNWs deposition, including the dip coating cycle times, coating speed, and the concentration of AgNW dispersion [168]. Generally, these yarns decorated with AgNWs exhibit not only an ultra-high sensitivity to external deformation, but also long-term cycling stability [169-171]. Taking advantage of the merits, the conductive fibers have been applied to prepare smart windows, implantable devices, smart clothes, and so on. [168, 172-174]. Recently, physical deposition and chemical reduction methods have also been demonstrated as possible routes to prepare conductive fibers. For instance, Hwang *et al.* have coated AgNW-wound micrometer scaled PET fiber mats via an ultrasonic spray method. It has significantly improved the mechanical durability and electrical stability of the devices [175].

2.2.2 Multi-directionally Stretchable Devices

The unidirectionally stretchable devices cannot respond to multi-directional deformations, to some extent, limiting its application fields. With advancement of technology, several multi-directionally stretchable devices have been demonstrated. Based on the physical structure of conductive network, the multi-directionally stretchable devices can function based on 2D planar patterns or films and 3D constructed networks.

2.2.2.1 2D Conductive Network

Common methods to construct 2D AgNW network are summarized in Figure 2.2, comprising of drop casting, spin coating, bar coating, vacuum filtration and transfer coating, spray coating, patterning, and printing, etc.

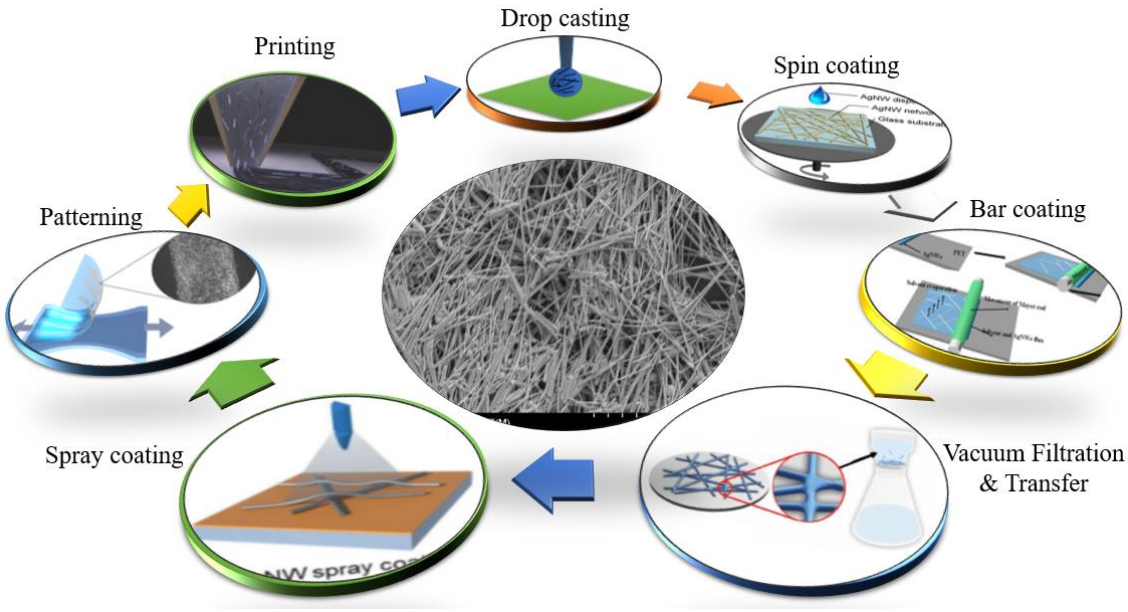

Figure 2.2 Different methods to fabricate the AgNW network [103, 176-180].

Drop casting preparation is realized by directly casting AgNW dispersion onto a target substrate surface, followed by solvent drying [33, 179, 181]. The AgNW network density depends on the concentration of dispersion and amount of drops casted in the area [182]. In addition, the substrate largely influences the coating morphology fabricated by drop casting [183]. This method is simple and efficient, but it has a limitation in practice that uneven distribution occurs due to coffee ring effect, which may need special consideration [184-185]. The nonuniform distribution of AgNWs likely brings out varying film thickness, which results in an issue that different local sites show different electrical resistance. To overcome this issue, Eslamian *et al.* demonstrated that by treating the substrate with ultrasonic vibration, the non-uniform distribution of AgNWs has been improved during the drop casting process [186].

Spin coating is widely used in laboratory environment. The preparation is a consecutive process containing dropping the AgNW dispersion onto a flat substrate, spreading the droplet into a thin wet film at a specific rotation speed, and producing a solid film after solvent evaporation [187-188]. The AgNW network performance is regulated by substrate, spinning fluid, and rotation speed, etc. The characteristic of spinning fluid (such as viscosity, volatility, surface tension, and solid concentration) and the substrate roughness and surface energy, determine the fluid spreading and evaporation rate, which significantly affects the final thickness and morphology of the coating [38]. The rotation speed is inversely proportional to the coating thickness

[189]. Too fast rotation speed tends to produce a broken conductive pathway, due to ultra-thin coatings, whereas low rotation speed can lead to uneven formation of conductive network due to possible AgNW aggregation.

Mayer-rod coating technique has been used to prepare transparent conductive coatings [190]. The formation process includes dispersing a solution or dispersion onto a substrate, followed by using a Mayer-rod to spread it out to form a uniform coating. The coating thickness can be determined by the line diameter and the Mayer-rod interval. The concentration of AgNW dispersion can be used to regulate the electrical performance of the coating. In addition, the coating density is also controlled by the number of coating cycles. It is worth noting that, the evaporation rate in Mayer-rod coating process is usually much faster than that in drop casting. The reason is due to the thin wet film generated by the Mayer-rod coating method, which can suppress some undesirable phenomena, e.g., coffee ring effect. An additional merit of this coating method is that the AgNWs become self-aligned under the shear stress during the coating process. The aligned AgNW assembly can enhance the wire-to-wire contacts and reduce the contact resistance between AgNWs that will be discussed later.

Vacuum filtration & transfer (VFT) technique has been employed to prepare transparent and stretchable electrodes [191-193]. Typically, three steps are involved: (1) filtering the AgNW suspension by a filter; (2) fabricating AgNW network on the filter surface; (3) transferring the network to an elastic substrate. In the first step, the pore size of the filter is generally selected to be about 30 μm considering the dimension of AgNWs. In the second step, the density of AgNW network is determined by the concentration and the amount of AgNW suspension. In the third step, a strong adhesion can be achieved because the AgNW network is completely embedded in the polymer. Furthermore, the flexibility and stretchability of electrodes are controlled by using various substrate materials, such as Polydimethylsiloxane (PDMS), Polyethylene terephthalate (PET), Polyethylene oxide (PEO), and Polyacrylamides (PAM), etc. Compared with other methods, VFT has the minimal waste of AgNWs to construct a conductive network. However, the disadvantage is that the film area is limited by the filter area.

To prepare a 2D conductive networks by spray coating method, an electrostatic sprayer or an airbrush is adopted [194-195]. Under an electric field or a compressed air, the AgNW suspension

is broken into fine droplets, precipitating on a target substrate. During this process, a series of parameters play an important role to construct the AgNW network, such as substrate temperature, spraying pressure, and scanning rate, etc. The substrate temperature can be used to regulate the evaporation rate which affects the AgNW distribution. Spraying pressure influences the droplet size and the coating uniformity. Scanning rate directly determines the amount of AgNW deposition that is proportional to the conductive pathway. The spray coating technique can fabricate AgNW networks on curve and irregular surfaces. In addition, it allows a homogeneous and large-area AgNW network thanks to its scalable coating process and capability of including multiple spraying nozzles. To better utilize these merits, it is expected to combine this technique with roll-to-roll process to achieve a large-scale production.

As a feasible approach to fabricate flexible and stretchable electrodes out of rigid materials, patterning has attracted many researchers' attention [196-197]. Various kinds of electrode shapes can be formed through additive deposition and subtractive removal processes by applying stencil masks and etch masks, respectively. [198-200]. Typically, electrodes have been patterned into fractal-shaped serpentine geometry, and Kirigami designs (such as cuts and folds) to render the desirable stretchability [201-202]. Similar to the wavy structures (or wrinkled structures) on the pre-strained substrates, the meandering patterns on solid substrates, or Kirigami designs enhanced the stretchability while maintaining the electrical contacts in the conductive network. Won *et al.* employed Kirigami method to make patterned electrodes. The designed pattern imparts excellent elasticity to the ultrathin colorless-polyimide electrode with tensile strain up to 400%. Meantime, through more than 10000 cycles of stretching, the electrode exhibits good reversibility and 80% optical transparency [203]. Chou *et al.* compared the electrical performance of straight line and serpentine line patterned AgNW electrodes. The results show that although its initial resistance is 7 times higher than that of straight line, the maximum strain of serpentine line is 5 times larger than its counterpart at the electrical disconnection. Furthermore, after 100 cycles stretching with 1 % strain, the resistance change of serpentine line (without PDMS backing layer) is only one-fifteenth of the resistance change of the straight-line one. Therefore, the serpentine line electrodes showed remarkable electrical stability [204].

Printing technology also attracts significant attention to fabricate flexible and stretchable

devices due to the advantage that it can directly pattern and construct the devices without any masks and templates. The commonly used printing technologies include inkjet printing [205-207], electrohydrodynamic (EHD) printing [208-209], aerosol jet printing [210-211], and screen printing [212-213], etc. Generally, these printing methods consist of three steps: (1) preparing a printable ink; (2) developing a printing process; followed by (3) optional post-printing treatments. However, each printing has different focus and requirements regarding the ink formulation and printing process. Inkjet printing deposits diluted AgNP inks or AgNW inks on flexible or stretchable substrates through piezo-actuated nozzles or thermal bubble ejectors. It can generate custom-designed patterns, and easily integrate different materials into conductive layers. EHD printing uses electric field to actuate the ink ejection, where electric charges accumulate near the surface of the ink meniscus at the nozzle tip. A droplet is ejected when the Coulomb force overcomes the surface tension and ink cohesion force. It has the advantage of printing viscous inks and utilizing small nozzle sizes. When operating at the cone-jet mode, the size of ejected droplets is much smaller than the corresponding nozzle size due to necking effect, which has the potential to realize high resolution printing. It also has been combined with the direct ink writing to print AgNW patterns [214]. Aerosol jet printing is evaluated as a strong competitor of the printing methods mentioned above. Numerous tiny droplets are generated in an atomizer and focused by a sheath gas when the aerosol is delivered to the printing nozzle. Screen printing, as a mass printing technique, is performed by using a squeegee to press a conductive ink through a stencil and print on the substrate. Different from other printing methods, screen printing is a contact printing process with a pre-patterned screen; usually the ink is highly viscous polymer composites with conductive materials. Although it is classified as 2D planar films in this review, the polymeric electrodes fabricated by screening printing usually possess larger thickness.

Table 2.2 Methods to prepare the AgNW network and corresponding characteristics

Method	Materials and Processes	Substrate	Property	Characteristic	Ref.
Drop casting	AgNW/ polyimide (PI) film	Glass	Resistance~20 Ω/sq Transmittance~83 %	Simple steps, likely uneven distribution	182
	AgNWs, ultra-long ~50 μm Aspect ratio >1000	PET	Resistance~20 Ω/sq Transmittance~90 %		215
Spin coating	Hot lamination process	Polycarbonate (PC) film	Resistance~12.5 Ω/sq Transmittance~94.5 %	Uniform distribution, tunable thickness	216
	AgNWs, diameter ~52 nm Aspect ratio ~1000	PET film	Resistance~54 Ω/sq Transmittance~92 %		217
	AgNW/ZnO composite film	PET film	Resistance~9 Ω/sq Transmittance~92 %		187
	AgNWs decorated with cobalt nanoparticles	Thermoplastic PI film	Resistance~52 Ω/sq Transmittance~94 %		218
Mayer-rod coating	AgNWS, diameter ~40 nm Length ~25±5 μm	Insulator surface	Resistance~30 Ω/sq	Large area, good alignment	219
	TiO_2-coated AgNW film Diameter ~10 nm Length ~80 μm	PET film	Resistance~80 Ω/sq Transmittance~75 %		220
	AgNWs with diameter ~500 nm Length ~10 μm	Polycarbonate (PC) film	Resistance~12.1 Ω/sq Transmittance~89.5 %		221
	hydrogen chloride (HCl) treatment	PET film	Resistance~175 Ω/sq Transmittance~75 %		222
Vacuum	AgNWs with diameter ~60 nm	Self-adhesive PET	Resistance~13 Ω/sq	Tunable	223

Filtration and Transfer	Length ~10 μm	substrate	Transmittance~67 %	thickness, small-scale production	
	AgNWs with diameter ~20~70 nm Length ~120 μm	PET film	Resistance~4.95 Ω/sq Transmittance~81 %		224
	AgNWs with diameter ~90 nm Length ~10 μm	Mixed esters of cellulose membranes	Resistance~50 Ω/sq Transmittance~85 %		225
	AgNWs with diameter ~200~250 nm Length ~20~30 μm	PDMS film	Resistance<1.0 Ω/sq cell viability~90 %		226
Spray coating	AgNWs with diameter ~25 nm Length ~90 μm	Glass	Resistance~10 Ω/sq Transmittance~87.4 %	Tunable thickness, large area coverage, various substrates	195
	spraying distance ~12 cm moving speed ~1.5 cm/s spraying pressure ~200 mbar	Organic p-i-n type solar cells	Resistance~10.7 Ω/sq Transmittance~84.3 %		195
	AgNWs with diameter ~50 nm Length ~20 μm	PI substrate	Resistance~ 4.64 Ω/sq Transmittance~87.3 %		227
Printing	AgNWs with diameter ~81±30 nm Length ~37±19 μm	AgNW/CNF screen printed on PET	Resistance~12±5 Ω/sq Transmittance~74.8 %	Custom-designed patterns, potential for large-scale production	228
	AgNWs with diameter ~25±5 nm Length ~20±5 μm	AgNW EHD jet printed on PET film	Resistance~45 Ω/sq Transmittance~90 %		209
	AgNWs with length~30 μm Aligned AgNWs	AgNW ink directly printed on silicone	Strain-sensing range 10 %~50 % Gauge factor~100		229
	Printing speed~40 mm/s Printing angle~45°	AgNW screen printed on PET film	Resistance~0.72 Ω/sq Roughness~2.7 to 1.1 μm		230
	AgNWs with diameter ~20 nm Length ~2 to 5 μm	AgNW ink inkjet printed on PET film	Resistance~13 or 23 Ω/sq Transmittance~81.9 % or 83.1%		231

2.2.2.2 3D Conductive Network

In addition to 2D planar conductive networks for flexible/stretchable electrodes, AgNW networks can be constructed through out of plane morphology or 3D arrangements.

One effective way to build the 3D conductive network is through 3D extrusion printing, or direct ink writing (DIW). As an additive manufacturing (AM) technique, it can realize a rapid prototyping by continuously stacking the sequential layers. The technique is viewed as a promising route to prepare various functional devices, such as electronics and energy storage devices [232-234].

The printing process is straightforward that the ink is directly extruded from the printing nozzle under compressed air and deposited through layer-by-layer means. However, the challenge is to develop a printable and reliable conductive ink formulation. Specifically, it requires shear-thinning property to facilitate the extrusion printing process, thixotropic property to quickly recover the viscosity when the stress is removed (i.e., when the thread is extruded and deposited) [235]. A typical example of conductive ink for 3D printing through DIW is shown in Figure 2.3a. The ink is composed of AgNWs, GO, and $Li_4Ti_5O_{12}$ (LTO) mixed with distilled water, where functional NWs are used as the base materials to integrate with GO to form a viscous and thixotropic paste. As a viscosity modifier, the incorporation of GO enhances the ink printability through thickening and stabilizing the ink formulation, as well as endowing the system with good mechanical toughness [236]. Yoon *et al.* prepared a conductive ink by mixing AgF, PDMS, Ecoflex, and MIBK solvent. By changing the mass ratio of AgF and polymer matrix, an excellent conductivity of 85.91 $S \cdot cm^{-1}$ (for conductive composites) was obtained on the 3D printed-structure [122]. Also, a AgF concentration gradient is realized by adopting polymer mixture instead of a single one. The reason is that the lower viscosity PDMS polymer diffuses out of the polymer composite during the drying process (Figure 2.3b) [122], which concentrates the AgFs inside and simultaneously forms an insulating barrier around the printed structures. In addition, Lei *et al.* have demonstrated 3D printing conductive filaments through fused deposition modeling, that are made from composites of AgFs and saturated

polyester and polyvinyl butyral. These works verified 3D printing is an efficient and green way to construct flexible and stretchable electrical devices [121].

However, a key challenge does exist for the 3D printing process through direct ink writing. Due to the intrinsic low surface tension of most liquid elastomers, the conductive fillers are easily wrapped and separated from other filler materials during ink mixing. Therefore, a large amount of conductive materials (e.g. ~70-80 wt.% or higher) needs to be incorporated in order to form conductive path in the printed composite conductors.

An alternative method is to modify a 3D flexible substrate or template with conductive materials. It involves depositing conductive materials on a 3D porous structure to form a multiple conductive pathway as depicted in Figure 2.3c. Then, the change of contacts among the conductive pathway upon deformation can transform into electrical responses to realize sensing purposes [237]. Different from the method of 3D printing composite ink, the conductive layer coats the pre-formed 3D structures to form the conductive pathway. Li *et al.* selected a 3D polyurethane (PU) sponge onto which AgNWs were deposited through dip coating method. Dopamine coating was carried out to enhance the adhesion between AgNW and sponge substrate. The fabricated structure shows a high electrical conductivity of more than 27.78 S/cm [238]. Similarly, Jesural *et al.* prepared a AgNW stretchable electrode on a wavy microprism-mediated PU substrate. The resistance of electrode remains stable under parallel uniaxial stretching and perpendicular stretching [239]. Sun *et al.* constructed a pressure sensor by depositing AgNW network on a nature rubber latex foam (NRLF). The sensor shows not only a high electrical conductivity, but also an ultra-flexibility and repeatability [237]. Wei *et al.* immersed a cotton sheet into AgNW suspension for several times to obtain a flexible pressure sensor. The results showed the cotton sheets resistance is inversely related to dip-coating cycle. The formed pressure sensor displays ultra-sensitivity, fast response, and high stability [240]. Chen *et al.* added nano-fillers in the ink formulation, which serve as rheology modifier and sacrificial templates. Those filler particles were removed by acid etch to obtain hierarchically porous structures. Through a dipping-drying process, CNTs were deposited onto the printed models which enables not only adjustable

mechanical property, but also provides an ultra-sensitivity and high resistance recoverability [241]. We included this reference here although CNTs instead of silver materials were employed. However, the principle can be applicable for the latter.

The 3D templating method is very effective in constructing conductive networks, however, poor adhesion between the conductive layer and polymer matrix can be an issue in certain conditions. On the other hand, directly 3D printing the Ag/polymer composites requires significant amount of silver materials to form the conductive pathway. Based on these reported works, a new method is proposed to utilize 3D printing and water-induced polymer swelling to fabricate 3D wrinkled stretchable sensors [63, 242]. In this method, soluble powders and commercial silicone polymers are selected to formula the printing ink which is 3D printed to form custom-designed patterns and structures. The printed patterns are soaked in an aqueous solution, where a dramatical swelling is created under the action of osmotic pressure as the doped powder releases. A conductive layer is then deposited on the swollen patterns via liquid processing. Finally, wrinkled conductive structures are formed upon removal of residual water in the swollen samples, as shown in Figure 2.3d and 2.3e. The prepared stretchable sensors possess hierarchical wrinkled structures on the 3D printed patterns rendering outstanding electrical performance.

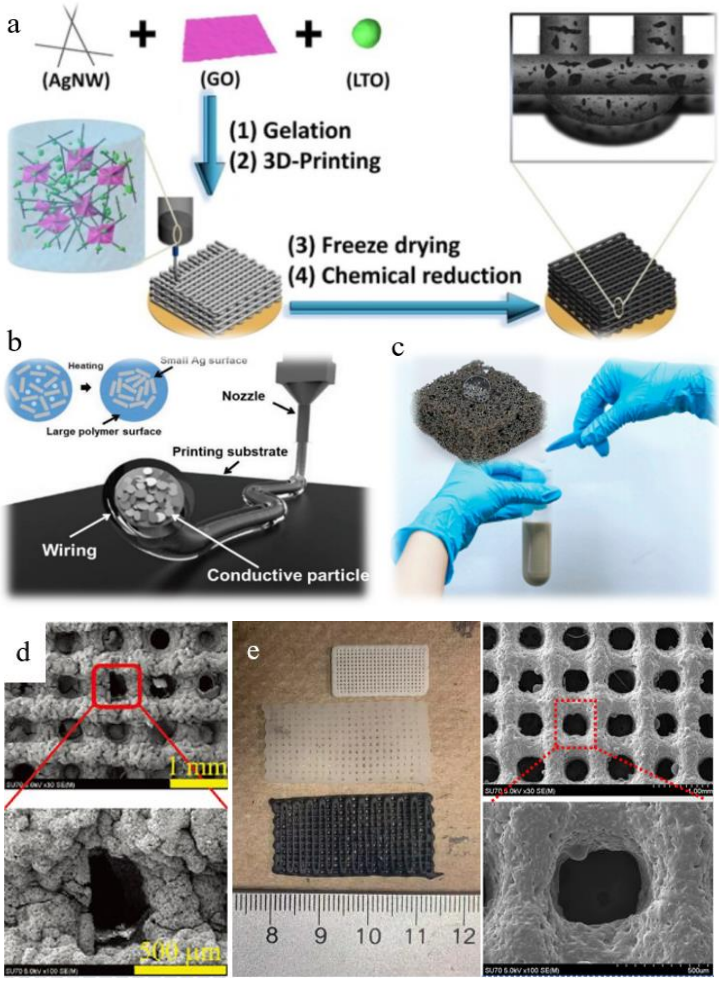

Figure 2.3 (a) Schematic diagram of preparing conductive ink for 3D printing [236]. (b) Direct printing the conductive ink with gradient concentration on the cross-section [243]. (c) Immersing the 3D structured sample into AgNW suspension [237]. (d) AgNPs deposited on 3D printed structures [63]. (e) Graphene deposited on 3D printed structure [242].

2.3 Enhancement in Electrical Conductivity of AgNW Networks

Because of its unique 1-D structure, AgNW network shows superior electrical reliability for flexible/stretchable devices when compared with 0-D AgNPs and 2-D AgNFs. The characteristics are attributed to the fact that excellent conductivity is preserved within each individual AgNW. Meanwhile, a conductive pathway is constructed as AgNWs contact each other. The 1-D shape of AgNWs facilitates maintaining the electrical contacts among the network upon deformation. This section reviews several methods to enhance the conductive network by effectively increasing the

contacts among the AgNW networks.

2.3.1 Morphology and Controlled Assembly of AgNWs

As briefly discussed in Section 2.2.1, various methods have been employed to synthesize AgNWs. Each approach tends to produce the AgNWs with different characteristics, such as length, diameter, surface treatment, which have a great impact on the conductivity of the network [244-245]. Park *et al.* constructed AgNW networks with the same density but different dimensions of AgNWs, and found that the resistance of AgNWs with narrower width displays fast increasing in a cyclic bending test [246]. Marus *et al.* compared the performance of AgNWs with various diameters in the range of 30 nm to 100 nm. The results show that as diameter increases, the optical transmittance improves and the sheet resistance decreases [247]. This group also has studied the relationship between the conductivity/transmittance and the AgNW length. Combined with simulation and experiment results, they drew the conclusion that longer AgNWs lead to a lower sheet resistance in a non-linear relationship [244]. The relationship between the dimension of AgNWs and electrical performance at different coverage densities is summarized in Figure 2.4a~2.4d. The AgNWs with longer length and larger diameter tend to have a higher transmittance and lower sheet resistance under the same coverage density. In addition, Wang *et al.* inferred that lower sheet resistance and 90~97.5% transmittances can be realized by reducing the PVP layer thickness on the AgNW surface without any post-treatment [248].

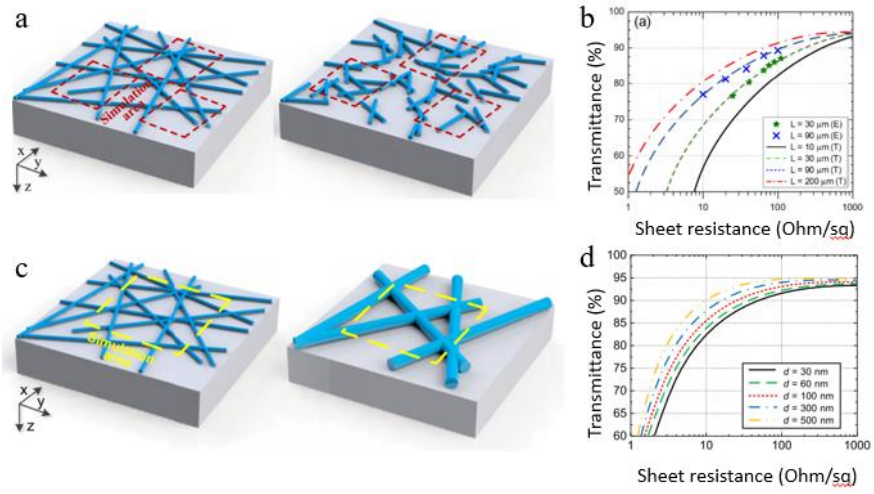

Figure 2.4 (a) AgNW film model with different lengths on substrate [244]. (b)

Transmittance and sheet resistance of AgNW film with different lengths [244]. (c) AgNW film model with different diameters on substrate [247]. (d) Transmittance and sheet resistance of AgNW film with different diameters [247].

Additionally, the conductivity of AgNW network can be enhanced by controlling the AgNW assembly process (Figure 2.5a) [249]. This can be attributed to the shortening of the effective path of electron transport, reduction of the electrical percolation threshold, and increase in the contact area among the aligned AgNW assembly. Xu *et al.* indicated that the resistance of AgNW network is certainly related with the orientation angle of NWs, and an electronic transport anisotropy of 10 times was exhibited on the aligned AgNWs while maintaining low resistance in all directions [250]. Takemoto *et al.* drew the similar conclusion that more aligned AgNWs tend to possess lower sheet resistance when compared with randomly distributed-AgNWs [251]. Thus, in this section, several methods were reviewed to achieve aligned AgNW distribution to enhance the conductivity of AgNW network.

Mayer rod coating is a common method to align the AgNWs, in which a wire-wound metering rod is dragged over the AgNW suspension on the substrate surface (Figure 2.5b). The combined interaction between shear stress alignment and potential electrostatic pinning (through substrate treatment) produced highly aligned AgNWs on the substrate along the coating direction [252]. Dong *et al.* prepared aligned-AgNW networks by Mayer coating followed by substrate stretching that the maximum alignment order even reached 0.97 [253]. Chen *et al.* fabricated a roller-induced AgNW network that showed low sheet resistance, high optical transmittance, and ultra-bending stability [254]. Yang *et al.* prepared cross-aligned AgNW networks by performing multiple times of bar coating in various directions. The crossed-alignment and multi-stacking structure promote the conductivity correspondingly [255].

With the capability of producing custom-designed complex patterns and the potential of large-scale production, various printing techniques have been employed to obtain AgNW alignment during printing process, such as capillary printing [249], gravure printing [256], inkjet printing [257], electro-hydrodynamic jet (EHD) printing [258], etc. In these processes,

the alignment of AgNWs is mainly realized under the action of capillary or shear forces (Figure 2.5c) [249, 251]. Here, taking EHD printing as an example. Parameters, such as printing speed, AgNW concentration, and ink viscosity, determine the morphology and electrical property of the printed structures. Cui *et al.* pointed out that fast printing speed tends to produce highly oriented AgNW network [214]. Li *et al.* compared the AgNW/PEO composites with different weight ratios, and proved that the EHD printed samples with a ratio of 90:10 possessed excellent electrical property thanks to the aligned AgNW network formed during printing [259].

The Langmuir-Blodgett (LB) assembly is a low cost and useful technique to arrange the AgNWs networks at the air-liquid interface, usually followed by dip coating to transfer the assembled NWs to a substrate as shown in Figure 2.5d [260, 261]. Under the action of uniaxial compression, NWs spread at the interface gradually form an aligned and close-packed NW layer [262]. Zhu *et al.* employed a modified LB assembly approach to fabricate aligned NWs. In the method, a spinning rod was designed to form a spinning Langmuir film to align the zinc oxide NWs under shear. They also studied the effect of surfactant on the quality of aligned NWs, which enhances the shear flow to furtherly improve the alignment of NWs. [263]. Duan *et al.* demonstrated that a heating water-bath can assist the assembly of AgNWs by introducing convective flow to bring the AgNWs to the air-water interface. Significant enhancement in the AgNW alignment has been obtained as compared with that in the absence of the convective flow [264]. Shi *et al.* fabricated hybrid films of GO and AgNWs using LB assembly method, and indicated that addition of GO not only enhances the adhesion between AgNWs and substrate, but also facilitates the release of silver ions to fight bacteria [265]. In view of the superior antibacterial property and optical property, the AgNW hybrid films could be very promising for the next generation multi-functional films, which will be reviewed in detail in section 2.4.3.

Although the conventional dip coating usually cannot render alignment of nanomaterials, some researchers modified the dip coating process to realize the shear-induced alignment of AgNWs, as shown in Figure 2.5e. When the substrate is pulled up,

the relative movement between the substrate and suspension bring out the shear force that controls the AgNWs' orientation [266]. The modified dip coating process is accompanied by fast evaporation of solvents and immobilization of aligned AgNWs. Pu *et al.* prepared aligned AgNWs by withdrawing PET substrate from AgNW ethanol suspension. They found out that the ratio of length and diameters (L/D) has an influence on the alignment order of AgNWs, where the ones with small and medium values are easier to produce the aligned-AgNWs because of their good dispersion and rigidity in nature [267]. In addition, coating speed can regulate the alignment of AgNW in the dip coating process. Shin *et al.* utilized a heat-assisted dip coating (to accelerate solvent drying) to achieve the aligned AgNWs. Higher temperature facilities the solvent evaporation and correspondingly the AgNW pinning and alignment. They further studied the effect of withdrawal speed on the degree of alignment, and draw a conclusion that the maximum alignment appears at 1 mm/s by comparing the orientation of AgNWs under various speeds [268]. Their explanation is that the withdrawal speed can regulate the deposition thickness that has a crucial influence on pinning the AgNWs.

Some researchers proposed to obtain highly oriented AgNWs by using an external electric field, leveraging the properties of material polarization and dispersion in a low dielectric solvent [269]. Driven by dielectrophoresis, the AgNWs align themselves along the applied electric field as shown in Figure 2.5f [270]. In the electrokinetic assembly process, the degree of alignment of AgNWs is determined by the electric field strength, frequency, and electrode geometric dimensions [271-273]. Regarding the electric field-induced transport, Farain *et al.* mentioned that it is necessary to select a suitable suspension medium with low conductivity and high viscosity to employ a large electric field in order to obtain controllable movement of AgNWs [271]. Wang *et al.* indicated that a higher order value of alignment is prone to appear at high frequency (1 MHz) than at low frequency (10 kHz) with the same electric field magnitude [273]. Paloma *et al.* investigated the effect of electric field frequency on the orientation of AgNWs in DNA semidilute suspensions. They noticed that a low frequency AC electric field (e.g., 1 Hz) can facilitate the formation of highly oriented-AgNWs under the assistance of orderly DNA coils formed by the

application of electric field [274].

In addition, magnetic field-assisted assembly has been used to obtain highly ordered AgNWs. The nonmagnetic AgNWs need further modification to respond to the external magnetic field. One approach is to decorate the AgNWs with Fe_3O_4 by a co-precipitation method before the assembly process [275]. The magnetic properties of the decorated-AgNWs can be regulated by the number of magnetic nanoparticles [276-277]. When applying an external magnetic field, the Fe_3O_4 coated-AgNWs can be aligned along with the applied magnetic field as shown in Figure 2.5g. It has been demonstrated that a highly-ordered NW film possessed superior conductivity and transparency when compared with those randomly deposited films [278].

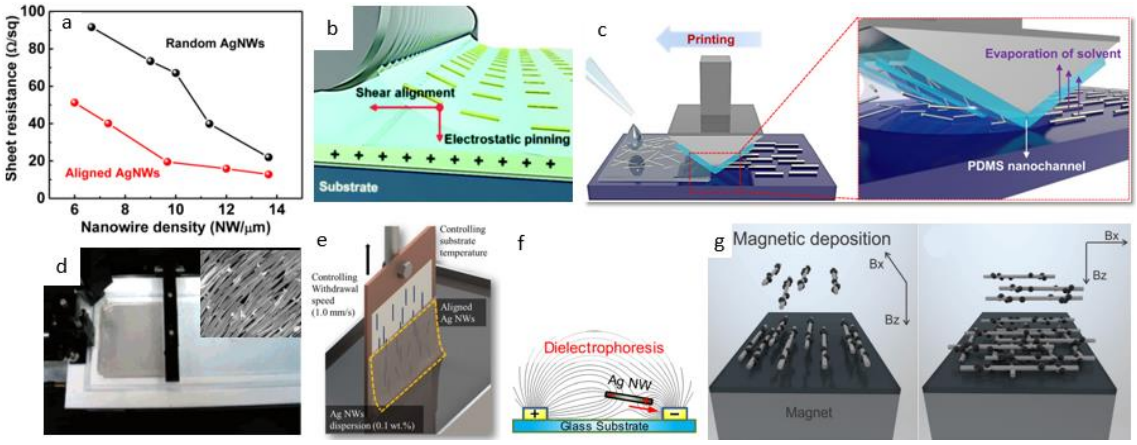

Figure 2.5 (a) Resistance of random AgNWs and aligned AgNWs [249]. (b) Schematic diagram of AgNW alignment during Mayer-rod coating process [252]. (c) Schematic diagram to form aligned AgNWs during capillary printing process [249]. (d) AgNW alignment during LB process [260]. (e) Process schematic of AgNW alignment during dip coating process [266]. (f) Schematic diagram of an AgNW oriented by the electric field [270]. (g) Schematic diagram of magnetic field-aligned AgNWs [278].

2.3.2 Modifying Conductive Network

As for AgNW network, the sheet resistance mainly arises at contact areas between nanowires. Reducing the contact resistance is crucial to enhance the conductivity of the network. Herein, the methods for contact resistance reduction are classified into three categories including heat-induced welding, chemically induced welding, and optically induced welding.

2.3.2.1 Heat-induced Welding

Heat-induced welding uses high temperature to melt NWs to reduce the contact resistance. Depending on heat sources, the heat-induced welding can be further classified into thermal annealing, electrical sintering, and electron beam welding, etc.

The thermal annealing has been applied as a simple and effective way to reduce the sheet resistance of AgNW network [279-282]. Figure 2.6a shows the morphology changes before and after a thermal welding process. With increase of temperature, the nanowire contact area increases in a certain temperature range [283]. Bardet *et al.* reported a continuous decrease of sheet resistance when the annealing temperature increases as shown in Figure 2.6b [284]. Generally, in the low temperature range, the resistance drop is caused by desorption of residues and degradation of polyvinylpyrrolidone (PVP). With increasing of temperature, the resistance drop slows down. When the temperature reaches the thermal annealing temperature, e.g., above 200 ℃, the electrical resistance further reduces because more sintered-junctions form. Rayleigh instability of AgNWs appears at a temperature exceeding 325 ℃, which degrades the conductive pathway leading to a rapid increase in the electrical resistance of AgNWs [282, 285]. In addition, it has been reported that a higher annealing temperature is required to effectively reduce the electrical resistance as the diameter of AgNWs increases [286]. Finally, the annealing duration also has an important effect on the thermal welding. Although sufficient time is needed to melt and fuse the joint contacts, prolonged annealing time is detrimental to the AgNW network because of the appearance of pathway interruption.

The electrical sintering technique modifies the AgNW network by controlling the current-assisted joule heat to enhance the network conductivity [287-289]. The local joule heating is produced at a high current density region near wire-wire contacts. The surface diffusion-induced electro-migration in these regions facilitates continued atomic movement and removal of surface ligands, which welds the poorly contacted-AgNWs and reshapes the conductive pathway. More than 7 orders of magnitude reduction in contact resistance has been obtained as a result of the electrical welding treatment [290]. To elucidate the relationship of current density with respect to the wire-wire contact shape,

researchers computed the distribution of current density at various contact morphologies by finite element simulation. The results showed that the electrical current crowding is reduced with increase of contact area between AgNWs (Figure 2.6c). At the same time, the current density is proved to uniformly distribute through the contact area [290]. Vafaei *et al.* further indicated that current welding not only reduces the contact resistance, but also ensures the stability of corresponding resistance [287]. As shown in Figure 2.6d~2.6e, a good linear relationship between voltage and current was obtained after the current welding process. Recently, a novel electrical sintering was demonstrated in which the charged-droplets of AgNW dispersion were concurrently sprayed and self-welded to form the AgNW network. With the deposition of the charged droplets, the electric charges flow through the entire conductive network, which brings out an electrical current. Owning to the contact resistance between AgNWs, Joule heating is produced and the welding of AgNWs spontaneously occurs [291].

The electron beam welding is another type of heat-induced welding. The specific welding process is described in Figure 2.6f. High energy electrons were generated and accelerated between the cathode and the anode in a vacuum chamber. They transferred energy onto the surface of AgNWs through irradiation. As a result, the contact points between nanowires were fused, causing a stable conductive joint structure [292]. Unlike other heat-induced welding, the electron beam welding can avoid some detrimental issues, e.g., requirement of heating the entire AgNW network in thermal welding process and a large variation in electrical resistance usually produced during electrical sintering process due to the nonuniformity of the network and welding current. In Figure 2.6h, researchers compared thermal welding and e-beam welding of AgNWs contacts [292]. Considering that the energy was transferred by accelerated electrons, and a fast-thermal gradient was formed in the melting process, it is possible to form an enhanced localized re-solidification among the AgNWs. Hong *et al.* studied the influence of irradiation time on the resistance of AgNW network [293]. As irradiation time increased, the sheet resistance clearly decreased. However, when irradiation time exceeded 120 seconds, the corresponding resistance reached plateau, almost remained constant (Figure 2.6g). The

morphologies of AgNW network at different irradiation durations (Figure 2.6i) supported the change in sheet resistance upon irradiation.

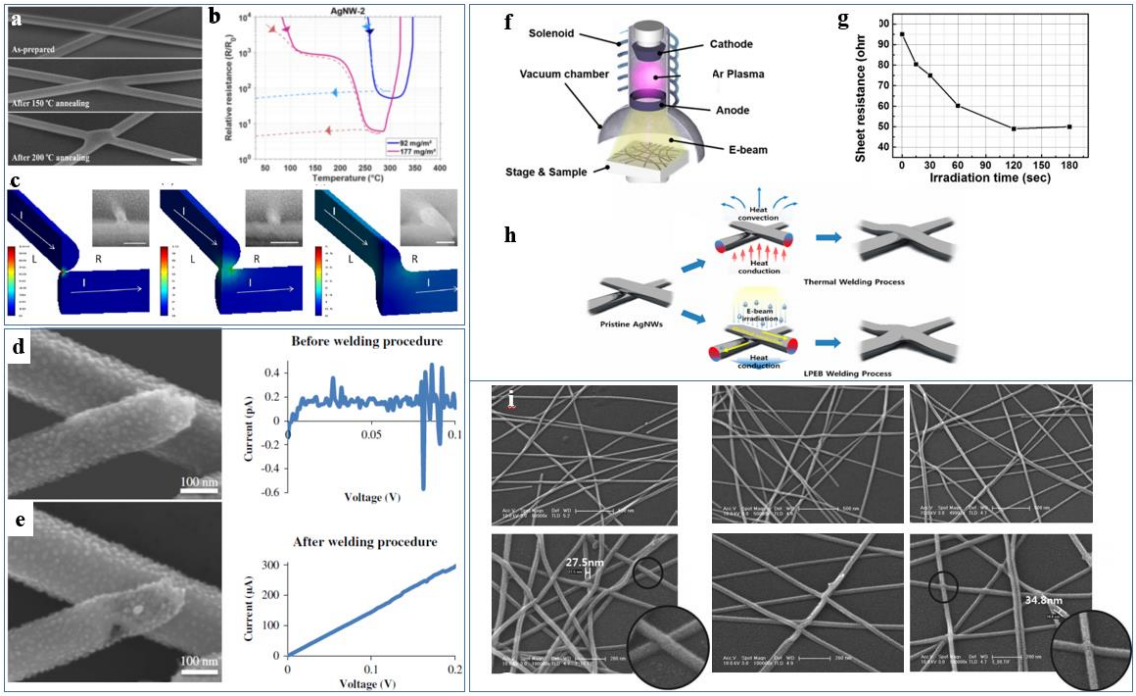

Figure 2.6 (a) Morphology of AgNW before and after thermal annealing welding process [283]. (b) Resistance of AgNW film with continuous thermal rate [284]. (c) Current density varying with contact morphology by Finite-element simulation [290]. (d) and (e) Morphology and electrical property before and after electrical welding process [287]. (f) Illustration for the electron beam process [292]. (g) Relationship between sheet resistance and irradiation time [293]. (h) Comparison between thermal annealing and electron beam welding [292]. (i) Morphologies of AgNW film after different irradiation times [293].

2.3.2.2 Chemical Welding

Chemical welding is totally different from the physical heat-induced welding techniques above. On the one hand, no external energy is required to fuse/weld the contact joints on the conductive network [294]. On the other hand, the chemical welding often proceeds in the liquid condition [295]. It is realized by incorporating additional reagents to enhance the contacts of AgNW network. Depending on the working mechanisms, chemical welding can be further classified into halide welding, electroless welding, and electroplating welding, etc.

The halide welding is realized by soaking a AgNW film into a sodium halide solution for a certain period of time (Figure 2.7a) [296]. Considering that oxygen molecules and halide ions generally dissolve in the solution, the Ag^+ can be produced by redox reaction as follows:

$$O_2 + 2H_2O + 4Ag \leftrightarrow 4Ag^+ + 4OH^- \quad 2.1$$

With the halide ions as the catalyst, the dissolved Ag^+ is redeposited by an autocatalytic reduction onto the AgNW network. Because the electrostatic potential near contact area is much higher than that of other sites on the AgNW surface, Ag^+ tends to deposit near the junction regions [296-297]. Therefore, a strong fusion between nanowires is realized to enhance the conductivity of the AgNW network as shown in Figure 2.7b.

Generally, the halide ions are considered as catalyst during the chemical welding. However, they seem to have an additional role in their interaction with AgNWs. A recent report showed that the chloride ion in halogen can also remove the insulation polymer layer on the AgNW surface [298]. As stabilizing and capping agent, PVP is usually used in the synthesis of AgNWs. As a result, the PVP is absorbed on the surface of the synthesized AgNWs by an oxygen atom of carboxylate group, which limits the conductivity of AgNW network. Given a stronger interaction between Cl^- and AgNW, Cl^- can replace the carboxylate group [298]. Upon detachment of PVP from the AgNW surface, AgNWs are prone to assemble together, which is driven by the fact that the PVP vacancy sites have a less repulsive force. Thus, under the action of aforementioned chemical welding, the conductivity of the AgNW networks is possibly further enhanced, because bare AgNWs directly contact each other without any PVP layer blocking at the contact interface. The enhanced electrical properties due to chemical welding treatment is shown in Figure 2.7c.

Electroless welding is different from the halide welding where it replaces the halide solution with silver ammonia and glucose mixture solution [177]. In this case, the reduced-AgNPs in the mixture solution can disperse across the entire network structure. Because AgNPs favorably deposit near the junction sites [299], the contact of AgNW joints are enhanced to achieve the electroless welding. The electroless welding process is described in Figure 2.7d. A reduction of more than 50% in the resistance has been obtained on the

electroless-welded AgNW film compared with the untreated AgNW film (Figure 2.7e).

Electroplating welding, on the other hand, involves an electrical current to reduce the metal ions to metals [300], which has been employed to enhance the conductivity of AgNW network. The electroplating welding technique has been broadly adopted in industrial roll-to-roll process due to the advantages of being cost efficient and simplicity [294]. Typically, the electroplating welding system is composed of power source, cathode, anode, and electrolyte. To enhance its conductivity, the AgNW film is selected as cathode (Figure 2.7f) [301]. When an electrical current is applied, the metal ions in electrolyte is reduced at the surface of cathode, so that the AgNW film is wrapped by the reduced metal particles and the contact area among the AgNWs increases. Using the electroplating method, a Ni shell layer is evenly plated onto the surface of silver nanowires as shown in Figure 2.7g [301]. Supported by the SEM images (Figure 2.7h), a nickel ions-bridge joining mechanism is proposed that the reduced nickel atoms fill the gaps between the AgNWs (Figure 2.7i) [302]. In this case, the sheet resistance of Nickle-decorated AgNW networks dropped up to 99%.

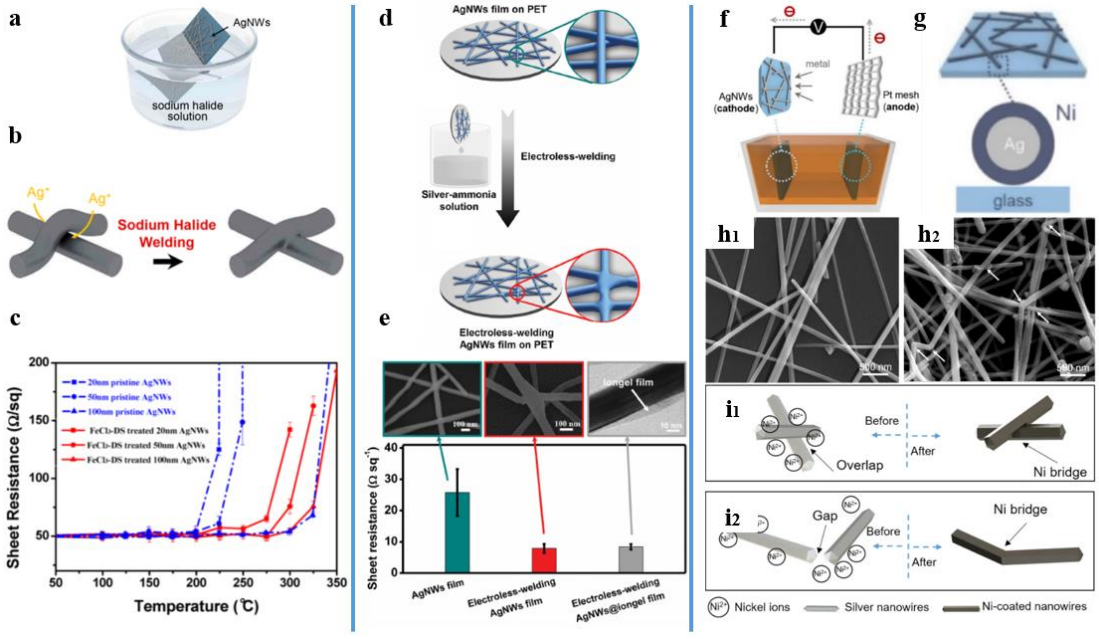

Figure 2.7 (a) Illustration of halide welding process [296]. (b) Schematic diagram of silver ions deposition during welding process [296]. (c) Sheet resistance variation of AgNWs before and after $FeCl_3$ treatment [303]. (d) Electroless welding of AgNW in silver-ammonia solution [177]. (e) Morphologies and sheet resistance difference between

the electroless welded samples and untreated samples [177]. (f) Schematic diagram of electroplating process of AgNW networks [301]. (g) Morphology of AgNWs coated with Ni shell [301]. (h) SEM images of pure AgNW and Ni-coated AgNW [302]. (i) Schematic diagram of the AgNWs connected by a Ni bridge [302].

2.3.2.3 Optically induced Welding

Optically induced welding is an effective method to enhance the AgNW network conductivity, which transfers the light energy to resonant heat energy to weld the AgNW joints [304-306]. In this process, a hot spot is produced at the contact point resulting in the fusing of nanowires together (Figure 2.8a). As the irradiation duration extends, the contact area increases, and the sheet resistance decreases correspondingly [307]. The influencing factors during the optical welding process are summarized as follows.

First of all, a light source, e.g., arc lamp, laser, flash light, or multiple light sources, is crucial to control the welding process. The resultant conductivity varies depending on the irradiation from different light sources [308]. For example, the sheet resistance of AgNWs network almost reduced by three orders of magnitude from 10^5 Ω/sq to 10^2 Ω/sq within 2 minutes of illumination of an ultraviolet A (UVA) lamp [309]. After the exposure of a Xenon flash light (pulse duration of 660 μs) at energy density of 10.3 J/cm^2, the sheet resistance of AgNW films dropped by 84.1% from 120 Ω/sq to 19 Ω/sq [305]. Welded only by white intense pulse light (IPL) from a xenon lamp, the resistance of the AgNW films decreased by 25.5%. However, under the near infrared radiation (NIR)-assisted IPL welding system, the resistance of the AgNW films dropped by 54.8% [310].

Secondly, wavelength can also lead to a different welding effect. Jang *et al.* selected the plasmatic flash light as the light resource, and simulated the generation of hot spot at different wavelengths by COMSOL. The results showed (Figure 2.8b) that with the increasing of light wavelength, the heat generated by absorbing the light energy gradually shifts from the junction area to the bottom and top layer. Taking advantage of this characteristic, a suitable wavelength can be selected to ensure the hot spot concentrated around the contact sites. As a result, the AgNW network can be welded under the action of surface plasmon effect [311].

Thirdly, the irradiation condition also influences the welding process [312]. Jiu *et al.* proved that the sheet resistance of AgNW network decreases with the increase of the light intensity within a specific range. Furthermore, the reduction trend gradually slows down until the light intensity exceeds a threshold value [313]. Chung *et al.* demonstrated a combined light irradiation strategy to weld the AgNWs, with the pre-treatment to remove the organic binder using UV light and the main welding step using flash white irradiation. The irradiation time of the pre-treatment affects the final sheet resistance of the AgNW film. The optimal condition of lowest sheet resistance was achieved by combining 60 seconds of UV pre-treatment and the main flash irradiation. As the UV irradiation time extends, the AgNWs were gradually embedded in the substrate, which nullifies the contribution of the flash white irritation [308].

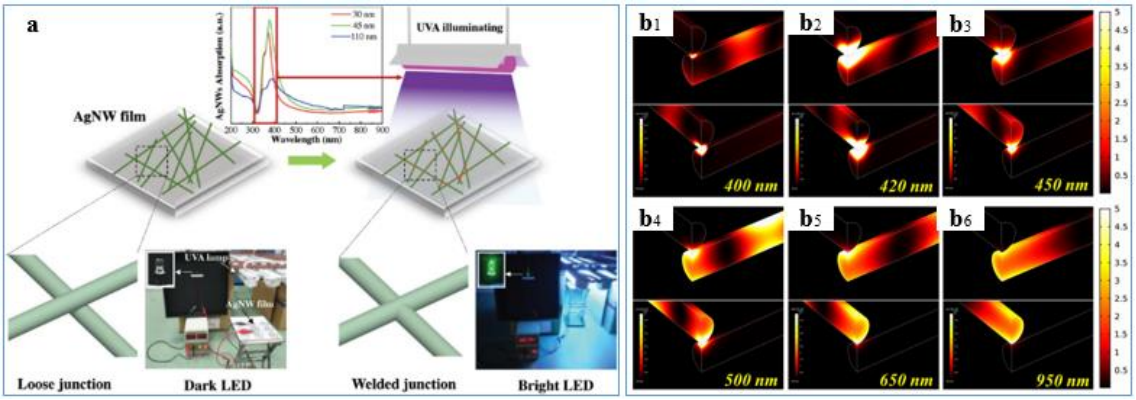

Figure 2.8 (a) Illustration of UVA-induced welding of AgNWs [309]. (b) Heat generation at a connection point with varying light wavelength [311].

2.3.3 Hybridization

By mixing with other functional materials, mechanical properties and conductivity of AgNW network can be improved and new functionality can be enabled. Typically, the corresponding functional materials comprise of carbon-based conductive materials, metal conductive materials, oxide materials, and conductive polymers, etc.

2.3.3.1 AgNW-conductive Layer Hybrid

One common hybridization has been formed between AgNWs and carbon-based materials. Carbon-based materials have excellent mechanical property although their conductivity is inferior to that of silver-based materials. By hybridization, it can promote not only a long-term stability (Figure 2.9a), but also electrical conductivity when

compared with pure AgNW or carbon-based materials (Figure 2.9b and 2.9c). As for a hybrid film, carbon-based materials are considered to provide structural support [314]. On the other hand, it can fill the void space among AgNWs [315].

There are several factors affecting the properties of the hybrid AgNW-carbon films. Firstly, the performance is closely related to the film structure. The most common type is the sandwich structure in which the AgNWs are wrapped by carbon materials [316]. It renders good thermal oxidation stability of AgNW network by reducing the exposure area to air [317]. In addition, a post treatment can improve the performance of hybrid films. For instance, the plasmonic welding enhances the junction between AgNWs. Meanwhile, it leads to a tight adhesion between AgNWs and carbon-based materials (Figure 2.9d). Therefore, the sheet resistance of hybrid film significantly decreases. At the same time, the sheet resistance also keeps stable with long-term bending cycles [318].

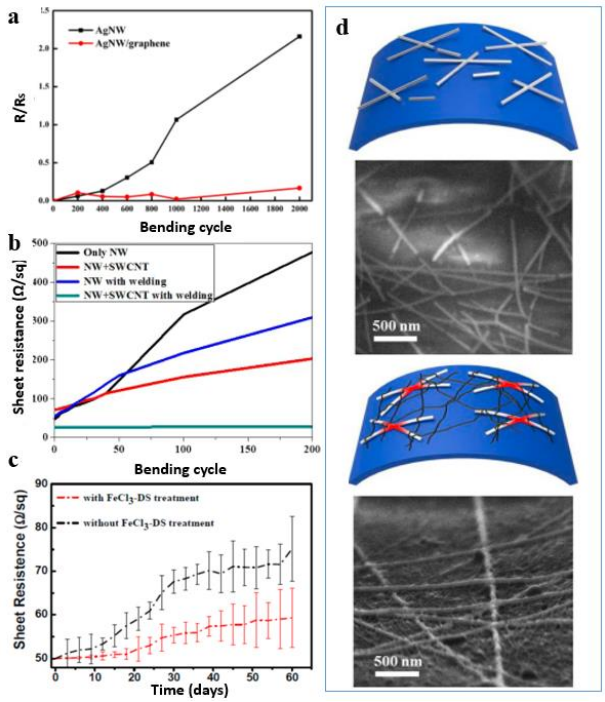

Figure 2.9 (a) Mechanical flexibility of AgNW/graphene hybrid film [319]. (b) Sheet resistance varying with bending cycle [318]. (c) Sheet resistance of different samples versus time when exposure to air condition for 60 days [303]. (d) Illustration and SEM images of AgNW network and AgNW/SWCNT hybrid structures [318].

2.3.3.2 AgNW-oxide Hybrid

Hybridizing oxides and AgNWs to enhance the conductive network have also been

adopted in recent studies. Depending on the oxide type, the methods can be furtherly divided into AgNW-metal oxide hybrid and AgNW-non-metal oxide hybrid. For this kind of hybrids, additional functionalities besides electrical property are usually sought after, e.g., thermal, mechanical and optical properties.

The classical AgNW-metal oxide composites include AgNW-ZnO (zinc oxide) hybrid and AgNW-TiO_2 (titanium dioxide) hybrid. Among them, the AgNW-ZnO composites exhibit superior flexibility, thermal and electrical stabilities [320-324], while the bare AgNW network is prone to damage or disconnect caused by local melting at a high temperature or a voltage ramp [320]. ZnO-coated AgNWs possess an excellent thermal stability even exceeding 500 ℃, owing to the hindered silver atomic diffusion in the presence of the thin oxide layer and improvement of the electrode interfaces [320]. Furthermore, since the bare AgNW network involves a large fraction of void space, the gap can be effectively filled by the ZnO buffer layer as shown in Figure 2.10a [325-326]. It not only collects the charge carrier, but also reduces the surface roughness [320]. Go *et al.* further reported a decrease in resistance of more than 50% by adding 7 wt.% ZnO [327]. Given these merits, the AgNW-ZnO composite is considered possessing a great potential for flexible electronics, transparent heater, and photovoltaic devices [320-322, 324].

AgNW-TiO_2 composites also attract researchers' attention. Given the cost benefit and the technology development, a sol-gel processing was employed to coat the TiO_2 layer onto the AgNW network [328-329]. Comparing with the pure AgNW film, the TiO_2 coated-AgNW film generally shows lower resistance, higher optical property, superior thermal & chemical stability, and structure durability [328-333]. Sohn *et al.* explained that the electrical performance is possibly promoted from two aspects including welding AgNW junctions via mechanical nano-pressing of TiO_2 on the surface of AgNWs and forming strong adhesion between TiO_2 and AgNWs through molecular interaction (Figure 2.10b) [331]. Song *et al.* studied the thermal stability of AgNW-TiO_2 films as shown in Figure 2.10c. As temperature exceeded 250 ℃, the resistance of bare AgNW film quickly increased whereas the value of TiO_2 coated-AgNW film had no significant change, indicating the contribution of the TiO_2 layer to the excellent thermal stability [328]. Chen *et al.* proved that

the TiO_2 layer effectively blocks the substrate from contacting with electrolyte, which limits the chemical corrosion of AgNWs. Meantime, the photovoltaic and surface durability of AgNWs have been significantly improved [330].

The AgNW-non-metal oxide hybrid mainly refers to AgNW-rGO mixture. It is highlighted by its superior thermal oxidation and chemical stability, owing to the excellent gas barrier property of the rGO film when it is coated on the AgNW film [334]. In addition, the sheet resistance of AgNW-rGO reduced by more than 50% when compared with the pristine AgNW film [335]. The possible reason is that rGO enhances the adhesion between AgNWs as illustrated in Figure 2.10d. Furthermore, with the increasing of temperature, conductivity advantage of AgNW-rGO became more obvious. For instance, as the temperature exceeded 70 °C, the sheet resistance of pure AgNW film was always higher than that of AgNW-rGO film even though the initial resistance value was the same. Especially, when the exposure time reached 192 hours, the pure AgNW network resistance increased 3-fold, whereas the resistance of the AgNW-rGO film increased less than 1.5-fold as shown in Figure 2.10e [334]. The difference is credited to the thermal oxidation stability where the existence of rGO effectively hinders the oxidation of AgNWs.

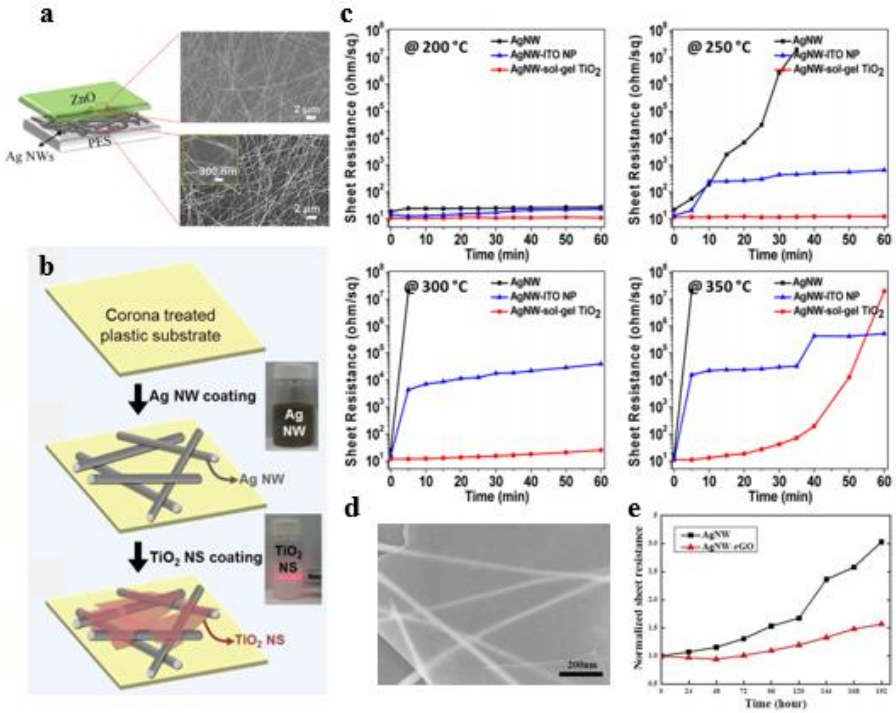

Figure 2.10 (a) Illustration and SEM images of AgNW film coated with ZnO [326]. (b) Schematic diagram of preparing a TiO_2-coated AgNW network [331]. (c) Sheet resistance of different samples changing with time under different temperature condition [328]. (d) Morphology of rGO coated-AgNW film [334]. (e) Sheet resistance of rGO coated-AgNW films varying with time [334].

2.3.3.3 AgNW-polymer Hybrid

Excellent property of AgNW-based hybrid electrodes can be realized by mixing AgNW and various conductive polymers. AgNW endows the hosting polymer with novel properties; Meantime, AgNW-polymer composite retains the characteristics of polymer matrix to a certain extent, such as elasticity, resilience, durability, stiffness, and mechanical strength, etc. Generally, the voids in AgNW network are filled with the polymer during the hybridizing process. The filled polymer assists in alleviating some intrinsic defects of AgNW network, such as poor interconnection between NWs and large surface roughness of AgNW films. Yun *et al.* demonstrated that the roughness of pristine AgNW film decreases by 78.2%, and root mean square roughness drops by 73.62% after mixing poly (3, 4-ethylenediowythiophene): poly (styrenesulfonate) (PEDOT:PSS) with AgNWs [30]. The integration of AgNW networks to a thin elastomeric layer has been commonly used to enable mechanical stability and stretchability particularly for stretchable and wearable devices. Liu *et al.* showed that under the fixation of PDMS, the AgNW network can endure ~100% stretching, ~315°twisting, and ~5 mm bending radius without obvious conductivity loss [336]. Additionally, the presence of AgNWs assisted its host polymer to increase the optical contrast, enhance the switching speed, and to improve the electrical conductivity in electrochromic devices. Lee *et al.* constructed a highly stretchable conductive fiber via embedding AgNWs and AgNPs in a styrene–butadiene–styrene (SBS) elastomeric matrix. The formed sample exhibited outstanding electrical conductivity (σ_0= 2450 S/cm), superior stretchability (900% elongation), and a wide range of strain sensing [157]. Zhang *et al.* compared the electrochromic polymer (ECP)/AgNWs composite films with the pure ECP film, and demonstrated that the optical contrast increased by 75% and 50% at initial and after 90 cycles, and the electrochemical

impedance of ECP/AgNWs composite film was always lower than that of the corresponding pure ECP film [337]. In some cases, a small amount of AgNWs was incorporated into the polymer matrix as fillers or additives. Moreno *et al.* adopted a simple solution mixing method to prepare AgNWs/PC nanocomposites, and the thermal stability of polycarbonate was improved significantly. Moreover, with 0.04 wt.% loading of AgNWs, the composites became conductive. As the loading reached 4.35 wt.%, the resistance dropped by eight orders of magnitude [338].

2.4 Applications

Up to now, various Ag nanomaterial-based flexible/stretchable devices have been developed for sensing, display, medical and energy applications. It is worth noting that only some representative examples are mentioned in this section of the review for the sake of brevity. Readers who are particularly interested in various applications of nanomaterial-enabled devices can refer to the review papers [339-342]. One pioneering work in 2013 reported the spectral transmittance of up to 97.9% obtained on a solution-processed AgNW network [323]. The figure of merit (FoM), which is taken as the ratio of electrical to optical conductivity, became very close to that of ITO. This discovery was employed to fabricate transparent film heaters [343]. Another seminal work reported highly flexible, stretchable and sensitive strain sensors based on the composite of AgNW network and elastomer in the sandwich structure [344]. Considering the high sensitivity and fast electrical response, the strain sensors were integrated into wearable devices to detect human finger motion and a smart glove device to control an avatar [344]. In 2015, a novel organic solar cell was fabricated by utilizing highly flexible and transparent electrodes based on the consecutively stacked layers of conductive polymer and AgNWs [345]. The new solar cells have significantly enhanced the power conversion efficiency and mechanical stability. In 2018, a AgNW-based flexible organic light-emitting diode (OLED) was formed in a single hot-pressing step, whose performance can match with that of ITO-based OLED devices [346]. In 2021, a novel composite (thermochromic powders hybridized with AgNWs) was employed to construct displays and touch sensors with excellent electrical and chromatic properties [347]. Recently, a hierarchical porous

AgNW network was developed for breathable electronics through photonic sintering with low sheet resistance and excellent mechanical durability [348]. The Ag nanomaterial-based devices have been widely applied in many diverse fields. We will briefly review them in the four categories of wearable sensors, flexible heaters, touch screens, lighting and display devices (Figure 2.11a~2.11e) [349-353].

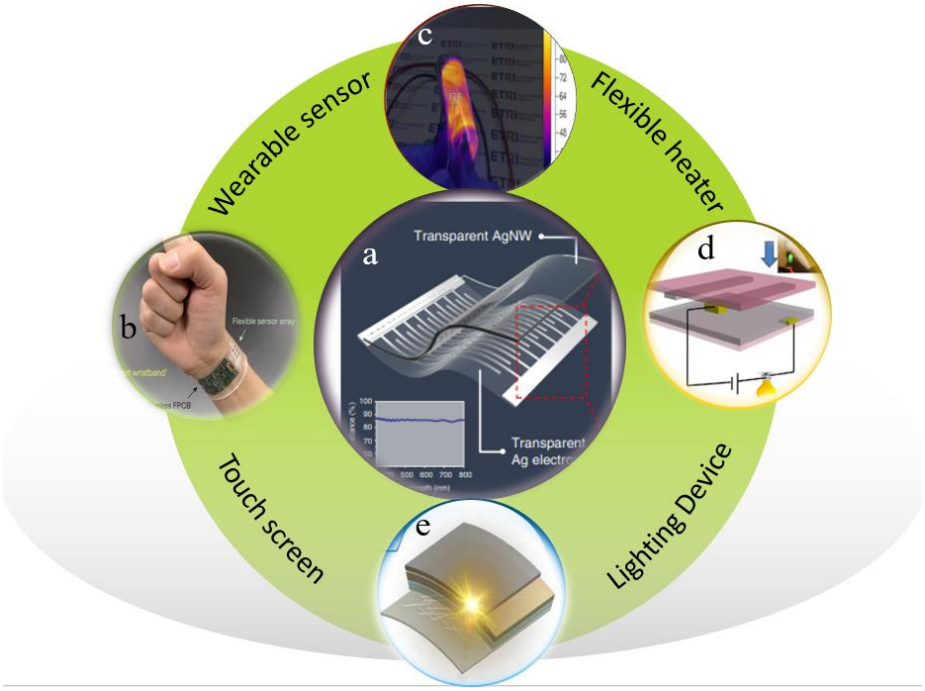

Figure 2.11 (a) Schematic diagram of transparent Ag electrode [352]. (b) Diagram of wearing a flexible sensor on human's wrist [350]. (c) AgNW film prepared heater showing a high flexibility [353]. (d) Prototype schematic of a touch screen by adopting AgNW film [349]. (e) Fabricating a flexible-OLED by using AgNW network [351].

2.4.1 Wearable Sensors

Wearable sensors quantitatively measure the shape change or deformation under stress in response to physical motions and contacts [354-357]. They play an important role in monitoring human health and keeping track of biological behavior and movements. Depending on their specific application fields, wearable sensors can be further classified into strain sensors, pressure sensors, and electrochemical sensors. Their sensing performance is usually evaluated with some parameters, such as stability, response time, sensitivity, and range of detection, [358] etc.

In recent years, a significant progress has been made in the development of Ag

nanomaterial-based wearable sensors. Take the pressure sensor as an example. In 2015, Joo *et al.* fabricated a AgNW-embedded PDMS pressure sensor based on capacitive sensing mechanism that exhibited sensitivity more than 3.8 kPa^{-1} and response time less than 150 ms [359]. Later, Shuai *et al.* prepared a pressure sensor comprising of elastomeric composites and embedded AgNWs, and obtained a high sensitivity of 2.94 kPa^{-1}. It is remarkable that the improvement has not compromised other features, e.g. detection limit, response time, and flexibility, and the sensor exhibited good reproducibility even during 1000 loading/ unloading cycles [360]. In 2017, Quan *et al.* constructed a flexible pressure sensor with sandwich structure. They demonstrated that the micro-structured pressure sensor exhibited higher sensitivity (1.1 kPa^{-1}), lower detection limit (1 Pa), and faster response time (< 1 s) when compared with the sensors without the micro-structure [361]. In 2019, Mao *et al.* demonstrated a pressure sensor assembled from AgNW-coated PDMS micropillar sheets. Although its pressure sensitivity is moderate (20.08 kPa^{-1}), the sensor response is highly reproducible for more than 10000 cycles [362]. At present, considering these advances, it is possible to promote the application of wearable sensors to more fields, such as robotic systems, flexible electronic skins, and advanced biomedical devices, etc.

2.4.2 Flexible Heaters

A flexible heater can transfer electrical energy into thermal energy by using the joule heating mechanism [363-364]. The performance is usually evaluated by electrical resistance, optical transmittance, operational stability, heating voltage, temperature rise and heating time, etc. [365] Flexible heaters have been adopted to defog and defrost mirrors and smart windows [363, 366]. Recently, the research trend about flexible heaters has gradually shifted towards wearable electronics [367]. Lan *et al.* prepared a AgNW-based heater for transparent thermotherapy pads. The heater increased the temperature to 74 ℃ within 20 seconds at 5 volts using Joule heating. In addition, the corresponding optical and mechanical properties and electrical conductivity maintained stable even after 10000 bending cycles [368].

2.4.3 Lighting Devices and Displays

AgNW conductive network is also widely used to prepare lighting devices. A

representative example is OLED devices that can emit light under an applied electric field. The devices can be fabricated by a solution process, such as coating and printing, which has the potential to manufacture large-area displays [369]. The AgNW-based OLEDs have attracted researchers' attention due to their excellent electroluminescent performance. An electrical current flow through the active layer material to light the OLED. Thus, reducing the sheet resistance is crucial to facilitate the charge transport. In addition, the surface roughness largely influences the characteristics of OLED, due to the charge carrier injection [38]. With these considerations, Lee *et al.* used an intense pulsed light to weld the interconnected AgNWs in 500 μs, and effectively reduced the roughness of AgNW film. The resultant lower surface fluctuation lessens the possibility of electrical shortages in OLEDs [351]. Yun *et al.* hybridized the AgNWs film with PEDOT: PSS to reduce the surface roughness. The treatment not only alleviated the non-uniformity in the electrical performance, but also reduced the electrical shortages among the AgNWs [30].

2.4.4 Touch Screens

As the demand for electronic devices grow explosively, such as laptop, smart phone, and automatic kiosks, touch screen has a great application market all over the world in the coming years. Considering its mechanical property, optical transmittance, and adhesion to substrate, the AgNW network is viewed as a potential candidate for touch screens. At present, the main issues limiting the development of the AgNW-based touch screens are the large surface roughness and the compromise of electrical conductivity and optical transmittance. Highly cross-aligned AgNW network could be a possible solution utilizing minimum conductive materials to achieve comparable electrical performance [252]. The majority of research work in this area has been demonstrated in small scale and research laboratories. To address the issue, Chen *et al.* developed a dynamic continuous process to make large-scale flexible transparent conductive films and touch screens. In their approach, new additives were adopted to regulate the dynamic process to stabilize and distribute the AgNWs, and enhance wetting, spreading, adjustment, and drying of the wet film. Under their efforts, a large flexible film (0.5 m ×10 m) and a touch screen of 32 inches were achieved. [370]. This work paves the way to realize the commercialization of

Ag nanomaterial-based flexible devices.

2.5 Summary and Perspective

This review systematically introduces the approaches to form Ag nanomaterial-based conductive pathway for flexible and stretchable electronics according to their deformation response direction, e.g., unidirectionally and multi-directionally responded electrodes. Various processing methods are surveyed, and the corresponding merits and limitations are discussed. Subsequently, we reviewed several ways to enhance the conductive network, e.g., regulating the assembly of AgNWs, modifying conductive networks physically and chemically, and selecting suitable hybridization. These treatments have effectively reduced the resistance between contact points and shortened the conductive pathway, which significantly enhanced the electrical property of the Ag nanomaterial-based electrodes. We finally display some common applications of the Ag nanomaterial-based devices. These devices reveal great unique advantages and value proposition in wearable sensors, and flexible lighting devices and displays. In summary, this review provides up-to-date advancements in the development of Ag nanomaterial-based flexible and stretchable electronic devices, which can assist and inspire researchers to leverage these technology advances in their research work for Ag nanomaterial-based devices and other functional devices.

In the future, more research effort should be made to improve stretchability of the Ag nanomaterial-based devices in all directions, i.e., omnidirectional stretchability. This can be achieved through careful designs of the AgNW network, alignment, patterning, in-plane and out-of-plane structures [371]. For specific applications, safety, comfort, and sustained operation of the devices are worthy of consideration. Especially, for the flexible electronics employed in detecting epidermal biopotential signals, some characteristics, such as self-adhesion, self-healing, being breathable, shape retention, are highly desirable, which have great positive influence on long-term operation. In order to realize commercialization of Ag nanomaterial-based devices, two aspects should be particularly focused, (i) the capability to print functional materials with well-controlled assembly and morphology, and (ii) stability of the flexible/stretchable

devices. New printing techniques should be developed to pattern and integrate silver nanomaterials with other functional materials, and to implement post treatments with a potential of large-scale fabrication. Silver nanomaterials are known to be prone to oxidization. The fundamental failure mechanisms of the AgNW conductive pathway over cyclic deformation are very complicated and still in development, which may involve mechanical fatigue, joule heating, material degradation through oxidation, or combination of these factors. Fundamental studies and experimental approaches to promote long-term stability should be considered, especially through collaboration of university and industrial sectors. It is believed that an increasingly wider range of applications and greater commercial potential of the Ag nanomaterial-based flexible and stretchable devices will be developed in the coming years.

CHAPTER 3 Study on Water-induced Polymer Swelling

3.1 Introduction

Polymer blend system, as a strategic material design concept, has attracted considerable attention in recent years, due to its simple process, low cost, and widespread applications, etc.[372-376] In a polymer blend system, functional materials are generally selected as fillers to dope the polymer matrix. By controlling the materials and processing parameters, the filler material endows the hosting polymer with novel properties, while the polymer/filler composite retains the characteristics of polymer matrix to a certain extent, such as elasticity, resilience, durability, stiffness, and mechanical strength, etc.[377-380] With these advances, the polymer composites have been adopted in many fields, such as high-efficiency polymer solar cells [381-384], drug-delivery systems [385-388], pipeline engineering [389-390], and soft electronics [391-393], etc.

Water swellable rubber (WSR) is a kind of polymer blend composites composed of elastomer with water-absorbent fillers. WSR has been widely used as sealants and caulks, water blocking materials in automotive and construction industries, oil and gas fields, etc.[394-395] More than two decades ago, it has been reported that by adding hydrophilic fillers, some polymer composites can obtain the swelling performance when immersed in aqueous solution [396]. Recently, Manaila *et al.* adopted flax, hemp, and wood sawdust as fillers to make nature rubber composites and showed the water-induced polymer swelling mainly depends on the filler nature and blend amount [397]. They calculated the kinetics of water absorption through Fick's law and categorized the water transport into Fickian diffusion and non-Fickian diffusion. Trakuldee *et al.* added sodium polyacrylate (SA)/sodium bentonite clay (SBC) hybrid filler into natural rubber (150 parts per hundred rubber, i.e., 60 wt.% in filler concentration), and obtained a swelling ratio of 400%-500% [398]. By regulating the SA/SBC ratio, the water swelling rate and swelling ratio have been modulated. In an epoxy/filler composite system, Sugiman *et al.* investigated water uptake of epoxy and inorganic fillers with varying water reactivity. Higher water uptake was obtained for water-reactive fillers, where the

water uptake behavior changes from pseudo Fickian in the neat epoxy to non-Fickian in the epoxy composites [399]. On the other hand, unreactive fillers did not affect the water uptake behavior.

The main reason for polymer swelling in water is that the polymer substrate generally is not completely impervious, therefore water molecules can transport inside the polymer matrix [400]. When water-reactive fillers, e.g., hydrophilic fillers, are added into the polymer matrix, the water molecules are attracted to the filler sites and bond to them. Particularly, if these hydrophilic fillers have a good solubility in water (different from the fillers in the WSR or epoxy polymers though), they are prone to dissolve when contacting aqueous solution, which results in an osmotic pressure gradient between the inner droplet solution and the external soaking medium [396]. Thus, water in external solution easily diffuses into the polymer composites, causing the boundary of internal cavity to shift outward [401]. The change, in return, gives rise to the increase of retractive pressure as the polymer chains are stretched. Under the interactions of osmotic pressure induced by fillers and retractive pressure from rubber, a polymer swelling process can be triggered. Up to now, researchers have achieved water absorption a few times higher than their original weight by choosing suitable polymer matrix and hydrophilic fillers. Without a doubt, the recent progress has provided a great potential to broaden its application fields.

In this work, the swelling behavior of the elastomer composites was systematically investigated to elucidate the effects of silicone property, filler type, filler concentration, film thickness, and temperature of soaking medium on the swelling ratio and water absorption. The findings in this work can provide an effective guidance in selecting the polymer blend system and operating conditions to obtain controlled swelling for various applications. This water-induced swelling is superior to the conventional polymer swelling approaches in light of the negative effects on human health and the environment by volatile and toxic organic solvents [27, 402-403]. Due to these advances, the water-induced swelling possesses a great potential to fabricate stretchable conductors with wrinkled structures, replacing the organic solvent-induced swelling process.

3.2 Experimental Section

3.2.1 Materials and Methods

Several silicone elastomers were selected among the commercially available products, including Ecoflex$^{00\text{-}50}$, Ecoflex$^{00\text{-}30}$, Dragon skin$^{10\ slow}$ (Smooth-on, Inc.), Sylgard 184, and Sylgard 186 (Dow Corning). The Smooth-on and Sylgard rubbers were separately prepared by mixing of part A & part B in weight ratio of 1:1 and hybridizing of polydimethylsiloxane (PDMS) base and curing agent in weight ratio of 10:1, respectively. The commercial 10-X powdered pure cane sugar (Domino Food, Inc.), as the filler materials, was adopted to dope the polymer matrix. A sieve with 105 μm-pores was utilized to filter the filler particles, the morphology of which is shown in Figure 3.1. Next, the prepared silicone polymers and the sugar fillers were mixed into polymer composites in the specified sugar concentration. To enhance the mixture uniformity, a planetary mixer (ARE-310, Thinky Mixer) was used for 2 minutes at 2000 rpm, followed by 30 seconds of defoam process to remove air bubbles inside the mixture.

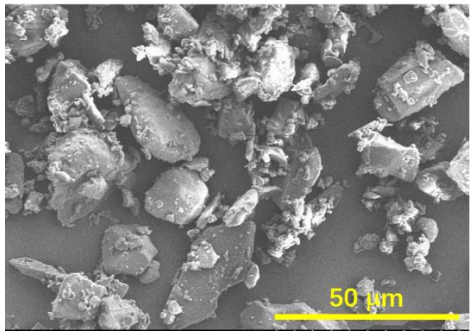

Figure 3.1 SEM image of the sugar particles used as additives to the silicone elastomers.

3.2.2 Fabrication of Conductive Elastomer Films and 3D Printed Structures

The elastomer/sugar composites were casted into a grooved mold to make the testing strips. The composites were then leveled and sealed by a cover sheet, followed by thermally curing at 50 ℃ for 24 hours. Finally, the elastomers were peeled off from the mold, and the strips with specific dimensions were fabricated.

The strips with dimensions of $20mm \times 10mm \times 1mm$ were chosen to construct

the soft strain sensing devices through vapor deposition. The first step is to soak the samples in deionized (DI) water for one, five, and ten days of immersion time, respectively. The elastomers with different swelling ratios were obtained after a given duration. Next, a sputter coater (POLARON) was employed to deposit gold film on the surface of swollen elastomers. The sputtering time was 150 seconds while keeping the vacuum at a range of 10~20 Pa. Finally, the obtained samples were dried in a convective oven at 50 ℃ for 24 hours.

To fabricate sensors with desirable 3D patterns, an extrusion-based 3D printer (EnvisionTec, 3D Bioplotter) was employed with a tapered nozzle (400 μm in diameter, Nordson). The 3D lattice model was designed by a CAD software (SolidWorks) and sliced into 320 μm of layer thickness by a supporting software (Prefactory) during the printing process. A series of printing parameters were adjusted to obtain uniform ink deposition and printing quality, including 1.5 bar of extrusion pressure, 10 mm/s of printing speed, 0.2 s of pre-flow, and 0 s of post-flow, etc.

The printed 3D lattice structure was then soaked in graphene aqueous solution (ACS Material, LLC) with 0.1 mg/mL concentration for three days to construct the stretchable conductors. In this case, the polymer swelling and graphene deposition were carried out simultaneously. Magnetic stirring at 400 rpm was used to assist thorough contacts between graphene and the 3D lattice structures. The fabricated samples finally were dried in air for 1 hour, followed by drying in a convective oven at 50 ℃ for another 23 hours.

3.2.3 Measurement and Characterization

The volume and weight of the composite strips were measured before immersion and after each 24-hour period of soaking in 100 mL DI water at room temperature. Compressed air and tissue paper were utilized to remove any residual water at the sample surface. Subsequently, vernier caliper and scale were used to measure the dimension and weight of the samples. A field-emission scanning electron microscope (FE-SEM, HITACHI, SU-70) with 5 kV operating voltage was employed to observe the 2D morphology of microstructures.

3.3 Results and Discussion

Figure 3.2 illustrates the water-induced polymer swelling process. Considering their ultrahigh water solubility, sugar particles were utilized to dope silicone elastomers to endow the hydrophilic property. Then, the polymer composites were soaked in aqueous solution. Accompanied with sugar dissolution and establishment of concentration gradient between interior and outside of the polymer composites, swelling is triggered under the action of osmotic pressure. The dynamic swelling process is regulated by the osmotic pressure and mechanical strength of the silicone matrix, which are influenced by silicone type, sugar concentration, sample thickness, temperature of soaking medium, and additives type.

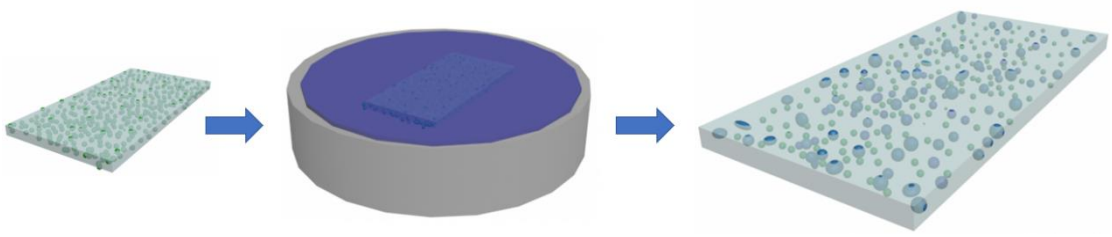

Figure 3.2 Schematic of the water-induced swelling process.

3.3.1 Silicone Type

We have studied the water swelling behavior of five commercial silicone elastomers doped with sugar particles, comprising of Ecoflex$^{00\text{-}50}$, Ecoflex$^{00\text{-}30}$, Dragon skin$^{10\ slow}$, Sylgard 184, and Sylgard 186. After soaking the polymer composite films in DI water, an isotropic swelling gradually occurred on each sample, and the differences in their swelling volume can be easily detected. To quantitatively evaluate their swelling characteristics, water absorption by weight and volume swelling were calculated based on Equation 3.1 and 3.2: [398]

$$\text{Water absorption (\%)} = \frac{W_1 - W_0}{W_0} \times 100\% \quad (3.1)$$

$$\text{Volume swelling (\%)} = \frac{V_1 - V_0}{V_0} \times 100\% \quad (3.2)$$

Where, W_0 and W_1 are the weight of rubber composites before and after immersion; V_0 and V_1 are the volume of the rubber composites before and after immersion, respectively.

The calculated results were summarized in Figure 3.3a and 3.3b. Different polymer composites exhibited different swelling ratios with an interesting finding that Sylgard 184 behaved significantly different from other silicone composites. The Sylgard 184/sugar hybrid reached their maximum volume swelling ratio (84%) and water absorption (49%) after only one day of immersion. With extension of immersion time, the volume swelling ratio and water absorption continuously reduced. However, the swelling ratio of other polymer composites show a monotonic growing trend although their growth rate is different in ten days of immersion. Among them, Ecoflex 30/sugar, Ecoflex 50/sugar, and Dragon Skin 10/sugar reveal similar swelling ratios during the course of immersion. Their volume swelling ratios attained 671%, 627%, and 712%, and the water absorption reached 327%, 359%, and 333%, respectively. As for Sylgard 186/sugar hybrid, the volume swelling ratio (~1060%) and water absorption (~670%) are much higher than its counterparts.

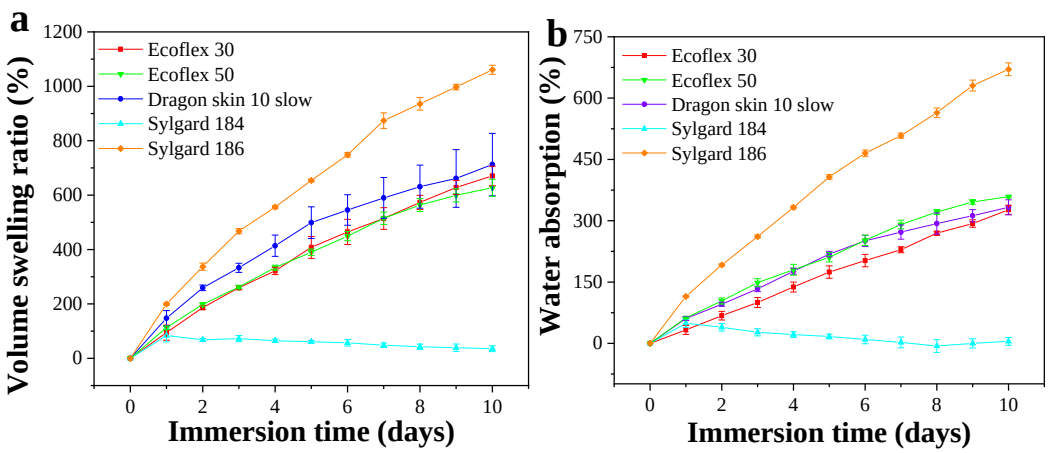

Figure 3.3 Swelling ratios of various commercial silicone elastomers mixed with 50 wt.% of sugar particles. (a) Volume swelling ratio with respect to the immersion duration. (b) Water absorption with respect to the immersion duration.

We attribute the distinct swelling behaviors among various silicones to their mechanical property (particularly elastic modulus) and viscosity, where the former works against the swelling caused by osmotic pressure and the latter plays an important role in the distribution of sugar particles inside the silicone matrix. According to the classical diffusion theory [401], water diffuses through the silicone matrix and gives rise to the sugar dissolution forming solution "droplets" in their local positions. A water

concentration gradient is established between interior and outside of these locations, which is the main driver to induce osmotic pressure. At the equilibrium, the osmotic pressure of sugar solution in the polymer (π_i), the osmotic pressure from external DI water (π_0) where the composite is soaked, are correlated with the elastic pressure (p) applied by the polymer matrix due to the formation and expansion of the droplet, according to Equation 3.3:[396]

$$\pi_i - \pi_0 = p \tag{3.3}$$

Among them,

$$\pi_i = \frac{c_i RT \rho_w}{c_w M_i},$$

$$\pi_0 = \frac{c_0 RT}{M_0}$$

Where c_i and M_i are the mass concentration and molecular weight of the sugar in the silicone rubber, c_0 and M_0 are the corresponding values in the soaking medium, c_w is the water concentration in the sugar "droplets", ρ_w is the density of water, p is the pressure required to enlarge the sugar "droplets" during swelling which also corresponds to the constraining stress exerted by the polymer chains against swelling; p is reversely proportional to the material elastic shear modulus and the extension ratio (or swelling ratio). In this work, since the soaking medium (DI water) was replaced every 24 hours, the sugar concentration in it (c_0) is considered negligible although sugar molecules do release to the soaking medium.

During the initial stage of soaking, π_i is at its maximum since c_w is at its minimum when the sugar particles are just dissolved forming the "droplets", and p is also the smallest. The osmotic pressure difference, hence, is mainly responsible for the initial rapid swelling. As immersion time extends, more water is absorbed into the polymer composites overcoming the increasing stress exerted by the polymer chains surrounding these cavities, which continuously induces the expansion of these droplet cavities. Correspondingly, the osmotic pressure difference between π_i and π_0 decreases until it reaches equilibrium with the increasing stress p. The complete swelling behavior of the Ecoflex 50/sugar composite was provided including the initial rapid swelling stage, slow-down swelling, and equilibrium stage [28]. In this part of the

work, we mainly focus on the swelling behaviors of polymers with different mechanical properties.

Figure 3.4 compares the elastic modulus (or Young's modulus) of various silicones used in this study. The Sylgard 184 possesses a much higher elastic modulus (3.9 MPa) than other polymers (0.15 Mpa~ Ecoflex 30, 0.22 MPa~ Ecoflex 50, 0.5 MPa~ Dragon skin slow 10, and 0.6 MPa~ Sylgard 186). This huge difference in elastic modulus E, (therefore, shear modulus G as well, according to $G = \frac{E}{2(1+\nu)}$, υ is the Poisson's ratio) indicates that it is more difficult for Sylgard 184/sugar hybrid to induce expansion deformation through swelling under the same osmotic pressure, which reasonably explains the fact that this hybrid reached its equilibrium in one day of soaking with the least swelling ratio, but other silicone composites manifested a conspicuous swelling.

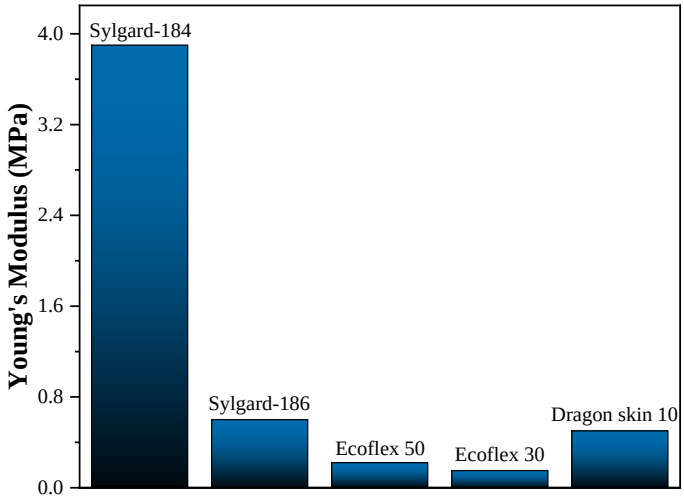

Figure 3.4 Young's modulus of different commercial elastomers.

For the silicones having similar elastic modulus (0.15 MPa to 0.6 MPa), the polymer viscosity is considered to bear the main responsibility in the different behaviors of water absorption. As shown in Figure 3.5, the viscosity of Sylgard 186 is 66.7 Pa·s, while the values of Ecoflex 30, Ecoflex 50, Dragon Skin 10 are 3 Pa·s, 8 Pa·s, and 23 Pa·s, respectively. It is conceivable that the sugar particles are relatively easier to be wrapped by the low viscosity polymers during the mixing process. In this case, more sugar particles embedded in polymer with lower viscosity are probably wrapped by the silicone completely, and water can only access to these particles through

diffusion. On the other hand, for high viscosity polymers, it is more difficult to completely wrap and embed the sugar particles in the polymer matrix, which indicates that microchannels surrounding these particles and even connected sugar networks can be formed facilitating faster water transport through direct capillary interactions [404].

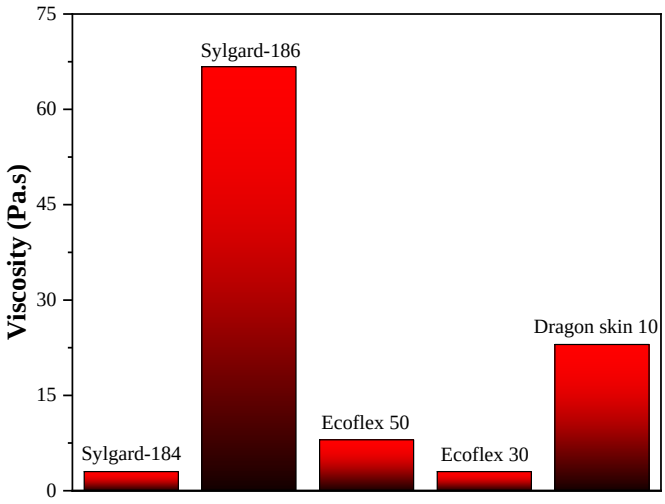

Figure 3.5 Viscosity of different commercial elastomers.

Two observations have supported the water transport mechanism through possible microchannels or networks in addition to diffusion. For a diffusion-controlled process, the water adsorption has a linear dependence with $\sqrt{t}$ [396, 398, 400, 404], while in our case the water absorption is much faster and exhibits close to linear relationship with immersion time *t* (more discussion later in this section). It was also noticed that during soaking, not only water diffuses and transports into the silicone matrix, but also the sugar particles dissolve and transport out of the silicone matrix, as evidenced by the fact that the final sample weight after completely water removal is less than the original weight of the silicone/sugar composites (e.g., ~9.8% weight reduction after water removal at the end of ten days for Ecoflex 50/sugar films). The volume swelling ratio and water adsorption, therefore, are the results of competition between the osmotic pressure and mechanical stress exerted by stretching of the polymer chains due to swelling, and the rate of water transport into the polymer matrix.

In the following parametric study, we have used Ecoflex 50/sugar composites to investigate the effects of selected processing parameters on the swelling performance. Based on the classical diffusion theory, three parameters are considered to play a crucial

role in controlling the swelling ratio of silicone composites, including sugar concentration, sample film thickness, and temperature of soaking medium. The control experiments were conducted on the Ecoflex 50/sugar composite films with 50 wt.% sugar concentration, film thickness of 1.5 mm, and soaked in DI water at room temperature.

3.3.2 Sugar Concentration

Ecoflex 50/sugar composite films with 10 wt.%, 30 wt.% and 50 wt.% of sugar particles were prepared for the swelling tests. For each sugar concentration, three samples with the same dimension ($L \times W \times T = 20\ mm \times 10\ mm \times 1.5\ mm$) were soaked in DI water for ten days. Their volume swelling ratio and water absorption are presented in Figure 3.6. A clear difference in the swelling behavior can be observed, where the samples doped with a higher sugar concentration exhibits a faster swelling rate. In addition, the increase trend of swelling slows down as immersion time extends. The average volume swelling ratio and water absorption of Ecoflex 50 silicone film with 50 wt.% of sugar reached 533% and 313% upon completion of ten days of soaking. In contrast, the corresponding values for the samples with 30 wt.% and 10 wt.% of sugar particles are 275% & 218% and 42% & 52%, respectively.

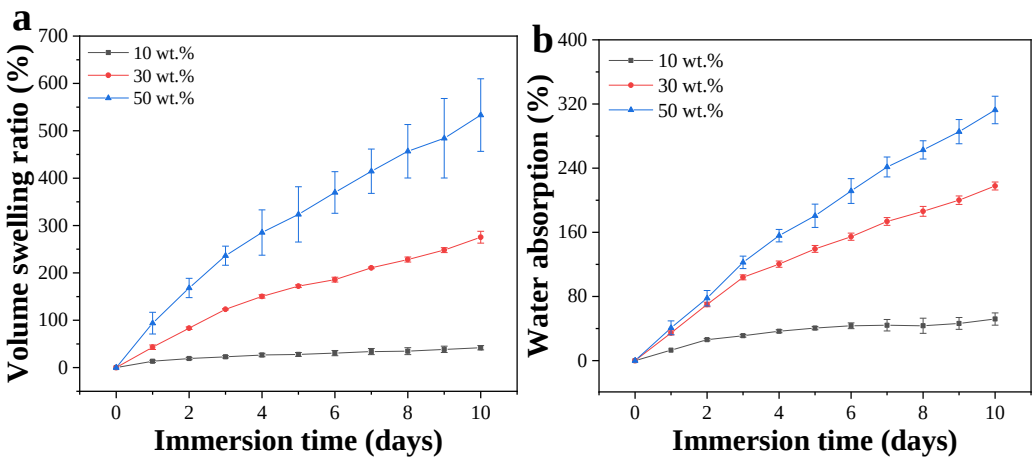

Figure 3.6 Swelling ratio of Ecoflex 50 silicone mixed with different amounts of sugar particles. (a) Volume swelling ratio with respect to the immersion duration. (b) Water absorption with respect to the immersion duration.

According to Equation 3.3, the samples with higher sugar concentration c_i obtain

a larger π_i, which gives rise to the faster swelling ratio with equal or similar π_0 and p. In addition, the polymer composite with a low sugar concentration is more likely to have well-wrapped isolated sugar particles distributed inside the silicone matrix, while for higher sugar concentrations, the sugar particles will have a better chance to connect with neighboring particles to form networks inside the polymer matrix. In other words, the water transport to the polymer composites with lower sugar concentrations will be dominated by diffusion, while in the composites with higher sugar concentrations, both diffusion and direct capillary interactions could contribute to the water transport.

It is worth noting that these sugar particles also act as viscosity modifier to improve the 3D printability of polymer materials. As shown in Figure 3.7, the pure Ecoflex 50 maintains a low and constant viscosity about 9 Pa·s for shear rates of 0~100 s^{-1}. By adding 10 wt.% sugar particles, the viscosity of the rubber composite was promoted to 20 Pa·s at the tested shear rate range. As sugar concentration reached 30 wt.%, the viscosity of rubber composites not only increased to 200 Pa·s at low shear rates, but also dropped with shear rate increasing. When 50 wt.% of sugar doped in the rubber composite, the viscosity surged to 4000 Pa·s at low shear rates, then an exponential decreasing trend is observed. Its shear thinning behavior indicates that the Ecoflex 50/sugar composite is suitable for 3D printing. The low viscosity at high shear rate suggests that the ink can be smoothly squeezed out of the printing nozzle. On the other hand, the high viscosity at low shear rate implies an excellent plasticity and capability to retain its structure fidelity after 3D printing.

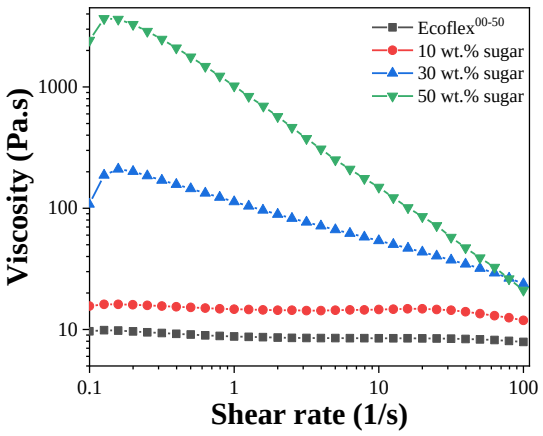

Figure 3.7 Viscosity of Ecoflex 50/sugar hybrids with different concentrations of sugar particles.

3.3.3 Sample Thickness

Sample thickness has a significant effect on the swelling ratio and water adsorption. Herein, three different thickness (i.e., 0.75 mm, 1.5 mm, and 2.25 mm) and the same sugar concentration (50 wt.%) were selected to characterize the swelling behaviors in ten days of immersion. The results are summarized in Figure 3.8. It shows that the final volume swelling ratios are 351%, 533%, and 698% for the samples with 2.25 mm, 1.5 mm, and 0.75 mm of thickness, respectively. Similar trend was obtained among these samples for water absorption. Therefore, both volume swelling ratio and water absorption are inversely correlated with the thickness of samples. In addition, the standard deviation of the thinner samples is much larger than that of the thicker samples.

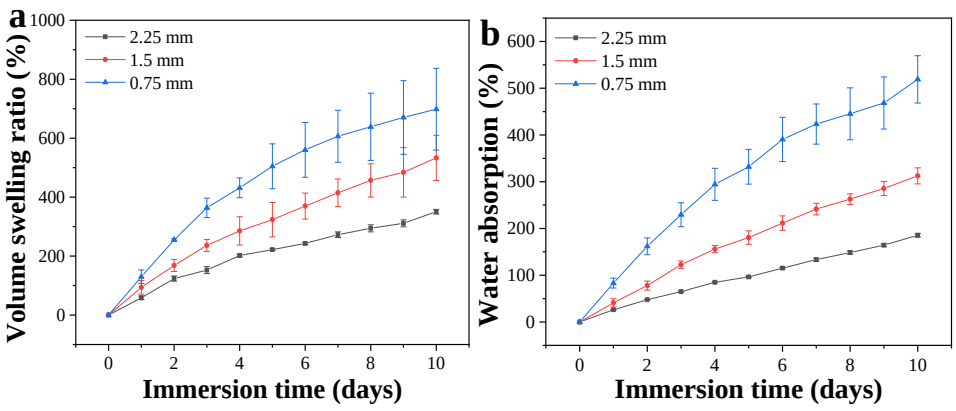

Figure 3.8 Swelling ratio of samples with different thicknesses. (a) Volume swelling ratio with respect to the immersion duration. (b) Water absorption with respect to the immersion duration.

In addition to the volume swelling ratio and water adsorption, we also calculated the thickness swelling ratio for the samples with different initial thickness:[405]

$$\text{Thickness Swelling (\%)} = \frac{d_1 - d_0}{d_0} \times 100\% \qquad 3.4$$

Where d_1 and d_0 are the thickness of the film composites before and after immersion. The results are summarized in Figure 3.9. After five days of immersion, the thickness swelling of samples with 0.75 mm, 1.5 mm, and 2.25 mm thickness reached 100%, 89%, and 77%, respectively. In the subsequent soaking, the swelling in the

thickness for thinner samples (e.g., 0.75 mm thickness) almost ceased, whereas the samples with 1.5 mm, and 2.25 mm thickness gradually increased to 112% and 93% of the swelling degree with a tendency to further increase afterwards. This indicates that it is easier for thinner samples to reach their water swelling saturation when compared with the thicker samples, which is consistent with the earlier appearance of slowing down in volume swelling ratio and water adsorption for thinner samples in Figure 3.8.

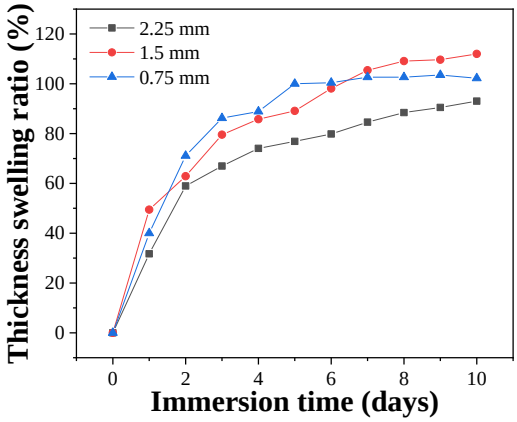

Figure 3.9 Thickness swelling ratio of samples with different film thicknesses.

Based on these results, we put forward a possible explanation of the swelling process across the sample thickness. As water molecules diffuse through the sample surface, the sugar particles located near the vicinity of the sample surface are firstly dissolved forming sugar “droplets”. These droplet cavities increase in size as more water transports into them under the action of osmotic pressure. With accumulation of these swollen droplets, a global expansion appears in dimensional change on these samples. Assuming the sample is composed of multiple layers, the swelling is initiated from the outermost layer. Meanwhile, the inner layer with insufficient swelling has a constraining effect on the swelling of the top layer. In this case, it can be imagined that for the thinner sample, the resistance from inner layers is smaller and it also takes shorter time for water molecules to transport through the thickness of the samples. Thus, the corresponding thinner samples exhibited a higher swelling ratio with respect to immersion time.

3.3.4 Temperature of Soaking Medium

Temperature is also identified as one of crucial factors to regulate the swelling of polymer composites. In order to study the effect of temperature, we soaked the Ecoflex 50/sugar hybrid in DI water at 5 ℃ (in a temperature-controlled refrigerator), 50 ℃ (in a heated beaker on a hot plate with stirring), and compared with the results obtained at room temperature. The room temperature is around 18~20 ℃ and we stated 20 ℃ in our discussion. The volume swelling ratio and water absorption during ten days of immersion are shown in Figure 3.10a and 3.10b.

There are dramatic differences in swelling ratio between the three test conditions even after the first day of soaking. The samples soaked in higher temperature solution has a much faster swelling rate. In the ten days of immersion, the volume swelling ratio and water absorption of the samples in 50 ℃ water surged to 1133% and 650%, while the samples in 20 ℃ water possessed 533% in volume swelling ratio and 313% in water absorption, and the ones in 5 ℃ solution rendered the least amount of swelling, i.e., 468% and 208% in volume swelling ratio and water absorption, respectively. Furthermore, the swelling ratio of the samples in 50 ℃ water reached the equilibrium state after seven days of immersion, whereas the swelling ratio of samples in lower temperature solutions still kept a relative stable increase trend upon the completion of the ten days of immersion. Our results also show that the samples immersed in high temperature solution are more prone to have a larger variation in swelling performance.

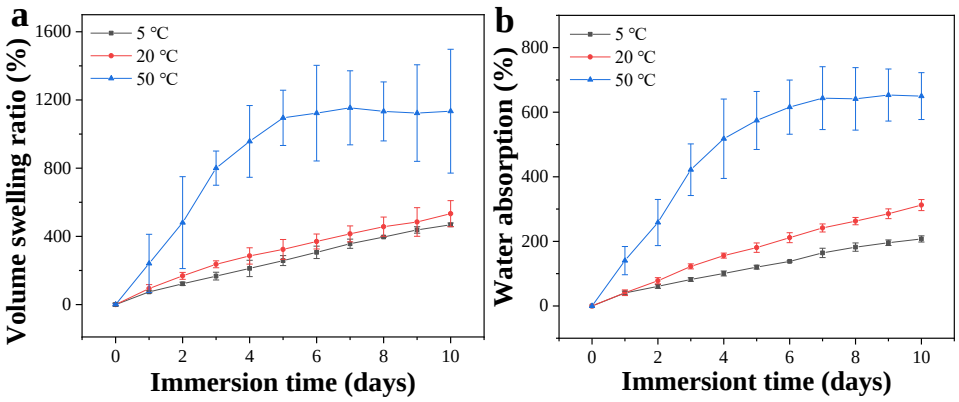

Figure 3.10 Swelling ratio in the aqueous solutions with different temperatures. (a) Volume swelling ratio with respect to the immersion duration. (b) Water absorption with respect to the immersion duration.

To explain the positive correlation of aqueous solution temperature and swelling rate of polymer composites, Stokes-Einstein equation is introduced, as shown in Equation 3.5:

$$\frac{D_{T_1}}{D_{T_2}} = \frac{T_1}{T_2} \times \frac{\mu_{T_2}}{\mu_{T_1}} \quad 3.5$$

Where, *D* is the diffusion coefficient, *T* is the corresponding absolute temperature, μ is the dynamic viscosity of the solvent. With the water viscosity at the testing temperatures, i.e., $\mu_{5\,℃} = 1.519$ mPa·s, $\mu_{20\,℃} = 1.005$ mPa·s, and $\mu_{50\,℃} = 0.549$ mPa·s, we can calculate the diffusion coefficients: $D_{20\,℃} \approx 1.593 D_{5\,℃}$ and $D_{50\,℃} \approx 3.215 D_{5\,℃}$. Combining with Fick's diffusion laws applied in the water absorption in the polymer composites [399], more water can transport through unit area at higher soaking temperatures. In addition, higher temperatures may also promote water transport through the microchannels and networks in the composites.

The mechanism of water transport under various conditions is further analyzed through the following equation:[397]

$$\log(WAP) = k + n\log t \quad 3.6$$

Where, *WAP* refers to water absorption percentage defined in Equation 3.1, and *t* is the immersion time. The determination of the diffusion parameters of *n* and *k* under various conditions of swelling is presented in Figure 3.11.

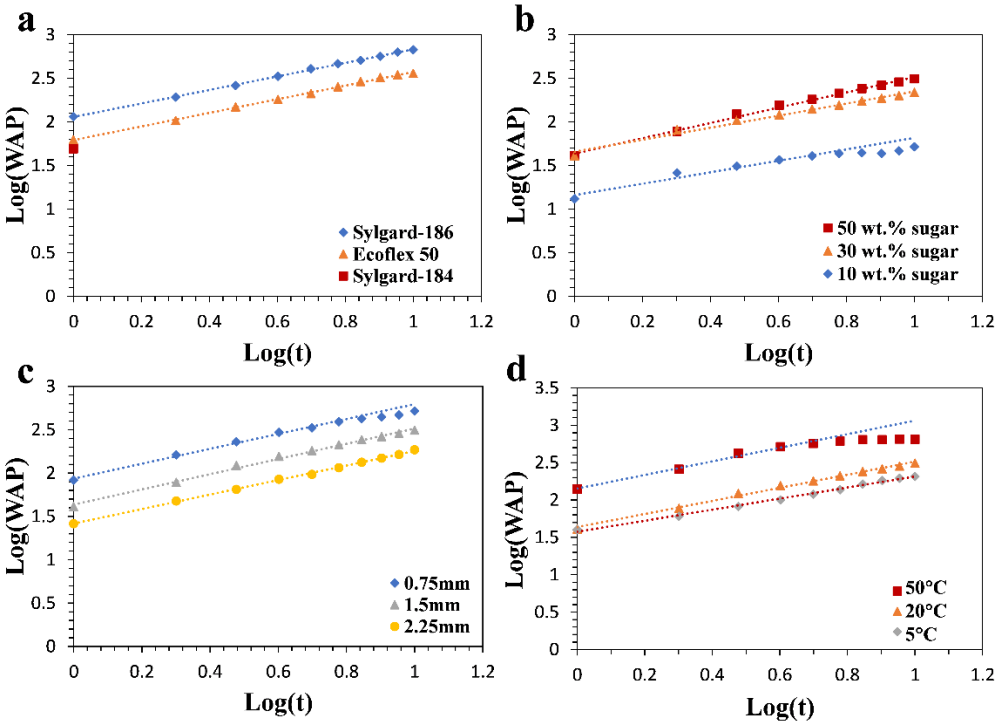

Figure 3.11 Determination of the diffusion parameters of *n* and *k* under various conditions of swelling: (a) Silicone type. (b) Sugar concentration. (c) Sample thickness. (d) Temperature of soaking medium.

Slope *n* and intercept *k* are fitted (Table 3.1) based on the water absorption results, which indicate the water transport mechanism and the initial interaction with water (i.e., water absorption after the first day of immersion), respectively. When *n* is close to 0.5, or the water absorption is proportional to $\sqrt{t}$, the water transport is Fickion diffusion-controlled, while a larger *n* indicates other mechanisms may be involved in the water transport depending on the polymer composite and water interactions [397, 400].

Table 3.1 Fitted values of slope *n* and intercept *k* under various conditions

		Slope *n*	Intercept *k*	Note
Silicone type	Sylgard 186	0.776	2.056	50 wt.% sugar;
	Ecoflex 50	0.781	1.791	1mm film thickness;
	Sylgard 184	N/A	1.693	room temperature.
Sugar Conc.	10 wt.%	0.656	1.160	Ecoflex 50;
	30 wt.%	0.690	1.657	1.5mm film thickness;
	50 wt.%	0.877	1.637	room temperature.
Film thickness	0.75mm	0.859	1.936	Ecoflex 50;
	1.5mm	0.877	1.637	50 wt.% sugar;
	2.25mm	0.838	1.417	room temperature.
Soaking Temp.	5°C	0.739	1.576	Ecoflex 50;
	20°C	0.877	1.637	50 wt.% sugar;
	50°C	0.911	2.153	1.5mm film thickness.

For all the cases except Sylgard 184, as shown in Table 3.1, the slopes *n* is larger than 0.5, indicating transport mechanisms other than diffusion also contribute to the water absorption. Microcracks or channels surrounding the sugar particles are likely present due to the moderate viscosity of Ecoflex 50 elastomer, allowing water transport through direct capillary interaction. Under a lower sugar concentration (e.g., 10 wt.%), both the *n* and *k* values are among the lowest, which can be attributed to the limited hydrophilic sites. As more sugar particles are added to the elastomer matrix, networks can also form which significantly promotes water transport indicated by the sharp increase in both *n* and *k* values (e.g., 50 wt.%). It is interesting to notice that addition of 30 wt.% sugar increases the initial water absorption significantly by introducing more hydrophilic sites, but exhibits only a slight increase in the slope *n*, indicating likely the absence of sugar network in the elastomer composites.

For the films with different thickness, the slopes *n* is very close to each other, while the initial water absorption exhibits the monotonic decrease from the thinnest to thickest samples. This shows that similar water transport mechanisms are involved in these

samples, while the initial water absorption is much higher for thinner ones when normalized with their original weight. At a lower soaking temperature (e.g., 5°C), both the slope *n* and intercept *k* are much lower than those at higher soaking temperatures, indicating higher temperature promotes both diffusion and direct capillary interactions through microchannels or networks.

Lastly, for Sylgard 186, its high viscosity likely introduces more microchannels surrounding the sugar particles and connected sugar particles forming networks. As a result, its initial water absorption is among the largest of all the testing cases. For Sylgard 184, the initial water absorption is considerable; however, the elastomer composite reached its maximum swelling in just one day due to the strong mechanical strength of the polymer chains.

3.3.5 Additives Type

In addition to the swelling of polymer composites doped with sugar particles, we investigated the water-induced swelling of 2D films comprising of Ecoflex$^{10\text{-}50}$ silicone doped with 50 wt.% of NaCl powders. The swelling differences can be easily observed between them during a long-term immersion. Based on Equation 3.1 and 3.2, we obtained the accurate swelling behaviors in Figure 3.12. Dramatical divergence occurs between the elastomer/NaCl composite film and the elastomer/sugar film in the volume swelling ratio and the water absorption. Among them, the Ecoflex$^{10\text{-}50}$ silicone/sugar composite possesses much slower swelling rate and lower volume swelling ratio and water absorption. Specifically, it took 26 days for the sample to reach swelling saturation, and the maximum volume swelling ratio and the water absorption are 1500% and 800%, respectively. Whereas the Ecoflex$^{10\text{-}50}$ silicone/NaCl composite exhibits a much higher swelling rate immediately after the start of the immersion test. Nearly 1000% of volume swelling ratio and 500% of water absorption was obtained after the first day of immersion. After soaking for 7 days, the sample reached swelling saturation, with the maximum volume swelling ratio and water absorption of about 3000% and 2000%, respectively.

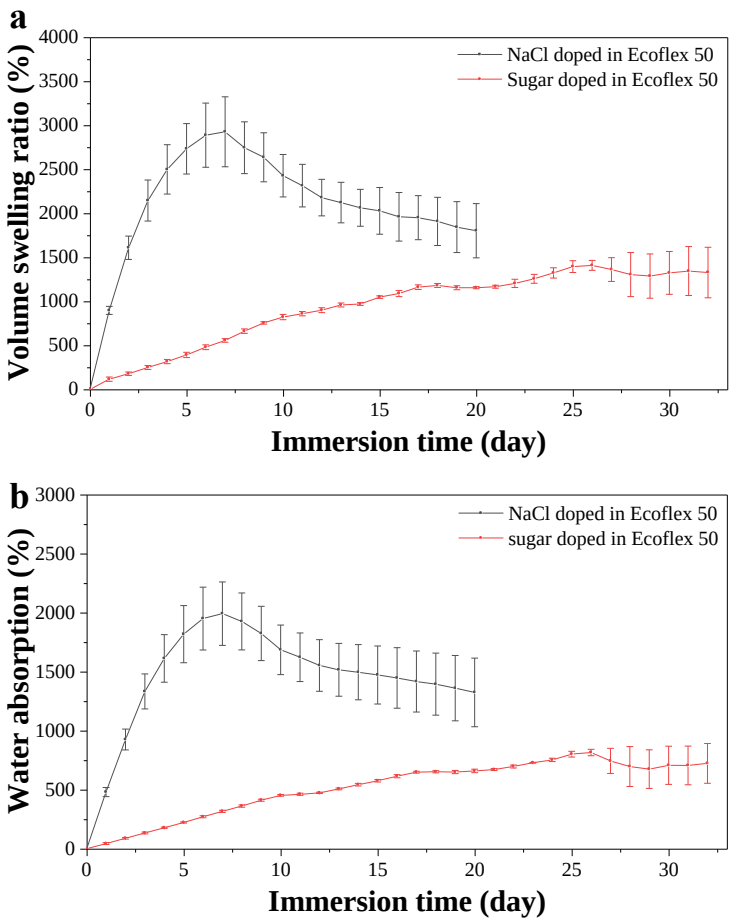

Figure 3.12 The swelling ratio of different polymer composites with immersion time. (a) Volume swelling ratio of polymer composite. (b) Water absorption of polymer composite.

In previous investigation, the osmotic pressure has been considered as the main mechanism causing the swelling of polymer composites. As the embedded additives dissolve in water, the solution "droplets" form in the elastomer substrate containing high concentration of solutes. Owing to the concentration gradient, more water diffuses into the interior pores from the soaking medium under the action of osmotic pressure according to the osmotic theory (Equation 3.7) [406]:

$$\pi = cRT \times i \qquad 3.7$$

Where, π is the osmotic pressure, c is the concentration of solute, R is the universal gas constant, T is the temperature in Kelvins, and i is Van't Hoff factor.

It is known that the solubility of sucrose and NaCl are about 2040 g/L and 360 g/L in DI water at 20 ℃. The molar mass of sucrose and NaCl are 342 g/mol and 58.44 g/mol, respectively. Suppose these hydrophilic substances in polymer composite reach

their maximum solubility when soaked in water. The initial molar concentrations of sucrose and NaCl in the "cavities" are calculated about 6 mol/L and 6.2 mol/L, respectively. Thus, it can be assumed that the initial concentration of sucrose is similar to that of NaCl in these "cavities". However, the total molar number of additives is probably attributed to the huge swelling difference. With the same weight of additives added to the elastomer, the molar amount of NaCl would be nearly six times higher than that of sugar powders, maintaining the high molar concentration of NaCl solution in these cavities during soaking.

Additionally, the Van't Hoff factor also differs between sucrose and NaCl. The van't Hoff factor i refers to the number of ions formed by the compound in solution. As a non-electrolyte in water, the i of sucrose is essentially 1. As for NaCl, it comprises of two ions i.e., sodium ion and chlorine ion, therefore the i has a value of 2 given complete dissociation. Combining these two factors, the osmosis pressure of NaCl should be much larger than that of sucrose. The discussion can reasonably explain that Ecoflex$^{10\text{-}50}$ silicone/NaCl composite possesses a higher swelling ratio than that of Ecoflex$^{10\text{-}50}$ silicone/sugar composite.

As the volume expansion of polymer composites proceeded and some NaCl ions being released to the soaking medium, the concentration gradient gradually decreases, which causes the decrease of osmotic pressure. In return, the water diffusion rate gradually decreases. When the volume swelling ratio reaches the maximum value, the osmotic pressure is balanced with contractile force, i.e., polymer chain systole. In the subsequent immersion process, the contractile force becomes larger than the decreasing osmotic pressure. As a result, the swelling ratio appears a decrease trend after 7 days of immersion.

3.4 Conclusion

Water-induced polymer swelling was achieved by introducing sugar or NaCl particles to the silicone matrix and soaking the composites in water. Swelling is driven under the interactions of osmotic pressure and constraining stress by the polymer chains. Different swelling behaviors among the selected silicone elastomers are attributed to

their mechanical property and viscosity. Silicones with a higher elastic modulus result in smaller swelling in both volume and water adsorption. Higher silicone viscosity may cause formation of microchannels surrounding the embedded sugar particles, through which water transport occurs accelerating the water absorption and swelling. Four processing parameters were investigated having crucial influence on the swelling of polymer composites, including concentration of additives, type of additives, film thickness, and temperature of aqueous solution. Higher additives concentrations, ionic electrolyte, additives with higher soluble, thinner films, and elevated temperatures promote the polymer swelling.

CHAPTER 4 Fabricating Soft Electronics based on Water-induced Polymer Swelling

4.1 Introduction

With advances in soft electronic technologies, flexible and stretchable conductors are commonly considered as the key components for the next generation flexible devices.[407-409] With excellent ductility, fatigue durability, ultra-sensitivity, and short response time, they have been widely used as sensors in various applications, such as human motion monitoring,[410-413] human-machine interface,[414-417] and soft robotics,[418-419] etc. These advantages bring forth huge economic benefits and drastically improve the quality of human life.

In the past decades, researchers have advanced the quality of the sensors, including higher stretchability, sensitivity, stability, and linearity, etc. Various technical approaches have been adopted to improve the performance of flexible and stretchable sensors, including selecting different conductive materials (such as graphene,[1-2] reduced graphene oxide (rGO),[3-4] carbon nanotube (CNT),[5-6] metal nanoparticles/wires/flakes,[7-9] etc.) and using various fabrication methods (such as drop casting,[10] spin coating,[11] spray coating,[12] Meyer rod,[13] printing,[14] etc.). Recently, some researchers proposed constructing wrinkled structures to obtain the sensors with excellent properties.[420-422]

One of the most common ways to fabricate the wrinkled structures is pre-stretching, which has proven a useful method.[371, 421, 423-424] Liang *et al.* sprayed silver nanowires (AgNWs) on a 20% pre-stretched polydimethylsoloxane (PDMS) film surface.[425] The result showed that a buckled microstructure was formed in the pre-stretched direction when the film resumed to zero strain. This geometrical feature was attributed to the better electrical performance since it could assist in relieving the majority of the stress during stretching in the pre-stretched direction. Zhang *et al.* pre-stretched the polytetrafluoroethylene nanocomposites with different concentrations of conductive filler materials,[426] and found that its tensile strength was improved by 42.9 %, although

the elongation at break and thermal conductivity deteriorated. Liu *et al.* deposited AgNWs onto the surface of PDMS film with the biaxial pre-stretching.[427] The obtained samples possessed more stable performance, such as superior electrical conductivity and ultra-reliability, when compared to the un-stretched or uniaxially pre-stretched samples.

Pre-stretching, however, inevitably brings about strain localization and micro-cracks, which produces a considerable negative effect on the fatigue life of the devices.[428] In this case, some researchers proposed taking advantage of swelling to induce the polymer deformation.[402] A uniform volume expansion can be obtained during the polymer swelling process. Gao *et al.* prepared a wrinkled sensor by using chloroform to swell PDMS followed by silver film deposition.[403] Upon the evaporation of chloroform, the PDMS film shrank forming the wrinkled conductive film because of the out-of-plane undulation. The cross-link ratio of PDMS and silver film deposition time were closely correlated with the wrinkled structure. Zhang *et al.* soaked the PDMS film in toluene to realize the swelling effect.[27] Then the swollen film was submerged into CNTs suspension to enable its conductivity.

Polymer swelling can overcome the drawbacks of the pre-stretching approach; however, organic solvents often have to be utilized in this process. Most of these organic solvents are volatile and toxic, producing adverse effects on human health and the environment. In this work, we report a water swelling strategy to replace the conventional organic solvent swelling. Ecoflex 50 silicone elastomer mixed with fine sugar particles were selected as the substrate materials. Due to its strong solubility in water, sugar has been widely used as a template material for flexible and stretchable devices.[429-430] When the silicone/sugar composites are exposed to water, the sugar particles embedded in the silicone matrix attract water due to its hydrophilicity. This forms a high concentration sugar solution in the pores that were originally occupied by the sugar particles. Under the osmosis principle, more water is drawn into these micro pores pushing the elastomer surrounding them and further enlarging these pores. The elastomer experiences significant swelling, which is leveraged to fabricate stretchable

sensors.

In this work, sensing devices have been prepared by molding and 3D printing of the composite materials. By immersing them in deionized (DI) water, these samples exhibited desirable swelling that linearly increases with soaking time. The conductive layers have been deposited by in-situ growing AgNPs, sputtering Au, depositing graphene, and attaching AgNWs on the swollen elastomer films/3D structures. Upon removal of the residual water, the swollen samples coated with conductive layer gradually shrink to form wrinkled structures with the out-of-plane undulation. We have evaluated the electrical properties of the fabricated strain sensors as well as its 3D printing capability.

4.2 Experimental Section

4.2.1 Materials and Preparation

The silicone elastomer is the commercial Ecoflex-50 (Smooth-on, Inc.), which was prepared by mixing part A and part B in weight ratio of 1:1. The sugar particles (Domino Foods, Inc.) was 10-X powdered pure cane sugar with cornstarch. Sodium chloride (NaCl ≥99%, ACS reagent, Sigma-Aldrich) was adopted. A sieve with 105 μm-pores was used to filter the sugar/NaCl particles. Then, the silicone elastomer and the fine sugar/ NaCl hybrid in the weight ratio of 1:1 was mixed in a planetary mixer (ARE-310, Thinky Mixer) for 2 minutes at 2000 RPM. Subsequently, a de-foam process was used for 30 seconds to remove any air bubbles inside the mixture. The elastomer/sugar composite was ready for molding or 3D printing.

4.2.2 Fabrication of Elastomer Films and 3D Printed Structures

A groove mold was designed to prepare the elastomer strips. The mold was made of glass, with dimensions of $20\text{mm} \times 10\text{mm} \times 1\text{mm}$. Before casting the elastomer into the mold, a universal model release (Smooth-on, Inc.) was applied to treat the mold surface for easy release. A cover glass was used to level and seal the elastomer in the groove mold. After 12 hours in air, the cured Ecoflex/soluble film was peeled off from the mold. To fabricate the printed structures, a 3D lattice model was designed in a CAD

software (Solidworks) followed by slicing. An extrusion-based 3D printer (EnvisionTec, 3D Bioplotter) with a smooth-flow tapered nozzle (400 μm in diameter, Nordson) were used to print the 3D lattice structures. The printing parameters were regulated for the best printing quality, including 1.5 bar of pressure, 10 mm/s of printing speed, 0.2 s of pre-flow, and 0 s of post-flow, etc.

4.2.3 Deposition of Conductive Layers

Followed by immersion of the elastomer/soluble films or structures in DI water for a given duration, the AgNPs were *in situ* deposited on the swollen substrates. Three steps were taken in the synthesis process. (1) In the first beaker, 1 g silver nitride ($AgNO_3$) was dissolved in 50 mL DI water, then ammonia was continually added until the solution became clear again. (2) In the second beaker, 1.125 g glucose was dissolved in 50 mL DI water. Meanwhile, 5 mL ethanol was dropwise added to the solution. (3) The silver ammonia solution was dropwise added into the solution in the second beaker while stirring on a shaker. The swollen elastomer substrates were immersed in the solution for AgNP deposition. Also, the thin Au film was sputtered onto the swollen polymer film, the graphene layer was deposited onto the 3D swollen polymer substrate, and the AgNWs were attached onto the 2D and 3D swollen structure.

AgNWs were synthesized using a modified polyol reduction method [344, 431]. 0.5 g PVP was dissolved in 50 mL EG solution in a round-bottomed flask with a stirring speed of 400 rpm. An oil-bath was used to keep the solution at 170 ℃ for 1 h to form a homogeneous solution. Next, 150 μL of NaCl/EG solution (0.1 mol/L) was added. After 10 minutes, 50 mL of $AgNO_3$/EG solution (10 g/L) was gradually dripped into the flask with a volumetric flow rate of 2.5 mL/min. Another 20 min at 170 ℃ was required to support the whole reaction process after completing the addition of $AgNO_3$/EG solution. Subsequently, the solution in the flask was cooled down to room temperature, and precipitated with acetone and centrifugated at 3000 rpm for 20 minutes. Finally, followed by three times' washing with ethanol through centrifugation to remove the residual PVP, the AgNW/ethanol suspension was obtained with a solid concentration of 10 mg/mL. The morphology of the synthesized AgNWs is shown in Figure 4.1a and

their lengths were counted via ImageJ, with an average length of 3.83 ± 2.042 μm (Figure 4.1b).

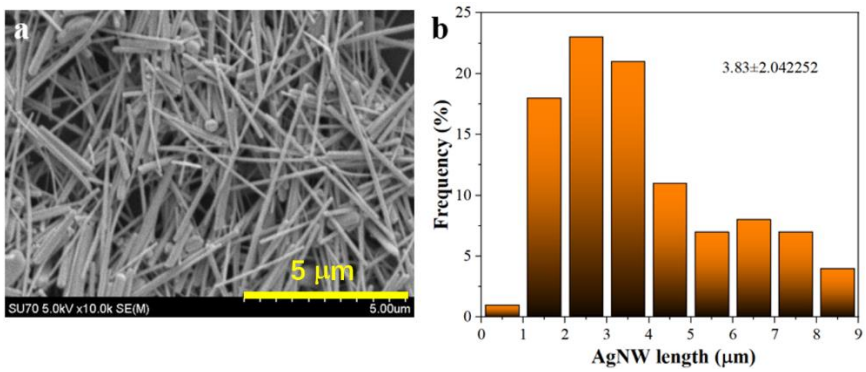

Figure 4.1 (a) SEM image of the AgNWs. (b) Histogram of the AgNW size distribution.

4.2.4 Measurement and Characterization

To observe the 2D surface morphology, a field-emission scanning electron microscope (FE-SEM, HITACHI, SU-70) with 5 kV operating voltage were employed. To minimize charging, the samples were sputtered with gold for 75 s (Denton Vacuum Desk V). Laser scanning confocal microscopy (ZEISS, LSM770, US) was utilized to characterize the 3D morphology and surface roughness. Fourier transform infrared spectroscopy (FTIR, NEXUS-470) was selected to identify the functional groups. Water contact angles on the elastomer films were characterized by a goniometer (OCA 15, DataPhysics). A 4-point probe system (Ossila, UK) was used to characterize the sheet resistance of the elastomer films. A digital multi-meter (Fluke 289 True-RMS) was employed to record the resistance change during the dynamic deformation processes. The cyclic stretching was conducted on a home-made stretcher controlled by a computer, at a speed of 0.5 mm/sec. The experiments of human motion detection were performed with a healthy adult. A written consent was obtained from the participant in this manuscript regarding the research experiments and publication.

4.3 Results and Discussion

4.3.1 In-situ Growing AgNPs on Swollen Polymer Substrate

The schematic in Figure 4.2a illustrates the process to fabricate the highly conductive silicone elastomer taking advantage of the environment-friendly water

swelling behavior. The swollen elastomer was obtained via immersion of the silicone/sugar hybrid in DI water ranging from a few days to weeks. Following the in-situ deposition of AgNPs, a uniform conductive layer can be formed on the swollen samples. Finally, by removing the residual water in the samples, the conductive layer along with the elastomer substrate shrinks to form the wrinkled structures.

We have characterized the swelling behavior of the 2D films consisting of the cured elastomer and sugar composite made by molding. After immersing the samples in DI water, an isotropic swelling gradually appears. Figure 4.2b shows the volume of specimens before and after 3 days of immersion. A significant volume expansion was clearly detected. The water absorption and volume expansion during immersion were summarized in Figure 4.2c and 4.2d. By the least square fitting, more than 95% linear relationship is determined in the swelling volume and water absorption with respect to the immersion time. Thus, it is possible to obtain a controllable swelling within the first 10 days of immersion. Considering the highly linear relationship and significant swelling effect, we have fabricated the samples within 10 days of immersion. The mechanism of water-induced swelling has been studied in chapter 3.

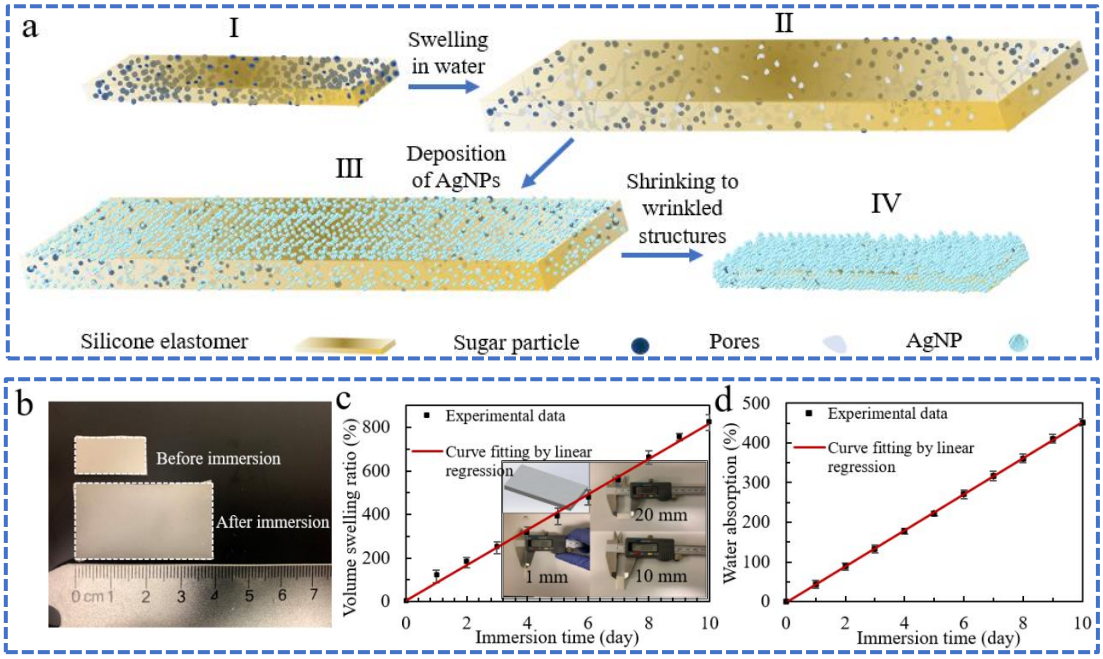

Figure 4.2 (a) Schematic of the fabrication process of stretchable elastomer conductors through water swelling and in-situ silver nanoparticle synthesis. (b) Comparison of the elastomer/sugar films before and after 3-day immersion. (c) Volume swelling ratio with respect to the immersion duration. The inset shows the original film dimensions before immersion. (d) Water absorption with respect to the immersion duration.

The surface morphology and roughness of the samples in the fabrication process are compared. The morphology of pure Ecoflex 50 film was displayed in Figure 4.3.

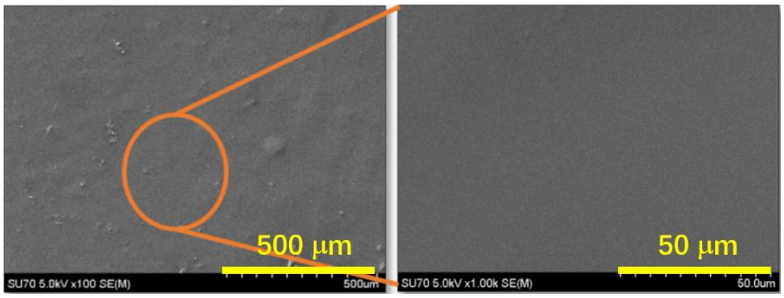

Figure 4.3 SEM image of the pure Ecoflex 50 film.

By adding 50 wt.% of sugar particles, the sugar-decorated silicone film became much rougher (Figure 4.4a). The surface roughness (R_a) of the silicone/sugar film increased to 3.1 µm, compared to the roughness of 0.188 µm on the pure silicone film, as shown in Figure 4.4g and 4.4h. After immersion in DI water for 23 days, the surface roughness R_a became 1.003 µm (Figure 4.4i), which significantly decreased due to

sugar releasing and polymer swelling. By removing the water through drying, the swollen film shrank to nearly its original size and noticeable void spaces appeared on its surface where the particles left after releasing (Figure 4.4j), with surface roughness R_a of 1.565 μm. Next, in-situ growing silver nanoparticles (AgNPs) were adopted to form a conductive layer on the silicone films. The complete chemical reactions are described as Formula 4.1, 4.2, and 4.3:[432-433]

$$2AgNO_3 + 2NH_3 \cdot H_2O = Ag_2O + 2NH_4NO_3 + H_2O \quad 4.1$$

$$Ag_2O + 4NH_3 \cdot H_2O = 2Ag(NH_3)_2OH + 3H_2O \quad 4.2$$

$$2[Ag(NH_3)_2]OH + C_6H_{12}O_6 = 2Ag\downarrow + C_6H_{12}O_7 + 4NH_3 + H_2O \quad 4.3$$

We have selected the pure silicone film (unswollen) and the 3-day swollen silicone/sugar film as the deposition substrate. After drying in oven, the morphologies of AgNPs with 15 min and 45 min deposition times were characterized and compared in Figure 4.4c~f. On the pure silicone film, an unevenly distributed AgNPs film was presented in Figure 4.4c after 15 min of deposition. As the deposition time extends to 45 min, a more uniform AgNPs film was formed, but several cracks can be easily detected (Figure 4.4d). The roughness of the sample (R_a) was 0.286 μm (Figure 4.4k) that increased by 52% in contrast to the pure silicone film. As for the swollen sample, a micro-wrinkled structure was obtained after 15 min of AgNP deposition. When the deposition time reaches 45 min, the wrinkled structure was further enhanced with a surface roughness of 8.808 μm (Figure. 4.4l). Compared to the substrate before the AgNP deposition (Figure 4.4h), the undulating wrinkle structure was attributed to the substrate roughness and stacked AgNPs after shrinking.

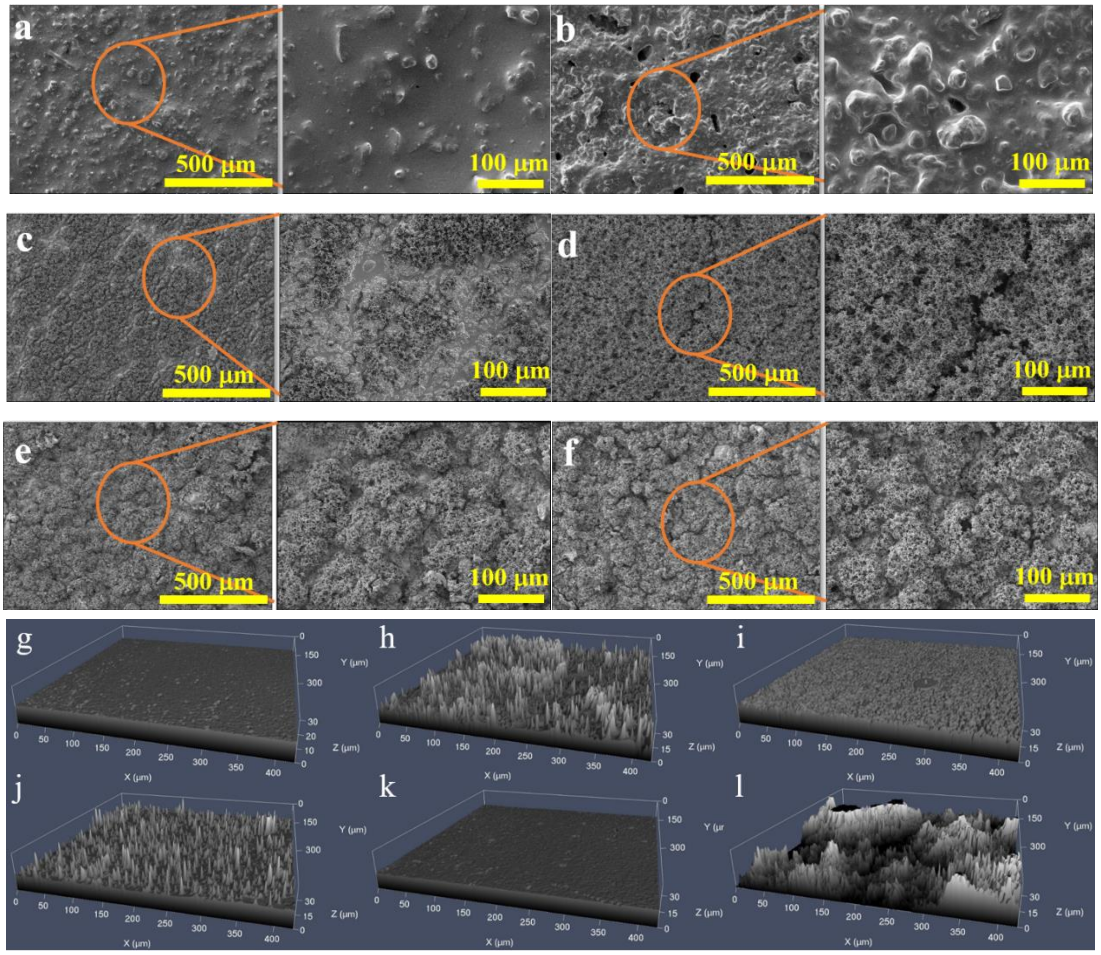

Figure 4.4 Morphology of the elastomer films: (a) Ecoflex/sugar film before immersion in DI water. (b) Ecoflex/sugar film after 3 days of immersion in DI water. Some sugar particles were still present in the film. (c) and (d) Pure Ecoflex films with 15 min and 45 min of AgNP deposition. (e) and (f) Water swollen Ecoflex/sugar film with 15 min and 45 min of AgNP deposition. (g) Surface roughness of the pure Ecoflex film. (h) Surface roughness of the Ecoflex/sugar film before immersion. (i) and (j) Surface roughness of the 3-day soaked Ecoflex/sugar film before and after drying. (k) and (l) Pure Ecoflex film and water swollen Ecoflex/sugar film with 45 min of AgNP deposition. Except the sample in (i), all the films were cured and dried for characterization.

Mechanical properties of the elastomer films were provided in Figure 4.5. Mechanical strength of the pure Ecoflex 50 film, Ecoflex 50/sugar film and the wrinkled film with AgNP deposition were characterized on Instron (MTS, Insight 30). Compared to that of pure Ecoflex 50 film, the stretchability of the Ecoflex 50/sugar

film was notably decreased, while the mechanical strength increased correspondingly. The mechanical strength of the wrinkled film was higher than that of the pure ecoflex film for smaller strains, probably due to the AgNP layer. For larger strains, its mechanical strength is inferior to its pure elastomer counterpart because of the formed porous structure in the elastomer substrate after releasing of the sugar particles.

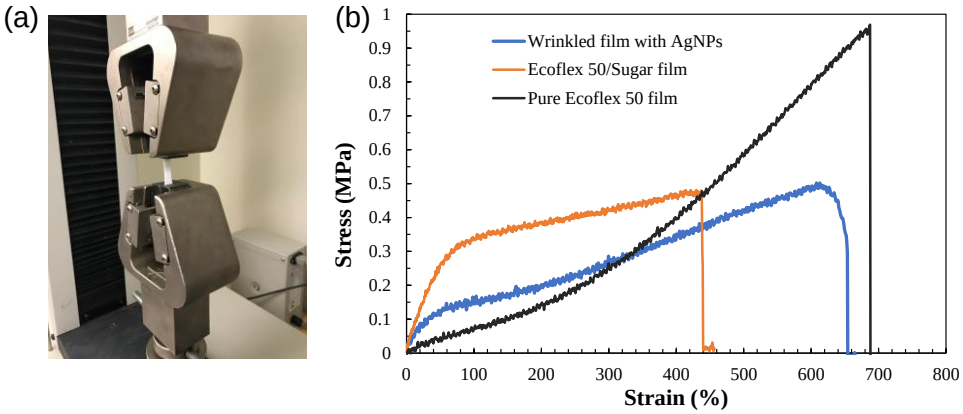

Figure 4.5 (a) An elastomer film in the tensile test. (b) Stress-Strain curves for pure Ecoflex 50 film, Ecoflex 50/sugar film, and the wrinkled film with AgNPs (60 min of deposition).

Electrical performance of the elastomer films has been characterized in Figure 4.6. Among them, Figure 4.6a and 4.6b exhibited the sheet resistance of the elastomer films with and without wrinkled structures at zero strain (no stretching), measured by the 4-point probe method. Three samples in each case and six different locations on each film were selected to reduce the measurement error and to evaluate the film uniformity. The resistances of the unwrinkled elastomer films (Figure 4.6a) were 5±2.7 Ω/sq, 4±1.3 Ω/sq, 1.4±1.13 Ω/sq, and 0.2±0.14 Ω/sq for 15 min, 30 min, 45 min, and 60 min of AgNP deposition, respectively. The results indicated that AgNP deposition time has a great influence on the conductivity of the unwrinkled films where the average resistance drastically decreases as the AgNP deposition time extends. The main reason was that a short deposition time (e.g., less than 60 min) cannot ensure that the deposited AgNPs fully cover the substrate surface. On the other hand, the large standard deviation was attributed to the uneven distribution of AgNPs and possible cracks, which was supported by the surface morphology in Figure 4.4c and 4.4d. As for the wrinkled films,

the resistance was 0.6 Ω/sq after 15 min deposition, which accounts only ~12 % of the unwrinkled film under the same deposition condition. As the AgNP deposition time extended to 30 min, 45 min, and 60 min, the resistances of the wrinkled films kept stable near 0.1 Ω/sq. Meanwhile, the standard deviation of the resistance on the wrinkled samples were 0.23, 0.02, 0.01, and 0.02 Ω/sq, respectively. The stable and low resistances indicated that the AgNPs have completely covered the elastomer samples, and a uniform conductive pathway has formed on the substrate enabled by the substrate swelling. Compared to the smooth Ecoflex film, the swollen film had a larger surface area enabling more silver nanoparticle deposition. In addition, the increased roughness and enhanced hydrophilicity on the Ecoflex/sugar film contributed to a stronger adhesion with the deposited AgNPs. After water evaporation, the wrinkled structures formed, bringing the AgNPs into closer contact. As a result, an outstanding improvement in electrical property has been achieved with the assistance of the wrinkled structures.

We have evaluated the electrical performance of the conductive elastomer films during cyclic stretching. The resistances of the wrinkled elastomer films were recorded during five stretching/releasing cycles with different strains. Figure 4.6c showed the resistance of the wrinkled films with 15 min of AgNP deposition under 10 % and 20 % strains. The maximum resistance reached 446 Ω at larger deformations. The wrinkled films with 30 min of AgNP deposition can respond to a 30 % tensile deformation as shown in Figure 4.6d. The maximum resistance surged to 723.8 Ω, and the resistance fluctuated sharply at this maximum strain. As for the wrinkled films with 45 min of AgNP deposition, the maximum strain percentage reached 60 % and the maximum resistance reduced to 293 Ω at its maximum strain (Figure 4.6e). With 60 min of AgNP deposition, the wrinkled film survived the strains up to 100% before resistance became unstable (Figure 4.6f). The maximum resistance further dropped to 129 Ω. The working strains demonstrated in this work are comparable to or higher than that in other published works.[8, 434-436]

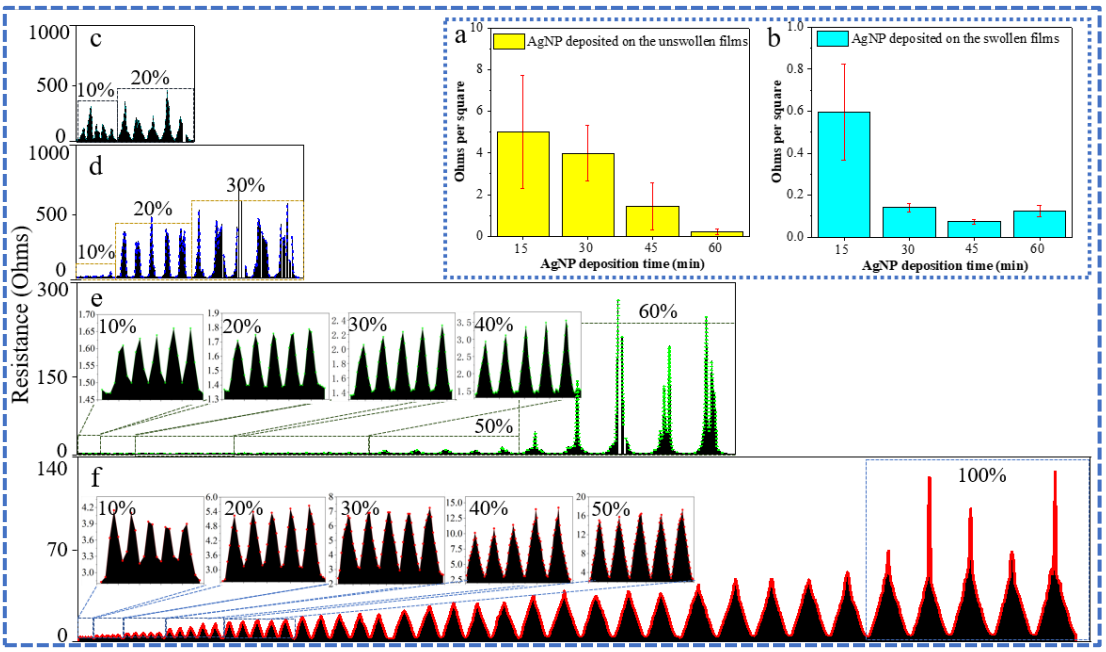

Figure 4.6 Electrical performance of the elastomer films. (a) Sheet resistance of the unwrinkled films. (b) Sheet resistance of the wrinkled films. (c)~(f) Resistance response under five cycles of increasing strains for the wrinkled elastomer films with 15 min, 30 min, 45 min, and 60 min of AgNP deposition times, respectively.

In contrast, the resistance of the pure elastomer films with AgNP deposition increased to MΩs even for as low as a 10% strain (Figure 4.7), indicating the inferior electrical performance especially under stretching. From the results above, we can summarize that the peak resistances of the wrinkled elastomer films all show an increasing trend when the stretching strain increases. Especially in the samples with longer AgNP deposition times (e.g., 60 min), the peak resistance exhibited a gradual and monotonic relationship as stretching strain increases to 100%, which is desirable for stretchable strain sensors.

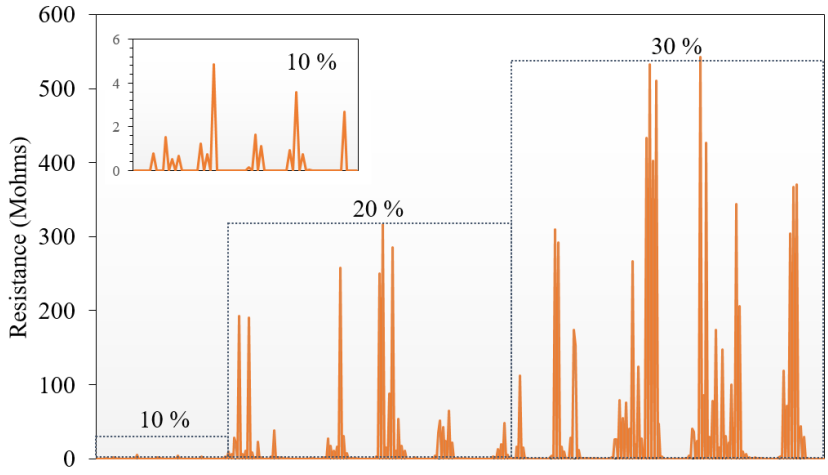

Figure 4.7 Resistance response under five cycles of increasing strains on the pure Ecoflex elastomer films with 60 min of AgNP deposition.

In addition to the strain magnitude, it is necessary to verify the performance repeatability of the wrinkled elastomer films over long-term cyclic deformations. Figure 4.8 displayed the resistance response during 550 stretching/releasing cycles when the elastomer film was stretched to 50 % strain and released back to the original strain condition.

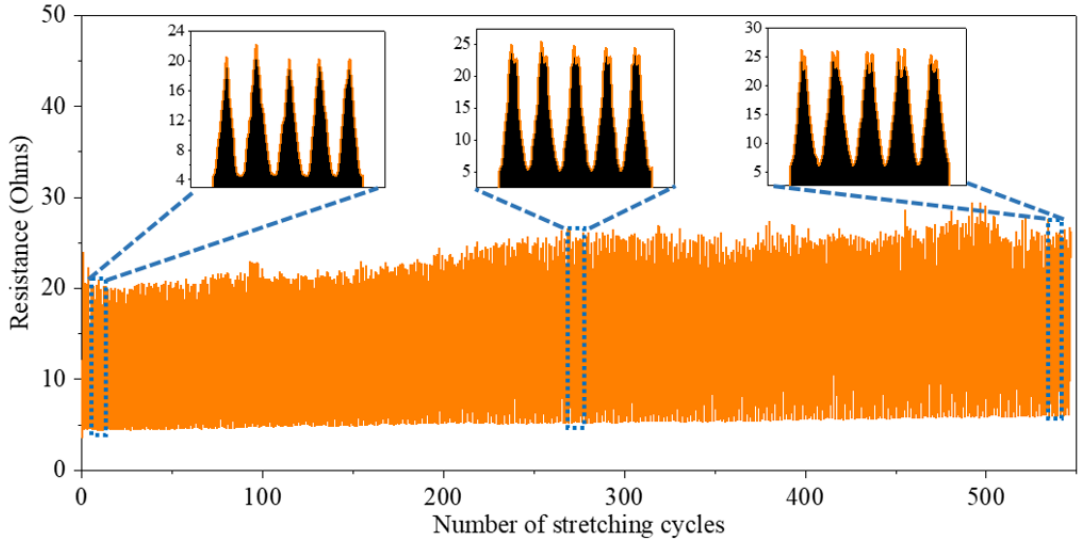

Figure 4.8 Resistance of the wrinkled elastomer films during 550 stretching/releasing cycles between 0 and 50% strain. 60 min of AgNP deposition was used.

The initial resistance of the elastomer film was about 3.6 Ω. During the first stretching of 50% strain, the resistance increased to 23.9 Ω and dropped to 4.4 Ω after releasing back to zero strain. Namely, the initial resistance increased by 22% after the first releasing cycle. In the subsequent 50 cycles of stretching, the resistance at zero

strain almost remained constant, but the resistance at 50% strain revealed a moderate decrease from 23.9 Ω to ~21.3 Ω. Similar phenomena have been reported.[207, 257] The 10.8% drop in resistance can be attributed to the conditioning process of the AgNPs on the wrinkled elastomer films, where they tend to rearrange themselves to achieve stable point-to-point contacts due to the cyclic stretching/releasing.[437] It is interesting to note that this behavior at the first stretching cycle has not been observed when gradually increasing the strains (Figure 4.6f), probably due to the conditioning and rearranging of the conductive path during stretching at the smaller strains. From 50 to ~275 stretching cycles, the resistances increased by about 10% and 20% at zero strain and 50% strain conditions, respectively. Under the repeated stretching, unavoidable displacements appeared between AgNPs, which leads to an irreversible increase in the number of disconnected AgNPs. This change brings about slight degradation of the conductive network. In the next 275 cycles of stretching, the resistance increased about 15.7% at zero strain, but still possessed as low as 6.08 Ω. The resistance at the 50% strain slightly fluctuated around 25 Ω. The enlarged views of resistance changed during the three stages, i.e., initial (1-50 cycles), intermediate (51-275 cycles), and final stage (276-550 cycles), are shown in the insets in Figure 4.8.

In addition to the resistance changes under stretching and releasing, a momentary drop in resistance appeared during the intermediate stage when stretched to the maximum strain, and widens gradually after the repeated stretching cycles. For instance, this momentary drop increased from 0.2 Ω in the intermediate stage to about 3 Ω in the final stage. A self-repair process was considered as a reasonable mechanism to explain this momentary drop in resistance. At the maximum deformation, the AgNPs can fill the formed cracks and bridge between the broken AgNPs.[438] As a result, a drastic increase of resistance was avoided at the maximum deformations. Microscopically, the wrinkled structure seemed less pronounced possibly due to the shifting and relocating of the AgNPs during the cyclic stretching process (Figure 4.9). Compared to the morphology of the AgNPs before stretching (Figure 4.9a and 4.9b), the wrinkled structure seemed less pronounced possibly due to the shifting and relocating of the

AgNPs (Figure 4.9c). No obvious change was identified on the AgNP agglomerates (Figure 4.9d).

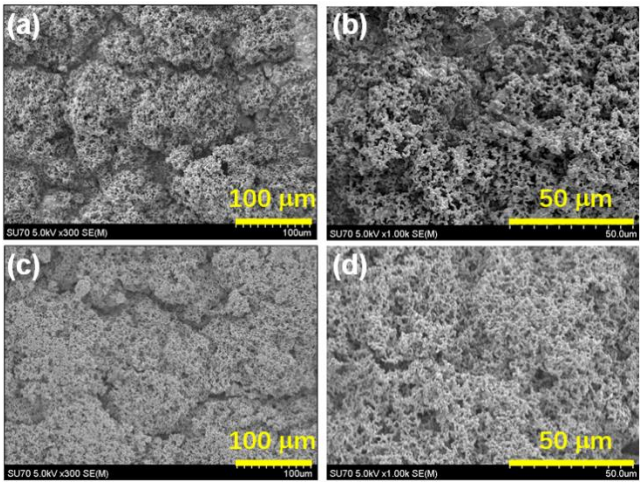

Figure 4.9 Morphology of the AgNPs before (a-b) and after (c-d) 550 stretching/releasing cycles at strain of 50%. 60 min of Ag NP deposition was used.

In order to fabricate sensing devices with on-demand shapes and design patterns, 3D printing technology was introduced. We first evaluated the viscosity of the printing inks and determine their printability (Figure 4.10a). Pure Ecoflex 50 elastomer had a low and constant viscosity (~9-10 Pa.s) at the shear rate of 0-100 s^{-1}. Therefore, pure Ecoflex 50 usually is not adopted as a 3D printing ink, due to the fact that the 3D shape and structures are not sustained after printing. However, the viscosity of the the Ecoflex/sugar hybrid was drastically promoted at low shear rates. With shear rate increasing, the viscosity exponentially dropped, indicating the desirable shear-thinning property for the extrusion-based 3D printing. The result indicated that the Ecoflex/sugar ink not only can be smoothly squeezed out from the printing nozzle, but also possesses an outstanding plasticity after 3D printing. In addition to its role in inducing swelling in the elastomer, this can be considered as another merit of adding sugar particles into the elastomer to enable 3D printability. A complex pattern with zig-zags was printed with the Ecoflex/sugar composite ink as shown in Figure 4.10a and 4.10b.

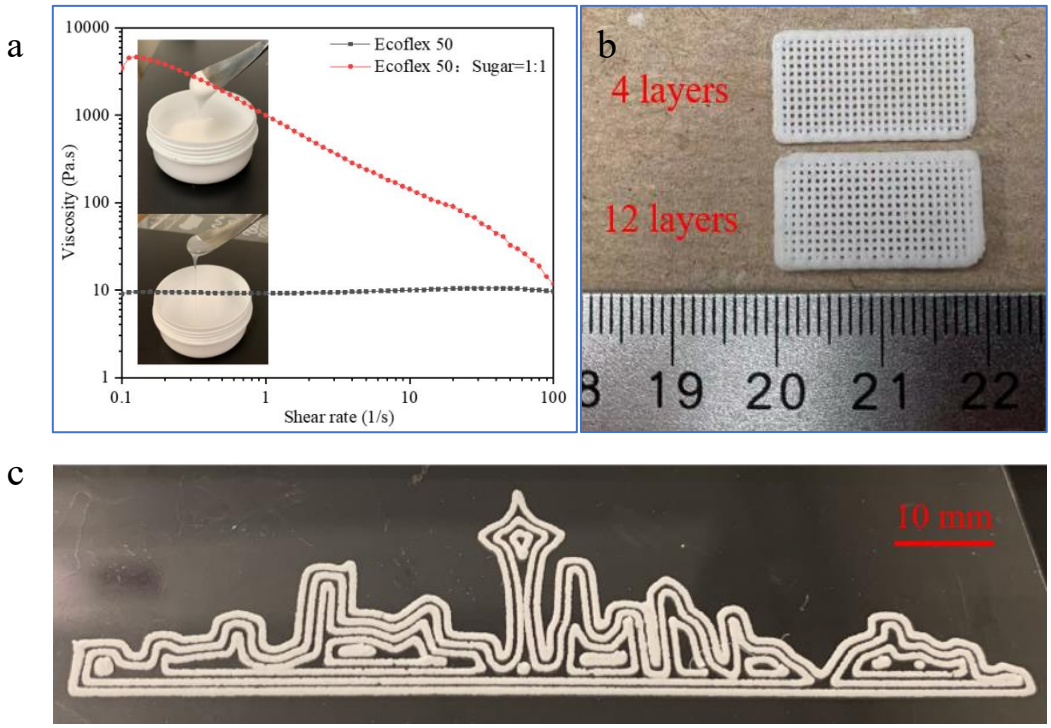

Figure 4.10 (a) Viscosity of the pure Ecoflex elastomer and the Ecoflex/sugar hybrid, 3D printed structures with the elastomer/sugar composite: (b) Lattice structures. (c) Skyline view pattern.

Three dimensional grid lattice structures have been printed with the same overall dimension as the molded solid films, and comparable swelling was achieved as shown in Figure 4.11a. The surface morphology of the printed strands were presented in Figure 4.11b. After immersion in DI water for 3 days, some sugar particles released and water refilled the pores, resulting in the swelling behavior. By removing the residual water inside the structure, a rough surface was formed as shown in Figure 4.11c. Finally, in-situ growing AgNPs on the swollen structure was carried out for 60 min to complete the wrinkled structure upon drying (Figure 4.11d).

We have assessed the performance of the 3D printed lattice structures for sensing. The resistance changes were recorded under various cyclic strains ranging from 10 % up to 100 % (Figure 4.11e). The increasing trend in resistance response can be clearly observed, which is highly consistent with that of the solid elastomer films. The electrical response with 5 stretching/releasing cycles, however, revealed a higher stability and repeatability for the same streching percentage, compared to the solid

elastomer films. The characteristics of the printed senors suggested potential applications for human motion monitoring. As one of the most often used human routine behaviors, bending at the arm joint was monitored by the printed sensor. Figure 4.11f summarized the resistance response under different arm bending angles. With the increasing of the bending angles from 0° to 10°, 20°, 30°, and 45°, the resistance increased from the orginal 1 Ω to 20 Ω, 50 Ω, 170 Ω, and 1300 Ω, respectively. In addition, leg press motion was monitored by the printed sensor as shown in Figure 4.11g. In the initial state, the sensor resistance was about 1 Ω. As the movement proceed, the resistance gradually increased, and eventually reached about 300 Ω. The five cycles of resistance response represented five repetitions of leg presses.The deviation between the five cycles was caused by the movement difference. Based on these results, it is proposed that the dynamic profile of resistance change can be employed to distinguish and monitor different human motions.

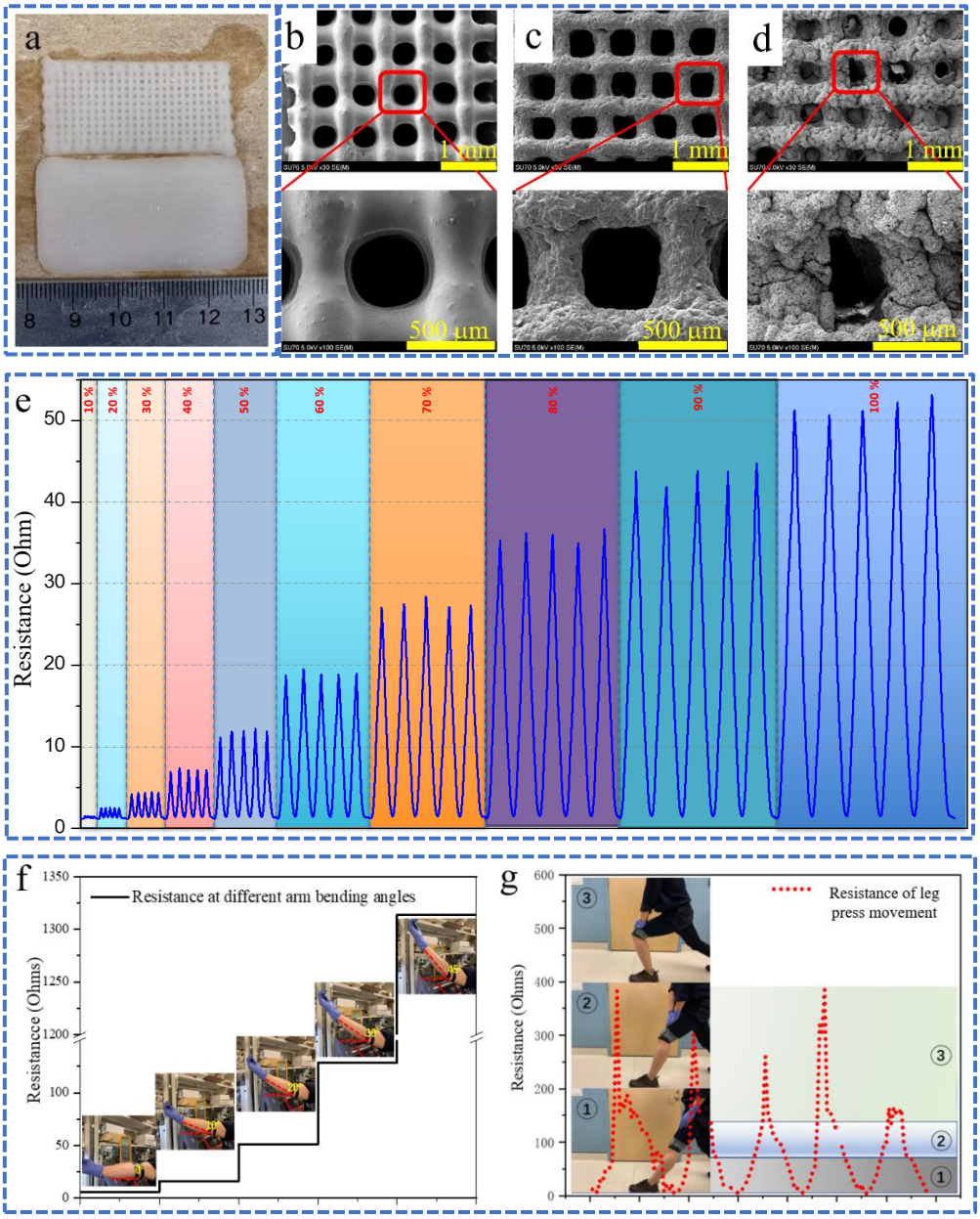

Figure 4.11 (a) Comparison of the swollen film and 3D printed lattices. (b)~(d) Surface morphology of the printed lattices at different steps: as-printed, after 3-day soaking, and after 60 min AgNP deposition, respectively. (e) Resistance response under five cycles of increasing strains on the printed lattice structure. (f) Resistance response to different arm bending angles. The sensor was attached to the participant's elbow. (g) Resistance response to leg press movement. The sensor was attached to the participant's knee.

4.3.2 Sputtering Au on Swollen Films through Vapor Deposition

We have investigated the volume swelling ratio of polymer matrix increases with

the extension of immersion time. In this part, we separately soaked the elastomer composites in DI water for different immersion durations to obtain different swelling ratios. By sputtering Au on the swollen films followed by a drying process, conductive wrinkled structures were formed on the Ecoflex 50 composite film.

The initial sample dimension was 20mm × 10mm × 1mm before immersion, as shown in Figure 4.12a. After swelling and Au sputtering treatment, the polymer composite films exhibited the gold color, as displayed in Figure 4.12b~d. These treated samples were subsequently dried in oven at 50 ℃ for 24 hours.

Surface morphonology of these films were characterized after drying. Very distinct folded and winkled structures were present on the Au-sputtered samples depending on the degree of swelling. Larger wrinkle wavelength and lighter amplitude can be observed on the samples with one day of water swelling, as exhibited in Figure 4.12e. As immersion time extended to five days and ten days, the winkles became much finer and their wavelength dramatically decreases (Figure 4.12f and 4.12g). Deep folds and creases are developed on the samples with ten days of swelling, as a result of shrinking from the largest swelling expansion.

We attributed the formation of wrinkled structures to the difference in elastic modulus between Ecoflex 50 composites and gold film during the water removal. In this aspect, the water-induced swelling plays a similar role as pre-stretching of polymers commonly used in fabricating wrinkled conductive devices [423, 439-440]. The modulus difference leads to the contraction of polymer chains and resistance against contraction of Au film during drying process. Thus, a larger shrinkage was prone to bring about severe folds since inward-curl and outward-protrusion can be simultaneously excited, as shown in Figure 4.12e~4.12g.

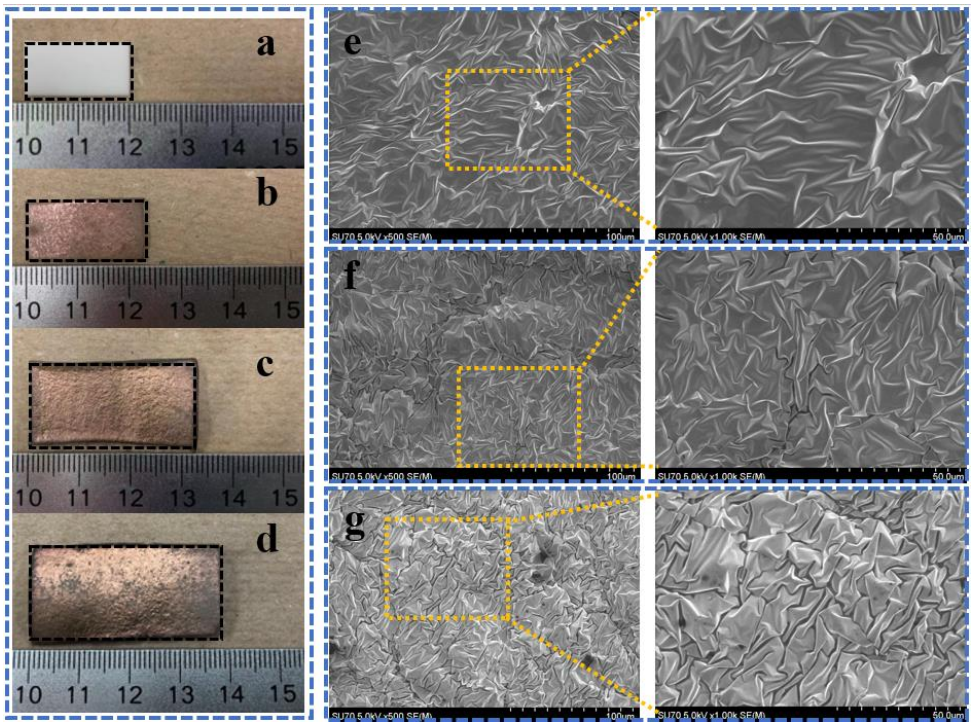

Figure 4.12 Morphology of the elastomer Ecoflex 50/sugar films. (a) Before immersion process. (b) and (e) After one day of immersion and Au sputtering. (c) and (f) After five days of immersion and Au sputtering. (d) and (g) After ten days of immersion and Au sputtering.

To explore the dynamic electrical property, the resistances of the samples with different structures have been characterized during cyclic stretching with different strains. The elastomer film, sputtered with Au at the unswollen state, cannot withstand any minute strains indicated by its resistance easily surging to infinity (not conductive anymore). The Au-deposited elastomer film with light wrinkles (Figure 4.12e) can respond to a 5% tensile deformation. With increase in the number density of wrinkles (Figure 4.12f), the dynamic electrical property has been significantly improved. Responses to a maximum strain of 50% were observed on the samples with five days of immersion. The improvement is possibly attributed to the release of the wrinkled structures during tensile deformation. Regarding the samples with the most extensive wrinkles (Figure 4.12g), the conductors survived the strains up to 100% with stable electrical response during five stretching/releasing cycles. The valley resistances kept constant around 32 Ω, and the peak value showed a steady upward trend with increase

of elongation (Figure 4.13a), for example, from 36 Ω at 10% of elongation, to 105 Ω at 50% and about 1100 Ω at 100% of elongation. This monotonic relationship is desirable for stretchable sensors.

Apart from testing with different strain magnitudes, we have demonstrated the repeatability of electrical performance on the wrinkled elastomer films over long-term cyclic deformations. Herein, the elastomers with ten days of swelling were selected. The resistance response has been recorded during about 400 stretching/releasing cycles when the sample was stretched to 60% strain and relaxed back to zero strain condition at the rate of 0.2 mm/s (Figure 4.13b). Consistent with previous observations on the stretchable electronic devices [207], the electrical resistance response on the Au coated wrinkled elastomer films also followed roughly three stages, including conditioning, stabilizing, and rising phases.

In the first stage, the peak resistance revealed a downward trend as stretching cycle increases. The resistance change ($\Delta R/R_0$) increased to 3.9 after the first stretching to 60% strain. In the subsequent stretching cycles, the maximum resistance changes continuously dropped to 2.4. The change in the conditioning stage can be attributed to the adjustment of the wrinkle structures and rearrangement of the contact points of conductive materials during the cyclic stretching/releasing. In the second stage, the resistance at 60% strain conditions remained relatively stable even though several minor fluctuations occurred within a range of 1.4~2.1. In addition, the resistance changes at zero strain showed less undulation when compared to those at the peaks. The maximum fluctuation in the valley resistance was less than 10%, which means an excellent recovery after releasing process. In the last stage of stretching cycles, both peak and valley resistance exhibited a steady increase trend. Among them, the resistance increased by about 30% at zero strain and 46% at the peak strain conditions from the previous stage, respectively. It can be hypothesized that an unavoidable structural change is created under the repeated stretching. Generally, an irreversible increase in the number of disconnected areas emerged during the cyclic deformation, which leads to the degradation of conductive film in this stage.

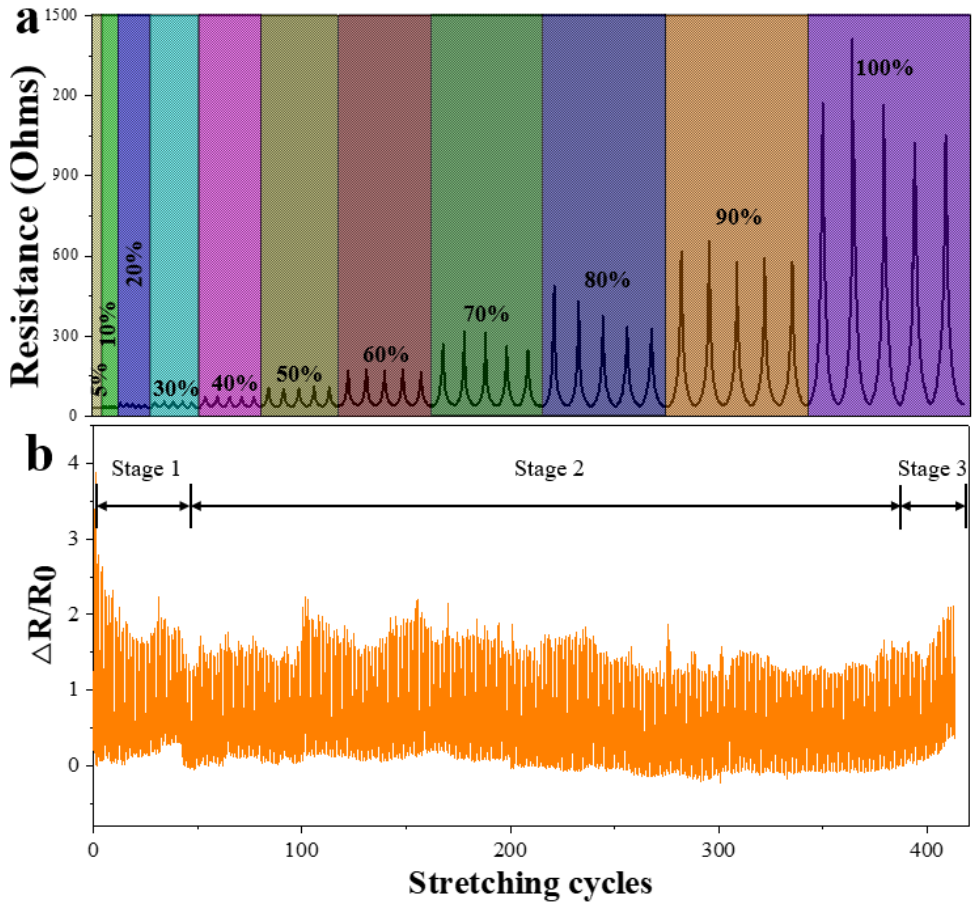

Figure 4.13 Electrical performance of elastomer films with ten days of immersion. (a) Resistance response under five cycles of increasing strains from 5% to 100%. (b) Resistance of wrinkled films during about 400 stretcing/releasing cycles between 0% and 60% strain.

Admittedly, Au sputtering is able to construct stretchable conductive films with the desired wrinkled structures. However, it is generally not recommended to bring water-contained samples into the sputtering chamber, which may cause potential damage to the vacuum pump and bring possible contamination to the system (although the water on the surface of the swollen samples were removed and the sputtering time was relatively short). In addition, as for devices with on-demand shapes and overhang or hollow carved patterns, the above method is no longer suitable since the sputtered Au cannot uniformly deposit on the inner surface of complex structures. To address these issues, we propose to deposit conductive materials on the elastomer through soaking in a graphene aqueous solution.

4.3.3 Concurrent Swelling and Graphene Deposition in Aqueous Solution

In this method, the samples were directly soaked in a graphene aqueous solution to achieve both the swelling of polymer composites and graphene deposition, which can improve the fabrication efficiency of wrinkled elastomers. Considering its good printability, Ecoflex 50 composite ink with 50 wt.% sugar was selected, and printed into a 3D lattice structure, as shown in Figure 4.14a. The sample was then immersed in a graphene aqueous solution for three days to obtain a certain volume swelling ratio and graphene deposition on the swollen structure indicated by the color change to black. Along with the water molecules being absorbed into the elastomer matrix, graphene sheets were carried to the elastomer composite surface. According to our previous work, hydroxyl groups were introduced into the polymer matrix by adding sugar particles [28]. When graphene sheets made contact with the surface of elastomer composites, hydrogen bonding and van der Waals interactions could promote the graphene deposition on the elastomer surface [441]. Finally, upon removal of residual water in the swollen samples, wrinkled layer was formed on the surface of 3D structure, which contributes to the electrical response to an external deformation.

Figure 4.14b~4.14d presented the surface morphologies of the printed strands after various processing steps. It can be seen that the surface is relatively smooth before immersion, with some protrusions of the sugar particles embedded in the polymer. After the samples were soaked in graphene aqueous solution for three days, the surface became much rougher and the lattices were somewhat distorted due to the mismatch of the elastic modulus of graphene and elastomer substrate. As a comparison, a printed lattice sample was soaked in DI water for three days, whose surface morphology was shown in Figure 4.14d. Similar rough surface was obtained, however, interestingly, the openings of the lattices became more of circular shape, probably due to the isotropic shrinking upon water removal.

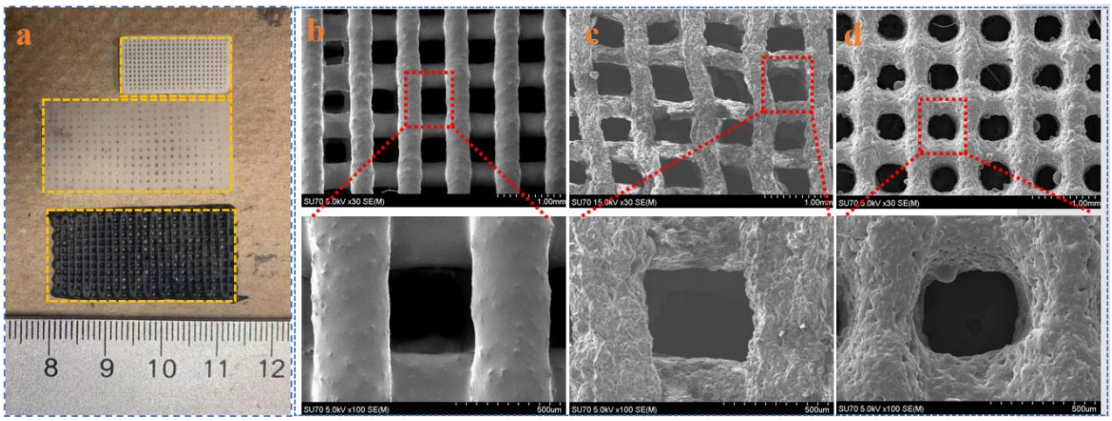

Figure 4.14 (a) Comparison of the 3D printed lattices before and after deposition of graphene (before water removal). (b~d) Surface morphology of the printed structures before immerison process, after immersion in graphene aqueous solution for three days, and after immersion in DI water for three days (for comparison).

Compared to the Au-sputtered elastomer films, the resistance of the Graphene-coated lattice structures exhibited much higher resistance of about 10 kΩ. To demonstrate the long-term durability for sensing, the electrical resistance of the 3D printed lattice structures was characterized under 100 stretching/releasing cycles at strains of 10%, 20%, 30%, and 40%, respectively (Figure 4.15). Similarly, the conditioning stage and the equilibrium stage were identified for the lower cyclic strains.

At 10% strain, the resistance response appeared a slight drop during the initial stretching cycles. As stretch cycle reached 10 times, the resistance at the peaks have decreased from 20 kΩ to 15 kΩ (25% reduction), and that at the valleys from 10 kΩ to 9 kΩ (10% reduction). In the subsequent stretching cycles, the resistance almost kept stable, which represents excellent repeatability (equilibrium stage). For larger strains, similar trends in resistance were observed, i.e., initial drop in resistance during the conditioning stage, and relatively stable in resistance change during the equilibrium stage. However, the magnitude in resistance at the maximum deformation were much higher, i.e., ~40 kΩ and 60 kΩ for strains of 20% and 30%, respectively. A striking change appeared as the stretching increased to 40% strain. Different from the moderate resistance changes during stretching at lower strains, the average peak resistance at 40% strain surged dramatically by more than 50 times. The peak values also exhibited a violent fluctuation throughout the whole stretching process in spite of the stability of

the valley resistance. It can be inferred from the results that the 40% elongation has damaged the graphene layer in some local sites, reaching the maximum deformation for the 3D lattice structures. Nevertheless, the 3D printed and graphene-coated stretchable sensors provided an outstanding electric response and stable repeatability at lower strains.

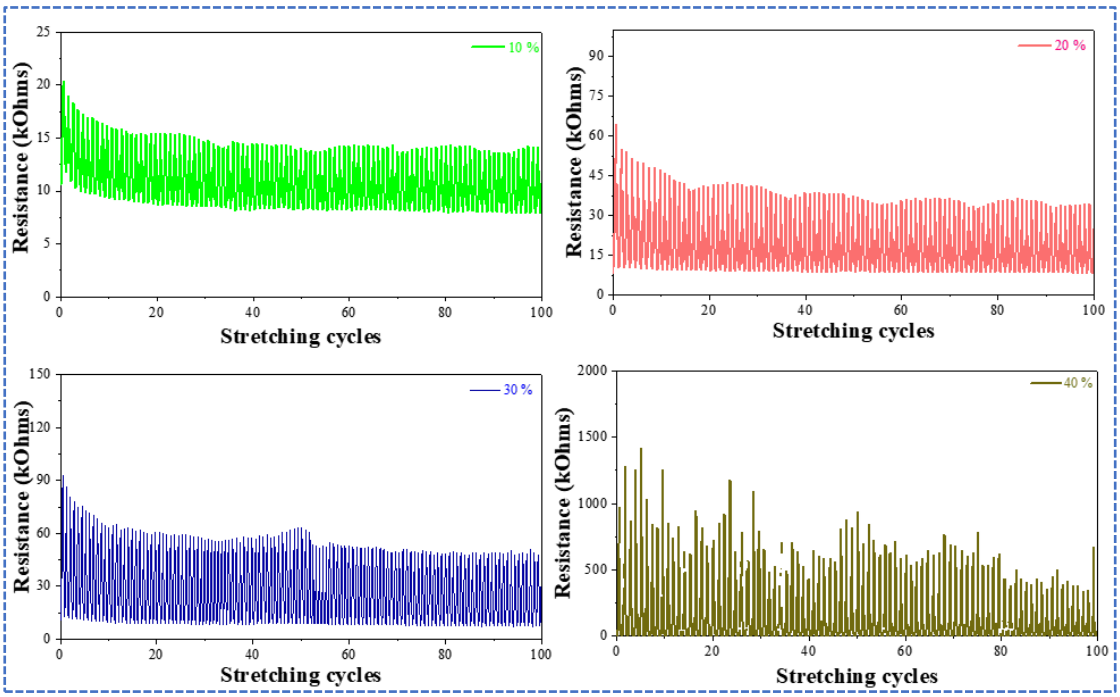

Figure 4.15 Resistance of the 3D printed and graphene-coated structures during 100 stretching/releasing cycles at different strains of 10%, 20%, 30% and 40%, respectively.

It is worth pointing out that the wrinkled structure on the graphene-deposited elastomer is inferior to the Au-sputtered samples. One reason is probably due to the extremely thin gold layer to render the nice wrinkled structures, while the graphene-deposited elastomers may involve multiple layers of graphene materials. Future work includes exploration of methods to assemble a thin layer of densely packed conductive materials on the elastomer composite surface through active interactions, e.g., electrostatic interaction,[32] electroless plating [442], but also having compatibility with aqueous solutions.

4.3.4 Fabricating AgNW-based Stretchable Sensors with Wrinkled Structures

Figure 4.16 illustrated the entire procedure of constructing the wrinkled conductive

3D structures, comprising of printing a desirable pattern, swelling and dopamine self-polymerization on the substrate, binding with AgNWs, and shrinking to form wrinkled structures. In the first step, NaCl particles were added into Ecoflex$^{00\text{-}50}$ silicone as the printing ink. In view of their high solubility and molar concentration, the doped particles trigger a significant osmotic pressure when polymer composites are immersed in an aqueous solution, which is crucial for water-induced polymer swelling. In addition, these NaCl powders act as a viscosity modifier to improve the printability of polymer materials. Next, the printed sample was soaked in dopamine aqueous solution where the polymer composite swells accompanying with deposition of dopamine particles. Subsequently, the dopamine-coated swollen sample was immersed in AgNW/ethanol suspension. Owing to the lone pair electrons of the functional groups of dopamine coating [443], a strong binding interaction between dopamine and AgNWs enhances the adhesion of AgNWs to the substrate. Uniform deposition of AgNWs was realized on the surface of swollen substrate. Finally, a conductive and wrinkled structure was formed by removal of residual water in the sample.

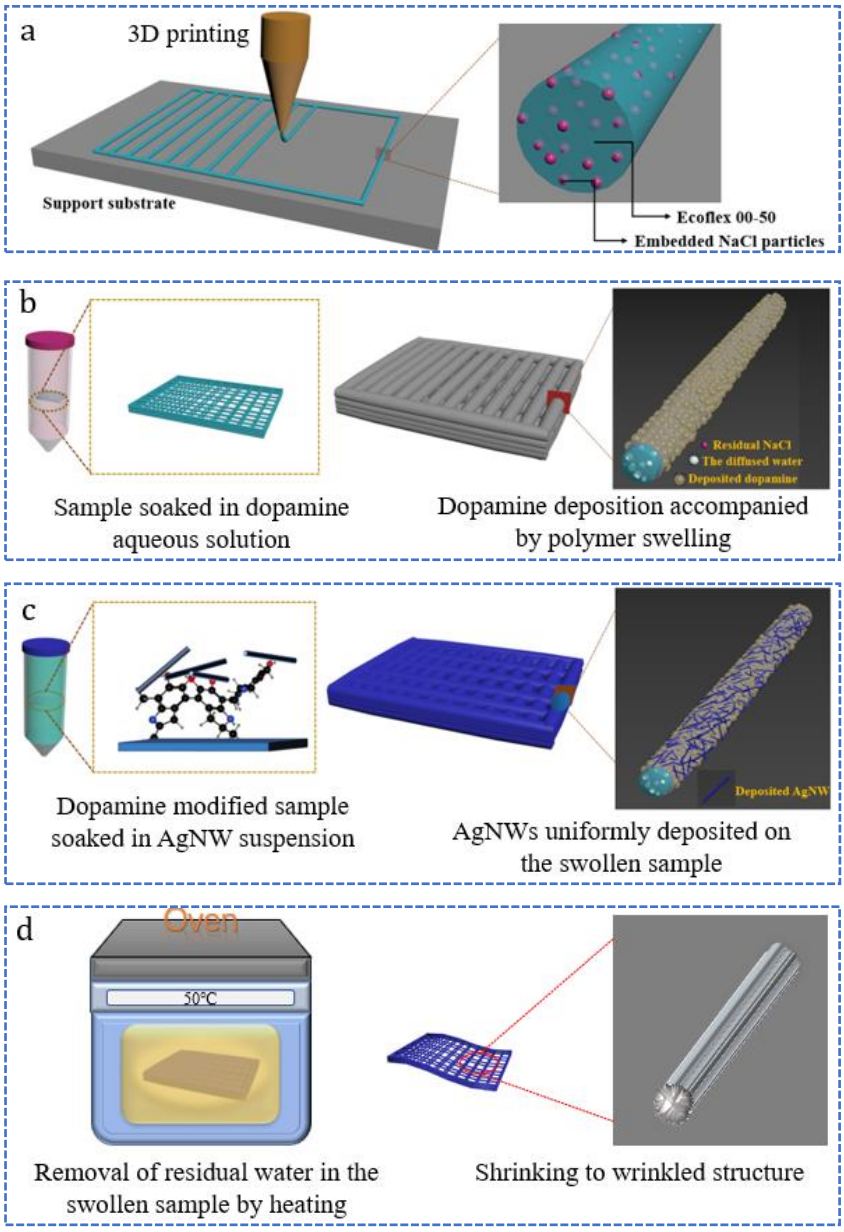

Figure 4.16 Schematic of the fabrication process of stretchable elastomer sensors by using water-induced swelling and dopamine-modification process. (a) Fabrication of desirable structures by 3D printing. (b) Swelling and dopamine treatment when immersed in dopamine aqueous solution. (c) Deposition of AgNWs on the dopamine-coated sample when soaked in AgNW/ethanol suspension. (d) Formation of the wrinkled structures upon removal of residual water in the sample.

Given the larger swelling ratio, the Ecoflex$^{10\text{-}50}$ silicone/NaCl composite was selected to fabricate the stretchable sensors. As shown in Figure 4.17a, the as-prepared sample has a smooth finish with a white color before any treatment. After soaked in

dopamine aqueous solution for 24 h, a near 900% of volume swelling ratio was achieved. The surface roughness clearly increased due to the dopamine coating, as shown in Figure 4.17b. It is noted that the color of sample became dark, which is attributed to the deposition of dopamine particles. The dopamine-coated swollen samples were then immersed into the AgNW/ethanol suspension. A strong binding interaction with AgNWs is created under the action of lone pair electrons of the functional groups of dopamine coating [443-444]. It is worth noting that the polymer swelling ratio remains unchanged in this process, owing to the negligible solubility of NaCl in ethanol. By removing the residual solvents, the sample's color became gray like the AgNW suspension (Figure 4.17c). Interestingly, the local morphology exhibits a hierarchical wrinkled structure that is similar to a flower in a bud. The change is aroused by the different Young's modulus between polymer substrate and conductive layer during the shrinking process. Compared with the structures formed by depositing silver nanoparticles on the swollen substrate [28], silver nanowires formed hierarchical wrinkle structures with conspicuous folds and creases probably due to the thin layer of AgNW percolation network.

To evaluate the surface wettability of the sample after different treatments, the water contact angles (WCA) were tested by the sessile drop method. The results were presented in Figure 4.17d. The WCA of Ecoflex/NaCl film was about 106°. After dopamine modification, the WCA decreased to 65°, which clearly indicates the enhanced hydrophilicity. Considering similar results have been mentioned in other published papers [445], we speculated that dopamine was successfully coated on the Ecoflex/NaCl composite film. Subsequently, the WCA surged to 130° after the deposition of AgNWs on the swollen films. Namely, the hydrophilicity transited to hydrophobicity, which is credited to the increase of surface roughness [446].

To further investigate the dopamine modification, the FTIR test was proceeded. The results were summarized in Figure 4.17e. Compared with the sample without any treatment, we noticed that two peaks appeared at 3450 cm^{-1} and 1600 cm^{-1} after dopamine modification. The changes were related to the stretching vibrations of N-H

groups and the deformation vibrations of N-H groups [447]. Considering the chemical structure of dopamine, it is reasonable to conclude that dopamine coating is successfully deposited on the surface of the polymer composites.

Deposition of AgNWs has been verified by X-ray diffraction (XRD) characterization. In Figure 4.17f, XRD pattern of samples were exhibited at different stages during the sample preparation. Before deposition of AgNWs, there were nine peaks, and their positions appeared at 2θ values of 28°, 32°, 44°, 53°, 57°, 66°, 76°, 83°, and 90.3°, which are attributed to NaCl crystals with the corresponding lattice planes of (111), (200), (220), (311), (222), (400), (420), (422), and (511), respectively. As AgNWs were deposited on the substrate, five XRD peaks were observed at 2θ of 38°, 42°, 65°, 76°, and 80°. The analysis results verify that the characteristic peaks are silver element, corresponding to lattice planes of (111), (200), (220), (311), and (331), respectively. In this case, we confirm that AgNWs are successfully deposited on the sample surface.

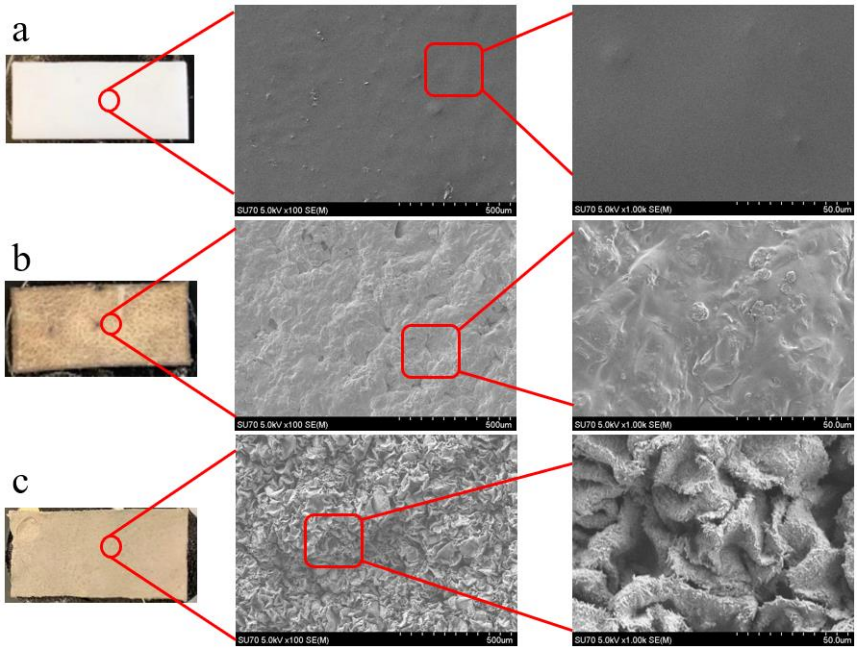

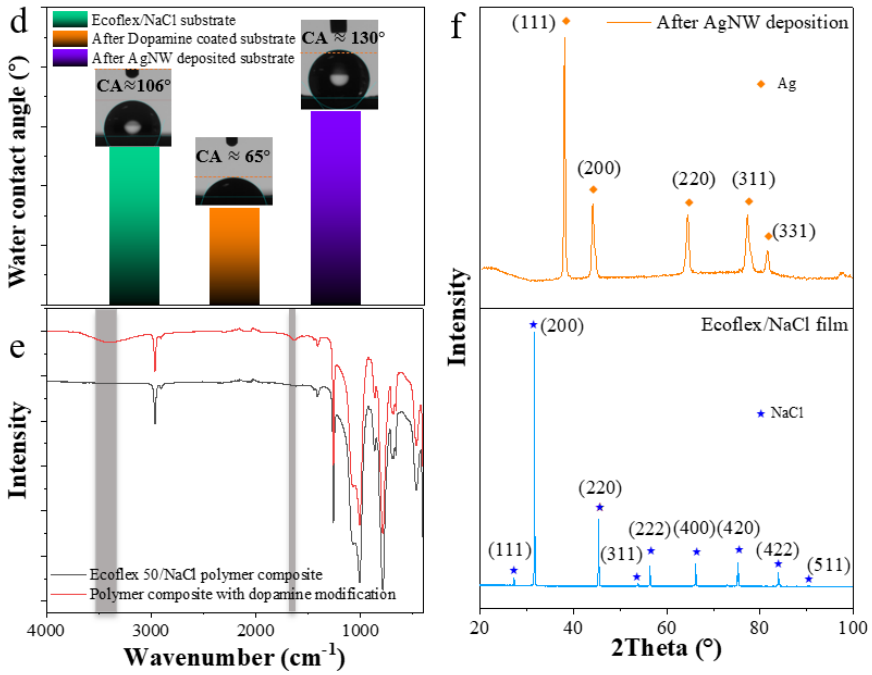

Figure 4.17 Surface morphologies after different treatments. (a) Ecoflex/NaCl film without any treatment. (b) Ecoflex/NaCl film after 24 h of dopamine modification. (c) Ecoflex/NaCl film after AgNW deposition process. (d) Water contact angles after different treatments. (e) FTIR results before and after dopamine modification (shaded locations indicate the peaks appeared after dopamine coating). (f) XRD results before and after deposition of AgNWs.

In addition to the composition analysis, mechanical property of the pure Ecoflex$^{00\text{-}50}$ silicone film, the Ecoflex$^{00\text{-}50}$/NaCl film, and the wrinkled film with AgNWs deposition were characterized on Instron (MTS, Insight 30), as shown in Figure 4.18. Compared with that of pure Ecoflex$^{00\text{-}50}$ film, the stretchability of the Ecoflex$^{00\text{-}50}$/NaCl film significantly decreased, while the mechanical strength more or less remained the same. The mechanical strength of the wrinkled film with AgNWs slightly decreased due to the porous structure in the elastomer substrate after releasing the salt particles, while stretchability improved moderately compared with the Ecoflex$^{00\text{-}50}$/NaCl film, but was still inferior to the pure Ecoflex film.

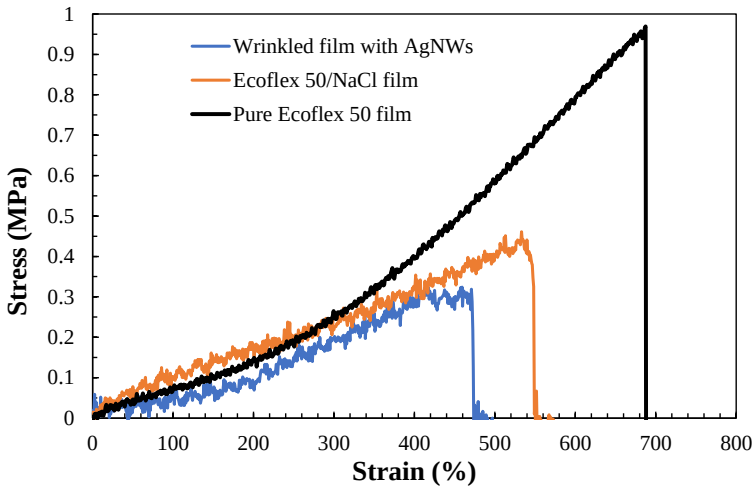

Figure 4.18 Stress-Strain curves for the pure Ecoflex 50 film, Ecoflex 50/NaCl film, and the wrinkled film with AgNWs.

In order to prepare stretchable sensors with desirable shapes or patterns, 3D printing was introduced. Lattice structures were printed and post-treated according to the procedures described in the Experimental section. We observed the morphologies and analyzed the element composition on the sample surface after each step, namely swelling and dopamine coating, and silver nanowire deposition. The results were exhibited in Figure 4.19 and Table 4.1.

In Figure 4.19a, the uniform structure and smooth line indicated the high quality of printed lattices. Silicon (Si), Carbon (C), and Oxygen (O) can be easily detected with 52.08 wt.%, 26.08 wt.%, and 20.70 wt.%, respectively in Figure 4.19d. These elements were from the silicone elastomer and evenly distributed in the local detection area. However, Na and Cl elements were barely detected (<1 wt.%) because these additive particles are embedded in the elastomer matrix.

After soaking in dopamine aqueous solution for 24 h, a dramatic swelling was triggered driven by osmotic pressure. Due to the increase of attachment area, more dopamine particles can deposit on the swollen 3D structure. Figure 4.19b exhibited the 3D printed structure with dopamine treatment after removing the residual water. The color changed from white to dark, and the surface roughness increased as release of NaCl particles and deposition of dopamine particles in the immersion process. As

shown in Figure 4.19e, meanwhile, the distribution of Si and O becames uneven. We also noticed that the content of C increased by 14.85% and Si dropped by 39.0%, while Na and Cl surged from being almost negligible before soaking to 12.55 wt.% and 9.31 wt.%. A rational explanation for these changes is the deposition of dopamine ($C_8H_{11}NO_2$) on the sample surface, and the transport of NaCl during the swelling of polymer composites into aqueous solution.

Following similar procedures with the elastomer films, under the swollen state, the dopamine-coated 3D printed lattice was soaked in AgNW/ethanol suspension to deposit AgNWs. Clear wrinkled structures were formed as shown in Figure 4.19c. Additionally, silver was clearly detected using EDS, and its distribution was closely related to the wrinkle structures as shown in Figure 4.19f. Further quantitative analysis showed that the content of silver increases from zero to 60.43 wt.%, indicating a large amount of AgNWs sticks on the surface, which reveals the potential for outstanding conductivity.

The hierarchal wrinkled structures of the conductive AgNW networks formed on the elastomer substrate enable good conductivity even when subjected to large external deformation, especially when compared with the silver nanoparticle-coated devices [25]. In addition, halide welding may contribute to the electrical conductivity of the AgNW network. As discussed earlier, sodium chloride molecules were present on the surface of the dopamine-coated elastomer composites. Considering some oxygen molecules easily dissolved in the solution, Ag^+ could be produced by redox reaction in Equation 4.4 [448], using the chlorine ions as catalyst. The dissolved Ag^+ was redeposited onto the AgNW network, preferentially near the AgNW junction regions because the electrostatic potential near these sites is higher than other areas, leading to reduction in contact resistance [297, 448].

$$O_2 + 2H_2O + 4Ag \leftrightarrow 4Ag^+ + 4OH^- \qquad 4.4$$

Furthermore, for the AgNWs produced by the modified polyol method, a thin layer of PVP usually is absorbed on the surface of AgNWs through an oxygen atom of carboxylate group (or a nitrogen atom of pyrrolidyl nitrogen group), which limits the

conductivity of AgNW networks [298]. Combined with the fact that Cl^- existed on the surface of elastomer composites, we speculated that the PVP is possibly detached from AgNW surface in our system. The reason is that the Cl^- can replace the carboxylate group due to stronger interaction between Cl^- and AgNWs [298]. The AgNWs without PVP experienced less repulsive forces, which drives the AgNWs to assemble together, further enhancing the electrical performance of the AgNW conductive pathway.

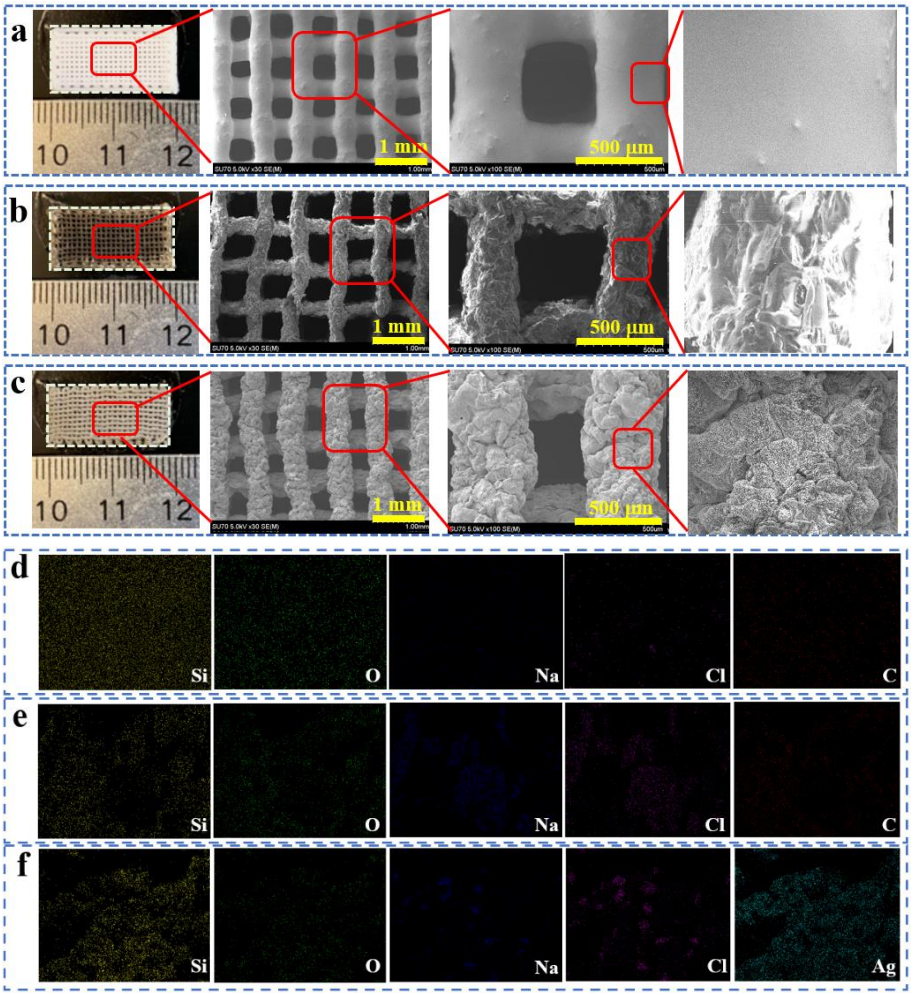

Figure 4.19 (a-c) Surface morphologies after each treatment step, i.e., as-printed, dopamine modification, and AgNW deposition. (d-f) Elemental composition after each treatment step from (a-c).

Table 4.1 Elemental composition (wt.%) by EDS after each treatment from Figure 4.19 (d-f).

Sample	C	O	Si	Na	Cl	Ag
Silicone/NaCl composite	26.08	20.70	52.08	00.56	00.58	
Dopamine-coated sample	40.93	24.18	13.04	12.55	9.31	
AgNW-coated sample	11.05	8.94	9.81	5.08	4.69	60.43

The electrical performance of the stretchable sensors with 3D printed structures has been evaluated. Firstly, the electrical responses were recorded in multiple stretching/releasing cycles from 10% up to ~100% stretch deformation (Figure 4.20a). At zero tensile deformation, the valley resistance kept constant near 22 Ω. Less than 10% fluctuation in the valley resistance was observed in the whole stretching process, which indicates that there exists a slight adjustment between conductive pathways when suffered different deformations. Whilst the peak resistance values showed a clear and smooth increase trend with increase of elongation. The maximum resistance response was about 23 Ω at 10% strain, and 56 Ω at 50% strain. When the deformation reached 100%, the resistance increased to 132 Ω.

Furthermore, gauge factor was calculated to evaluate the sensitivity of the 3D printed sensors according to Equation 4.5:

$$\text{gauge factor} = \frac{(\Delta R/R_0)}{\varepsilon} \qquad 4.5$$

Where ΔR is the resistance change upon elongation, R_0 is the original resistance, and ε is the applied strain. The calculated results were presented a clear change with the increase of elongation percentage. The gauge factor increased sharply from 0.45 to 3.5 when the elongation increased from 10% to 50%. Subsequently, the value presented a slight upward trend from 60% to 100% strain. Finally, the gauge factor kept constant near 3.8 as stretching strain reached 100%.

As another important figure of merit, repeatability of electrical performance was characterized to assess the long-term stability of 3D printed sensors. Herein, the prepared sensor was stretched to 50% elongation deformation and relaxed back to its

original condition at a rate of 0.5 mm/s. 500 stretching/releasing cyclic deformations were completed, and their electrical responses were shown in Figure 4.20b. The initial resistance was about 22 Ω and the peak resistance at the 50% strain reached 56 Ω. In subsequent cycles of stretching, the resistances at zero strain and 50% strain almost remain constant except some sparse fluctuations. It is noted that the value changes are always no more than 15% in each fluctuation, which notifies that there appears some slight adjustment in the local conductive pathway. Additionally, an interesting phenomenon is observed that the resistance changes became very stable as stretching cycles exceeded 300 times. The possible reason is that conditioning of conductive network is completed.

Electrical response rate is also evaluated on the fabricated stretchable sensors. Here, we compared the relative resistance response of the 3D printed sensors at 50% strain with various stretching frequencies of 0.005, 0.01, 0.05, 0.1, and 0.5 Hz. The results were depicted in Figure 4.20c. When the stretching frequency increased from 0.005 Hz to 0.5 Hz, the relative resistance response remained almost constant, which indicates the diverse tensile rate has little effect on the electrical response. These results indicate that the fabricated sensors not only exhibit durability in multiple stretching/releasing cycles, but also can quickly respond to dynamic deformations.

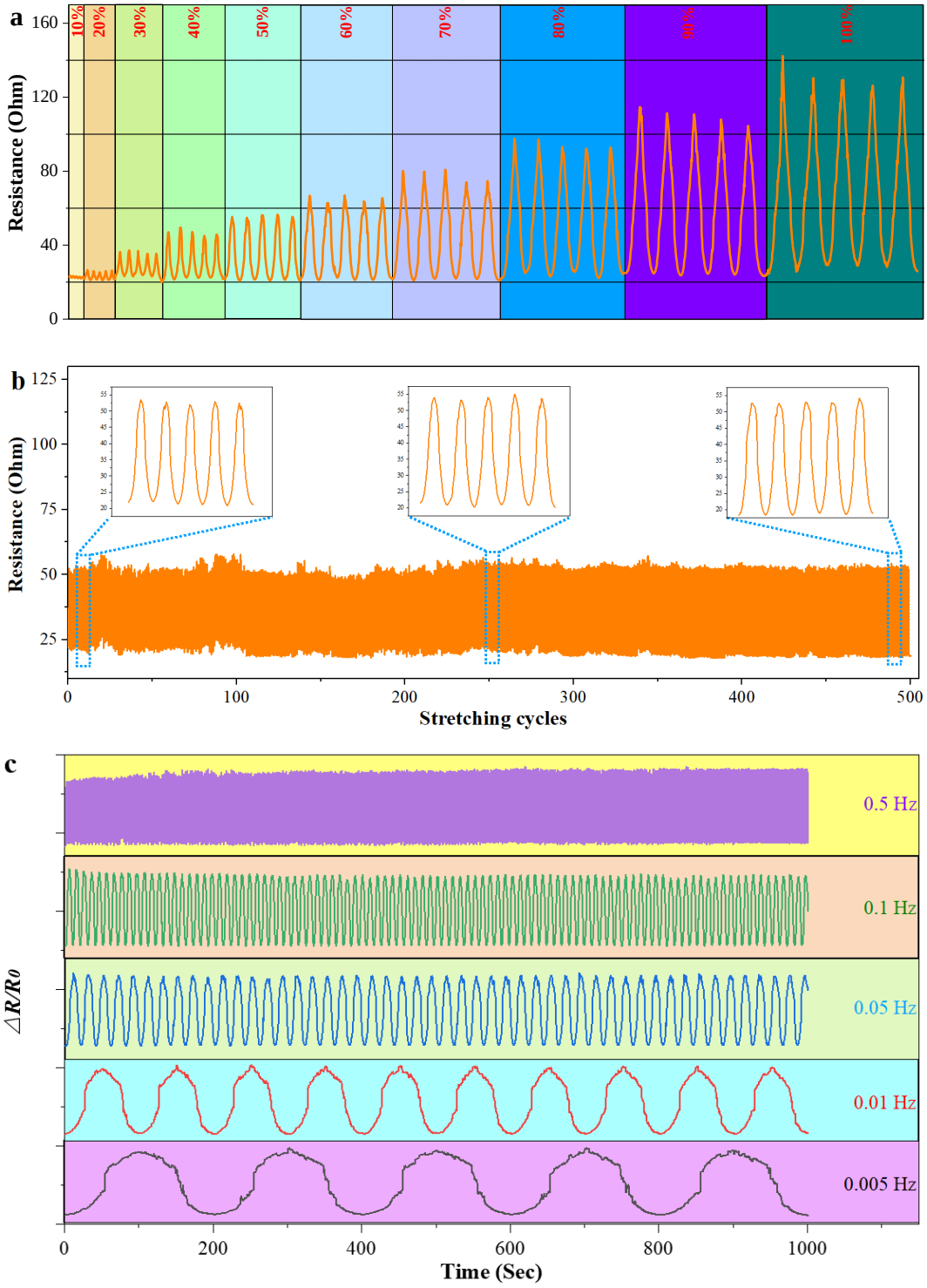

Figure 4.20 (a) Resistance changes with different tensile strains. (b) Resistance response to 50% strain during 500 cycles. (c) Resistance response to 50% strain at different stretching frequencies.

In addition to tensile deformation, the fabricated sensor can monitor dynamic twisting and bending deformations. The electrical responses were shown in Figure

4.21a and 4.21b in multiple deformation cycles. The relative resistance response increased as the deformation increased; then dropped back when the sample gradually recovered its original condition. It is noted that the response waveform varies between different deformation modes. For example, the magnitude of resistance change for twisting is larger than that for bending, probably because the former involves small curvatures of deformation and the corresponding change of conductive pathway.

To study the possibility as a skin-mountable human motion detector, the prepared stretchable sensors were attached to different parts of human body. We collected the signals of the sensor in response to periodic bending of finger and elbow in Figure 4.21c. With continuous increasing of bending angle from 0 ° to 90 °, the relative resistance responses exhibited resistance changes with good repeatability. The electrical responses for finger bending showed a sharp waveform, whereas the signal for elbow bending revealed a much larger and plateaued resistance increase. In both cases, the resistance resumed when the finger and elbow returned to their original conditions. The changes are probably attributed to the different deformation modes, where the sensor on the finger experienced dominantly tensile deformation while the one on the elbow may be subjected to bi-directional deformation. As a result, we can infer the movement of the human body is based on the waveform of the electrical signals.

Additionally, a stretchable sensor was conformally fixed to a tester's neck to detect the vocal muscle motion when he was speaking. As the tester separately pronounced the words "Hi, "Ha", and "A", the relative resistance responses exhibited apparently distinct patterns (Figure 4.21d). Clearly, characteristic peaks are triggered as each word is pronounced. In this situation, we speculate that pronouncing different sounds can stimulate different electrical responses because the vibration amplitude of larynx muscles changed.

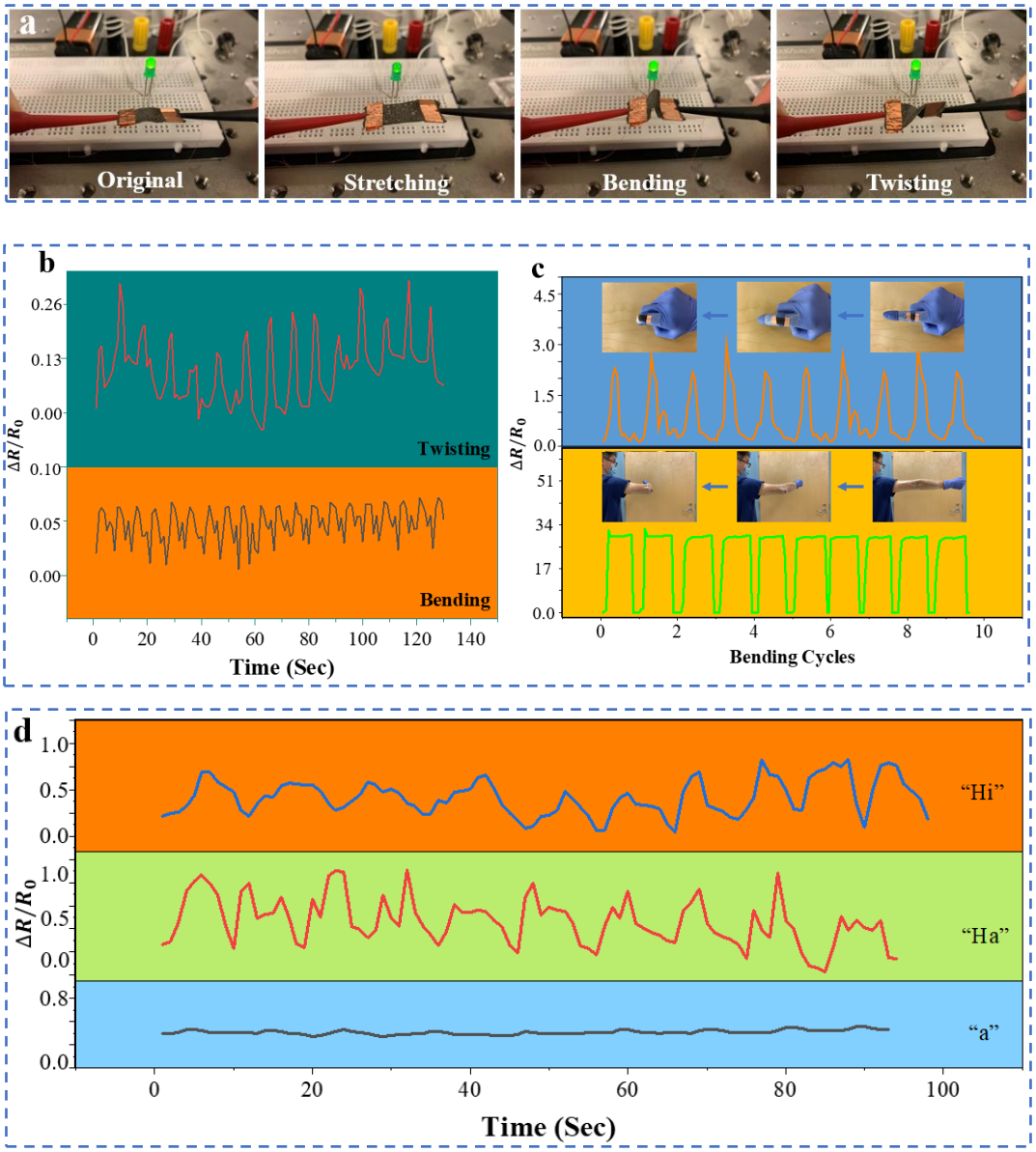

Figure 4.21 (a-b) Resistance response to dynamic deformations. (c-d) Resistance response to human body movement.

4.4 Conclusion

In summary, we present some simple strategy of leveraging polymer swelling in fabricating stretchable elastomer conductors.

(1) The wrinkled sensor depositing a conductive AgNP layer has some highlights deserving emphasis, including in-situ growing AgNPs on the swollen elastomer films can effectively form a wrinkled conductive structure, and the formed sample has a low sheet resistance. The conductive elastomers can respond to a wide range of strains from

10 % to 100 %. They also show decent electrical stability over 550 stretching cycles. The elastomer/sugar composite exhibits good 3D printability, which is important in fabricating functional devices with designed shapes and patterns. The facile and environment-friendly approach along with the demonstrated 3D printability show a great potential in fabricating stretchable electronic devices with complex shapes/structures and superior performance.

(2) Wrinkled conductive elastomer films have been prepared by sputtering Au on the surface of the swollen films through vapor deposition. 3D printed and graphene-coated structures have been achieved through concurrently swelling and graphene deposition by soaking the printed structures in graphene aqueous solution. The stretchable conductors prepared by both methods have exhibited conspicuous wrinkled structures and very good electrical response to mechanical strains.

(3) The dopamine layer acts as binder layer to promote adhesion between the AgNWs and elastomer substrate to produce a uniform and robust conductive pathway. The hierarchical wrinkled structure provides more opportunity to form the AgNW conductive pathway that enables superior electrical properties under various deformations. The fabricated stretchable sensor can respond to a wide range of strains from 10% to 100%, with good repeatability and quick response to dynamic deformations, which holds a great potential in wearable electronics for healthcare monitoring and rehabilitation.

CHAPTER 5 Constructing Flexible Electrodes with Desirable Pattern via 3D Printing Transfer

5.1 Introduction

With the rapid development in electronic technologies, many advanced devices have been designed, comprising industrial robots, thin-film transistors, foldable smartphones, e-skin, wearable equipment, etc. The progress realizes the demands of customers, promotes the human life quality, and provides a pathway for electronic updates. As a critical component in these products, flexible electronics have received much attention. It is a common concept that flexible electronics play a crucial role in future devices.

To fabricate flexible electronics, different methods have been proposed, including encapsulating conductive layer with elastomer, mixing conductive materials with soft matrix, post-treating flexible substrate, etc. Among them, encapsulation has been widely reported in recent years, due to its outstanding features like low cost, high efficiency, stable performance. The common steps include (a) spreading liquid polymer on the conductive layer, (b) self-encapsulating conductive layer into a flexible matrix, and (3) peeling off the cured polymer where the conductive layer is embedded [29]. To now, researchers have selected graphene, carbon nanotube (CNT), metallic nanowires, etc. as conductive materials. Spraying, spinning, filtration, etc. have been employed to form conductive layers. Additionally, some liquid polymers, i.e., poly(dimethylsiloxane) (PDMS), poly(ethylene terephthalate) (PET), and Ecoflex silicone [449], have been used as flexible substrates. Various methods, such as bar coating, pouring, spinning, etc. have been utilized to encapsulate the conductive materials. The prepared samples have been demonstrated to possess an electrical response to external deformation.

To improve the property, some conductive composite materials have been utilized to replace single conductive material. Yun *et al.* used indium-doped zinc oxide (IZO) to decorate AgNW network. It not only enhances the interconnection between wires, but also reduces the surface roughness of AgNW film. The improvement can broaden

their application in organic light-emitting diodes (OLEDs) [30]. Chen *et al.* applied a reactive ink on AgNW film, and used a chemical reaction to weld AgNWs connection. The sintering process can promote the mechanical strength and the conductivity of AgNW film [31]. Also, preparing a semi-embedded wrinkled conductive layer has been considered as an effective way to reinforce mechanical and electrical performance. Huang *et al.* fabricated AgNW/PDMS electronics by a pre-stretching and post-embedding process. The conductive wavy structure can be formed along stretched direction, which endows the sample with high conductivity and electrical stability [450].

Unfortunately, these attempts can only be used to construct simple film structure. It damages the electrodes mechanical stability and electrical sensitivity. On the other hand, it limits the application of flexible electrode. Thus, it is necessary to prepare a flexible electronic with desirable patterns.

One feasible solution is cutting out partial film to capture a shaped electronic. Yao *et al.* acquired a flexible electronic with desired pattern by using laser scribing on AgNW/TPU composites. The fabricated electronics ideal for E-textile applications due to its conductive, compliant, stretchable, and washable, etc. [451] Cui *et al.* tailored a curable AgNW/PI film into a Kirigami structure by laser cutting. The modification enables the captured sample constant resistance up to 100% tensile strain [283].

Another possible way is transferring a designed conductive layer onto the polymer matrix. Jung *et al.* obtained a patterned MoS2/rGO conductive layer via a soft lithographic patterning approach. Subsequently, it was transferred onto PET film to form a highly sensitive gas sensor [32]. Jeong *et al.* formed an AgNW layer with a channel shape by attaching polymide (PI) masking film on the bottom PDMS before introducing AgNW solution. Then, the patterned conductive layer was transferred on top of PDMS film to construct a gas sensor. By selecting a suitable channel length, a high sensitivity, superior durability, repeatability, and hysteresis, etc. can be realized [33]. Furthermore, preparing a replica mold to shape the conductive layer is gradually adopted. Liu *et al.* obtained a flexible matrix structure by pouring liquid polymer into a designed solid mold, followed by dropping graphene suspension onto the flexible structure. After

thermal treatment, a flexible sensor can be formed, which illustrates a high sensitivity, deformation limits, and repeatability, etc. [34]

However, the aforementioned methods generally perfers polymers with low viscosity because it is necessary for polymers to evenly spread on surface of the conductive layer, and seep into interior of conductive layer to achieve encapsulation. Therefore, there are limited options of polymers in the transfer process, which narrows down the application of means. Meantime, designing special mold, using laser scribing, and patterning conductive layers complicate the transfer process, surge the cost, and hinder large-scale applications, etc.

In this report, we designed an effective approach to fabricate a flexible electrode with a complex pattern by utilizing 3D printing. For one thing, the polymer with high viscosity has been demonstrated to enable encapsulation of the conductive layer. Moreover, we just need one facile step to construct the samples, which can be used to replace multiple treatments in previous reports. Thence, we broaden the application, achieved a strightforward process, and reduced the cost, etc. The advancements can provide a novel idea to construct a stable flexible electronic.

5.2 Experimental Section

5.2.1 Materials

The commercial LIM6050 liquid silicone rubber (Momentive Performance Materials Inc.) was selected as the elastomer matrix. According to the instruction, we mixed its part A and Part B in weight ratio of 1:1. The pure graphene aqueous solution (ACS Material, LLC) with 1 mg/mL concentration was adopted to prepare a conductive substrate layer. These materials were used as received without any further modification.

5.2.2 Preparation of 3D Printable Ink

To prepare a uniform polymer composite, we manually stirred the silicone blend for 30 seconds at first. Then, a planetary mixer (ARE-310, Thinky Mixer) was adopted to mix it for 5 minutes at 2000 RPM. Finally, a 30~seconds of defoam process was proceed to remove air bubbles inside the mixture.

5.2.3 Preparation of Graphene Conductive Layer

To obtain a even graphene conductive layer, a manual blade coating machine was utilized. Polyethylene terephthalate (PET) was employed as the substrate in blade coating process. Before scraping, the PET matrix was ultrasonically rinsed with ethanol and deionized (DI) water for 5 minutes, respectively, then air dried. It is worth noting that we selected various scrape height between blade and PET substrate. The coating machine was dragged at speed of 0.01 m/s to ensure the integrity and uniformity of the coating.

5.2.4 Encapsulating Conductive Layer into Flexible Matrix

To combine the flexible silicone and the conductive layer, 3D printing technology was adopted. We used a CAD software (SolidWorks) to design a desired pattern. Then, a supporting software (Prefactory) was utilized to slice the layer into a thickness of 320 μm. Next, we employed an extrusion-based 3D printer (EnvisionTec, 3D Bioplotter) with a tapered nozzle (400 μm in diameter, Nordson) to print. Notedly, the un-dried graphene film was selected as the conductive substrate. A series of printing parameters were adjusted for the best printing quality, such as 4.2 bar of extrusion pressure, 10 mm/s of printing speed, 0.2 s of pre-flow, and 0 s of post-flow, etc. Finally, the printed samples were peeled off from the conductive layer after 24 hours of curing in air .

5.2.5 Measurement and Characterization

The morphologies of samples were separately observed via a metallographic microscope (Nikon ECLIPSE MA200, Japan) and a field-emission scanning electron microscope (FE-SEM, HITACHI, SU-70) with 5 KV operating voltage. An Energy Dispersive Spectrometer (EDS) with 15 KV operating voltage was adopted to collect the element content. A Fourier transform infrared (FT-IR) spectrometer (Nicolet iS50) were used to identify the functional groups. A rheometer (MCR 301, Anton Paar) was used to measure the viscosity of LIM6050 silicone and graphene aqueous solution.

We employed a digital tensile machine (MTS 30, USA) to measure the global mechanical property. The samples with 0°, 45°, 90°, and honeycomb lattice structures were tested, separately. To ensure a stable mechanical response, a tensile rate of 5 mm/s

was utilized. Furthermore, we simulated the stress and strain distribution in local as elongation appears. In the approach, Ansys Mechanical was used to conduct finite element analysis at the 0°, 45°, 90°, and honeycomb lattice samples with 0.4 mm filament radius, 10 mm length and width, and 1 mm depth, capped at both lengthwise ends with an additional 1 mm by 1 mm by 10 mm block. The built-in rubber, silicone material with the Mooney-Rivlin model was used. Meshing was conducted with default mechanical physics preferences for the 0°, 45° and 90° lattices and default Nonlinear mechanical physics preferences for the honeycomb lattice. Each sample was stretched to 2.5 mm for a strain of 25% by applying a displacement on one end and fixed support on the other. The displacement was ramped over 1-time step of 1 s for the 0° and 90° lattices, 25 steps for the 45° lattice, and 150 steps for the honeycomb lattice. Large deflections were turned on for the solution. Displacement, equivalent Von-Mises stress, and strain were plotted for each sample.

A 4-point probe system (Ossila, UK) was employed to characterize the sheet resistance of the conductive layer and the graphene-embedded polymer matrix. A digital multi-meter (Fluke 289 True-RMS) was utilized to show the resistance in static conditions. We applied digit multimeters (KEYSIGHT, 34465A, 6 1/2 and Fluke 289 True-RMS) to record the resistance changes during the dynamic deformation processes. The cyclic stretching proceeded on a home-made stretcher controlled by a computer.

5.3 Results and Discussion

We displayed three different approaches to achieve a conductive layer transferred onto flexible polymer matrix. Figure 5.1a exhibits one of the most common methods where the polymer was spreaded onto a conductive layer. Utilizing penetration function, polymer with low viscosity can encapsulate the conductive layer as elastomer cured. Figure 5.1b shows the updated approach that conductive layer was patterned to special shape. A similar method was repeated as above to achieve conductive layer transfer. High sensitivity and mechanical stability can be achieved. Meanwhile, desirable conductive patterns were realized. However, some pre-treatments, i.e., UV/O_3, plasma, mask, etc. were involved to create the conductive patterns, which complicates the

process and increases cost.

In our project, we propose to utilize 3D printing technology to achieve conductive layer transferring onto flexible substrate as shown in Figure 5.1c. There is a three-step process: (1) conductive material is evenly dispersed to form conductive layer; (2) 3D printing is applied to form desired pattern on conductive layer by extruding liquid polymer; (3) printed polymer substrate is peeled from conductive layer after polymer cured. Due to the capsulation, the conductive material can be transferred onto flexible substrate. Thus, a flexible conductive device can be constructed.

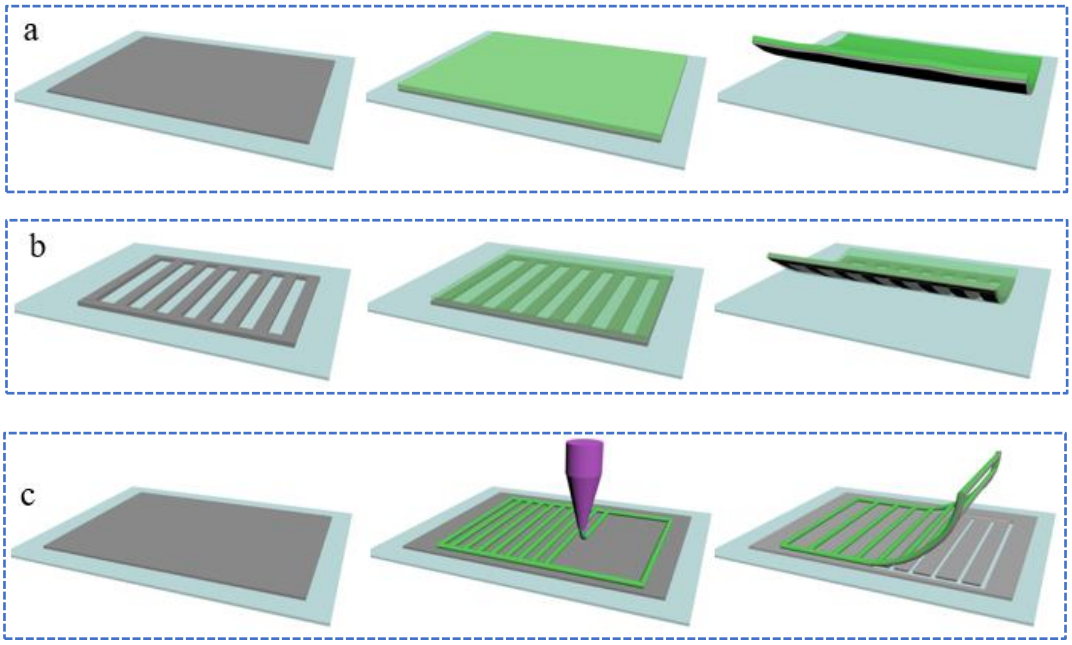

Figure 5.1 Scheme of common approaches to construct flexible electrode via transfer.

In the first step, we compared three-blade coating heights comprising of 50 μm, 100 μm, and 200 μm. Under a constant drag speed of~ 0.01 m/s, the formed conductive layers after drying are displayed in Figure 5.2. Considering the intact of the conductive layer, the height with 200 μm is selected for the next procedure. From the top and cross-section morphologies, it can be observed that the graphene layer is dense, and its thickness is about tens of micro meters.

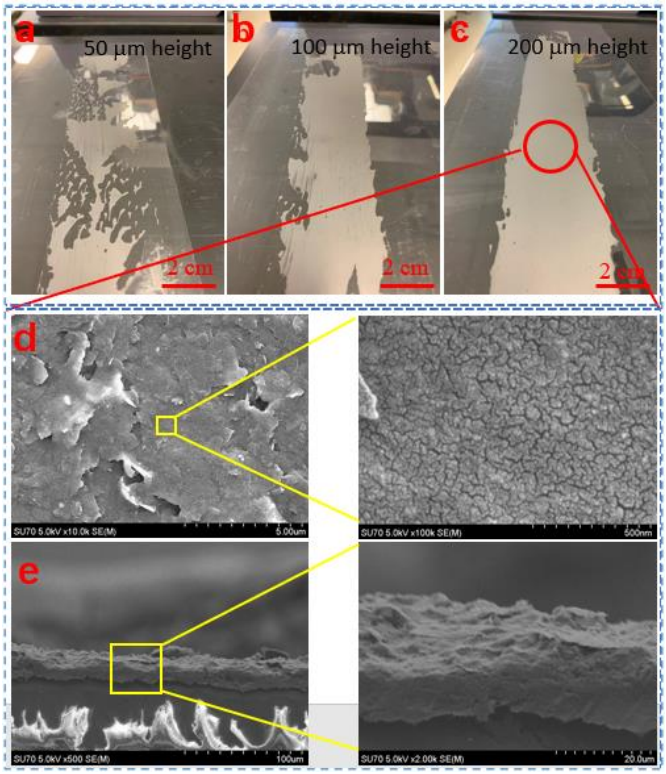

Figure 5.2 Graphene film after blade coating with different height (a) 50 μm, (b) 100 μm, (c) 200 μm. (d) Surface morphology. (e) Cross-section morphology.

In subsequent process, an interesting phenomenon is observed that the 3D printed polymer is almost unable to capsulate the dried graphene layer. But the uncured graphene layer can be successfully transferred in the same condition. Herein, we cite the theory about transfer printing to interpret the difference. From the viewpoint, our transfer system can be divided into three parts comprising of the PET substrate, the graphene layer, and the extruded polymer. Among them, the conductive layer and the patterned polymer can be viewed as donors and acceptors, respectively.

In the transfer program, the critical peel forces between PET/donor and donor/acceptor are crucial. When $F_{PET/donor} < F_{donor/acceptor}$, the conductive layer can be picked-up. While the transfer is possible to fail as $F_{PET/donor} > F_{donor/acceptor}$. The peel force have been defined relating with the energy release rate (G) and the wide (in the out-of-plane direction) (w) in Formulae 5.1 and 5.2.

$$F_{PET/donor} = wG_{critical}^{donor/acceptor} \quad 5.1$$

$$F_{donor/acceptor} = wG_{critical}^{PET/donor} \quad 5.2$$

Due to w is constant in the system, G is considered to control the transfer process. Feng *et al.* deduced a schematic diagram of G for the PET/donor interface and the donor/acceptor interfaces, as shown in Figure 5.3.

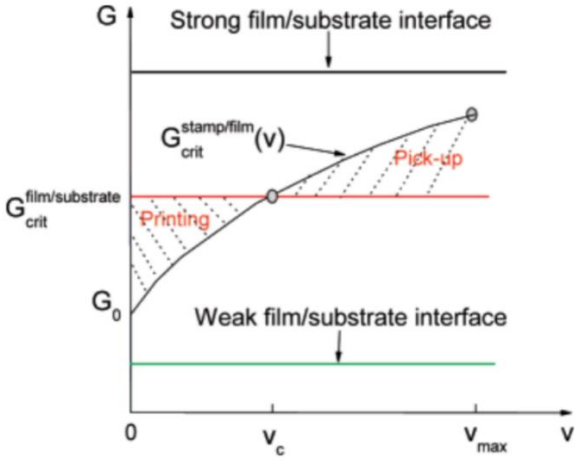

Figure 5.3 The criterion for kinetically controlled transfer printing.

In their conclusion, G is related to peel velocity (v). When $G_{critical}^{\frac{donor}{acceptor}}(v) > G_{critical}^{PET/donor}$, the transfer can proceed. Considering the fact that the dried graphene is hard to be transferred, and the uncured graphene is easily encapsulated at any v, we can infer that $G_{critical}^{PET/donor}$ increases as the graphene layer dries. Therefore, we suggest that the undried graphene layer is necessary in 3D printing transfer.

Based on above procedure, we get the samples as shown in Figure 5.5a. The liquid graphene suspension was prepared as the conductive film via blade coating. Figure 5.4 provides more characteristics about the graphene solution. The results manifest the graphene aqueous solution can maintain a film shape, namely without spreading, after blade coating.

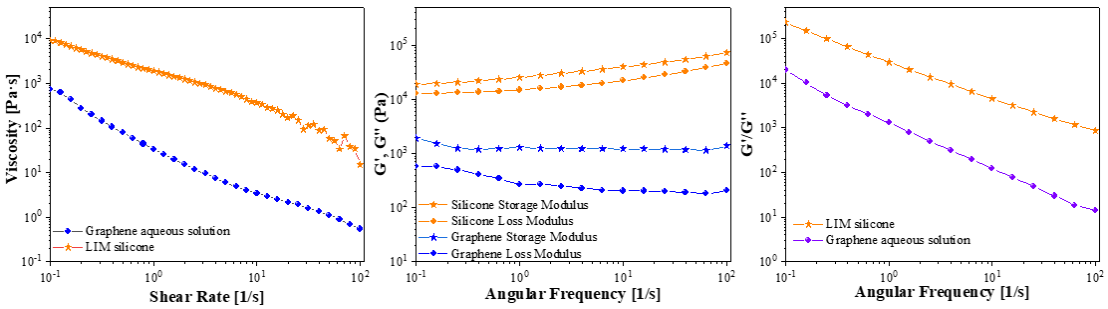

Figure 5.4 Viscosity of graphene solution in the process.

The graphene suspension with high concentration is crucial to form the phenomenon. Afterward, the polymer ink was engraved on top of the undried graphene layer via 3D printing. With the curing of the extruded polymer, the graphene layer was encapsulated in polymer matrix. The reason is explained according to the transfer printing principle [452]. Figure 5.5b and 5.5c present the morphologies of the cross-section and surface. It can be seen that the transferred graphene layer is even, and its thickness is close to the dried & un-transferred graphene film. Figure 5.5d further proves the effectiveness of the transfer process by comparing the element content of the polymer matrix and the graphene-embedded polymer. Specifically, the carbon concentration increases by 24.28% after encapsulation. Thus, it is believable that graphene is certainly transferred onto a flexible substrate.

We then measured the sheet resistance of the un-encapsulated graphene layer and the graphene embedded polymer at a dried state. The results as exhibited in Figure 5.5e. Although the transferred graphene layer endows the polymer conductive performance, the resistance increases by two orders of magnitude. The reason is due to the fact that the polymer encapsulates the conductive materials, and damages some conductive pathway. Additionally, the printed polymer lines with various diameters were used to encapsulate the graphene. The formed samples are displayed in Figure 5.5f, and the resistance values increase by 40 Ω and 66 Ω as the encapsulated graphene wide decreases from 500 μm to 300 μm and 150 μm. Since the embedded graphene wide can be controlled during 3D printing, we speculate the printing parameters have a crucial effect on the encapsulation.

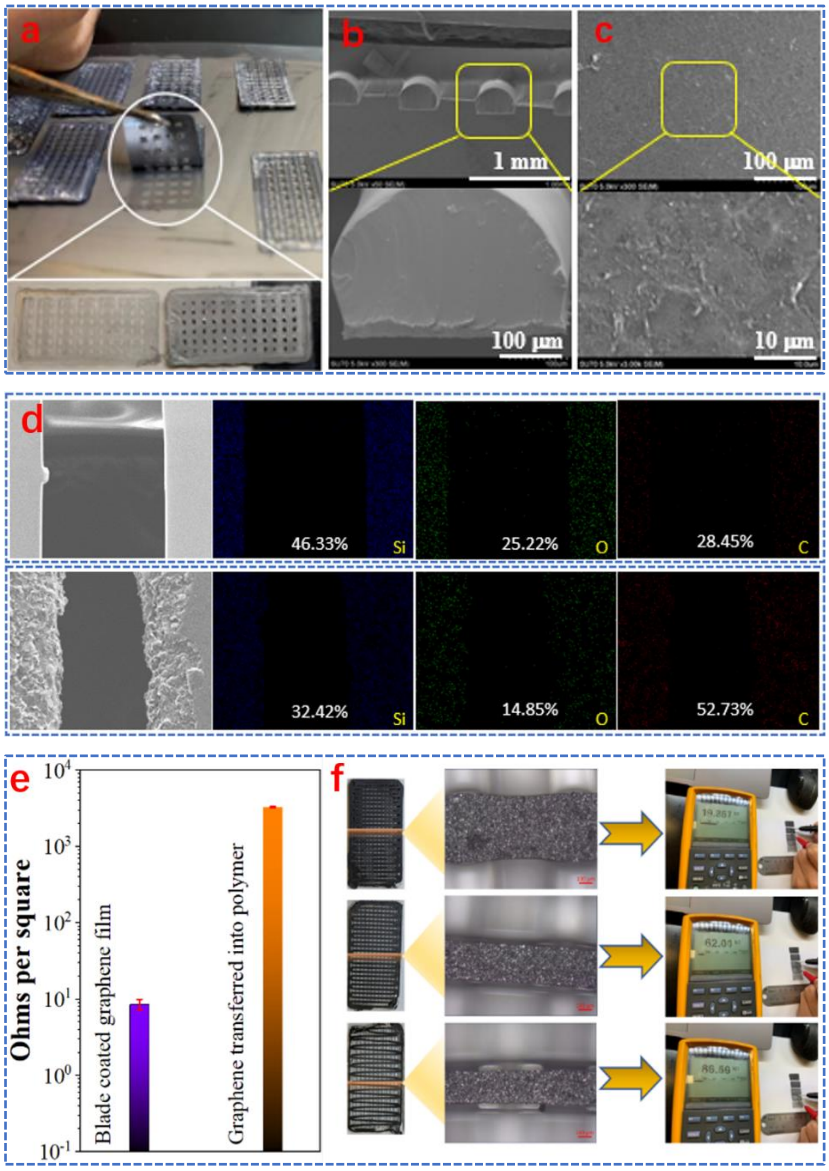

Figure 5.5 Transferring graphene layer into LIM silicone via 3D printing. (a) Graphene transfer process. (b) Cross-section morphology after transferring. (c) Surface morphology after transferring. (d) Element content analysis with and without graphene transferred into polymer. (e) Resistance of the graphene layer and graphene transferred into polymer. (f) Resistance of the sample with different diameter of the printed line.

To verify our hypoethsis, different 3D printing parameters are adopted. Figure 5.6a~5.6c show different printing heights between the nozzle tip and PET substrate. When the printing height is 0.3 mm (Figure 5.6a), the narrow space forces the extruded polymer to spread out. Thus, the graphene embedded area is able to increase on the printed baseline. As the printing height increases to 0.5 mm, the printed line-wide is

similar to the diameter of the printing nozzle (≈0.4 mm). In addition, the connection area between each line appears to have slight expansion deformation, which notifies a strong layer-to-layer adhesion. When the printing height reaches 0.75 mm, the width of the printed line reduces again. Meanwhile, there are no shape changes between line connection zones. The results ascrib to the large space between nozzle and PET substrate, which brings about the squeezed polymer cannot immediately adhere to the conductive layer, but slowly touches the substrate under the action of gravity. Hence, the adhesion between each layer is damaged.

Besides, the distance of the printed lines is considered as an unignorable factor to regulate the printing transfer. We compared three types of line distances in Figure 5.6d~5.6f. When the line distance was 0.8 mm (Figure 5.6d), the printed structure can be maintained within each layer. Namely, the printed underlying layer is sufficient to support the upper structure. However, as the line distance increases to 1.2 mm, the printed line on the upper layer appears deformed. The reason is that the gravity of polymer line overcomes the shear force caused by the viscoelasticity of the LIM silicone. In the case, a small part of the printed lines in the upper layer adheres to the graphene layer. When the line distance reaches 1.5 mm, the bottom layers fails to support the upper lines, which leads to the large area of upper line to collapse.

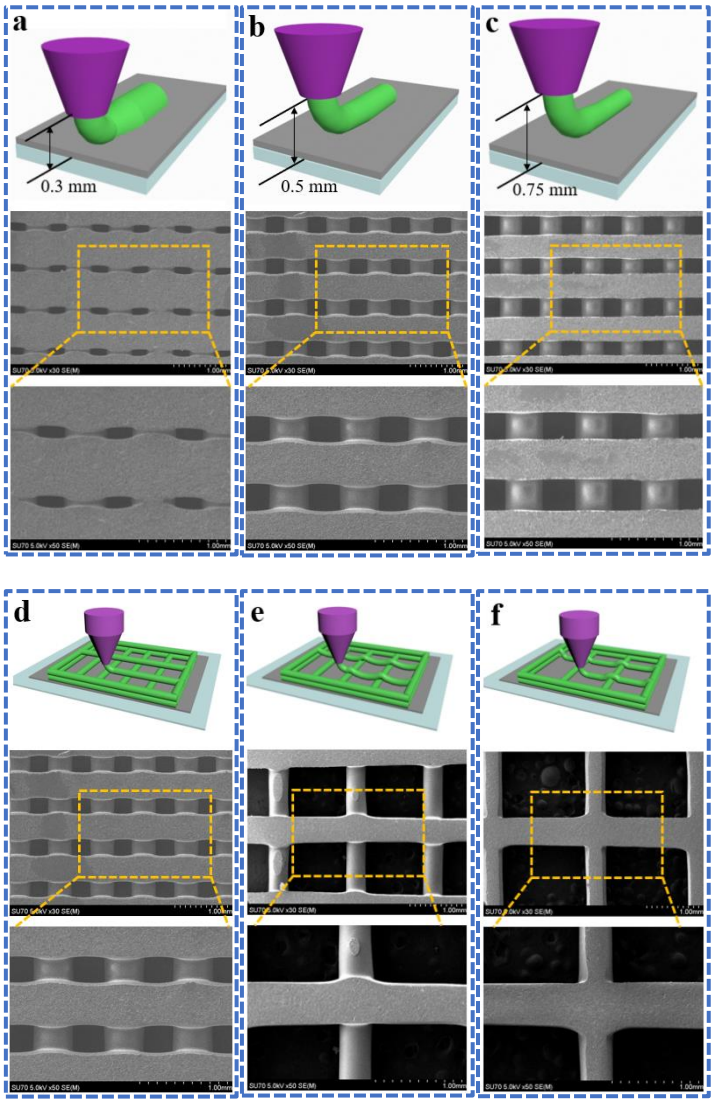

Figure 5.6 Different printing height (a) 0.3 mm height, (b) 0.5 mm height, and (c) 0.7 mm height. Different printed line distance (d) 0.8 mm line distance, (e) 1.2 mm line distance, and (f) 1.5 mm line distance.

According to the result, we deem the 0.5 mm~ printing height and the 0.8 mm~ line distance as the feasible printing parameters in our printing transfer system. Utilizing the enactment, we have constructed the graphene embedded sample with various patterns, including line structure with 0°, 45°, and 90°, and honey comb structure. These samples are employed to investigate the influence of the structure on performance of the fabricated soft electrodes.

First of all, we observed the surface morphologies of the samples with different structures, as shown in Figure 5.7. Before stretch deformation, the graphene layers were

embedded in different patterned structures, as shown in Figure 5.7a~5.7d. The dense and uniform graphene layers were clearly decorated at the bottom of the printed flexible matrix.

As horizontal elongation increases, the surface morphologies appear changes. As for the line structure with 0°, the horizontal lines of the stretched sample become longer and narrower (Figure 5.7e) when compared with that of the unstretched sample (Figure 5.7a). Moreover, the inlayed graphene in the stretched sample appears to be in obvious alignment along the stretching direction in a local scope. The morphologies of line structure with 45° illustrate that the elongation before (Figure 5.7b) and after stretching (Figure 5.7f) is not as large as the value of the sample with 0° in the same condition. The reasonable explanation is the change in angles offsets the length change to a certain extent. Figure 5.7g and 5.7h describe the line structure with 90°. It shows that there is no clear transform on the vertical lines as stretching proceeds, while the horizontal lines on the contour leads to an elongation in global and an alignment in local. For the sample with honey comb structure, a dramatic change appears after (Figure 5.7i) the stretching process. The hollow space of the hexagon becomes flat, which unveils that the deformation is concentrated near the area. The graphene along the edge of the hexagon generates an alignment.

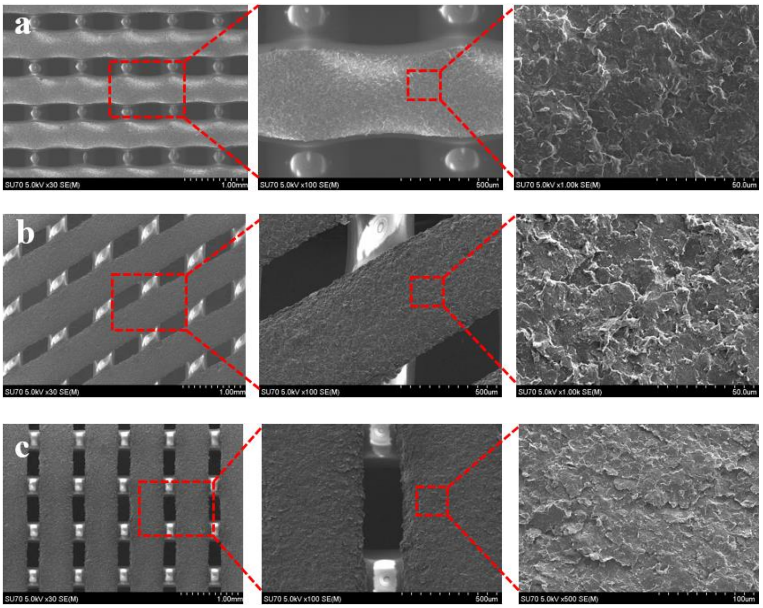

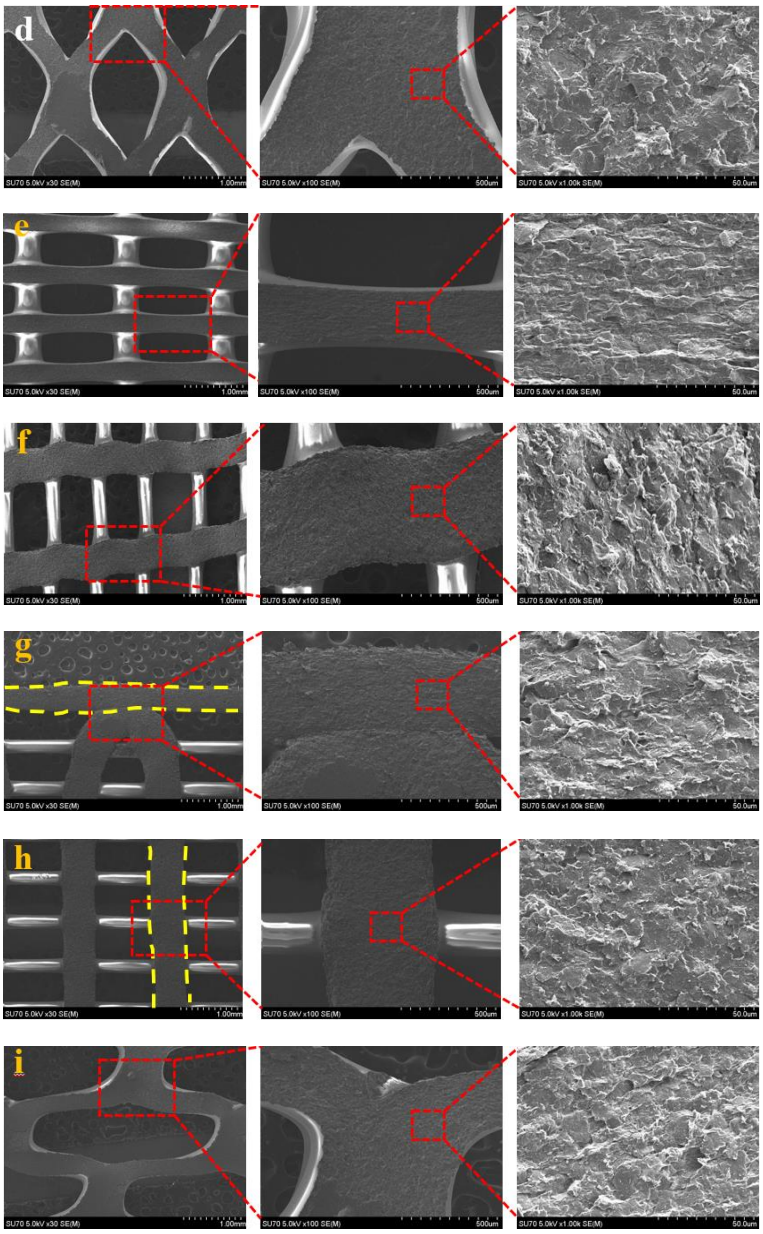

Figure 5.7 Morphologies of the samples with different structures before and after the stretching process. (a)~(d) line structure with 0°, 45°, and 90°, and honey comb structure before stretching. (e)~(i) Line structure with 0°, 45°, and 90°, and honey comb structure after horizontal stretching.

Furthermore, the mechanical property of the samples with different structures is explored. Figure 5.8a records the stress-strain curves of the samples before and after encapsulating with graphene layers in tensile measurement.

Before graphene was transferred, the samples (pure LIM silicone) with four various structures present different mechanical characteristics, which are recorded by

a solid line. Among them, the sample with 0°~ line structure shows the highest stress tolerance (about 1.2 MPa). The value of elongation reaches 760% at its breakage. As for the line structure with 90°, the maximum stress and strain values are about 1 MPa and 660%, respectively. The aforementioned values, for the sample with 45°~ line structure, further decreases to 0.8 MPa and 520%. The sample with the honey comb structure reveals the worst mechanical property, e.g., 0.7 MPa~ ultimate stress and 430%~ maximum strain.

The dashed line reflects the mechanical properties of the sample after conductive graphene layer is encapsulated in the polymer matrix. Two characteristics are worth noting: (1) the mechanical performance of the different samples exhibits a similar order as that of the unembedded samples. Namely, the maximum stress and strain of the line structure with 0°＞ the line structure with 90°＞ the line structure with 45°＞ the honey comb structure. (2) The mechanical property of the graphene embedded samples is undermined to a certain extent when compared with those samples fabricated with pure silicone. For example, the ultimate stress and the maximum strain of 0°~ line structure decreases by about 17% and 13%, separately. For the line structures with 45° and 90°, and the honey comb structure, the corresponding values are 25% and 17.3%, 43% and 22.7%, 17% and 0%, respectively.

It is clear that the encapsulation of graphene certainly results in an unignorable negative impact on the mechanical properties of the polymer matrix. It is due to the fact that the embedded graphene layer occupies the space of the LIM silicone on the bottom surface of the substrate. Still, the excellent mechanical performance of our graphene-decorated polymer deserves emphasis when compared with reported samples (Table 5.1).

Table 5.1 Summary of mechanical property of different samples.

Materials	Fabrication method	Maximum stress or force	Maximum strain	Reference
Graphene, SR	Filling patterned mold	493.79 kPa	60%	453
Graphene, SEBS	3D printing	0.4 N	1960%	454
rGO, PFs	Dip coating	250 kPa	100%	455
SR, graphene, CCB	Mixing	3.0 MPa	123%	456
GASs, PDMS	Dynamic spinning process	≈90 mN	70%	457
rGO, SC	Mixing	≈20 kPa	500%	458
MF@rGO, SEBS	Dip coating	0.2~0.3 MPa	50%	459
Graphene, LIM silicone	3D printing	1.2 MPa	760%	This work

To vividly display the outstanding tensile behavior, we stretched the samples (with and without graphene embedded) from original length (≈10 mm) to 600% strain, as shown in Figure 5.8b and 5.8c. The samples always maintain their integrity after multiple stretching cycles.

Additionally, the simulation method is adopted to analyze the stress distribution from a micro viewpoint. Figure 5.8d~5.8g display the stress distribution on the samples with a different structure under a 25% elongation case. It is noted that yellow, green, and blue colors represent large stress, medium stress, and small stress, respectively. For the line structures with 0° (Figure 5.8d) and 90° (Figure 5.8f), the stress on the horizontal line is much greater than the values on the vertical line. The stress on the

structure with 45° (Figure 5.8e) is between the value on 0° and 90° samples. For the sample with honey comb structure, the stress distribution appears to have conspicuous divergence. Namely, the stress mainly concentrates on the non-vertical lines of the sample. Furthermore, the large stress generally exerts on the contour line along the stretching direction among the different samples. From these details, we can refer that the stress in the network structure is mainly distributed in the tensile direction.

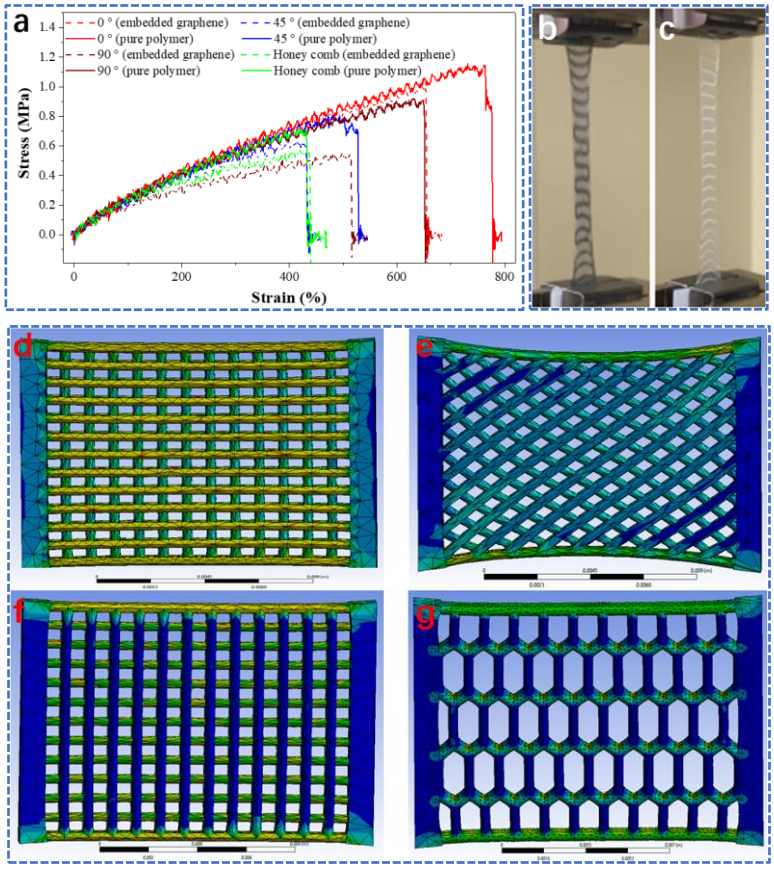

Figure 5.8 Mechanical property from experiment and simulation. (a) Stretching test results of samples with different structures. (b) and (c) Stretching the samples with and without graphene embedded. (d)~(g) Stress distribution in simulation.

The aforementioned stretching results illustrate that the mechanical properties are closely related to the sample structure. Next, we analyzed the tensile-electrical performance of the graphene embedded samples with different patterns.

Before the formal stretching, we pre-stretched the sample to 50% strain for 500 times. As displayed in Figure 5.9, the maximum resistances appear a dramatic drop in the initial stage of stretching/releasing cycles. The process is defined as conditioning.

An unavoidable displacement between graphene sheets in the process is considered as a main propulsion to cause visible degradation of the conductive network. With the increase of stretching cycles, the electrical responses gradually reached a stable condition. Reasonable speculation is an adjustment of the outer graphene repairs the inner cracks and bridge of the conductive pathway when the flexible matrix is elongated.

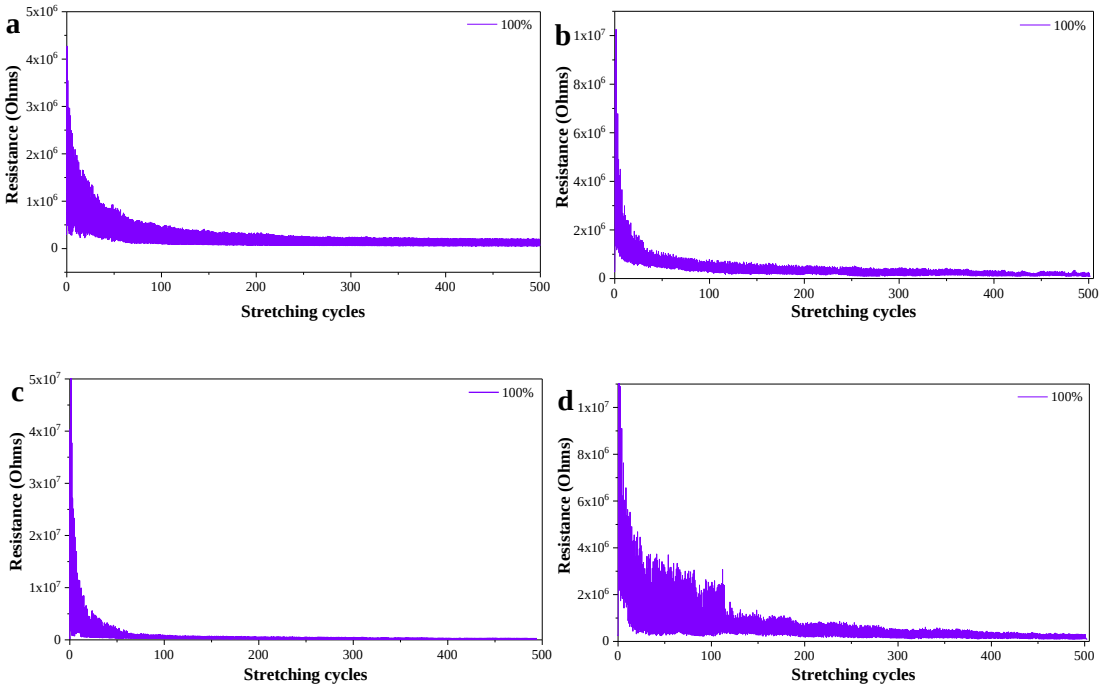

Figure 5.9 Resistance response of the samples with different structures to 50% strain during 500 cycles

Then, we investigated the electrical property of the soft electronics with various structures in ten stretching/releasing cycles with different strains. Figure 5.10a~5.10d record the dynamic electrical response of the samples. It shows that the different samples possess similar resistances (near 5×10^4 Ω) before stretching. Meantime, they all have a wide response range from 10% to 120% strains, and a steady increase of the maximum resistance as the elongation ratio increase.

However, some clear differences among the samples with different structures cannot be neglected. For the line structure with 0° (Figure 5.10a), the maximum resistance reaches 9×10^5~2×10^6 Ω at 120% strains. It is noted that the resistance peaks appear to have a significant drop under the maximum elongation. The valley

resistance fluctuates less than 5% when $\varepsilon < 80\%$, and increases by about 50% when $\varepsilon > 100\%$. The sample with 45°~line structure has an increase trend for valley resistance as the magnitude strain increases. The maximum fluctuation surged to 300%. The peak resistance values was kept around 4.5×10^5 Ω at the maximum strain, which is the lowest among the four samples. For the line structure with 90°, the increased ratio of peak resistance is conspicuously promoted as $\varepsilon > 100\%$. Compared with the other samples, the valley resistance was found to be stable during whole stretching range. The sample with honey comb structure has a similar resistance response with the 0° ~line structure sample. At maximum elongation, the peak resistances are around 2.5×10^6 Ω, and have a decreasing trend in multiple stretching. Also, a noticeable promotion for valley resistance can be observed at larger strain.

To further investigate the structure influence on electrical performance, we calculated their gauge factor according to Equation 5.3:

$$\text{Gauge Factor} = \frac{(\Delta R/R_0)}{(\varepsilon)} \qquad 5.3$$

Where ΔR is the resistance change upon elongation, R_o is the original resistance, and ε is the applied strain. The consequences are displayed in Figure 5.10e. The visible differences manifest their various electrical sensitivity. Among them, the line structure with 45° showed the lowest gauge factor (about 1.8). The value was more stable than other sample during the entire strain range. The highest gauge factor is contributed from the structure with 90°. Different from other samples, the value of the 90°~line structure revealed a monotonic increase trend with the increase of elongation percentage. Especially, the gauge factor increased by 186% as strain increased from 100% to 120%. The line structure with 0° and the honey comb structure had a similar gauge factor. The values were around 3~5. The result indicates that the line structure with 90° is more sensitive, while the line structure with 45° is more stable in response to external elongation.

We further compared the electrical response properties of the fabricated samples with other reported carbon-based strain sensors. Gauge factor and strain sensing range are selected as the index for the characteristics. From Figure 5.10f and Table 5.2, it can be captured that the sensor, via transferring graphene layer into LIM silicone matrix in 3D printing, has a great device performance.

Table 5.2 Electrical response properties of fabricated samples with other reported carbon-based strain sensors

Materials	Strain sensing range (%)	Gauge factor	References
GNP, CNT	0.6	96	460
CNT yarn	1	0.5	461
CNT	0.8	6.42	462
Reduced GO, Elastic tap	82%	150	463
Graphene, AgNP	14.5%	475	464
Graphene	0.008%	389	465
Graphene, carbon black	10%	2.1	466
CNT	530%	25	467
Reduced GO	100%	154.8	468
Graphene	20%	42.2	469
Graphene	150%	2	470
CNT	410%	12	471
Graphene, glass fiber	11.27	14.56	472
Graphene, LIM silicone	10~120%	1~17.2	This work

After pre-stretching, we recorded the electrical response of different samples during one thousand cyclic deformations at 100% strains. The results show in Figure 5.10f~5.10i, which demonstrate the electrical repeatability of the sample with different

structures. All sample peak resistances exhibited a downward trend during the first 100 release cycles. The maximum resistances of different samples separately dropped from 8×10^5 Ω to 4×10^5 Ω (Line structure with 0°), from 2×10^5 Ω to 1×10^5 Ω (Line structure with 45°), from 2×10^6 Ω to 5×10^5 Ω (Line structure with 90°), and from 9×10^5 Ω to 6×10^5 Ω (Honey comb structure), etc. It is unneglected that the valley resistances appeared slight decrease as well, although the ratio is far less than that of peak resistances. The changes can be attributed to the adjustment of conductive pathway, where the graphene sheet repairs the cracks caused in the stretching process. In the subsequent stretching cycles from 100 to 500 times, the valley resistances kept constant. But the peak resistances still had some slight fluctuations, which a deviation less than 20%. It means the stability of the conductive network is further promoted, via self-repair process. As the deformation cycle exceed 500 times, the electrical responses of lattice structures (including 0°, 45°, and 90°) exhibited an ultra-repeatability, which is a highlight for soft electronics. However, the peak resistance of the honey comb structure has jumped by 50% at the 520th stretching cycle. The reason is that the flexible matrix is broken due to its poor mechanical property.

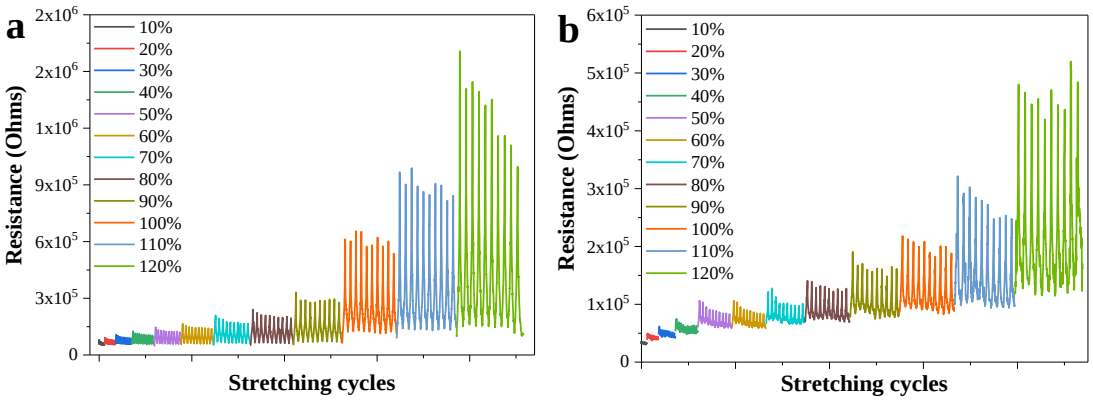

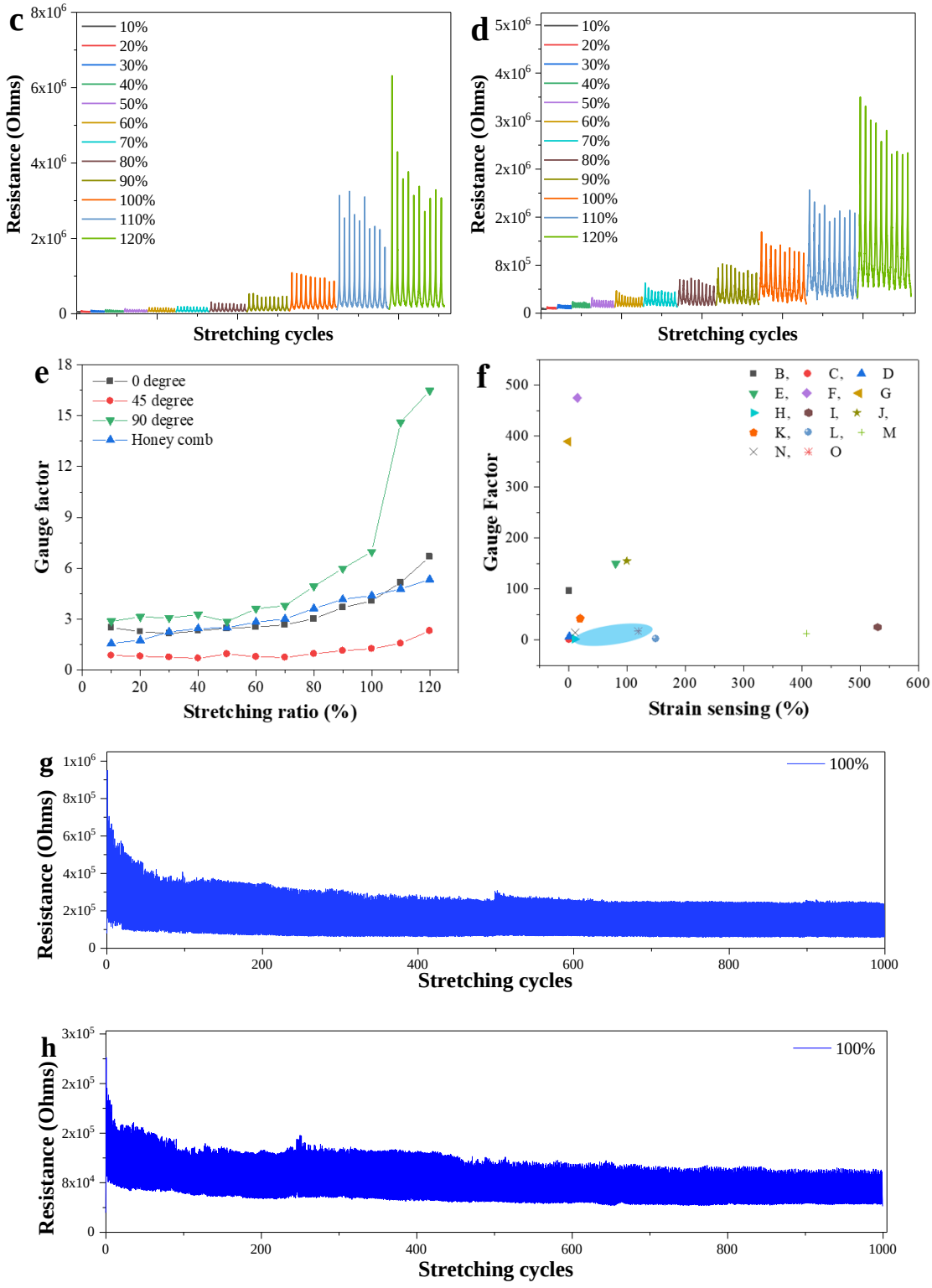
c
Resistance (Ohms)
Stretching cycles
10%
20%
30%
40%
50%
60%
70%
80%
90%
100%
110%
120%
d
Resistance (Ohms)
Stretching cycles
e
Gauge factor
Stretching ratio (%)
0 degree
45 degree
90 degree
Honey comb
f
Gauge Factor
Strain sensing (%)
B, C, D
E, F, G
H, I, J,
K, L, M
N, O
g
Resistance (Ohms)
Stretching cycles
100%
h
Resistance (Ohms)
Stretching cycles
100%

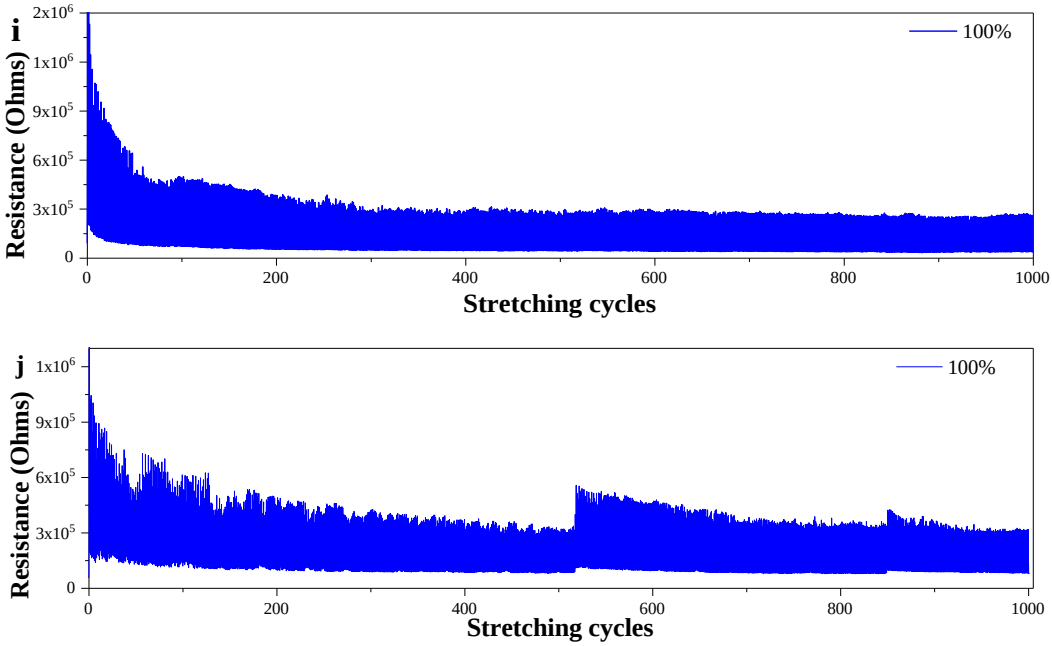

Figure 5.10 Electrical performance of the different samples. (a)~(d) Resistance changes of the samples with different structures with different tensile strains. (e) Gauge factors of the sample with different structures. (f) Comparison of gauge factors between different samples. (g)~(j) Resistance response to 100% strain during 1000 cycles.

Considering the advantages of a large strain sensing range and ultra-high repeatability, the fabricated soft electronic has potentials to be utilized to monitor full range human activities. Hence, we conformally attached the sample (lattice structure with 0°) to human body by adhesive tape. The fixed sample was employed to collect the signals in response to periodic vigorous and subtle movements.

Figure 5.11a~5.11d annal the large motions of human joints, such as finger bending, wrist bending, elbow bending, and knee bending, etc. The relative resistance responses reveal excellent repeatability as the bending angle continuously increases. Also, the average peak values are about 3, 1.2, 2.3, and 4, respectively. The difference is probably caused by the deformation degree and the deformation modes during human movement. Conversely, we can adopt changes to refer the corresponding human action.

Furthermore, the sample is able to effectively detect small deformations, such as vocal muscle pulsation and facial expression. As an adult tester shows a classical Beat-

Box, a clear relative resistance response can be captured as shown in Figure 5.11e. The relative resistance is about 0.3. Also, when tester shows a unpredicted expression, the fold of the forehead skin can cause an electrical resistance response, and the relative value is about 1. It is noted that the action-response waveform is sharper than that of the others. The results further demonstrate the sensitivity of the constructed samples.

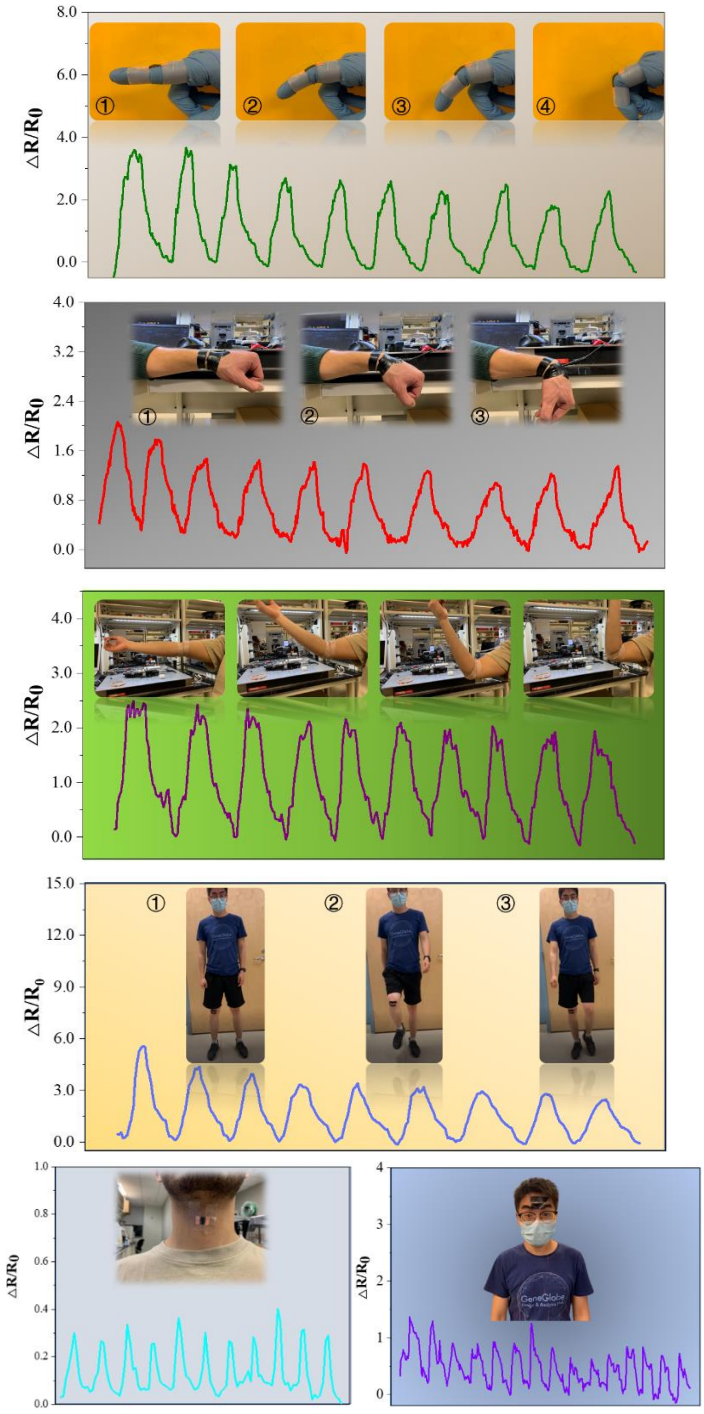

Figure 5.11 Resistance response to human body movement.

5.4 Conclusions

We present a novel strategy to construct soft electronics via transferring graphene conductive layer into flexible polymer substrate. In this method, the liquid LIM silicone was extruded onto the undried graphene layer along a designed pathway in the 3D printing process. A self-encapsulation effect was triggered with an assistance of air pressure and adhesion behavior of polymer. Facile procedure and reliable transfer notify a great potential to promote this approach.

To improve the quality of the constructed samples, we continuously optimized the factors in the transfer process. The undried graphene layer is an indispensable condition to achieve encapsulation, due to the low energy release rate. Also, the feasible printing parameters were validated, such as printing height of 0.5 mm and line distance of 0.8 mm, in our printing transfer system.

Based on the advancements, we fabricated the soft electronics with different complex patterns, such as line structure with 0°, 45°, and 90°, and honey comb structure. The influence of the structure on the mechanical and electrical performances was confirmed. The line structure with 0° has the highest elongation tolerance (760%~ strain and 1.2 MPa~ stress), while the value for honey comb structure reduced to 430%~ strain and 0.7 MPa~ stress. Besides, the line structure with 90° possesses the highest gauge factor, whereas the lowest gauge factor was obtained from the 45° line structure.

Totally, the prepared samples show excellent mechanical as well as electrical performances, including >400% elongation deformation, wide strain response ranges from 10% to 120%, and high electrical response repeatability, etc. They revealed a great possibility to be utilized in wearable electronics for human movement monitoring and rehabilitation.

CHAPTER 6 3D Printing used to Transfer Assembled AgNWs into Elastomer

6.1 Introduction

Flexible electronics are widely considered as the crucial components for next-generation electronics. Due to outstanding ductility, fatigue durability, high sensitivity, etc., they have been applied in diverse fields. To design a flexible electronic with excellent performance, many approaches have been proposed. Generally, they have three steps comprising of a selection of materials, formation of the conductive network, and integration of functional layer and flexible matrix.

AgNWs have been the most promising candidate materials for advanced flexible electronics, owing to the superior conductivity, high transmittance, cost-effectiveness, synthesis scalability, suitability for mass production, solution processing, excellent flexibility, etc. [473] There are several methods to prepare AgNW network, comprising of spin coating, drop-casting, spray coating, rod coating, and many others. They generally form a random AgNW network, which results in some challenges, involving the insufficient contact of individual AgNWs, the aggregation of AgNWs, and the trade-off between electrical conductivity and optical transmittance.

To promote the functionality of future flexible electronics, researchers have proposed to tackle the challenges for conventional random AgNW networks via improving the assembly structure of AgNWs network [474]. According to their conception, the assembled AgNWs exhibit lower electrical percolation thresholds, leading to higher transmittance at similar resistance or lower resistance at similar transmittance [249]. Up to now, a variety of assembly strategies have been developed, which can be divided into the external fields-based assembly, the interface-based assembly, and the other assembly methods [475]. Among them, the interface-based assembly is commonly accepted as the simplest and the most effective approach [476]. In this concept, the interfaces provide a significant platform for the organization of NWs based on

interfacial-ordering effects. A microscopic version of “logs-on-a-river” can be used to vividly describe the situation. Fluids flows and rheological behavior can assist the NWs to form dense arranged conductive structure.

Guided by the notion, researchers have confirmed the applicability of the Langmuir-Blodgett (LB) assembly [477], the horizontal dip-coating method [478], the heat-assisted dip-coating method [479], and the capillary printing, etc. They have been successfully used as sensing matrixes for surface-enhanced Raman scattering applications, optoelectronic devices, transparent conductors, and other fields. However, the majority of these approaches require essential necessities, such as controlling multiple variables, additional transfer process, and forthputting of special devices, which not only limits the cost-effectiveness, but also harms the scalable assembly. In this case, we put forward a compressed air-assisted assembly. In this method, an interface of two phase, e.g., air/water, can pin AgNWs. Compressed air, instead of tools or devices, provide shear force to drive the oriented movement of AgNWs. The dense AgNWs array can gradually form as compressed air exert. The approach is facile and rational, which is possible to be used in a scaled production.

Apart from the assembly of AgNWs, the integration of conductive materials and elastomer is crucial to obtain flexible electronics with ultra-performance. Related methods have been reported, including surface functionalization, mixing with other functional materials, applying physical pressure [480], encapsulating with a capping layer, etc. Zhang *et al.* adopted poly dopamine to functionalize the Polyurethane Sponge. It endows a strong adhesion and hydrophilicity to the PU skeleton, enhancing the performance of prepared flexible sensors [481]. Jing *et al.* prepared a carbon nanotube (CNT)/AgNW-polyethylene terephthalate (PET) hybrid film via a mechanical pressing-transfer process at room temperature. It shows that the mechanical pressing can reduce the surface roughness of the film. On the other hand, the adhesion between conductive layer and flexible substrate is enhanced [482]. Amjadi *et al.* utilized the encapsulation technique to embed AgNW network in PDMS matrix. The formed sample not only is a tunable gauge factor, but also has high stretchability up to 70% [344]. These approaches

indeed enhance the adhesion between AgNW network and flexible substrate, but still exhibits some disadvantages, e.g., lacking pattern control and labor-consuming [483]. The drawbacks damage the electrical sensitivity of the products. Furthermore, they limit the application range.

To simultaneously realize a pattern and strong adhesion, researchers have made tremendous efforts. Yang *et al.* employed a microchannel wetting method to prepare patterned AgNWs. In detail, the AgNW aqueous solution was dispersed on the substrate with hydrophobic/hydrophilic micropatterns. With the evaporation of aqueous, the patterned conductive nanowires were formed, which exhibited good conductivity in various applications [484]. Yao *et al.* adopted laser scribing and heat press lamination to prepare flexible textile. The laser scribing can generate the arbitrary patterns for AgNW composites, and heat press can encapsulate the shaped AgNW composites with firm bonding onto a soft matrix. The integrated samples showed not only an outstanding electrical property, but also an ultra-mechanical performance [485]. Song *et al.* utilized the electrospray to deposit a patterned AgNWs on the PMMA substrate. A grounded electrolyte solution (EDGE) was adopted to pretreat the substrate. Then, AgNWs were attracted to form patterned structure via strong electrostatic attraction of electrolyte solution collector. In the method, the coverage ratio of AgNWs is much higher than the value in the conventional ways under the same condition. The formed samples have the potential to be used in wearable devices in diverse fields [451].

However, most of these approaches have some existing issues, including wasting a large amount of AgNWs, requirement of complex pretreatment, or assistance of special tools. The drawbacks damage the economic effect, increase the manufacturing procedures, and limit the application fields. To avoid these disadvantages, we proposed to transfer AgNWs into elastomer via 3D printing. Specifically, the LIM silicone was printed on the AgNW network with the desirable patterns. With peeling of the cured silicone, the AgNWs were removed forming a patterned conductive network. It not only forms the various complex patterns, but also simplifies the process.

In summary, we have designed a deterministic assembly to form a wearable sensor in a facile process. It comprises of the arrangement of AgNWs with assistance of the capillary force produced on the air/water interface and the shear force induced by compressed air, as well as the forming of a desired functional layout in a single 3D printing step. Taking into consideration of excellent mechanical property, electrical performance, and anti-bacterial property, the formed sample has the potential to be used in wearable devices for many applications.

6.2 Experimental

6.2.1 Materials and Preparation

The silicone rubber is the commercial LIM^{TM} 6050-D2 (Momentive Performance Materials Inc.), which was prepared by mixing part A and part B in weight ratio of 1:1 according to the instruction from vendor. Polyethylene terephthalate (PET) films (MELINEX ST505) with 125 μm thickness was supplied by TEKRA. Sodium chloride (NaCl ≥99%), Polyvinylpyrrolidone (PVP-K30), and silver nitrate ($AgNO_3$, 99%, ACS reagent) were purchased from Sigma-Aldrich. Ethanol (99.5% purity), acetone (99.5% purity), and ethylene glycol (EG, 100% purity) were obtained from VWR. Deionized (DI) water was produced by a Direct-Q water purification system (Millipore Sigma). These materials were used as received without any further modification.

6.2.2 Preparation of AgNWs

A modified polyol reduction method was used to synthesize AgNWs [257, 486]. Briefly, 0.5 g PVP was dissolved in 50 mL of EG in a round-bottomed flask under a stirring speed of 400 rpm. We then employed an oil-bath to keep the solution at 170 ℃ for 1 hour to form a homogeneous solution. Next, 150 μL of 0.1 mol/L NaCl/EG solution was added in the homogeneous solution. After 10 min, 0.5 g of $AgNO_3$, uniformly dissolved in 50 mL of EG, was constantly dripped into the flask with a volumetric flow rate of 2.5 mL/min. Another 20 min at 170 ℃ was required to support the reaction. Subsequently, the solution in flask cooled down to room temperature, and precipitated with acetone and centrifugated at 3000 rpm for 20 minutes. The AgNWs then were washed three times with ethanol via centrifugation to remove the residual PVP, and re-

dispersed in DI water to acquire an AgNW aqueous suspension with a solid concentration of 10 mg/mL. A drop-casting method was adopted to prepare a densely packed AgNW network with assistance of compressed air. More details were stated in discussion section. The dimension of the synthesized AgNWs was counted via the software of ImageJ. The results were summarized in Figure 6.1, which indicates that the average length and diameter are $6.07 \pm 2.0563\ \mu m$ and 84.07 ± 15.9853 nm, respectively.

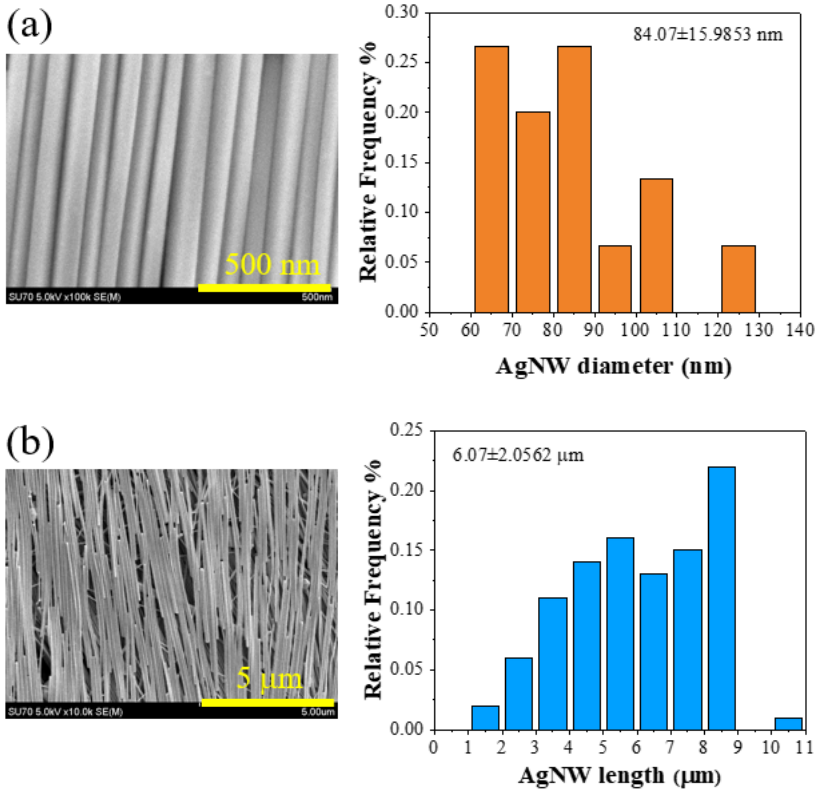

Figure 6.1 Dimension of the synthesized AgNWs. (a) AgNW diameter. (b) AgNW length.

6.2.3 Transferring AgNW Network into Elastomer

3D printing was employed to transfer AgNWs into elastomer matrix. To obtain a uniform printing ink, we manually stirred the silicone part A and part B for 30 sec. Next, a planetary mixer (ARE-310, Thinky Mixer) was employed to mix it for 5 min at 2000 RPM. Finally, a defoam procedure proceeds for 30 seconds in the mixture. Subsequently, we used computer-aided design (CAD) software (SolidWorks) to design

the desirable shape patterns. An extrusion-based 3D printer (EnvisionTec, 3D Bioplotter) with a tapered nozzle (400 μm in diameter, Nordson) was employed to print on a dried AgNW film. A series of printing parameters were described in discussion section. Finally, after a 24 h of curing, the printed samples were peeled off from an AgNW layer at various speeds.

6.2.4 Measurement and Characterization

The microstructures and the assembled AgNWs were observed via a field-emission scanning electron microscope (FE-SEM, HITACHI, SU-70) with a 5 kV operating voltage. An Energy Dispersive Spectrometer (EDS) was operated at 15 kV to calculate the element content. The surface 3D morphologies and the line roughness were obtained by laser scanning confocal microscopy (ZEISS, LSM770, US). An X-ray Diffractometer (XRD, SmartLab, Japan) using Cu Kα radiation in the 2θ range of 20~100° was performed to identify the crystalline structure of the AgNW film before and after transferring. A goniometer (OCA 15, DataPhysics) was employed to examine the water contact angles (WCAs). A commercial camera was utilized to record the samples at different steps.

To qualitatively exam the flexibility, the sample was forced to various morphs by human. Also, a digital tensile machine (MTS 30, USA) was employed to quantitatively test the mechanical property. The specimens were mounted to the device with gauge length of 10 mm. The tensile speed was kept at 5 mm/s to get a stable mechanical response.

A 4-point probe system (Ossila, UK) was employed to calculate the sheet resistance of the sample in static state. A digit multimeter (KEYSIGHT, 34465A, 6 1/2 and Fluke 289 True-RMS) was performed to record the resistance changes during the dynamic deformation processes. It is noted that the cyclic stretching with a speed of 0.5 mm/sec was implemented on a home-made stretcher controlled by a computer. The sample was attached to a healthy adult to detect his movement at different parts.

E. coli (ATCC53496) and S. aureus (ATCC 25923) were used for the antibacterial experiment. Bacteria were cultured in Luria-Bertani (LB) broth at 37°C overnight

before the test. LIM silicone and AgNW films were cut into 0.5×1.0 cm pieces and sterilized with 75% ethanol for 15 min before being transferred to a 24-well plate. The liquid culture of E. coli and S. aureus was diluted to approximate 10^5 CFU/mL by fresh LB broth and added 0.5 mL to separate wells with film pieces. The plate was statically incubated at 37°C for 24 h. The films were aseptically removed. The bacterial suspensions were transferred to Eppendorf tubes and well mixed by a Vortexer. Agar plate counting was performed to determine the number of living cells in the bacterial suspensions incubated with different films.

6.3 Results and Discussion

Figure 6.2 displays the entire process of fabricating the flexible sensor by transferring the dense arranged AgNWs into elastomer in 3D printing. The procedure is comprised of two main steps. (1) The compressed air-induced capillary force and shear force were used to array AgNWs on the surface of the aqueous droplet, as described in Figure 6.2a. With the evaporation of the water, the area of the droplet surface decreased, which further induce the AgNWs densely packed together. (2) An extrusion-based 3D printing was employed to encapsulate the AgNW network. Due to the high extrusion pressure of the printing and the strong adhesion of the liquid silicone, AgNWs can be successfully transferred into the flexible matrix, which is exhibited in Figure 6.2b.

Based on forementioned process, a soft electronic can be fabricated. The extruded LIM silicone provides an excellent flexibility. Meanwhile, the embedded AgNWs ensure a reliable conductivity. As shown in Figure 6.2c~6.2e, the prepared samples possess three merits including ultra-mechanical property, high electrical performance, and antibacterial property. Considering these advantages, the electronics are possible to be used as a wearable sensor to detect human motions and physiological information.

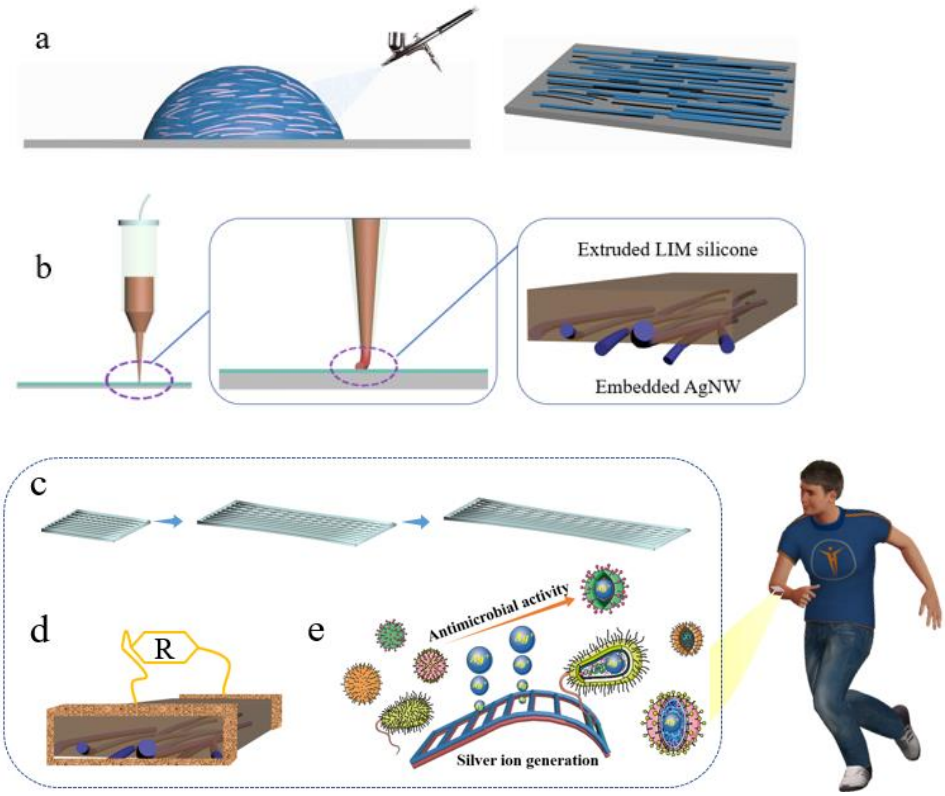

Figure 6.2 (a) Arranged AgNWs triggered by capillary force and shear force induced by compressed air. (b) Encapsulation of AgNW network via 3D printing. (c)~(e) Schematic of the ultra-mechanical stretch-ability, electrical property, and antibacterial performance of the sample.

To array AgNWs, we adopted compressed air to act on the surface of AgNWs aqueous droplet. The detailed procedure was described in Figure 6.3.

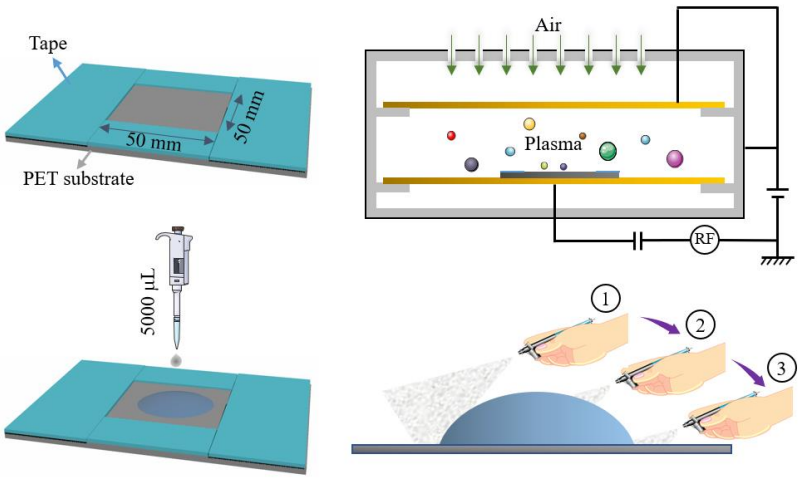

Figure 6.3 Schematic illustration of the procedure to form densely packed AgNW film.

First of all, a commercial PET film was selected as the substrate. Its exposed area is about $10 \times 10\,\mathrm{mm}$ via overlay of a commercial tape at the edge. After cleaned by ethanol and acetone, the PET substrate was modified via air plasma in a plasma cleaner (PDC-001-HP, HARRICK PLASMA). From Figure 6.4, we obtained the water contact angle gradually decreased from 81.4° to 46.4°, 21.9°, and 13° as the plasma treatment time increased from 0 sec to 30 sec, 60 sec, and 300 sec.

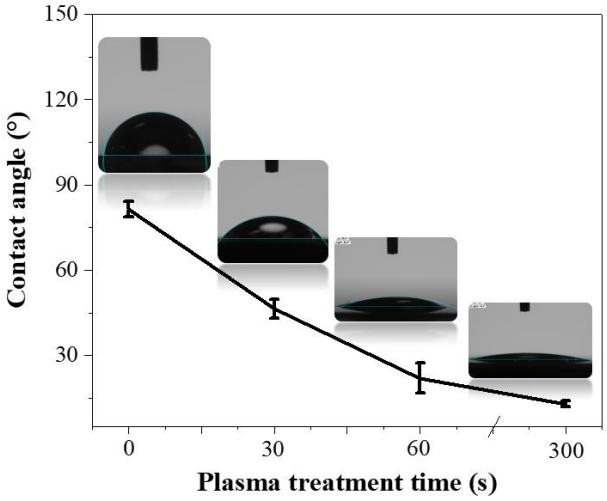

Figure 6.4 Contact angle after different plasma treatment time.

The results clearly indicate that the hydrophilic property of the PET is enhanced. Meanwhile, the increase ratio of the hydrophilicity slows down with the extension of the plasma treatment time. It suggests a suitable treatment time not only dramatically promotes the hydrophilicity of the substrate, but also saves time and increases efficiency. Thus, the plasma treatment time is selected as 300 sec to render the exposed area with super hydrophilic property in a limited time.

We subsequently dropped the AgNW suspension with 5000 μL volume on the modified area. The liquid was normalized into a designed shape in this case. Next, a commercial air brush (Model G22, Master Airbrush) produced compressed air on the suspension pool. Meanwhile, the air brush was dragged from the center to the edge at a speed of 0.1 mm/min. It is noted a pump (TC-20 series, USA) provides a constant pressure during 0~0.1 bar, and the distance between droplet surface and brush nozzle is about 20 mm. Figure 6.5 reveals more details about applying compressed air on the surface of AgNW suspension. In the initial state, the color of the solution was gray

(Figure 6.5a). As compressed air was exerted, the edge area on the surface appeared metallic color (Figure 6.5b). With the extension of blowing time, the area with metallic color increased (Figure 6.5c). The color difference can be clearly observed in the third stage. We preliminary assume the change was caused by the dense pack of the AgNWs on the liquid surface.

Figure 6.5 Exerting compressed air on the surface of the AgNW aqueous solution.

We compared the droplet surface condition with and without compressed air acting. Figure 6.6a shows that the droplet surface appeared a full metallic color after compressed air blowing for a long time. Unlike, the droplet without compressed air exerting was gray in Figure 6.6b. After evaporation of the droplets, two different morphologies of AgNW networks were observed in Figure 6.6c and 6.6d. They clearly shows that the AgNW film, with an assistance of compressed air, possessed not only a high orientation, but also a tight pack. To quantitatively represent the orientation of the AgNWs with different conditions, the OrientationJ, an ImageJ plug-in based on structure tensors was adopted. The statistic results were summarized in the histogram, which manifests a conspicuous difference between different AgNW films. In Figure 6.6e, the AgNWs, with the assistance of compressed air had an orientation angle of 93°. However, as for the AgNWs without any revision, there was no obvious orientation angle. Namely, a random distribution emerged between AgNWs. An inserted color map in Figures 6.6e and 6.6f, shows the processed SEM image, also confirmed the aforementioned statistics. It is stated that the hue, saturation, and brightness in the inset figure reflects the orientation, coherency, and original source image.

To understand the formation of the dense arrangement of AgNWs, we analyze the AgNW state in an aqueous solution, the function of compressed air, and the evaporation of aqueous solution. Generally, there are three situations for a single AgNW in an

aqueous solution as displayed in Figure 6.6g. The first condition is AgNW suspends in the inner of solution. When the system is at rest, the main forces applying on AgNW comprise of a weight force ($F_G = -\rho_{AgNW}\pi R^2 Lg\vec{e}$) and a buoyancy force ($F_b = \rho_{water}\pi R^2 Lg\vec{e}$), where the unit vector $\vec{e}$ points vertically upward, ρ_{AgNW} and ρ_{water} are the density of AgNW and water, R is the AgNW diameter, and L is the AgNW length. Considering $\rho_{AgNW} > \rho_{water}$, we can obtain $F_G > F_b$ that means AgNWs are prone to move downward. The inference is consistent with the phenomenon that AgNWs occurred precipitation in a long-term stationary state.

The second is AgNW attached to the liquid/air interface. In this condition, the capillary force (F_c) induced by Laplace pressure and surface tension is triggered. Suppose the AgNW height submerged in water is equal to the radius of the AgNW. The $F_c \approx 2RL\gamma\vec{e}$ where γ is the aqueous surface tension. The force is opposited to F_G because the air/liquid interface is convex. Meanwhile, the AgNW volume soaked in aqueous solution changes, so that the forces vary as $F_G = -\rho_{AgNW}\pi R^2 Lg\vec{e}$, and $F_b = \rho_{water}\frac{\pi R^2 L}{2}g\vec{e}$. We roughly use $R = 84\ \text{nm}$ and $L = 6\ \mu\text{m}$ for the synthesized AgNW, $\gamma = 72.75\ \text{mN/m}$ for the water solvent, $\rho_{AgNW} \approx 10.5\ \text{g/cm}^3$, and $\rho_{water} \approx 1\ \text{g/cm}^3$. It can be inferred that $F_c + F_B > F_G$. The calculation supports the AgNW can be pinned on the interface of water/air.

These two cases emerge when the aqueous film thickness is larger than the AgNW diameter. When the aqueous film thickness is less than the AgNW diameter, the third position of AgNW occurs. A capillary condensation results in a formation of a capillary meniscus. Under the circumstances, the capillary force changes the direction, due to the curvature of the interface of air/liquid changes to concave. It assists to localize the AgNW to a stationary substrate. Also, the F_G remains constant, but F_b reduces. Thus, the total force maintains the AgNW at rest.

From Figure 6.6a~6.6f, it can be conducted that compressed air is crucial for the formation of the AgNWs assembly. Combined with the experiment results, we have

came up with a theoretical process as described in Figure 6.6h. Originally, AgNWs uniformly disperse in the aqueous solution, and proceed a Brownian motion. As compressed air exerted on the surface, two types of movement of AgNWs are induced. Inside of the droplet, the vortexes are produced due to the component of compressed air normal to the air-water interface. They accelerate the movement of AgNWs, and provide more opportunities for AgNWs to move outward. Once AgNWs are attached to the interface of air-water, they are fixed under the interaction of F_b, F_c, and F_G. Additionally, the component of compressed air is paralleled to the air-water interface facilitates the shear movement on the top layer of aqueous solution. Those AgNWs are trapped on the interface moves along the orientation, and are continuously packed at the edge of the droplet. As air brush moves, the densely packed AgNWs almost cover the whole droplet surface, which exhibits a metallic color in Figure 6.6a. It is noted that the results show a high repeatability in fresh AgNW aqueous solution with high concentration (>10 mg/mL) based on the preliminary contrast test.

Water evaporation also has an important effect on the arrangement of AgNWs. According to the images displayed in Figure 6.7, the AgNW aqueous solution in the experiment exhibits a constant contact line mode. Namely, the droplet height decreases, and the contact area between the substrate and the liquid remains constant as the evaporation proceed. Based on the characteristic, a schematic is drawn to depict the AgNW array's formation in an evaporation process (Figure 6.6i). In the early evaporation, there are some unfilled narrow space between AgNWs caused by imperfect packs in above steps. With the evaporation, the area of the air/water interface decreases. If the amount of AgNWs was constant on the droplet surface, the distance between tracked NWs reduces. Thus, it leads to a denser packed of AgNW networks.

However, the AgNW solution without compressed air exerting has a silight difference in evaporation process. As described in Figure 6.8, there are a few AgNWs pinned on the liquid/air interface owning to Brownian motion at the beginning. The amount can be ignored when compared with those in air-assisted systems. The surmise is reasonable to explain that no metallic layer occurs on the droplet surface without air-

assistant. Subsequently, the majority of AgNWs naturally drops in solutions due to the effect of gravity, forming a random AgNW network. Therefore, there is no obvious orientation on the AgNW film.

Moreover, the similar appearances are noticed in the aforementioned evaporation proceeses. Due to the large curvature at the edge of droplet, the water surface tension initiates the capillary flow. It has been widely considered as a reason for the coffee ring formation. Besides, when the water film thickness is less than the AgNW diameter as the evaporation proceeds, the capillary meniscus at the air/water/solid interface line occurs, causing retention and immobilization of AgNWs on PET substrate surface.

By comparison, there are some resembling and diverse properties between different distributed AgNW films. The AgNW film with dense-pack illustrates a lower sheet resistance at zero strain (no stretching) in a 4-point probe test. As shown in Figure 6.6j, the resistance of the arranged AgNW film dropped by 50% compared with that of the random AgNW film. The reason is that the contact area between AgNWs increased. Meanwhile, the resistance deviation on the random AgNW film was observed to be 4.5 times higher than the aligned AgNW film. It supports the conductive pathway to become more uniform across the entire AgNW film under the function of compressed air. The water contact angle on the different AgNW films were measured, as shown in Figure 6.6h. It reveals values on aligned and random AgNW films are 35.6° and 27.4°, separately. They both manifest the super hydrophilic performance and wettability, which means the liquid can easily disperse on the surface of the different AgNW films.

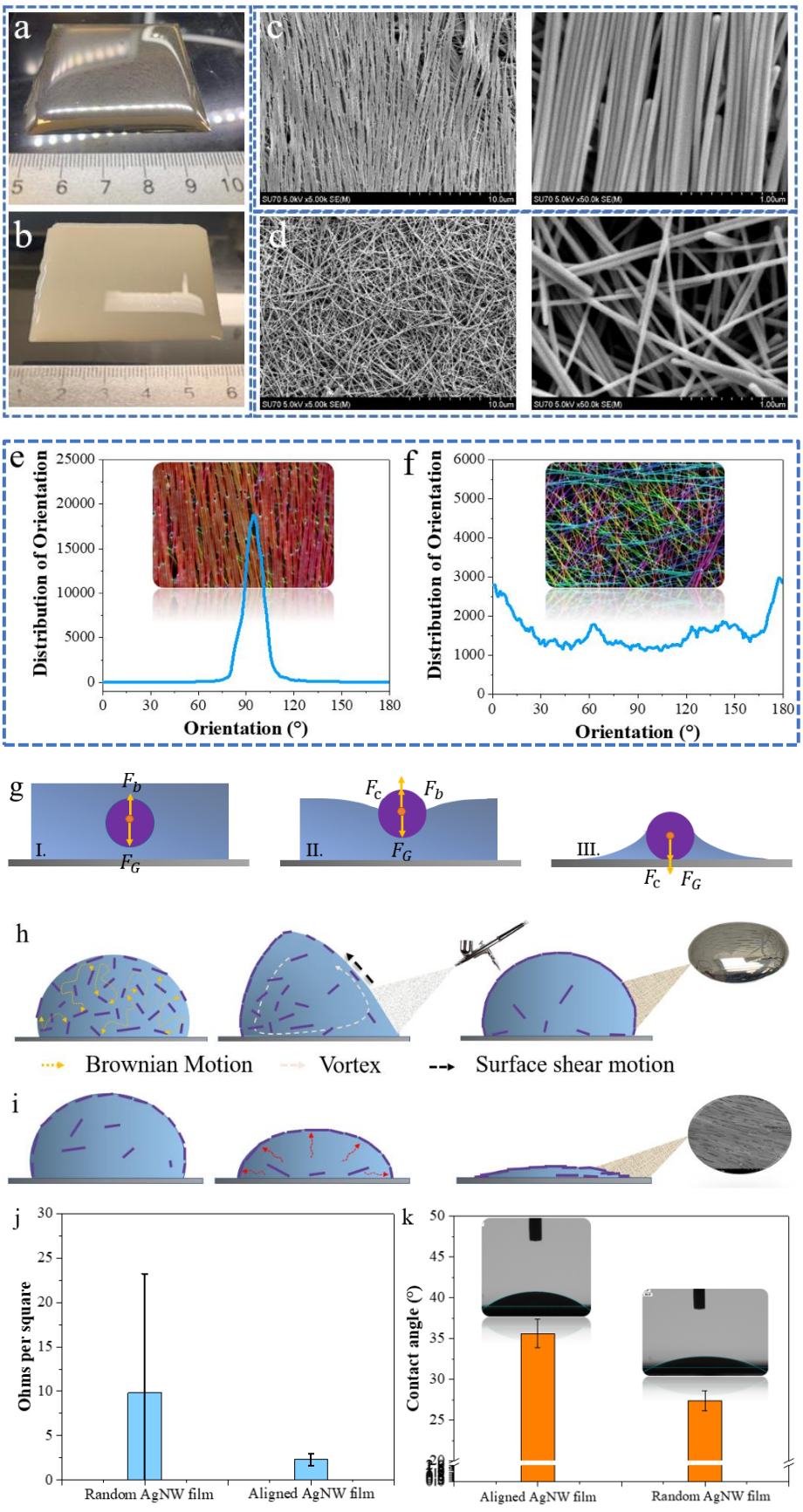

Figure 6.6 Procedure of preparing densely packed AgNWs and their performance

exhibition. (a)~(b) Surface morphologies of AgNWs aqueous with and without assistance of compressed air. (c)~(d) Morphologies of AgNW films with and without assistance of compressed air. (e)~(f) Histogram of the AgNW orientation shown in (c) and (d). The insets in (e and f) are the HSB mapping images of the AgNWs. (g) Three positions of single AgNW in aqueous solution. (h) Arrangement process of AgNWs under assistance of compressed air. (i) Dense pack of AgNWs in aqueous evaporation. (j) Electrical resistance of random and aligned AgNW film. (k) Water contact angle on random and aligned AgNW film.

Figure 6.7 Evaporation process of the AgNW aqueous solution.

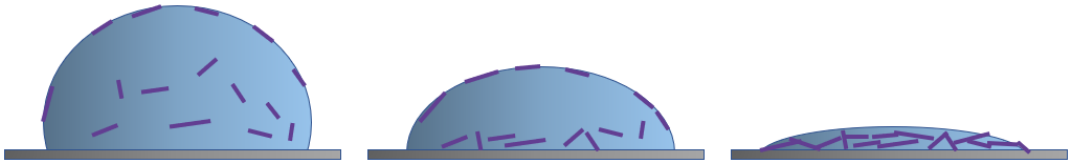

Figure 6.8 Formation of random AgNW film.

In constructing soft electronics, one of the most important steps is combining an elastomer matrix with conductive layer. In this project, we proposed to use 3D printing to transfer AgNW film into elastomer, replacing traditional transfer printing techniques. As one of the advantages of the method, various desirable patterns can be fabricated, rapidly.

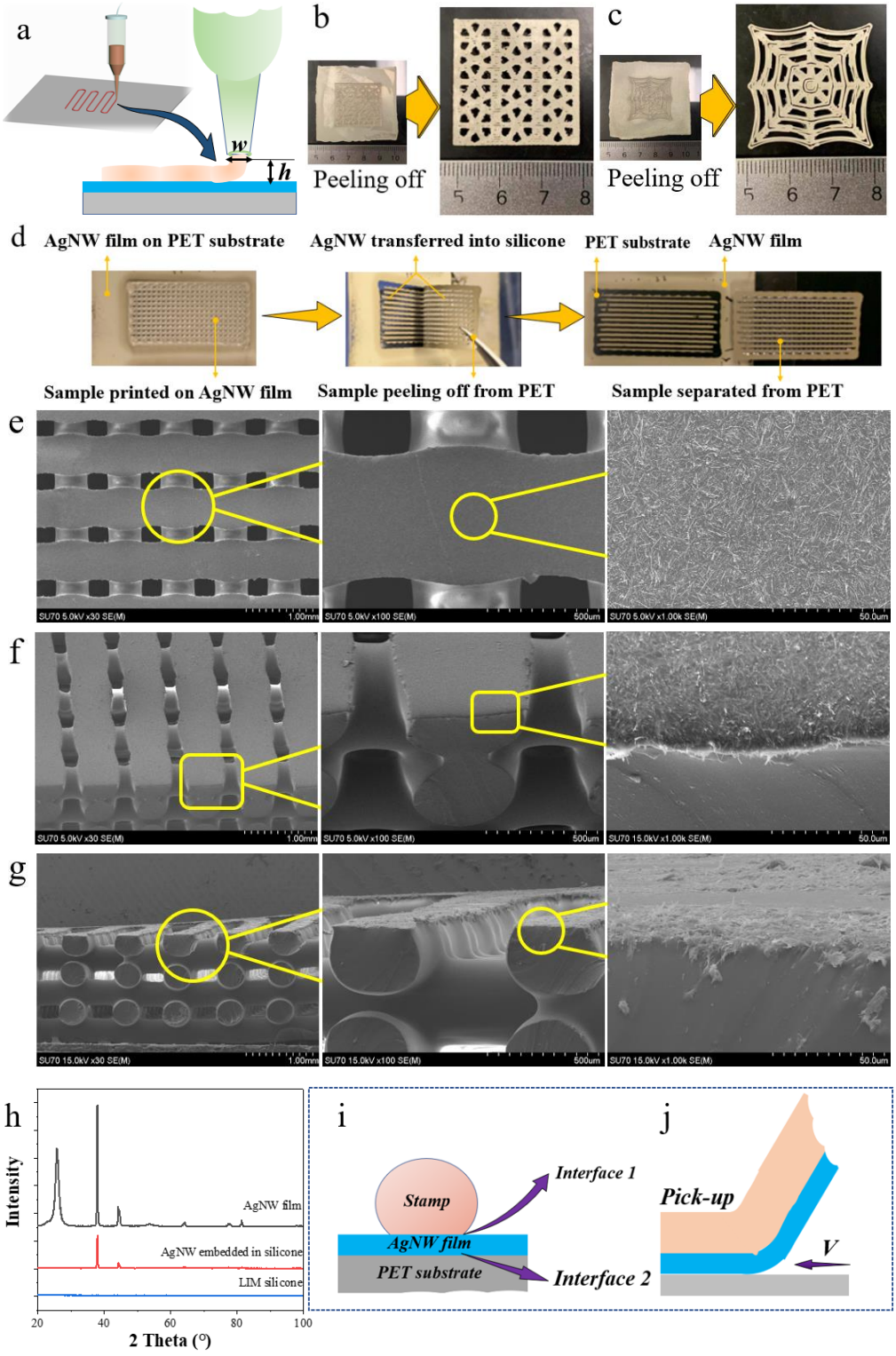

Figure 6.9 (a) Schematic illustration of printing desirable patterns on the AgNW film. (b)~(d) Peeling off the printed complex elastomer from the AgNW film. (e)~(g) Morphologies of AgNWs embedded in elastomer from top view, 45° tilting angle, and cross section. (h) XRD results of LIM silicone, AgNW film, and AgNW embedded into LIM silicone. (i) Illustration of the cross-section of the printed line. (j) Peeling

the printed sample from AgNW film.

Figure 6.9a depicts the printing process. The liquid LIM silicone was extruded on the surface of the prepared AgNW film. It is noted that printing parameters are closly related to enhance the quality of printed shapes. For instance, when the printing height is too small, the bottom lines became flat showing in Figure 6.10, which prevents forming an ideal shape.

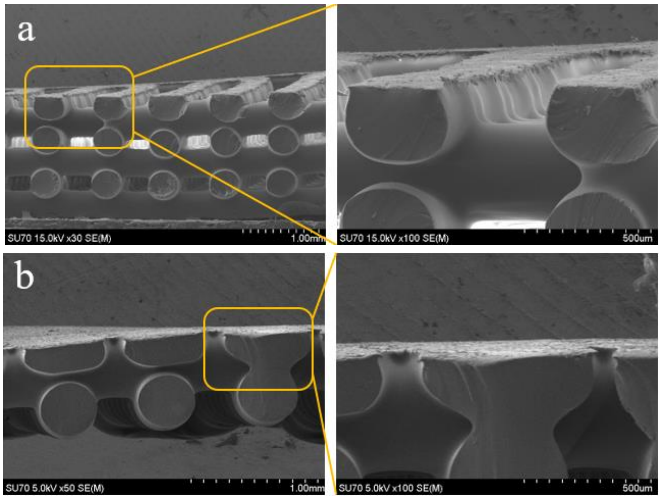

Figure 6.10 The different printing height produce different bottom line shapes.

The reason for above modification is that the limited space between nozzle tip and substrate cannot contain the polymer with the extruded volume. Thus, the silicone with excess volume is forced to move outward, which creates the deformation of line shape. By comparison, a series of printing parameters were adjusted for the best printing quality, comprising of 3.8 bar of extrusion pressure, 5 mm/s of printing speed, 0.2 s of pre-flow, 0 s of post-flow, and 320 μm of height, etc.

Based on the setting, we separately built the weave structure (Figure 6.9b), the spider web structure (Figure 6.9c), and the scaffolding structure (Figure 6.9d) on the AgNW film. A high precise molding of the 3D printing is reflected via these exquisite patterns. For another thing, AgNWs are transferred into the printed silicone followed by peeling process. We selected the scaffolding structure with $20 \times 10 \times 1$ mm volume as an example to show more details about the transfer process (Figure 6.9d). A visible color change appeared on the AgNW film and the bottom of the peeled silicone. The varying is undoubtedly credited to the fact that AgNWs were picked up as the

silicone was peeled. To acquire more evidence, we then observed the peeled silicone from top view, 45° tilting angle, and cross-section. The morphologies are recorded in Figure 6.9e~6.9g. They distinctly displays the bottom of the printed silicone structure sticking a dense AgNW layer with thickness of 10 μm. The transferred AgNW layer is not only intact, but also manifests uniform distribution.

In addition to above global and local morphologies, we also verify the AgNWs' transfer from the perspective of phase analysis. The X-ray diffraction (XRD) characterization results are summarized in Figure 6.9h, where the three lines separately reflect the outcome of the AgNW film, the LIM silicone, and the LIM silicone peeled from AgNW film. Among them, the LIM silicone, as an amorphous material, absolutely have no diffraction peaks. As for the AgNW film, there are seven peaks, and their positions occur at 2θ values of 25.9°, 38°, 44°, 53°, 64°, 77°, and 81.5°, which attributes to Ag crystals with the corresponding lattice planes of (210), (111), (200), (142), (220), (311), and (222), respectively. For the LIM silicone peeled from AgNW film, five XRD peaks were observed at 2θ of 38°, 44°, 64°, 77°, and 81.5°, which are considered as the characteristic peaks of silver element. Their lattice planes are (111), (200), (220), (311), and (222), respectively. The results further confirmed that AgNWs are transferred into the polymer substrate.

To better understand the transfer process, we drew the illustration of the cross-section of the printed line in Figure 6.9i. There are two interfaces in the system, including the LIM silicone/AgNW film interface (Interface 1) and the AgNW film/PET matrix interface (Interface 2). According to the classic printing transfer theory, the competing fracture between the interfaces determines whether the AgNW film can be transferred. When the interface 1 is stronger than the interface 2, such that the AgNW film can be picked up along with the peeling of the cured silicone, as displayed in Figure 6.9j. Inspired by the deduction, we employed a commercial tape to stick the AgNW film and the face of the AgNW embedded elastomer, respectively. As shown in Figure 6.11, many AgNWs were noticed to stuck on the tape. However, there were only a few AgNWs stripped from the AgNW embedded sample. The results partially confirmed that interface 1 is stronger than the interface 2, explaining the occurrence of the transfer.

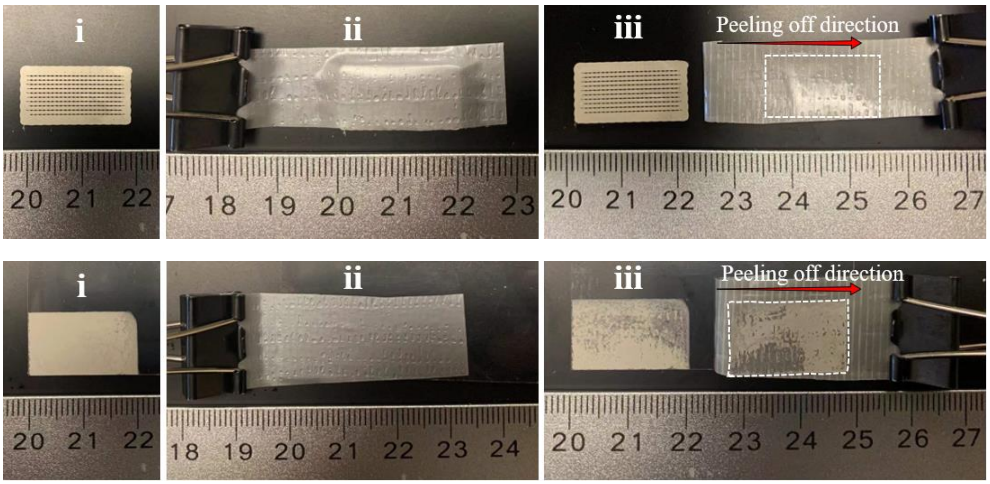

Figure 6.11 Commercial tape used to stick AgNW film with and without embedded into polymer

Furthermore, it is widely accepted that the peeling velocity is related to the transfer. Feng *et al.* reported a kinetically controlled transfer printing process, and established a standard rule to predict the transfer (Figure 6.12). It manifests that the transfer is possible to vanish when the peel velocity is less than the critical peeling velocity (V_c) in a certain situation. Considering the feature, we used fast, medium, and slow peel velocity around 1~10 mm/s, 0.1~1 mm/s, and 0.01~0.1 mm/s. The results all revealed that AgNWs can be encapsulated into the elastomer matrix. Therefore, we speculate that the transfer is attributed to the weak interface 2 in the transfer system, due to the limited range of modulation in adhesion strength.

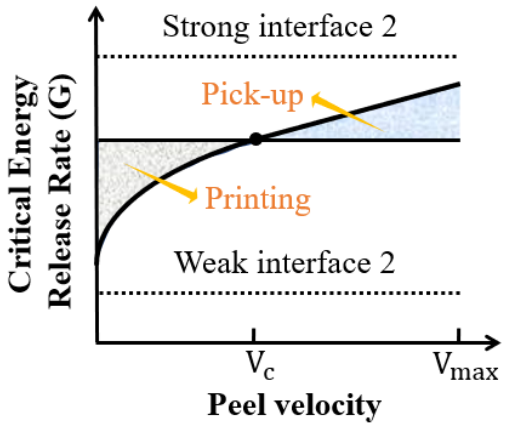

Figure 6.12 Criterion for kinetically controlled transfer printing.

After AgNWs are transferred into the silicone substrate in the 3D printing, we

investigated characteristics of the prepared sample, including mechanical property, electrical property, and anti-bacterial property.

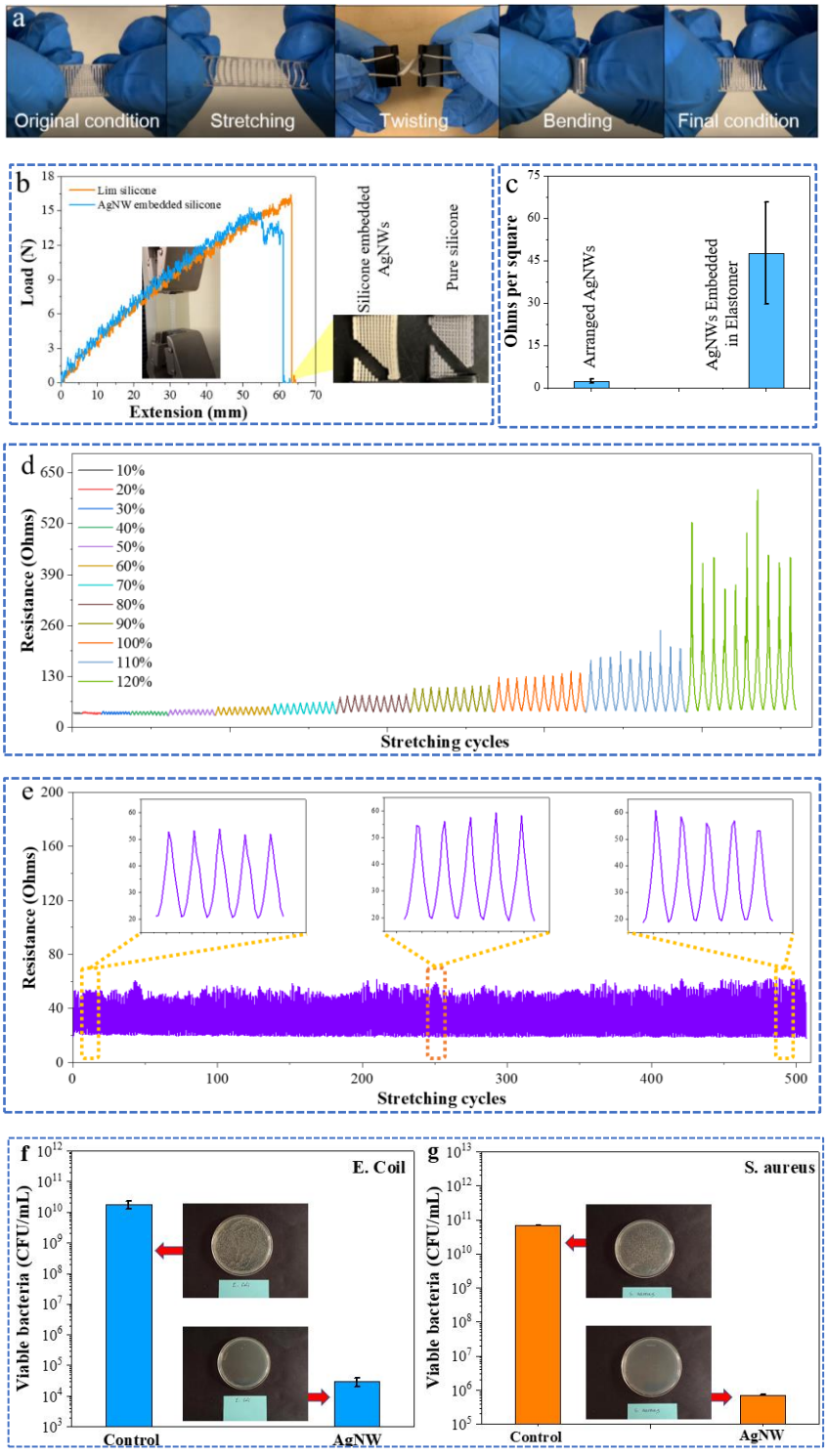

Figure 6.13 (a) Sample suffered to various deformation. (b) Mechanical stretching test of LIM silicone and AgNW embedded silicone. (c) Sheet resistance of the AgNW film and the AgNW embedded sample. (d) Resistance response under ten cycles of

increasing strains for the fabricated sample. (e) Resistance of the sample during 500 stretching/releasing cycles between 0% and 50% strain. Antibacterial activities of AgNW silicone film against (f) E. coli and (g) S. aureus.

Figure 6.13a exhibits the sample suffering from different deformation. Originally, the sample was gently held in human hands. We subsequently exerted twisting, stretching, and bending on the sample, and the conspicuous deformations can be captured. Finally, the external work was countermanded, and the deformed sample restored its original dimension. At this state, there were no obvious changes appearing on the sample. We further quantitatively characterized the mechanical properties by recording the stress-strain curves before and after AgNWs were transferred into LIM silicone. Both of the samples showed an ultra-stretchability as depicted in Figure 6.13b.

Additionally, the electrical performances of the samples were evaluated. We firstly measured the sheet resistance of the sample at zero strain (no stretching) by the 4-point probe method. To reduce the test error, three samples in each case and three different locations on each sample were selected. The results were summarized in Figure 6.13c, which exhibits that the average resistances of the AgNW film are about 2.305±0.7 Ω/sq and 47.613±18.106 Ω/sq before and after transferring into elastomer substrate. Namely, the sheet resistance and the standard deviation increased about 20.7~ and 25.9~times during the 3D printing transfer process. The changes are thought to be related with the encapsulation process. In details, part of AgNWs are wrapped by the silicone rubber under the assistance of the extrusion pressure and adhesion of liquid polymer in the extrusion-based 3D printing. The contact area of AgNWs decreased, as expressed in Figure 6.14. On the other hand, when the printed sample peeled off, the original AgNW conductive pathways were partially broken, which resulted in a local adjustment of AgNW networks. These factors are responsible for the changes of the sheet resistances.

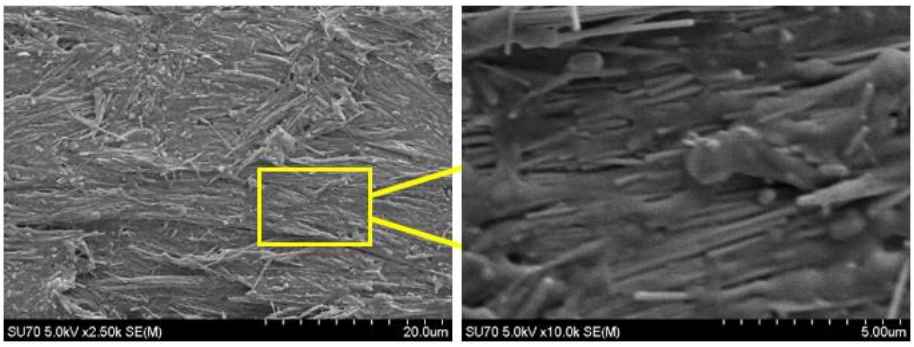

Figure 6.14 AgNWs transferred into polymer substrate.

Moreover, the electrical property of the polymer embedded with AgNWs during cyclic stretching is analyzed. In Figure 6.13c, we recorded the electrical resistances during ten cycles of stretching/releasing from 10% up to ~120% stretch deformation. There are three highlights. (1) The sample have a wide strain response range. Under multiple stretching/releasing cycles, the sample survives the strain up to 120% before electrical resistance become unstable. It means the formed sample has an excellent stretchability. For another thing, the embedded AgNWs remain conductive pathways even though under large deformation. (2) The valley resistance is stable in entire dynamic test. Specifically, in multiple stretching/releasing cycles with same elongation percent, the maximum standard deviation of the valley resistance is 1.2, appearing at 110% strains. As for the dynamic cycles with various stretching ratios, the valley resistance varies less than 2 Ω when tensile deformation< 70%. Notedly, the resistance before stretching is about 32 Ω. As stretching reaches 70%, the valley resistance suddenly increased by 16.65%. In subsequent stretching, the valley resistance fluctuates within 4 Ω. (3) The peak resistance reveals a smooth and monotonic relationship with the increase of elongation. The maximum resistance responses are 36.11 Ω, 51.76 Ω, and 442.33 Ω at strain of 10%, 60%, and 120%, respectively. Such characteristics are favored for stretchable strain sensors.

We further calculates the gauge factor to quantitatively evaluate the sensitivity when the fabricated sample was used as a sensor, according to Equation 5.1. The calculated results are depicted in Figure 6.15. The values display a slight upward trend from 10% to 80% strain. Next, the gauge factor promotes sharply from 1.731 to 7.587

as elongation surged from 90% to 120%. This varying indicates that the prepared sample has a stable electrical response to the limited external stretching and a high sensitivity to the large tensile deformation.

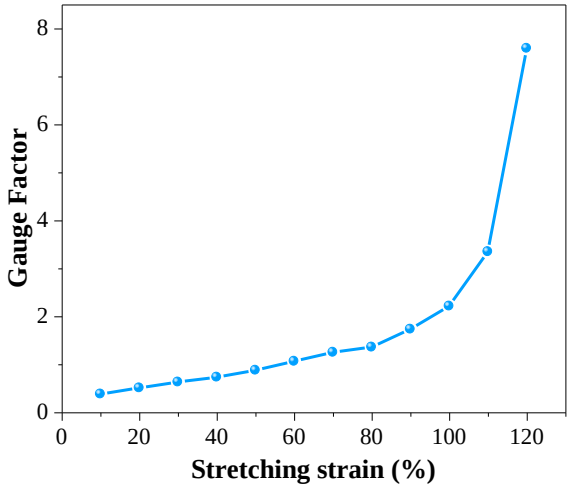

Figure 6.15 Gauge factor of the fabricated flexible sensor.

Apart from the strain magnitude, the electrical repeatability, as another crucial figure of merit, is captured to assess the long-term stability of constructed samples. Figure 6.13e displays the resistance response in 500 cycles of stretching/releasing, where the sample is strained up to 50% and then released back to its original position. The initial resistance is about 19 Ω, then increased to 53 Ω during the first stretching of 50% strain. It should be supplemented that the original resistance varies slightly between different samples, due to the diversity of the AgNW network and the adjustment in the transfer systems. The assumption can be proved by a large standard deviation in the 4-point probe test. When the sample returned to the zero strain, the valley resistance reaches 22.5 Ω, increased by 18.5% compared with the original value. The change is ascribed to the drastic adjustment of the position of AgNWs.

In subsequent stretching/releasing cycles, the resistance at zero strain no longer shows any obvious changes. The peak resistance, however, always presents some sparse fluctuations. The value changes are less than 20% in each fluctuation. To acquire more details, we separately magnified the resistance-strain curves at the initial, the intermediate, and the final stages of the stretching/releasing cycles, as shown in inset of Figure 6.13e. These three curves possess similar shapes, and valley resistance kept

constant at each stage. The peak resistance, however, occured a visible change. We reputed that the prepared sample has an outstanding electrical restore performance. Namely, the AgNW conductive pathway can retrieve its initial state after multiple stretching deformations. Also, a minor adjustment in AgNW network should be responsible for the resistance change at the maximum stretching. Compared with the reported flexible sensor, we believe that the sample with limited resistance varying in this manuscript is suitable as a sensor to detect external deformation.

To demonstrate the antibacterial effects of AgNW embedded silicone, it was tested against E. coli and S. aureues to represent Gram-negative and Gram-positive bacteria, respectively. Figure 6.13f and 6.13g show the significant antibacterial properties of AgNW films compared to LIM films as control groups. AgNW films reduced viable bacteria of both strains by more than four orders of magnitude after 24h of incubation indicating a broad-spectrum antibacterial activity.

Due to the large strain sensing range and high repeatability, the fabricated sample is possible to monitor full range of human activities. To confirm, the sample was conformally attached to an adult human body in different positions via commercial tape. We separately collected signals in response to periodic movement of finger (Figure 6.16a), wrist (Figure 6.16b), elbow (Figure 6.16c), and shoulder (Figure 6.16d). The results exhibited that the relative resistance smoothly changes as the bending angles continuously increase from 0° to 90°. Owing to differences in deformation degree, relative resistance are different. The values of the finger and wrist bending (≈ 3) are observed to be larger than that of the elbow and shoulder movement (≈ 0.5). Also, in 10 cycles of bending/releasing, the sample shows a good repeatability. The maximum resistances are similar, and the values resumed when the deformations returned to their original condition.

Additionally, the leg-press movements with various speeds were also monitored, displayed in Figure 6.16e. At the maximum amplitude of the motion, the relative resistances are about 4. Although the speed of movement varies, the electrical response approached, which indicates that our sample can accurately detect the movement with

different speeds. In Figure 6.16f, the sample was mounted on human knee to detect walking. When an adult tester naturally walks at the speed of 1.5 mm/s, the relative resistance real-time changes. The similar response peaks suggest that the sample can calculate human steps. It is noted that the slight deviations between multiple cycles are produced due to the movement difference.

Apart from above large deformation movement, some small deformation can be captured as well. As shown in Figure 6.16g, a sensor was fixed to a tester's forehead to detect the facial expression. When the monitored tester make a surprised expression, the mild facial muscle movement causes an electrical signal that the relative resistance drops to 0.6. While the sensor is attached to human neck (in Figure 6.16h), the nod with slight amplitude can trigger a fluctuation in electrical signals. The average relative resistance further drops by 0.2. We finally set the sensor to a tester's throat (in Figure 6.16i). As the tester swallow, a distinct electrical pattern can be grasped. The average electrical amplitude reduces to 0.23, which signifies that our sensor possesses a high sensitivity that can capture even slight movements.

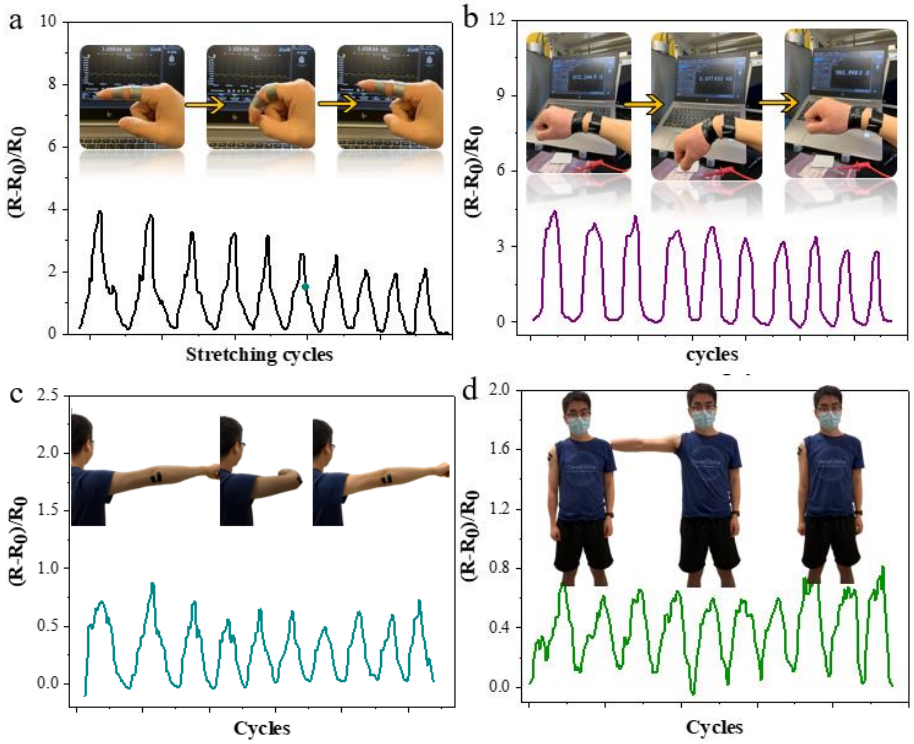

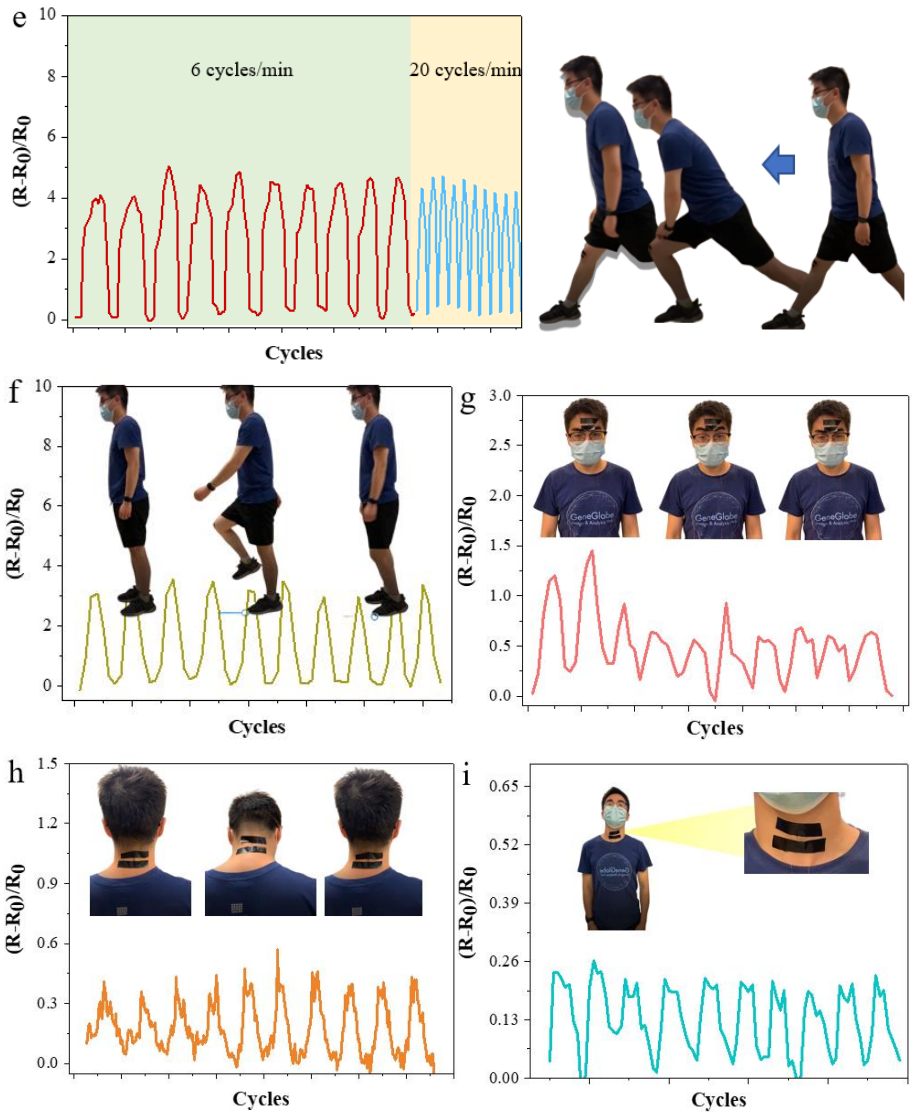

Figure 6.16 Resistance response to human body movement.

6.4 Conclusions

In this investigation, a facile and rational strategy is proposed to prepare stretchable and wearable sensors. There are two crucial steps including preparing densely arranged AgNWs on surface of aqueous droplet and transferring AgNW network into polymer matrix via 3D printing.

To obtain densely packed AgNWs, compressed air is used as an auxiliary means. It stimulates the vortexes inside of droplet, which accelerates the motion of AgNWs in an aqueous solution. When AgNWs reach the droplet surface, they are trapped under the function of the water surface tension. Meanwhile, compressed air facilitates the shear movement on the aqueous solution surface. Those AgNWs pinned on the droplet

surface moved along as well, and continuously packed at the droplet edge. With the extension of blowing time and movement of air brush, the AgNWs densely packed area increases till to the whole surface. In subsequent evaporation, the distance between AgNWs further decreased due to the reduction of the droplet surface area in evaporation. Finally, a close-packed AgNW network is formed.

3D printing is utilized to transfer the AgNW film into the polymer substrate. It not only simplifies the transfer process, but also achieves complex desirable patterns. The formed sample can tolerate more than 300%~strain. Also, we observe a wide electrical-strain response range from 10% to 120%, as well as high electrical response repeatability (>500 cycles of stretching/releasing). An excellent anti-bacterial property reveals the sample is suitable to be applied in wearable devices.

CHAPTER 7 Conclusions and Future Directions

7.1 Conclusions

The main purpose of this investigation is to employ 3D printing technology to fabricate soft electronics. 3D printing, as additive manufacturing, has some advantages compared to other methods in preparing soft electronics, including realizing rapid prototyping, constructing various complicated structures, controlling of real-time feedback, and others.

In this dissertation, I fully utilized the advantages of 3D printing technology. 3D wrinkled structures were fabricated by taking advantage of 3D printing and water-induced polymer swelling. The unique 3D wrinkled structures improve the electrical performance of the formed soft electronics. Additionally, 3D printing was employed to encapsulate the conductive layers into the polymer matrix. A strong adhesion between them was achieved. Meanwhile, different patterns can be acquired, which show great potentials to produce in a large scale.

7.1.1 Water-induced Polymer Swelling and Its Application in Soft Electronics

In this project, we introduced soluble powders, e.g., sugar and NaCl, into polymer matrix. As the polymer composites immersed in an aqueous solution, a conspicuous polymer swelling can be observed. We systematically investigated the swelling phenomenon, and recorded the volume swelling and water absorption with a long-term immersion. Based on the recording, we put forward that the interaction of osmotic pressure, contractile stress from polymer, and Laplace pressure trigger the swelling of polymer composite.

In addition, to obtain a controllable water-induced polymer swelling, we designed multiple comparison tests. First of all, 50 wt.% of sugar was doped into various types of commercial polymer substrate, such as Ecoflex $^{00\text{-}50}$ silicone, Ecoflex $^{00\text{-}30}$ silicone, Dragon skin 10 slow silicone, Sylgard 184 silicone, and Sylgard 186 silicone, etc. When these polymer composites were soaked in water under the same external conditions, different swelling ratios and speeds were noticed. For instance, the sylgard 186/sugar

composite exhibits the highest swelling ratio, while the sylgard 184/sugar composite possess the lowest swelling ratio in the same immersion time. The difference was credit to Young's modulus and viscosity of the polymer because these factors have an important effect on the additives dissolution and the contractile stress of polymer chain.

Secondly, the sugar concentration was studied as a factor to control the swelling of polymer composite. When the concentration of sugar increased from 10 wt.% to 30 wt.% and 50 wt.%, the swelling ratio of different sample appears an obvious divergence. With the increased of concentration of additives, the swelling ratio of polymer composite increases as well. The change is related to the different osmotic pressure induced by the sugar dissolved in the immersion process.

Thirdly, the thickness of polymer composites can regulate the swelling ratio. For example, when the thickness reduced from 2.25 mm to 1.5 mm and 0.75 mm, the volume swelling ratio of polymer composite drops from 698% to 533% and further to 351%, respectively. It is caused by the different contractile stress of the internal polymer composite.

Additionally, we investigated the influence of the soaking medium temperature on the polymer composite's swelling. It clearly shows that the swelling ratio increases as the temperature increased, which can be explained by the Stokes-Einstein equation. With the medium temperature increase, the diffusion rate is accelerated. Thus, the osmotic pressure increased in the same immersion condition.

Finally, the type of additives can regulate the polymer swelling. To confirm that, we added the 50 wt.% of sugar and NaCl into Eco-flex $^{00\text{-}50}$ silicone, separately. After a long-term continuous immersion, a conspicuous difference was grasped. The maximum volume swelling and water absorption of the NaCl/ Eco-flex $^{00\text{-}50}$ silicone composite are about 3000% and 2000%, respectively. However, the corresponding values for the sugar/ Eco-flex $^{00\text{-}50}$ silicone composite are 1500% and 800%.

By regulating the forementioned effect factors, we can obtain a swollen sample with desired dimensions in immersion process. In subsequent steps, different conductive layers were separately deposited on the swollen samples via in-situ growing

AgNPs in solution, sputtering Au through vapor deposition, depositing graphene in aqueous solution, and attaching AgNWs by surface modification, etc. Next, leveraging the mechanic mismatch, the wrinkle conductive structures can be formed as swollen samples shrink back to their original dimensions. The fabricated samples all manifest outstanding mechanical property, electrical sensitivity, large electrical response range, and high repeatability, etc. Considering these characteristics, the samples can detect human movements. The excellent outputs imply the formed samples can be adopted as stretchable and wearable sensors.

7.1.2 Encapsulating Conductive Material into Polymer via 3D Printing

In this study, 3D printing was utilized to encapsulate the organic/inorganic conductive layer into polymer substrate. There are some merits for our printing transfer when compared with conventional approaches, comprising of simplifying the transfer process, constructing various desirable patterns, and enhancing the adhesion between conductive materials and polymer matrix, etc.

In the project of transferring graphene layer into polymer matrix, we focused on the effect of patterns on the performance of samples. We constructed different structures to transfer the graphene layer into polymer substrate. The line structure with 0°, 45°, and 90°, and the honey comb structure were separately fabricated. Their mechanical and electrical properties were tested, and the results showed that the line structure with 0° has the highest elongation toleration (760%~ strain and 1.2 MPa~ stress), while the value for honey comb structure reduces to 430%~ strain and 0.7 MPa~ stress. Besides, the line structure with 90° possesses the highest gauge factor, whereas the lowest gauge factor was obtained from the line structure with 45°. Besides, all of these graphene embedded samples with different patterns display >400% elongation deformation, wide strain response ranges from 10% to 120%, high electrical response repeatability, etc. They reveal a great possibility to be utilized in wearable electronics for human movement monitoring and rehabilitation.

In another investigation, we transferred AgNWs into polymer matrix to form soft electronics. There are two highlights in the process, including preparing arranged

AgNWs and transferring AgNW network into polymer matrix via 3D printing. We used compressed air to obtain the assembled AgNWs on surface of an aqueous droplet. The compressed air stimulates the vortexes inside of droplets, accelerates the motion of AgNWs in aqueous droplet. As AgNWs reach the droplet surface, they are trapped with the assistance of the water surface tension. Besides, compressed air facilitates the shear movement on aqueous droplet surface. The AgNWs pinned on the droplet surface move along the shear movement, and continuously pack at the droplet edge. With the time extension and the air brush movement, the AgNWs densely packed area increases till to the whole surface. In subsequent evaporation, the distance between AgNWs further decrease due to the reduction of the droplet surface area. In this case, the assembly of AgNWs can be formed.

Also, 3D printing was employed to transfer the assembled AgNWs into polymer matrix. The classic printing transfer theory can be used to explain this procedure. By peeling the printed sample from the AgNW film, we noticed that the AgNWs can be successfully transferred into elastomer. The fabricated sample can tolerate more than 300%~strain. Also, we observed a wide electrical-strain response range from 10% to 120%, and a high electrical response repeatability (>500 cycles of stretching/releasing). An excellent anti-bacterial property reveals the sample is possible to be applied in wearable devices.

7.2 Future Works

Apart from soft electronics, 3D printing of the elastomer materials can be used to design and develop other functional devices with desirable properties. Combined with the preliminary experiments, we proposed some future research directions.

7.2.1 3D Printing of Antibacterial Polymer Devices

We hope to design drug-eluting polymer devices with a drug-loaded bulk and a drug-free coating. On the one hand, the fabricated sample can regulate the rate of drug release. On the other hand, various desirable structures can be printed in a facile process. Generally, the first step in the proposal is to introduce drug particles, S-nitroso-N-

acetylpenicillamine (SNAP), into the silicone matrix. The morphologies of drug particles were displayed in Figure 7.1a. The average size of the particles was counted by software of ImageJ, which is about 27.1 μm (Figure 7.1b).

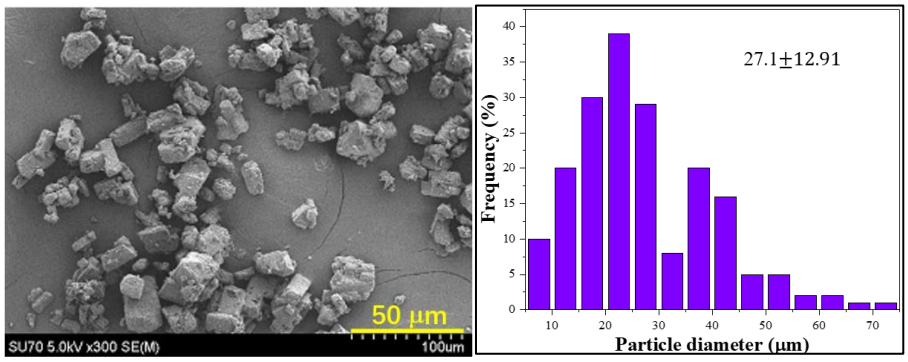

Figure 7.1 (a) SEM images of SNAP powders. (b) ImageJ counting results about SNAP powders.

Also, we selected Momentive silicone and PDMS as the ingredient of elastomer matrix in our preliminary experiment. By physically mixing drug and elastomer, the polymer composite became green color, as shown in Figure 7.2a. Also, the viscosity of polymer composite is almost same as before and after drug addition, which means the printing quality remained constant.

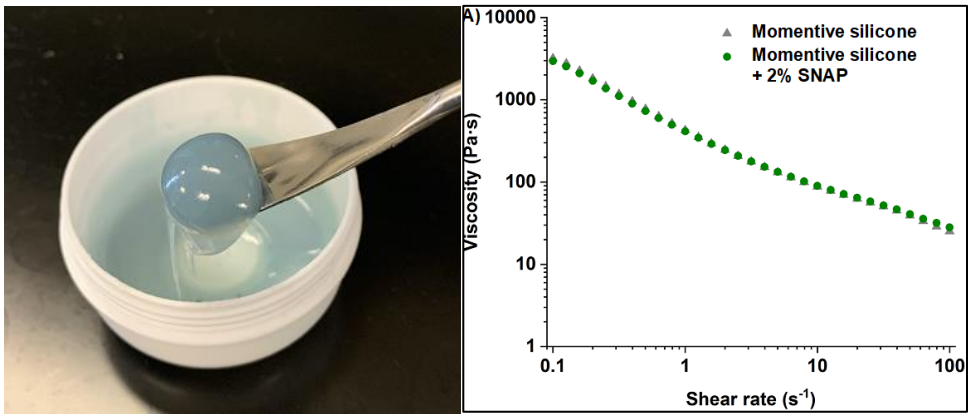

Figure 7.2 (a) Photo of the SNAP-silicone ink. (b) Shear viscosity for the Momentive silicone ink (without addition of tin catalyst) before and after loading of 2% SNAP.

We preliminary printed some SNAP-loaded silicone tubes, as displayed in Figure 7.3. The sample contained 2 wt.% SNAP powders. The high-viscosity Momentive silicone that can be extruded based on its shear-thinning property and quickly vulcanize upon exposure to ambient moisture is used as the base-ink for 3D printing. When water molecules are transported into the silicone matrix, the loaded drug particles

decomposed and released nitric oxide (NO) enabling antibacterial properties.

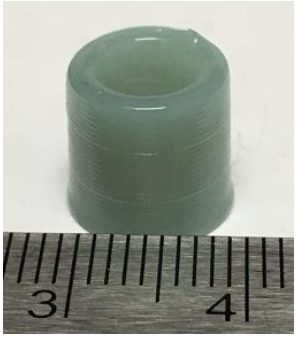

Figure 7.3 Photo of a 3D-printed SNAP-loaded silicone tube.

To minimize the drug release rate, we added polydimethylsiloxane, a low-viscosity silicone, into the printing system. The silicone diffused outwards upon deposition to form a drug-free outermost layer without compromising the integrity of the printed structures. The spontaneously formed drug-free coating dramatically reduces the surface roughness of the implantable devices (Figure 7.4) and serves as a protective layer to suppress the burst release of drugs.

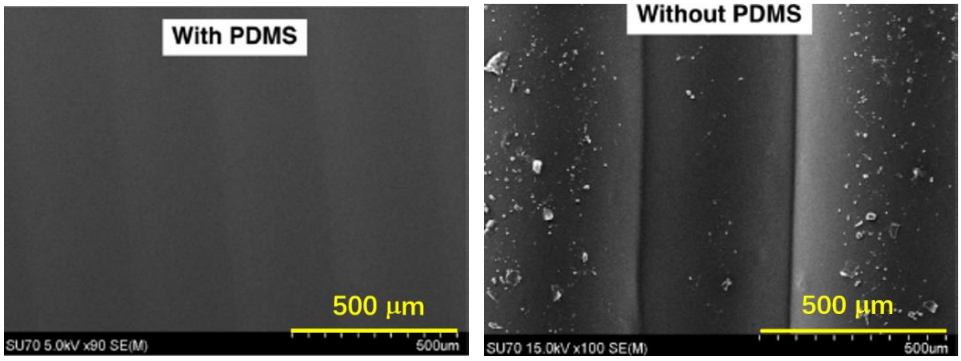

Figure 7.4 Surface morphology of the printed sample with and without PDMS.

The printed samples are valid to stabilize the release drug in several weeks or months, which offers an opportunity to produce the drug-loaded devices in a customized manner.

However, Momentive silicone is non-biocompatible and toxic to the cells, which is a disadvantage to biological and medical applications. In the case, we searched for a new addition of curing silicone (LIM 6050), a non-toxic polymer, to replace the Momentive silicone. We plan to develop a new ink formulation and printing process to fabricate a drug release device, especially to form a protective layer on the printed structures by utilizing the diffuse of PDMS in the ink components during printing

process. Due to different viscosity and Young's modulus, we suppose the drug release rate may change during immersion process. More details and performance will be investigated in the near future.

7.2.2 Fabricating Actuator via 3D Printing and Water-induced Polymer Swelling

It has been reported that 3D printing is possible to rapidly fabricate the actuator. The method has full freedom to form functional composite at a large resolution range of filament diameter. To now, researchers have developed various actuators. Based on the stimulation resource, they can be divided into the thermal-triggered actuator, light-responsive actuator, electric-responsive actuator, water-responsive actuator, magnetic-responsive actuator, etc. Among them, the water-responsive actuator was formed by the printed bilayer structure that can be programmed to change its morphology as time elapsed when immersed in water. The partial materials used in the preparation comprising of cellulose and hydrogel. Due to the forming of hydrogen bonds of hydroxyl groups, the water can be absorbed into hydrogel matrix, which results in a water-induced swelling. Meanwhile, the part without cellulose kept its original volume. Thus, the fabricated sample with multi-layers changes their morphing because of the swelling ratio mismatch at different part.

Inspired by above method, we want to utilize the water-induced polymer swelling (we stated in chapter 3) to replace conventional water-responsive hydrogel. In details, 3D printing can be employed to form a flower shape with multiple materials. The stamen of flower is printed with Momentive silicone that is hydrophobicity. Meanwhile, the petal of flower is formed with Momentive/sugar composite. In hypothesis, when the sample is soaked in aqueous solution, the petal of flower is able to appear swelling under the interaction of osmotic pressure and contract stress. At the same time, the stamen of flower maintains its original dimension. In this case, the composite structure can appear a swelling ratio mismatch, therefore a structural deformation can be triggered. Furthermore, it is possible to obtain a desirable morphing change via regulating the concentration of sugar, the immersion time, the temperature of aqueous solution, and the type of silicone.

References

(1) Luo, Z.; Li, X.; Li, Q.; Tian, X.; Fan, T.; Wang, C.; Wu, X.; Shen, G. In Situ Dynamic Manipulation of Graphene Strain Sensor with Drastically Sensing Performance Enhancement. *Advanced Electronic Materials*, 2000269.
(2) Liu, D.-S.; Ryu, H.; Khan, U.; Wu, C.; Jung, J.-H.; Wu, J.; Wang, Z.; Kim, S.-W. Piezoionic-powered graphene strain sensor based on solid polymer electrolyte. *Nano Energy* **2021,** *81*, 105610.
(3) Zhao, X.; Xu, L.; Chen, Q.; Peng, Q.; Yang, M.; Zhao, W.; Lin, Z.; Xu, F.; Li, Y.; He, X. Highly conductive multifunctional RGO/CNT hybrid sponge for electromagnetic wave shielding and strain sensor. *Advanced Materials Technologies* **2019,** *4* (9), 1900443.
(4) Jia, Y.; Yue, X.; Wang, Y.; Yan, C.; Zheng, G.; Dai, K.; Liu, C.; Shen, C. Multifunctional stretchable strain sensor based on polydopamine/ reduced graphene oxide/ electrospun thermoplastic polyurethane fibrous mats for human motion detection and environment monitoring. *Composites Part B: Engineering* **2020,** *183*, 107696.
(5) Qin, B.; Li, B.; Zhang, J.; Xie, X.; Li, W. Highly sensitive strain sensor based on stretchable sandwich-type composite of carbon nanotube and poly(styrene–butadiene–styrene). *Sensors and Actuators A: Physical* **2020,** *315*, 112357.
(6) Sun, X.; Qin, Z.; Ye, L.; Zhang, H.; Yu, Q.; Wu, X.; Li, J.; Yao, F. Carbon nanotubes reinforced hydrogel as flexible strain sensor with high stretchability and mechanically toughness. *Chemical Engineering Journal* **2020,** *382*, 122832.
(7) Han Min, S.; Asrulnizam, A. M.; Atsunori, M.; Mariatti, M. Properties of Stretchable and Flexible Strain Sensor Based on Silver/PDMS Nanocomposites. *Materials Today: Proceedings* **2019,** *17*, 616-622.
(8) Min, S.-H.; Lee, G.-Y.; Ahn, S.-H. Direct printing of highly sensitive, stretchable, and durable strain sensor based on silver nanoparticles/multi-walled carbon nanotubes composites. *Composites Part B: Engineering* **2019,** *161*, 395-401.
(9) Lu, Y.; Sun, H.; Cheng, J.; Myong, J.; Mehedi, H. M.; Bhat, G.; Yu, B. High performance flexible wearable strain sensor based on rGO and AgNWs decorated PBT melt-blown non-woven fabrics. *Sensors and Actuators A: Physical* **2020,** *315*, 112174.
(10) Neella, N.; Gaddam, V.; Rajanna, K.; Nayak, M. M.; Srinivas, T. In *Highly flexible and sensitive graphene-silver nanocomposite strain sensor*, 2015 IEEE SENSORS, 1-4 Nov. 2015; 2015; pp 1-4.
(11) Hong, S. K.; Yang, S.; Cho, S. J.; Jeon, H.; Lim, G. Development of a Waterproof Crack-Based Stretchable Strain Sensor Based on PDMS Shielding. *Sensors (Basel)* **2018,** *18* (4), 1171.
(12) Hempel, M.; Nezich, D.; Kong, J.; Hofmann, M. A novel class of strain gauges based on layered percolative films of 2D materials. *Nano letters* **2012,** *12* (11), 5714-5718.
(13) Zhang, M.; Wang, C.; Wang, Q.; Jian, M.; Zhang, Y. Sheath-Core Graphite/Silk Fiber Made by Dry-Meyer-Rod-Coating for Wearable Strain Sensors. *ACS applied materials & interfaces* **2016,** *8 32*, 20894-9.

(14) Marra, F.; Minutillo, S.; Tamburrano, A.; Sarto, M. S. Production and characterization of Graphene Nanoplatelet-based ink for smart textile strain sensors via screen printing technique. *Materials & Design* **2021,** *198*, 109306.
(15) Zou, Q.; Zheng, J.; Su, Q.; Wang, W.; Gao, W.; Ma, Z. A wave-inspired ultrastretchable strain sensor with predictable cracks. *Sens. Actuator A Phys.* **2019,** *300*, 111658.
(16) Donaldson, L. Wrinkles and folds could benefit flexible electronics. *Mater. Today* **2013,** *16* (9), 308.
(17) Tang, J.; Guo, H.; Zhao, M.; Yang, J.; Tsoukalas, D.; Zhang, B.; Liu, J.; Xue, C.; Zhang, W. Highly Stretchable Electrodes on Wrinkled Polydimethylsiloxane Substrates. *Sci. Rep.* **2015,** *5* (1), 16527.
(18) Yan, J.; Ma, Y.; Li, X.; Zhang, C.; Cao, M.; Chen, W.; Luo, S.; Zhu, M.; Gao, Y. Flexible and high-sensitivity piezoresistive sensor based on MXene composite with wrinkle structure. *Ceram. Int.* **2020,** *46* (15), 23592-23598.
(19) Yang, J.; Xu, Y.; Guo, Q.; Yin, F.; Yuan, W. Highly stretchable pressure sensors with wrinkled fibrous geometry for selective pressure sensing with minimal lateral strain-induced interference. *Compos. B. Eng.* **2021,** *217*, 108899.
(20) Lee, G.-B.; Sathi, S. G.; Kim, D.-Y.; Jeong, K.-U.; Nah, C. Wrinkled elastomers for the highly stretchable electrodes with excellent fatigue resistances. *Polym. Test.* **2016,** *53*, 329-337.
(21) Liu, C.; Cai, J.; Li, X.; Zhang, W.; Zhang, D. Flexible and tunable electromagnetic meta-atom based on silver nanowire networks. *Mater. Des.* **2019,** *181*, 107982.
(22) Chu, Z.; Jiao, W.; Li, J.; Guo, H.; Zheng, Y.; Wang, R.; He, X. A novel wrinkle-gradient strain sensor with anti-water interference and high sensing performance. *Chem. Eng. J.* **2021,** *421*, 129873.
(23) Sahoo, B. N.; Woo, J.; Algadi, H.; Lee, J.; Lee, T. Superhydrophobic, Transparent, and Stretchable 3D Hierarchical Wrinkled Film-Based Sensors for Wearable Applications. *Adv. Mater. Technol.* **2019,** *4* (10), 1900230.
(24) Chen, W.; Liu, L.-X.; Zhang, H.-B.; Yu, Z.-Z. Kirigami-Inspired Highly Stretchable, Conductive, and Hierarchical Ti3C2T x MXene Films for Efficient Electromagnetic Interference Shielding and Pressure Sensing. *ACS nano* **2021,** *15* (4), 7668-7681.
(25) Bae, J.-S.; Lee, Y.-S.; Li, J.; Liang, J.; Chen, D.; Pei, Q.; Lee, S.-B. The Feasibility of Healable Electronics and Mechanical Behavior of Silver Nanowire (AgNW)/Healable Polymer Composite. *Adv. Mater. Technol.* **2018,** *3* (6), 1700364.
(26) Gao, N.; Zhang, X.; Liao, S.; Jia, H.; Wang, Y. Polymer swelling induced conductive wrinkles for an ultrasensitive pressure sensor. *ACS Macro Lett.* **2016,** *5* (7), 823-827.
(27) Zhang, R.; Ying, C.; Gao, H.; Liu, Q.; Fu, X.; Hu, S. Highly flexible strain sensors based on polydimethylsiloxane/carbon nanotubes (CNTs) prepared by a swelling/permeating method and enhanced sensitivity by CNTs surface modification. *Composites Science and Technology* **2019,** *171*, 218-225.
(28) Yang, Y.; Duan, S.; Zhao, H. Highly Conductive Silicone Elastomers via Environment-Friendly Swelling and In Situ Synthesis of Silver Nanoparticles. *Adv.*

Mater. Interfaces **2021,** *8* (8), 2100137.
(29) Lee, K.-W.; Kim, Y.-H.; Du, W. X.; Kim, J.-Y. Stretchable and Low-Haze Ag-Nanowire-Network 2-D Films Embedded into a Cross-linked Polydimethylsiloxane Elastomer. *nanomaterials* **2019,** *9* (4), 576.
(30) Yun, H. J.; Kim, S. J.; Hwang, J. H.; Shim, Y. S.; Jung, S.-G.; Park, Y. W.; Ju, B.-K. Silver Nanowire-IZO-Conducting Polymer Hybrids for Flexible and Transparent Conductive Electrodes for Organic Light-Emitting Diodes. *Scientific Reports* **2016,** *6* (1), 34150.
(31) Chen, S.-P.; Liao, Y.-C. Highly stretchable and conductive silver nanowire thin films formed by soldering nanomesh junctions. *Physical Chemistry Chemical Physics* **2014,** *16* (37), 19856-19860.
(32) Jung, M. W.; Kang, S. M.; Nam, K.-H.; An, K.-S.; Ku, B.-C. Highly transparent and flexible NO2 gas sensor film based on MoS2/rGO composites using soft lithographic patterning. *Applied Surface Science* **2018,** *456*, 7-12.
(33) Jeong, H.; Noh, Y.; Ko, S. H.; Lee, D. Flexible resistive pressure sensor with silver nanowire networks embedded in polymer using natural formation of air gap. *Composites Science and Technology* **2019,** *174*, 50-57.
(34) Liu, Y.; Huang, J.; Ding, G.; Yang, Z. High-performance and wearable strain sensors based on graphene microfluidics and serpentine microchannels for human motion detection. *Microelectronic Engineering* **2020,** *231*, 111402.
(35) Tan, Y. J.; Godaba, H.; Chen, G.; Tan, S. T. M.; Wan, G.; Li, G.; Lee, P. M.; Cai, Y.; Li, S.; Shepherd, R. F.; Ho, J. S.; Tee, B. C. K. A transparent, self-healing and high-κ dielectric for low-field-emission stretchable optoelectronics. *Nat. Mater.* **2020,** *19* (2), 182-188.
(36) Yang, Y.; Song, Y.; Bo, X.; Min, J.; Pak, O. S.; Zhu, L.; Wang, M.; Tu, J.; Kogan, A.; Zhang, H.; Hsiai, T. K.; Li, Z.; Gao, W. A laser-engraved wearable sensor for sensitive detection of uric acid and tyrosine in sweat. *Nat. Biotechnol.* **2020,** *38* (2), 217-224.
(37) Song, E.; Li, J.; Won, S. M.; Bai, W.; Rogers, J. A. Materials for flexible bioelectronic systems as chronic neural interfaces. *Nat. Mater.* **2020,** *19* (6), 590-603.
(38) Sohn, H.; Park, C.; Oh, J.-M.; Kang, S. W.; Kim, M.-J. J. M. Silver nanowire networks: Mechano-electric properties and applications. *Materials* **2019,** *12* (16), 2526.
(39) Jung, J.; Cho, H.; Yuksel, R.; Kim, D.; Lee, H.; Kwon, J.; Lee, P.; Yeo, J.; Hong, S.; Unalan, H. E. Stretchable/flexible silver nanowire electrodes for energy device applications. *Nanoscale* **2019,** *11* (43), 20356-20378.
(40) Zhu, Q.-B.; Li, B.; Yang, D.-D.; Liu, C.; Feng, S.; Chen, M.-L.; Sun, Y.; Tian, Y.-N.; Su, X.; Wang, X.-M. A flexible ultrasensitive optoelectronic sensor array for neuromorphic vision systems. *Nat. Commun.* **2021,** *12* (1), 1-7.
(41) Ding, Y.; Cui, Y.; Liu, X.; Liu, G.; Shan, F. Welded silver nanowire networks as high-performance transparent conductive electrodes: Welding techniques and device applications. *Appl. Mater. Today* **2020,** *20*, 100634.
(42) Espinosa, N.; García-Valverde, R.; Urbina, A.; Krebs, F. C. A life cycle analysis of polymer solar cell modules prepared using roll-to-roll methods under ambient conditions. *Sol. Energy Mater Sol. Cells* **2011,** *95* (5), 1293-1302.

(43) Lee, J. C.; Min, J.; Jesuraj, P. J.; Hafeez, H.; Kim, D. H.; Lee, W. H.; Choi, D. K.; Cha, J. H.; Lee, C. M.; Song, M. Improved stability of silver nanowire (AgNW) electrode for high temperature applications using selective photoresist passivation. *Microelectron. Eng.* **2019,** *206*, 6-11.
(44) Mustonen, P.; Mackenzie, D.; Lipsanen, H. Review of fabrication methods of large-area transparent graphene electrodes for industry. *Front. Optoelectron.* **2020,** *13* (2), 91-113.
(45) Zhu, Y.; Deng, Y.; Yi, P.; Peng, L.; Lai, X.; Lin, Z. Flexible transparent electrodes based on silver nanowires: Material synthesis, fabrication, performance, and applications. *Adv. Mater. Technol.* **2019,** *4* (10), 1900413.
(46) Kwon, J.; Suh, Y. D.; Lee, J.; Lee, P.; Han, S.; Hong, S.; Yeo, J.; Lee, H.; Ko, S. H. Recent progress in silver nanowire based flexible/wearable optoelectronics. *J. Mater. Chem. C.* **2018,** *6* (28), 7445-7461.
(47) Huang, X.; Qi, X.; Boey, F.; Zhang, H. Graphene-based composites. *Chem. Soc. Rev.* **2012,** *41* (2), 666-686.
(48) Zaaba, N.; Foo, K.; Hashim, U.; Tan, S.; Liu, W.-W.; Voon, C. Synthesis of graphene oxide using modified hummers method: solvent influence. *Procedia Eng.* **2017,** *184*, 469-477.
(49) Wang, Y.; Chen, Z.; Mei, D.; Zhu, L.; Wang, S.; Fu, X. Highly sensitive and flexible tactile sensor with truncated pyramid-shaped porous graphene/silicone rubber composites for human motion detection. *J. Compos. Sci.* **2022,** *217*, 109078.
(50) Ousaleh, H. A.; Charti, I.; Sair, S.; Mansouri, S.; Abboud, Y.; Bouari, A. E. Green and low-cost approach for graphene oxide reduction using natural plant extracts. *Materials Today: Proceedings* **2020**.
(51) Wu, J.; Lin, Z.; Weng, X.; Owens, G.; Chen, Z. Removal mechanism of mitoxantrone by a green synthesized hybrid reduced graphene oxide@ iron nanoparticles. *Chemosphere* **2020,** *246*, 125700.
(52) Coleman, J. N.; Khan, U.; Blau, W. J.; Gun'ko, Y. K. Small but strong: a review of the mechanical properties of carbon nanotube–polymer composites. *Carbon* **2006,** *44* (9), 1624-1652.
(53) Kim, B.-J.; Park, J.-S. Applications of Carbon Nanotubes to Flexible Transparent Conductive Electrodes. In *Carbon Nanotubes-Recent Progress*; IntechOpen: 2017.
(54) Zhao, K.; Wang, J.; Kong, W.; Zhu, P. Facile Green synthesis and characterization of copper nanoparticles by aconitic acid for catalytic reduction of nitrophenols. *Journal of Environmental Chemical Engineering* **2019**, 103517.
(55) Chawla, P.; Kumar, N.; Bains, A.; Dhull, S. B.; Kumar, M.; Kaushik, R.; Punia, S. Gum arabic capped copper nanoparticles: Synthesis, characterization, and applications. *International Journal of Biological Macromolecules* **2020,** *146*, 232-242.
(56) Varghese, B.; Kurian, M.; Krishna, S.; Athira, T. Biochemical synthesis of copper nanoparticles using Zingiber officinalis and Curcuma longa: Characterization and antibacterial activity study. *Materials Today: Proceedings* **2020**.
(57) Singh, M.; Rana, S. Silver and copper nanowire films as cost-effective and robust transparent electrode in energy harvesting through photovoltaic: A review. *Materials Today Communications* **2020,** *24*, 101317.

(58) Ibrahim, N.; Akindoyo, J. O.; Mariatti, M. Recent Development in Silver-Based Ink for Flexible Electronics. *Journal of Science: Advanced Materials and Devices* **2021**.
(59) Zhang, L.; Song, T.; Shi, L.; Wen, N.; Wu, Z.; Sun, C.; Jiang, D.; Guo, Z. Recent progress for silver nanowires conducting film for flexible electronics. *Journal of nanostructure in chemistry* **2021**, 1-19.
(60) Zhou, H.; Song, Y. Fabrication of Silver Mesh/Grid and Its Applications in Electronics. *ACS Applied Materials & Interfaces* **2021,** *13* (3), 3493-3511.
(61) Vural, M.; Behrens, A. M.; Ayyub, O. B.; Ayoub, J. J.; Kofinas, P. Sprayable Elastic Conductors Based on Block Copolymer Silver Nanoparticle Composites. *ACS Nano* **2015,** *9* (1), 336-344.
(62) Zhang, S.; Hua, C.; He, B.; Chang, P.; Du, M.; Liu, Y. High-conductivity, stable Ag/cellulose paper prepared via in situ reduction of fractal-structured silver particles. *Carbohydrate Polymers* **2021,** *262*, 117923.
(63) Yang, Y.; Duan, S.; Zhao, H. Highly Conductive Silicone Elastomers via Environment-Friendly Swelling and In Situ Synthesis of Silver Nanoparticles. *Advanced Materials Interfaces* **2021,** *8* (9), 2100137.
(64) Lim, C.; Shin, Y.; Jung, J.; Kim, J. H.; Lee, S.; Kim, D.-H. Stretchable conductive nanocomposite based on alginate hydrogel and silver nanowires for wearable electronics. *APL Materials* **2018,** *7* (3), 031502.
(65) Yang, Y.; Xu, B.; Hou, J. Solution-Processed Silver Nanowire as Flexible Transparent Electrodes in Organic Solar Cells. *CHINESE JOURNAL OF CHEMISTRY* **2021,** *39* (8), 2315-2329.
(66) Hao, T.; Wang, S.; Xu, H.; Zhang, X.; Xue, J.; Liu, S.; Song, Y.; Li, Y.; Zhao, J. Stretchable electrochromic devices based on embedded WO3@AgNW Core-Shell nanowire elastic conductors. *Chemical Engineering Journal* **2021,** *426*, 130840.
(67) Mohammed Ali, M.; Maddipatla, D.; Narakathu, B. B.; Chlaihawi, A. A.; Emamian, S.; Janabi, F.; Bazuin, B. J.; Atashbar, M. Z. Printed strain sensor based on silver nanowire/silver flake composite on flexible and stretchable TPU substrate. *Sensors and Actuators A: Physical* **2018,** *274*, 109-115.
(68) Claypole, A.; Claypole, J.; Kilduff, L.; Gethin, D.; Claypole, T. Stretchable Carbon and Silver Inks for Wearable Applications. *Nanomaterials (Basel)* **2021,** *11* (5), 1200.
(69) Jiang, Y.; Liu, L.; Chen, L.; Zhang, Y.; He, Z.; Zhang, W.; Zhao, J.; Lu, D.; He, J.; Zhu, H.; Gong, Y.; Zheng, L. R.; Wang, Y.; Li, Z.; Qin, Y. Flexible and Stretchable Dry Active Electrodes With PDMS and Silver Flakes for Bio-Potentials Sensing Systems. *IEEE Sensors Journal* **2021,** *21* (10), 12255-12268.
(70) Jafry, A. T.; Lee, H.; Tenggara, A. P.; Lim, H.; Moon, Y.; Kim, S.-H.; Lee, Y.; Kim, S.-M.; Park, S.; Byun, D.; Lee, J. Double-sided electrohydrodynamic jet printing of two-dimensional electrode array in paper-based digital microfluidics. *Sensors and Actuators B: Chemical* **2019,** *282*, 831-837.
(71) Kant, T.; Shrivas, K.; Ganesan, V.; Mahipal, Y. K.; Devi, R.; Deb, M. K.; Shankar, R. Flexible printed paper electrode with silver nano-ink for electrochemical applications. *Microchemical Journal* **2020,** *155*, 104687.
(72) Kim, K.; Jung, M.; Kim, B.; Kim, J.; Shin, K.; Kwon, O.-S.; Jeon, S. Low-voltage, high-sensitivity and high-reliability bimodal sensor array with fully inkjet-printed

flexible conducting electrode for low power consumption electronic skin. *Nano Energy* **2017,** *41*, 301-307.
(73) Htwe, Y.; Chow, W.; Suriati, G.; Thant, A.; Mariatti, M. Properties enhancement of graphene and chemical reduction silver nanoparticles conductive inks printed on polyvinyl alcohol (PVA) substrate. *Synthetic Metals* **2019,** *256*, 116120.
(74) Baccarin, M.; Ciciliati, M. A.; Oliveira, O. N.; Cavalheiro, E. T. G.; Raymundo-Pereira, P. A. Pen sensor made with silver nanoparticles decorating graphite-polyurethane electrodes to detect bisphenol-A in tap and river water samples. *Materials Science and Engineering: C* **2020,** *114*, 110989.
(75) Kolya, H.; Kuila, T.; Kim, N. H.; Lee, J. H. Bioinspired silver nanoparticles/reduced graphene oxide nanocomposites for catalytic reduction of 4-nitrophenol, organic dyes and act as energy storage electrode material. *Composites Part B: Engineering* **2019,** *173*, 106924.
(76) Zhao, F.; Zhou, M.; Wang, L.; Huang, Z.; Chu, Y. One-step voltammetric deposition of l-proline assisted silver nanoparticles modified glassy carbon electrode for electrochemical detection of hydrogen peroxide. *Journal of Electroanalytical Chemistry* **2019,** *833*, 205-212.
(77) AlAqad, K. M.; Abulkibash, A. M.; Al Hamouz, O. C. S.; Saleh, T. A. Silver nanoparticles decorated graphene modified Carbon paste electrode for molecular methimazole determination. *Chemical Data Collections* **2017,** *11*, 168-182.
(78) Huang, J.; Zhao, M.; Hao, Y.; Li, D.; Feng, J.; Huang, F.; Wei, Q. Flexible, Stretchable, and Multifunctional Electrospun Polyurethane Mats with 0D-1D-2D Ternary Nanocomposite-Based Conductive Networks. *Advanced Electronic Materials* **2021,** *7* (1), 2000840.
(79) Fekry, A. M.; Abdel-Gawad, S. A.; Tammam, R. H.; Zayed, M. A. An electrochemical sensor for creatinine based on carbon nanotubes/folic acid /silver nanoparticles modified electrode. *Measurement* **2020,** *163*, 107958.
(80) Kim, Y.; Zhu, J.; Yeom, B.; Di Prima, M.; Su, X.; Kim, J.-G.; Yoo, S. J.; Uher, C.; Kotov, N. A. Stretchable nanoparticle conductors with self-organized conductive pathways. *Nature* **2013,** *500* (7460), 59-63.
(81) Ashkarran, A.; Ahadian, M.; Nezhad, M. H. Stability, size and optical properties of colloidal silver nanoparticles prepared by electrical arc discharge in water. *The European Physical Journal Applied Physics* **2009,** *48* (1), 10601.
(82) Rashed, H. H. Silver nanoparticles prepared by electrical arc discharge method in DIW. *Engineering and Technology Journal* **2016,** *34* (2 Part (B) Scientific), 295-301.
(83) Zhang, H.; Zou, G.; Liu, L.; Tong, H.; Li, Y.; Bai, H.; Wu, A. Synthesis of silver nanoparticles using large-area arc discharge and its application in electronic packaging. *Journal of Materials Science* **2017,** *52* (6), 3375-3387.
(84) Kshirsagar, P.; Sangaru, S. S.; Malvindi, M. A.; Martiradonna, L.; Cingolani, R.; Pompa, P. P. Synthesis of highly stable silver nanoparticles by photoreduction and their size fractionation by phase transfer method. *Colloids and Surfaces A: Physicochemical and Engineering Aspects* **2011,** *392* (1), 264-270.
(85) Liu, H.; Ge, Q.; Xu, F.; Qu, X.; Fu, H.; Sun, J. Dissolved black carbon induces fast photo-reduction of silver ions under simulated sunlight. *Science of The Total*

Environment **2021,** *775*, 145897.
(86) Khan, Z.; Al-Thabaiti, S. A.; Obaid, A. Y.; Al-Youbi, A. O. Preparation and characterization of silver nanoparticles by chemical reduction method. *Colloids and Surfaces B: Biointerfaces* **2011,** *82* (2), 513-517.
(87) Liu, J.; Li, X.; Zeng, X. Silver nanoparticles prepared by chemical reduction-protection method, and their application in electrically conductive silver nanopaste. *Journal of Alloys and Compounds* **2010,** *494* (1), 84-87.
(88) Lee, B.; Koo, S. Preparation of silver nanoparticles on the surface of fine magnetite particles by a chemical reduction. *Journal of Industrial and Engineering Chemistry* **2011,** *17* (4), 762-766.
(89) Lokman, M. Q.; Rusdi, M. F. M.; Rosol, A. H. A.; Ahmad, F.; Shafie, S.; Yahaya, H.; Rosnan, R. M.; Rahman, M. A. A.; Harun, S. W. Synthesis of silver nanoparticles using chemical reduction techniques for Q-switcher at 1.5 μm region. *Optik* **2021,** *244*, 167621.
(90) Wang, H.; Qiao, X.; Chen, J.; Ding, S. Preparation of silver nanoparticles by chemical reduction method. *Colloids and Surfaces A: Physicochemical and Engineering Aspects* **2005,** *256* (2), 111-115.
(91) Guzmán, M. G.; Dille, J.; Godet, S. Synthesis of silver nanoparticles by chemical reduction method and their antibacterial activity. *International Journal of Materials and Metallurgical Engineering* **2008,** *2* (7), 91-98.
(92) Cañamares, M. V.; Garcia-Ramos, J. V.; Gómez-Varga, J. D.; Domingo, C.; Sanchez-Cortes, S. Comparative Study of the Morphology, Aggregation, Adherence to Glass, and Surface-Enhanced Raman Scattering Activity of Silver Nanoparticles Prepared by Chemical Reduction of Ag+ Using Citrate and Hydroxylamine. *Langmuir* **2005,** *21* (18), 8546-8553.
(93) Sharma, V. K.; Yngard, R. A.; Lin, Y. Silver nanoparticles: green synthesis and their antimicrobial activities. *Advances in colloid and interface science* **2009,** *145* (1-2), 83-96.
(94) Nayak, S. P.; Ramamurthy, S. S.; Kumar, J. K. K. Green synthesis of silver nanoparticles decorated reduced graphene oxide nanocomposite as an electrocatalytic platform for the simultaneous detection of dopamine and uric acid. *Materials Chemistry and Physics* **2020**, 123302.
(95) Zhao, X.; Xu, W.; Yi, W.; Peng, Y. A flexible and highly pressure-sensitive PDMS sponge based on silver nanoparticles decorated reduced graphene oxide composite. *Sensors and Actuators A: Physical* **2019,** *291*, 23-31.
(96) Naqvi, T. K.; Srivastava, A. K.; Kulkarni, M. M.; Siddiqui, A. M.; Dwivedi, P. K. Silver nanoparticles decorated reduced graphene oxide (rGO) SERS sensor for multiple analytes. *Applied Surface Science* **2019,** *478*, 887-895.
(97) Fu, C.; Yan, C.; Ren, L.; Zeng, X.; Du, G.; Sun, R.; Xu, J.; Wong, C.-P. Improving thermal conductivity through welding boron nitride nanosheets onto silver nanowires via silver nanoparticles. *Composites Science and Technology* **2019,** *177*, 118-126.
(98) Barmpakos, D.; Tsamis, C.; Kaltsas, G. Multi-parameter paper sensor fabricated by inkjet-printed silver nanoparticle ink and PEDOT: PSS. *Microelectronic Engineering* **2020,** *225*, 111266.

(99) Wang, Z.; Liu, Y.; Zhang, D.; Gao, C.; Wu, Y. Mussel-inspired self-healing PDMS/AgNPs conductive elastomer with tunable mechanical properties and efficient antibacterial performances for wearable sensor. *Composites Part B: Engineering* **2021,** *224*, 109213.
(100) Liao, S.; Zhang, Y.; Pan, X.; Zhu, F.; Jiang, C.; Liu, Q.; Cheng, Z.; Dai, G.; Wu, G.; Wang, L. Antibacterial activity and mechanism of silver nanoparticles against multidrug-resistant Pseudomonas aeruginosa. *International journal of nanomedicine* **2019,** *14*, 1469.
(101) Fan, M.; Si, J.; Xu, X.; Chen, L.; Chen, J.; Yang, C.; Zhu, J.; Wu, L.; Tian, J.; Chen, X.; Mou, X.; Cai, X. A versatile chitosan nanogel capable of generating AgNPs in-situ and long-acting slow-release of Ag+ for highly efficient antibacterial. *Carbohydrate Polymers* **2021,** *257*, 117636.
(102) Araki, T.; Jiu, J.; Nogi, M.; Koga, H.; Nagao, S.; Sugahara, T.; Suganuma, K. Low haze transparent electrodes and highly conducting air dried films with ultra-long silver nanowires synthesized by one-step polyol method. *Nano Research* **2014,** *7* (2), 236-245.
(103) Gebeyehu, M. B.; Chala, T. F.; Chang, S.-Y.; Wu, C.-M.; Lee, J.-Y. Synthesis and highly effective purification of silver nanowires to enhance transmittance at low sheet resistance with simple polyol and scalable selective precipitation method. *RSC advances* **2017,** *7* (26), 16139-16148.
(104) Zhao, T.; Sun, R.; Yu, S.; Zhang, Z.; Zhou, L.; Huang, H.; Du, R. Size-controlled preparation of silver nanoparticles by a modified polyol method. *Colloids and Surfaces A: Physicochemical and Engineering Aspects* **2010,** *366* (1-3), 197-202.
(105) Darmanin, T.; Nativo, P.; Gilliland, D.; Ceccone, G.; Pascual, C.; De Berardis, B.; Guittard, F.; Rossi, F. Microwave-assisted synthesis of silver nanoprisms/nanoplates using a “modified polyol process”. *Colloids and Surfaces A: Physicochemical and Engineering Aspects* **2012,** *395*, 145-151.
(106) Castro, K. B.; Cooper, J. B. Single-pot two-temperature synthesis of high aspect ratio silver nanowires with narrow size distribution. *Inorganica Chimica Acta* **2020,** *507*, 119569.
(107) Lee, H. S.; Kim, Y. W.; Kim, J. E.; Yoon, S. W.; Kim, T. Y.; Noh, J.-S.; Suh, K. S. Synthesis of dimension-controlled silver nanowires for highly conductive and transparent nanowire films. *Acta Materialia* **2015,** *83*, 84-90.
(108) Hemmati, S.; Harris, M. T.; Barkey, D. P. Polyol Silver Nanowire Synthesis and the Outlook for a Green Process. *Journal of Nanomaterials* **2020,** *2020*, 9341983.
(109) Sonntag, L.; Eichler, F.; Weiß, N.; Bormann, L.; Ghosh, D. S.; Sonntag, J. M.; Jordan, R.; Gaponik, N.; Leo, K.; Eychmüller, A. Influence of the average molar mass of poly(N-vinylpyrrolidone) on the dimensions and conductivity of silver nanowires. *Physical Chemistry Chemical Physics* **2019,** *21* (18), 9036-9043.
(110) Madeira, A.; Papanastasiou, D. T.; Toupance, T.; Servant, L.; Tréguer-Delapierre, M.; Bellet, D.; Goldthorpe. Rapid synthesis of ultra-long silver nanowires for high performance transparent electrodes. *Nanoscale Advances* **2020,** *2* (9), 3804-3808.
(111) Shin, J. W.; Lim, H.-R.; Cho, H.-B.; Kwon, Y.-T.; Choa, Y.-H. Segregation-controlled self-assembly of silver nanowire networks using a template-free solution-

based process. *Nanoscale* **2021,** *13* (18), 8442-8451.
(112) Wang, X. M.; Chen, L.; Sowade, E.; Rodriguez, R. D.; Sheremet, E.; Yu, C. M.; Baumann, R. R.; Chen, J. J. Ultra-Uniform and Very Thin Ag Nanowires Synthesized via the Synergy of Cl(-), Br(-) and Fe(3+) for Transparent Conductive Films. *Nanomaterials (Basel)* **2020,** *10* (2).
(113) Choi, H.-J.; Kang, B.-C.; Ha, T.-J. Self-reconfigurable high-weight-per-volume-gelatin films for all-solution-processed on-skin electronics with ultra-conformal contact. *Biosensors and Bioelectronics* **2021,** *184*, 113231.
(114) Lu, L.; Chen, X.; Qiao, F.; Rui, Y.; Gu, D.; Yu, H.; Hou, J.; Chen, F.; Liu, F.; Yang, Y. High stable bifacial irradiated triple-mesoporous perovskite solar cells based on AgNWs@PEDOT composite electrodes. *Materials Letters* **2021,** *288*, 129348.
(115) Han, J.; Yang, J.; Gao, W.; Bai, H. J. A. F. M. Ice-Templated, Large-Area Silver Nanowire Pattern for Flexible Transparent Electrode. **2021,** *31* (16), 2010155.
(116) Ma, C.; Liu, Y.-F.; Bi, Y.-G.; Zhang, X.-L.; Yin, D.; Feng, J.; Sun, H.-B. Recent progress in post treatment of silver nanowire electrodes for optoelectronic device applications. *Nanoscale* **2021,** *13* (29), 12423-12437.
(117) Mazur, M. Electrochemically prepared silver nanoflakes and nanowires. *Electrochemistry Communications* **2004,** *6* (4), 400-403.
(118) Zhang, Y.; Zhu, P.; Li, G.; Cui, Z.; Cui, C.; Zhang, K.; Gao, J.; Chen, X.; Zhang, G.; Sun, R. PVP-Mediated Galvanic Replacement Synthesis of Smart Elliptic Cu–Ag Nanoflakes for Electrically Conductive Pastes. *ACS applied materials & interfaces* **2019,** *11* (8), 8382-8390.
(119) Kaviya, S.; Santhanalakshmi, J.; Viswanathan, B. Biosynthesis of silver nano-flakes by Crossandra infundibuliformis leaf extract. *Materials Letters* **2012,** *67* (1), 64-66.
(120) Matsuhisa, N.; Kaltenbrunner, M.; Yokota, T.; Jinno, H.; Kuribara, K.; Sekitani, T.; Someya, T. Printable elastic conductors with a high conductivity for electronic textile applications. *Nature communications* **2015,** *6* (1), 1-11.
(121) Lei, Z.; Chen, Z.; Zhou, Y.; Liu, Y.; Xu, J.; Wang, D.; Shen, Y.; Feng, W.; Zhang, Z.; Chen, H. Novel electrically conductive composite filaments based on Ag/saturated polyester/polyvinyl butyral for 3D-printing circuits. *Composites Science and Technology* **2019,** *180*, 44-50.
(122) Yoon, I. S.; Oh, Y.; Kim, S. H.; Choi, J.; Hwang, Y.; Park, C. H.; Ju, B. K. 3D Printing of Self-Wiring Conductive Ink with High Stretchability and Stackability for Customized Wearable Devices. *Advanced Materials Technologies* **2019,** *4* (9), n/a-n/a.
(123) Lee, C.-J.; Jung, K.-H.; Min, K. D.; Park, B.-G.; Jung, S.-B. Fabrication and characterization of Ag flake hybrid circuits with IPL-sintering. *Journal of Materials Science & Technology* **2020**.
(124) Ding, S.; Jiang, Z.; Chen, F.; Fu, L.; Lv, Y.; Qian, Y.; Zhao, S. Intrinsically Stretchable, Transient Conductors from a Composite Material of Ag Flakes and Gelatin Hydrogel. *ACS Applied Materials & Interfaces* **2020,** *12* (24), 27572-27577.
(125) Hilal, M.; Han, J. I. Improving the conductivity of PEDOT:PSS to nearly 1 million S/m with graphene on an ITO-glass substrate. *Synthetic Metals* **2018,** *245*, 276-285.

(126) Aleksandrova, M.; Kurtev, N.; Videkov, V.; Tzanova, S.; Schintke, S. Material alternative to ITO for transparent conductive electrode in flexible display and photovoltaic devices. *Microelectronic Engineering* **2015,** *145*, 112-116.
(127) Wang, X.; Zhi, L.; Müllen, K. Transparent, conductive graphene electrodes for dye-sensitized solar cells. *Nano letters* **2008,** *8* (1), 323-327.
(128) Wu, J.; Becerril, H. A.; Bao, Z.; Liu, Z.; Chen, Y.; Peumans, P. Organic solar cells with solution-processed graphene transparent electrodes. *Applied physics letters* **2008,** *92* (26), 237.
(129) Qiu, T.; Luo, B.; Liang, M.; Ning, J.; Wang, B.; Li, X.; Zhi, L. Hydrogen reduced graphene oxide/metal grid hybrid film: towards high performance transparent conductive electrode for flexible electrochromic devices. *Carbon* **2015,** *81*, 232-238.
(130) Wan, C.; Jiao, Y.; Li, J. Flexible, highly conductive, and free-standing reduced graphene oxide/polypyrrole/cellulose hybrid papers for supercapacitor electrodes. *Journal of Materials Chemistry A* **2017,** *5* (8), 3819-3831.
(131) Wiggins-Camacho, J. D.; Stevenson, K. J. Effect of Nitrogen Concentration on Capacitance, Density of States, Electronic Conductivity, and Morphology of N-Doped Carbon Nanotube Electrodes. *The Journal of Physical Chemistry C* **2009,** *113* (44), 19082-19090.
(132) Jang, S.; Seo, Y.; Choi, J.; Kim, T.; Cho, J.; Kim, S.; Kim, D. Sintering of inkjet printed copper nanoparticles for flexible electronics. *Scripta Materialia* **2010,** *62* (5), 258-261.
(133) Hashimi, A. S.; Ginting, R. T.; Chin, S. X.; Lau, K. S.; Nohan, M. A. N. M.; Zakaria, S.; Yap, C. C.; Chia, C. H. Fast microwave-assisted synthesis of copper nanowires as reusable high-performance transparent conductive electrode. *Current Applied Physics* **2020,** *20* (1), 205-211.
(134) Ahn, B. Y.; Lorang, D. J.; Lewis, J. A. Transparent conductive grids via direct writing of silver nanoparticle inks. *Nanoscale* **2011,** *3* (7), 2700-2702.
(135) Yoon, S.; Kim, H.-K. Cost-effective stretchable Ag nanoparticles electrodes fabrication by screen printing for wearable strain sensors. *Surface and Coatings Technology* **2020,** *384*, 125308.
(136) Shinde, M. A.; Lee, D.-J.; Kim, B.-J.; Kim, H. Highly conductive and smooth surfaced flexible transparent conductive electrode based on silver nanowires. *Thin Solid Films* **2019,** *685*, 366-371.
(137) Shinde, M. A.; Mallikarjuna, K.; Noh, J.; Kim, H. Highly stable silver nanowires based bilayered flexible transparent conductive electrode. *Thin Solid Films* **2018,** *660*, 447-454.
(138) Singh, M.; Prasher, P.; Kim, J. Solution processed silver-nanowire/zinc oxide based transparent conductive electrode for efficient photovoltaic performance. *Nano-Structures & Nano-Objects* **2018,** *16*, 151-155.
(139) Jon, S.; Sin, G.; Kim, G.; Jong, G.; Ri, J. Flexible perovskite solar cells based on AgNW/ATO composite transparent electrodes. *Synthetic Metals* **2020,** *262*, 116286.
(140) Singh, S. B.; Kshetri, T.; Singh, T. I.; Kim, N. H.; Lee, J. H. Embedded PEDOT:PSS/AgNFs network flexible transparent electrode for solid-state supercapacitor. *Chemical Engineering Journal* **2019,** *359*, 197-207.

(141) Hu, X.; Wang, S.; Zhang, H.; Wang, Y.; Hang, C.; Wen, J.; Tian, Y. Silver flake/polyaniline composite ink for electrohydrodynamic printing of flexible heaters. *Journal of Materials Science: Materials in Electronics* **2021,** *32* (23), 27373-27383.
(142) Zhu, C.; Guan, X.; Wang, X.; Li, Y.; Chalmers, E.; Liu, X. Mussel-Inspired Flexible, Durable, and Conductive Fibers Manufacturing for Finger-Monitoring Sensors. *Advanced Materials Interfaces* **2019,** *6* (1), 1801547.
(143) Amba Sankar, K. N.; Mohanta, K. Preparation of Highly Conductive Yarns by an Optimized Impregnation Process. *Journal of Electronic Materials* **2018,** *47* (3), 1970-1978.
(144) Lu, Y.; Jiang, J.; Yoon, S.; Kim, K.-S.; Kim, J.-H.; Park, S.; Kim, S.-H.; Piao, L. High-performance stretchable conductive composite fibers from surface-modified silver nanowires and thermoplastic polyurethane by wet spinning. *ACS applied materials & interfaces* **2018,** *10* (2), 2093-2104.
(145) Shin, Y.-E.; Cho, J. Y.; Yeom, J.; Ko, H.; Han, J. T. Electronic Textiles Based on Highly Conducting Poly(vinyl alcohol)/Carbon Nanotube/Silver Nanobelt Hybrid Fibers. *ACS Applied Materials & Interfaces* **2021,** *13* (26), 31051-31058.
(146) Chen, Y.; Deng, Z.; Ouyang, R.; Zheng, R.; Jiang, Z.; Bai, H.; Xue, H. 3D printed stretchable smart fibers and textiles for self-powered e-skin. *Nano Energy* **2021,** *84*, 105866.
(147) Kim, C.-L.; Lee, J.-J.; Oh, Y.-J.; Kim, D.-E. Smart wearable heaters with high durability, flexibility, water-repellent and shape memory characteristics. *Composites Science and Technology* **2017,** *152*, 173-180.
(148) Shi, B.; Wang, T.; Shi, L.; Li, J.; Wang, R.; Sun, J. Highly stretchable and strain sensitive fibers based on braid-like structure and sliver nanowires. *Applied Materials Today* **2020,** *19*, 100610.
(149) Lu, Y.; Sun, H.; Cheng, J.; Myong, J.; Mehedi, H. M.; Bhat, G.; Yu, B. High Performance Flexible Wearable Strain Sensor based on rGO and AgNWs decorated PBT Melt-blown non-woven Fabrics. *Sensors and Actuators A: Physical* **2020**, 112174.
(150) Gong, W.; Hou, C.; Guo, Y.; Zhou, J.; Mu, J.; Li, Y.; Zhang, Q.; Wang, H. A wearable, fibroid, self-powered active kinematic sensor based on stretchable sheath-core structural triboelectric fibers. *Nano Energy* **2017,** *39*, 673-683.
(151) Han, J. T.; Choi, S.; Jang, J. I.; Seol, S. K.; Woo, J. S.; Jeong, H. J.; Jeong, S. Y.; Baeg, K.-J.; Lee, G.-W. Rearrangement of 1D Conducting Nanomaterials towards Highly Electrically Conducting Nanocomposite Fibres for Electronic Textiles. *Scientific Reports* **2015,** *5* (1), 9300.
(152) Granero, A. J.; Wagner, P.; Wagner, K.; Razal, J. M.; Wallace, G. G.; in het Panhuis, M. Highly Stretchable Conducting SIBS-P3HT Fibers. *Advanced Functional Materials* **2011,** *21* (5), 955-962.
(153) He, Y.; Du, E.; Zhou, X.; Zhou, J.; He, Y.; Ye, Y.; Wang, J.; Tang, B.; Wang, X. Wet-spinning of fluorescent fibers based on gold nanoclusters-loaded alginate for sensing of heavy metal ions and anti-counterfeiting. *Spectrochimica Acta Part A: Molecular and Biomolecular Spectroscopy* **2020,** *230*, 118031.
(154) Yang, Z.; Jia, Y.; Niu, Y.; Zhang, Y.; Zhang, C.; Li, P.; Zhu, M.; Li, Q. One-step wet-spinning assembly of twisting-structured graphene/carbon nanotube fiber

supercapacitor. *Journal of Energy Chemistry* **2020**.
(155) Yang, H.-S.; Kim, Y.-M.; Choi, H.; Jang, J.; Youk, J. H.; Lee, B.-S.; Yu, W.-R. Electrochemical wet-spinning process for fabricating strong PAN fibers via an in situ induced plasticizing effect. *Polymer* **2020**, 122641.
(156) Tian, G.; Zhou, J.; Xin, Y.; Tao, R.; Jin, G.; Lubineau, G. Copolymer-enabled stretchable conductive polymer fibers. *Polymer* **2019,** *177*, 189-195.
(157) Lee, S.; Shin, S.; Lee, S.; Seo, J.; Lee, J.; Son, S.; Cho, H. J.; Algadi, H.; Al-Sayari, S.; Kim, D. E. Ag nanowire reinforced highly stretchable conductive fibers for wearable electronics. *Advanced Functional Materials* **2015,** *25* (21), 3114-3121.
(158) Wang, J.; Huang, S.; Lu, X.; Xu, Z.; Zhao, Y.; Li, J.; Wang, X. Wet-spinning of highly conductive nanocellulose–silver fibers. *Journal of Materials Chemistry C* **2017,** *5* (37), 9673-9679.
(159) Yang, Z.; Dou, F.; Yu, T.; Song, M.; Shi, H.; Yao, X.; Xu, L.-Y.; He, J.-H.; Cao, J.; Zhang, L. On the cross-section of shaped fibers in the dry spinning process: Physical explanation by the geometric potential theory. *Results in Physics* **2019,** *14*, 102347.
(160) Zhao, Y.; Dong, D.; Gong, S.; Brassart, L.; Wang, Y.; An, T.; Cheng, W. A Moss-Inspired Electroless Gold-Coating Strategy Toward Stretchable Fiber Conductors by Dry Spinning. *Advanced Electronic Materials* **2019,** *5* (1), 1800462.
(161) Yan, W.; Dong, C.; Xiang, Y.; Jiang, S.; Leber, A.; Loke, G.; Xu, W.; Hou, C.; Zhou, S.; Chen, M.; Hu, R.; Shum, P. P.; Wei, L.; Jia, X.; Sorin, F.; Tao, X.; Tao, G. Thermally drawn advanced functional fibers: New frontier of flexible electronics. *Materials Today* **2020,** *35*, 168-194.
(162) Zhang, Q.; Cai, J.; Gao, Q. Simulation and experimental study on thermal deep drawing of carbon fiber woven composites. *Journal of Materials Processing Technology* **2014,** *214* (4), 802-810.
(163) Qu, Y.; Nguyen-Dang, T.; Page, A. G.; Yan, W.; Das Gupta, T.; Rotaru, G. M.; Rossi, R. M.; Favrod, V. D.; Bartolomei, N.; Sorin, F. Superelastic multimaterial electronic and photonic fibers and devices via thermal drawing. *Advanced Materials* **2018,** *30* (27), 1707251.
(164) Ko, E.-H.; Kim, H.-J.; Lee, S.-M.; Kim, T.-W.; Kim, H.-K. Stretchable Ag electrodes with mechanically tunable optical transmittance on wavy-patterned PDMS substrates. *Scientific reports* **2017,** *7*, 46739.
(165) Zhao, Y.; Dong, D.; Wang, Y.; Gong, S.; An, T.; Yap, L. W.; Cheng, W. Highly Stretchable Fiber-Shaped Supercapacitors Based on Ultrathin Gold Nanowires with Double-Helix Winding Design. *ACS Applied Materials & Interfaces* **2018,** *10* (49), 42612-42620.
(166) Lu, C.; Park, S.; Richner, T. J.; Derry, A.; Brown, I.; Hou, C.; Rao, S.; Kang, J.; Moritz, C. T.; Fink, Y.; Anikeeva, P. Flexible and stretchable nanowire-coated fibers for optoelectronic probing of spinal cord circuits. *Science Advances* **2017,** *3* (3), e1600955.
(167) Hu, D.; Xu, X.; Miao, J.; Gidron, O.; Meng, H. A Stretchable Alternating Current Electroluminescent Fiber. *Materials* **2018,** *11* (2).
(168) Lian, Y.; Yu, H.; Wang, M.; Yang, X.; Li, Z.; Yang, F.; Wang, Y.; Tai, H.; Liao, Y.; Wu, J. A multifunctional wearable E-textile via integrated nanowire-coated fabrics. *Journal of Materials Chemistry C* **2020**.

(169) Pu, J.-H.; Zhao, X.; Zha, X.-J.; Bai, L.; Ke, K.; Bao, R.-Y.; Liu, Z.-Y.; Yang, M.-B.; Yang, W. Multilayer structured AgNW/WPU-MXene fiber strain sensors with ultrahigh sensitivity and a wide operating range for wearable monitoring and healthcare. *Journal of Materials Chemistry A* **2019,** *7* (26), 15913-15923.
(170) Zhu, G.-J.; Ren, P.-G.; Guo, H.; Jin, Y.-L.; Yan, D.-X.; Li, Z.-M. Highly Sensitive and Stretchable Polyurethane Fiber Strain Sensors with Embedded Silver Nanowires. *ACS Applied Materials & Interfaces* **2019,** *11* (26), 23649-23658.
(171) Sun, T.; Xiu, F.; Zhou, Z.; Ban, C.; Ye, T.; Ding, Y.; Liu, J.; Huang, W. Transient fiber-shaped flexible electronics comprising dissolvable polymer composites toward multicolor lighting. *Journal of Materials Chemistry C* **2019,** *7* (6), 1472-1476.
(172) Huang, W.-R.; He, Z.; Wang, J.-L.; Liu, J.-W.; Yu, S.-H. Mass Production of Nanowire-Nylon Flexible Transparent Smart Windows for PM2.5 Capture. *iScience* **2019,** *12*, 333-341.
(173) Cheng, Y.; Wang, R.; Sun, J.; Gao, L. Highly Conductive and Ultrastretchable Electric Circuits from Covered Yarns and Silver Nanowires. *ACS Nano* **2015,** *9* (4), 3887-3895.
(174) Chatterjee, K.; Tabor, J.; Ghosh, T. K. Electrically conductive coatings for fiber-based e-textiles. *Fibers* **2019,** *7* (6), 51.
(175) Hwang, C.; Song, W.-J.; Han, J.-G.; Bae, S.; Song, G.; Choi, N.-S.; Park, S.; Song, H.-K. Batteries: Foldable Electrode Architectures Based on Silver-Nanowire-Wound or Carbon-Nanotube-Webbed Micrometer-Scale Fibers of Polyethylene Terephthalate Mats for Flexible Lithium-Ion Batteries (Adv. Mater. 7/2018). *Advanced Materials* **2018,** *30* (7), 1870042.
(176) Compton, B. G.; Lewis, J. A. 3D-Printing of Lightweight Cellular Composites. *Advanced Materials* **2014,** *26* (34), 5930-5935.
(177) Xiong, W.; Liu, H.; Chen, Y.; Zheng, M.; Zhao, Y.; Kong, X.; Wang, Y.; Zhang, X.; Kong, X.; Wang, P. Highly Conductive, Air-Stable Silver Nanowire@ Iongel Composite Films toward Flexible Transparent Electrodes. *Advanced Materials* **2016,** *28* (33), 7167-7172.
(178) Wang, Y.; Yang, X.; Du, D.; Zhao, Y.; Zhang, X. New Insights into Flexible Transparent Conductive Silver Nanowires Films. *Int J Mol Sci* **2019,** *20* (11), 2803.
(179) Chen, Y.; Carmichael, R. S.; Carmichael, T. B. Patterned, Flexible, and Stretchable Silver Nanowire/Polymer Composite Films as Transparent Conductive Electrodes. *ACS Applied Materials & Interfaces* **2019,** *11* (34), 31210-31219.
(180) Oh, J. S.; Oh, J. S.; Yeom, G. Y. Invisible silver nanomesh skin electrode via mechanical press welding. *Nanomaterials* **2020,** *10* (4), 633.
(181) Wang, G.; Xu, W.; Xu, F.; Shen, W.; Song, W. AgNW/Chinese Xuan paper film heaters for electro-thermochromic paper display. *Materials Research Express* **2017,** *4* (11), 116405.
(182) Guo, X.; Liu, X.; Luo, J.; Gan, Z.; Meng, Z.; Zhang, N. Silver nanowire/polyimide composite transparent electrodes for reliable flexible polymer solar cells operating at high and ultra-low temperature. *RSC Advances* **2015,** *5* (32), 24953-24959.
(183) Zhao, C.; Xing, L.; Xiang, J.; Cui, L.; Jiao, J.; Sai, H.; Li, Z.; Li, F. Formation of

uniform reduced graphene oxide films on modified PET substrates using drop-casting method. *Particuology* **2014,** *17*, 66-73.
(184) Zhang, Z.; Si, T. Controllable assembly of silver nanoparticles based on the coffee-ring effect for high-sensitivity flexible strain gauges. *Sensors and Actuators A: Physical* **2017,** *264*, 188-194.
(185) Fox, D. W.; Schropp, A. A.; Joseph, T.; Azim, N.; Li Sip, Y. Y.; Zhai, L. Uniform Deposition of Silver Nanowires and Graphene Oxide by Superhydrophilicity for Transparent Conductive Films. *ACS Applied Nano Materials* **2021,** *4* (8), 7628-7639.
(186) Eslamian, M.; Zabihi, F. Ultrasonic Substrate Vibration-Assisted Drop Casting (SVADC) for the Fabrication of Photovoltaic Solar Cell Arrays and Thin-Film Devices. *Nanoscale Research Letters* **2015,** *10* (1), 462.
(187) Chen, Y.; Lan, W.; Wang, J.; Zhu, R.; Yang, Z.; Ding, D.; Tang, G.; Wang, K.; Su, Q.; Xie, E. Highly flexible, transparent, conductive and antibacterial films made of spin-coated silver nanowires and a protective ZnO layer. *Physica E: Low-dimensional Systems and Nanostructures* **2016,** *76*, 88-94.
(188) Guo, X.; Guo, C. W.; Wang, C.; Li, C.; Sun, X. M. AlGaInP LED with low-speed spin-coating silver nanowires as transparent conductive layer. *Nanoscale Research Letters* **2014,** *9* (1), 670.
(189) Li, W.; Zhang, H.; Shi, S.; Xu, J.; Qin, X.; He, Q.; Yang, K.; Dai, W.; Liu, G.; Zhou, Q. Recent progress in silver nanowire networks for flexible organic electronics. *Journal of Materials Chemistry C* **2020,** *8* (14), 4636-4674.
(190) Zhang, S.; Liu, X.; Lin, T.; He, P. A method to fabricate uniform silver nanowires transparent electrode using Meyer rod coating and dynamic heating. *Journal of Materials Science: Materials in Electronics* **2019,** *30* (20), 18702-18709.
(191) Xu, W.; Xu, Q.; Huang, Q.; Tan, R.; Shen, W.; Song, W. Fabrication of Flexible Transparent Conductive Films with Silver Nanowire by Vacuum Filtration and PET Mold Transfer. *Journal of Materials Science & Technology* **2016,** *32* (2), 158-161.
(192) Zhang, F.; Hu, J.; Zhao, P.; He, P.; Mi, H.-Y.; Guo, Z.; Liu, C.; Shen, C. Multifunctional electromagnetic interference shielding films comprised of multilayered thermoplastic polyurethane membrane and silver nanowire. *Composites Part A: Applied Science and Manufacturing* **2021,** *147*, 106472.
(193) Yang, S.; Wang, Y.-Y.; Song, Y.-N.; Jia, L.-C.; Zhong, G.-J.; Xu, L.; Yan, D.-X.; Lei, J.; Li, Z.-M. Ultrathin, flexible and sandwich-structured PHBV/silver nanowire films for high-efficiency electromagnetic interference shielding. *Journal of Materials Chemistry C* **2021,** *9* (9), 3307-3315.
(194) Kim, T.; Canlier, A.; Kim, G. H.; Choi, J.; Park, M.; Han, S. M. Electrostatic Spray Deposition of Highly Transparent Silver Nanowire Electrode on Flexible Substrate. *ACS Applied Materials & Interfaces* **2013,** *5* (3), 788-794.
(195) Selzer, F.; Weiß, N.; Kneppe, D.; Bormann, L.; Sachse, C.; Gaponik, N.; Eychmüller, A.; Leo, K.; Müller-Meskamp, L. A spray-coating process for highly conductive silver nanowire networks as the transparent top-electrode for small molecule organic photovoltaics. *Nanoscale* **2015,** *7* (6), 2777-2783.
(196) Shin, K.; Park, J. S.; Han, J. H.; Choi, Y.; Chung, D. S.; Kim, S. H. Patterned transparent electrode with a continuous distribution of silver nanowires produced by an

etching-free patterning method. *Scientific Reports* **2017,** *7* (1), 40087.
(197) Pan, C. T.; Yang, T. L.; Wang, S. Y.; Yen, C. K.; Ju, S. P.; Hung, C. W.; Shiue, Y. L. Study on optical films with AgNWs using UV laser patterning. *Optical Materials* **2018,** *77*, 55-66.
(198) Cho, E.-H.; Hwang, J.; Kim, J.; Lee, J.; Kwak, C.; Lee, C. S. Low-visibility patterning of transparent conductive silver-nanowire films. *Opt. Express* **2015,** *23* (20), 26095-26103.
(199) Yoo, B.; Kim, Y.; Han, C. J.; Oh, M. S.; Kim, J.-W. Recyclable patterning of silver nanowire percolated network for fabrication of flexible transparent electrode. *Applied Surface Science* **2018,** *429*, 151-157.
(200) Um, D.-S.; Lee, Y.; Kim, T.; Lim, S.; Lee, H.; Ha, M.; Khan, Z.; Kang, S.; Kim, M. P.; Kim, J. Y.; Ko, H. High-Resolution Filtration Patterning of Silver Nanowire Electrodes for Flexible and Transparent Optoelectronic Devices. *ACS Applied Materials & Interfaces* **2020,** *12* (28), 32154-32162.
(201) Zheng, M.; Chen, Y.; Liu, Z.; Liu, Y.; Wang, Y.; Liu, P.; Liu, Q.; Bi, K.; Shu, Z.; Zhang, Y.; Duan, H. Kirigami-inspired multiscale patterning of metallic structures via predefined nanotrench templates. *Microsystems & Nanoengineering* **2019,** *5* (1), 54.
(202) Lee, H.; Park, H., Fractal geometry microelectrodes and uses thereof. Google Patents: 2019.
(203) Won, P.; Park, J. J.; Lee, T.; Ha, I.; Han, S.; Choi, M.; Lee, J.; Hong, S.; Cho, K.-J.; Ko, S. H. Stretchable and Transparent Kirigami Conductor of Nanowire Percolation Network for Electronic Skin Applications. *Nano Letters* **2019,** *19* (9), 6087-6096.
(204) Chou, N.; Kim, Y.; Kim, S. A Method to Pattern Silver Nanowires Directly on Wafer-Scale PDMS Substrate and Its Applications. *ACS Applied Materials & Interfaces* **2016,** *8* (9), 6269-6276.
(205) Hassan, G.; Bae, J.; Lee, C. H. Ink-jet printed transparent and flexible electrodes based on silver nanoparticles. *Journal of Materials Science: Materials in Electronics* **2018,** *29* (1), 49-55.
(206) Finn, D. J.; Lotya, M.; Coleman, J. N. Inkjet Printing of Silver Nanowire Networks. *ACS Applied Materials & Interfaces* **2015,** *7* (17), 9254-9261.
(207) Huang, Q.; Al-Milaji, K. N.; Zhao, H. Inkjet printing of silver nanowires for stretchable heaters. *ACS Applied Nano Materials* **2018,** *1* (9), 4528-4536.
(208) Yang, S. M.; Lee, Y. S.; Jang, Y.; Byun, D.; Choa, S.-H. Electromechanical reliability of a flexible metal-grid transparent electrode prepared by electrohydrodynamic (EHD) jet printing. *Microelectronics Reliability* **2016,** *65*, 151-159.
(209) Li, X.; Park, H.; Lee, M. H.; Hwang, B.; Kim, S. H.; Lim, S. High resolution patterning of Ag nanowire flexible transparent electrode via electrohydrodynamic jet printing of acrylic polymer-silicate nanoparticle composite overcoating layer. *Organic Electronics* **2018,** *62*, 400-406.
(210) Laurent, P.; Stoukatch, S.; Dupont, F.; Kraft, M. Electrical characterization of Aerosol Jet Printing (AJP) deposited conductive silver tracks on organic materials. *Microelectronic Engineering* **2018,** *197*, 67-75.
(211) Tu, L.; Yuan, S.; Zhang, H.; Wang, P.; Cui, X.; Wang, J.; Zhan, Y.-Q.; Zheng, L.-

R. Aerosol jet printed silver nanowire transparent electrode for flexible electronic application. *Journal of Applied Physics* **2018,** *123* (17), 174905.
(212) Hu, D.; Zhu, W.; Peng, Y.; Shen, S.; Deng, Y. Flexible carbon nanotube-enriched silver electrode films with high electrical conductivity and reliability prepared by facile screen printing. *Journal of Materials Science & Technology* **2017,** *33* (10), 1113-1119.
(213) Chlaihawi, A. A.; Narakathu, B. B.; Emamian, S.; Bazuin, B. J.; Atashbar, M. Z. Development of printed and flexible dry ECG electrodes. *Sensing and Bio-Sensing Research* **2018,** *20*, 9-15.
(214) Cui, Z.; Han, Y.; Huang, Q.; Dong, J.; Zhu, Y. Electrohydrodynamic printing of silver nanowires for flexible and stretchable electronics. *Nanoscale* **2018,** *10* (15), 6806-6811.
(215) Tseng, S.-H.; Lyu, L.-M.; Hsiao, K.-Y.; Ho, W.-H.; Lu, M.-Y. Surfactant-free synthesis of ultralong silver nanowires for durable transparent conducting electrodes. *Chemical Communications* **2020,** *56* (42), 5593-5596.
(216) Yu, S.; Li, X.; Zhao, L.; Wu, M.; Ren, Q.; Gong, B.; Li, L.; Shi, H. Simultaneously improved conductivity and adhesion of flexible AgNW networks via a simple hot lamination process. *Synthetic Metals* **2020,** *267*, 116475.
(217) Wang, H.; Wang, Y.; Chen, X. Synthesis of uniform silver nanowires from AgCl seeds for transparent conductive films via spin-coating at variable spin-speed. *Colloids and Surfaces A: Physicochemical and Engineering Aspects* **2019,** *565*, 154-161.
(218) Sharma, B.; Kim, J.-S.; Sharma, A. Transparent AgNW-CoNPs conducting film for heat sensor. *Microelectronic Engineering* **2019,** *205*, 37-43.
(219) Albano, L. G. S.; Boratto, M. H.; Nunes-Neto, O.; Graeff, C. F. O. Low voltage and high frequency vertical organic field effect transistor based on rod-coating silver nanowires grid electrode. *Organic Electronics* **2017,** *50*, 311-316.
(220) Lee, D. G.; Lee, D.; Yoo, J. S.; Lee, S.; Jung, H. S. Effective passivation of Ag nanowire-based flexible transparent conducting electrode by TiO 2 nanoshell. *Nano Convergence* **2016,** *3* (1), 1-7.
(221) Junaidi; Triyana, K.; Harsojo; Suharyadi, E. High-Performance Silver Nanowire Film on Flexible Substrate Prepared by Meyer-rod Coating. *IOP Conference Series: Materials Science and Engineering* **2017,** *202*, 012055.
(222) Liu, C.-H.; Yu, X. Silver nanowire-based transparent, flexible, and conductive thin film. *Nanoscale research letters* **2011,** *6* (1), 75-75.
(223) Lee, J. H.; Huynh-Nguyen, B.-C.; Ko, E.; Kim, J. H.; Seong, G. H. Fabrication of flexible, transparent silver nanowire electrodes for amperometric detection of hydrogen peroxide. *Sensors and Actuators B: Chemical* **2016,** *224*, 789-797.
(224) Xie, H.; Yang, X.; Du, D.; Zhao, Y.; Wang, Y. Flexible transparent conductive film based on random networks of silver nanowires. *Micromachines* **2018,** *9* (6), 295.
(225) Wang, Y.; Feng, T.; Wang, K.; Qian, M.; Chen, Y.; Sun, Z. A Facile Method for Preparing Transparent, Conductive, and Paper-Like Silver Nanowire Films. *Journal of Nanomaterials* **2011,** *2011*, 935218.
(226) Kisannagar, R. R.; Jha, P.; Navalkar, A.; Maji, S. K.; Gupta, D. Fabrication of Silver Nanowire/Polydimethylsiloxane Dry Electrodes by a Vacuum Filtration Method for Electrophysiological Signal Monitoring. *ACS Omega* **2020,** *5* (18), 10260-10265.

(227) Wan, F.; He, H.; Zeng, S.; Du, J.; Wang, Z.; Gu, H.; Xiong, J. Silver nanowire network for flexible transparent electrodes based on spray coating at a low DC electric field and plasma treatment. *Nanotechnology* **2020,** *31* (32), 325302.
(228) Hoeng, F.; Denneulin, A.; Reverdy-Bruas, N.; Krosnicki, G.; Bras, J. Rheology of cellulose nanofibrils/silver nanowires suspension for the production of transparent and conductive electrodes by screen printing. *Applied Surface Science* **2017,** *394*, 160-168.
(229) Lu, H.-C.; Liao, Y.-C. Direct Printed Silver Nanowire Strain Sensor for Early Extravasation Detection. *Nanomaterials (Basel)* **2021,** *11* (10), 2583.
(230) Li, D.; Lai, W. Y.; Feng, F.; Huang, W. Post-Treatment of Screen-Printed Silver Nanowire Networks for Highly Conductive Flexible Transparent Films. *Advanced Materials Interfaces* **2021,** *8* (13), 2100548.
(231) Wang, Y.; Wu, X.; Wang, K.; Lin, K.; Xie, H.; Zhang, X.; Li, J. Novel Insights into Inkjet Printed Silver Nanowires Flexible Transparent Conductive Films. *Int J Mol Sci* **2021,** *22* (14), 7719.
(232) Qian, C.; Li, L.; Gao, M.; Yang, H.; Cai, Z.; Chen, B.; Xiang, Z.; Zhang, Z.; Song, Y. All-printed 3D hierarchically structured cellulose aerogel based triboelectric nanogenerator for multi-functional sensors. *Nano Energy* **2019,** *63*.
(233) Park, S. H.; Kaur, M.; Yun, D.; Kim, W. S. Hierarchically Designed Electron Paths in 3D Printed Energy Storage Devices. *Langmuir* **2018,** *34* (37), 10897-10904.
(234) Liu, S.; Shi, X.; Li, X.; Sun, Y.; Zhu, J.; Pei, Q.; Liang, J.; Chen, Y. A general gelation strategy for 1D nanowires: dynamically stable functional gels for 3D printing flexible electronics. *Nanoscale* **2018,** *10* (43), 20096-20107.
(235) Zhu, Z.; Guo, S. Z.; Hirdler, T.; Eide, C.; Fan, X.; Tolar, J.; McAlpine, M. C. 3D Printed Functional and Biological Materials on Moving Freeform Surfaces. *Advanced Materials* **2018,** *30* (23), n/a-n/a.
(236) Sun, C.; Liu, S.; Shi, X.; Lai, C.; Liang, J.; Chen, Y. 3D printing nanocomposite gel-based thick electrode enabling both high areal capacity and rate performance for lithium-ion battery. *Chemical Engineering Journal* **2020,** *381*, 122641.
(237) Sun, Y.; Du, Z. A Flexible and Highly Sensitive Pressure Sensor Based on AgNWs/NRLF for Hand Motion Monitoring. *Nanomaterials (Basel)* **2019,** *9* (7).
(238) Li, L.; Zhu, C.; Wu, Y.; Wang, J.; Zhang, T.; Liu, Y. A conductive ternary network of a highly stretchable AgNWs/AgNPs conductor based on a polydopamine-modified polyurethane sponge. *RSC Adv.* **2015,** *5* (77), 62905-62912.
(239) P. Justin Jesuraj, C. S., and Dong Hyun Kim, *et al.* Direction-dependent stretchability of AgNW electrodes on microprism-mediated elastomeric substrates. *AIP Advances* **2018,** *8* (6), 10.1063/1.5026742.
(240) Wei, Y.; Chen, S.; Lin, Y.; Yuan, X.; Liu, L. Silver nanowires coated on cotton for flexible pressure sensors. *J. Mater. Chem. C* **2016,** *4* (5), 935-943.
(241) Chen, Q.; Cao, P. F.; Advincula, R. C. Mechanically Robust, Ultraelastic Hierarchical Foam with Tunable Properties via 3D Printing. *Advanced Functional Materials* **2018,** *28* (21), n/a-n/a.
(242) Yang, Y.; Zhao, H. Water-induced polymer swelling and its application in soft electronics. *Applied Surface Science* **2022,** *577* (1), 151895.

(243) Yoon, I. S., Oh, Youngsu, and Kim, Sun Hong. 3D Printing of Self-Wiring Conductive Ink with High Stretchability and Stackability for Customized Wearable Devices. *Advanced Materials Technologies* **2019**, 1900363.
(244) Marus, M.; Hubarevich, A.; Lim, R. J. W.; Huang, H.; Smirnov, A.; Wang, H.; Fan, W.; Sun, X. W. Effect of silver nanowire length in a broad range on optical and electrical properties as a transparent conductive film. *Optical Materials Express* **2017,** *7* (3), 1105-1112.
(245) Kiran Kumar, A. B. V.; wan Bae, C.; Piao, L.; Kim, S.-H. Silver nanowire based flexible electrodes with improved properties: High conductivity, transparency, adhesion and low haze. *Materials Research Bulletin* **2013,** *48* (8), 2944-2949.
(246) Park, M.; Kim, W.; Hwang, B.; Han, S. M. Effect of varying the density of Ag nanowire networks on their reliability during bending fatigue. *Scripta Materialia* **2019,** *161*, 70-73.
(247) Marus, M.; Hubarevich, A.; Fan, W.; Wang, H.; Smirnov, A.; Wang, K.; Huang, H.; Sun, X. W. Optical haze of randomly arranged silver nanowire transparent conductive films with wide range of nanowire diameters. *AIP Advances* **2018,** *8*, 035201.
(248) Wang, J.; Jiu, J.; Araki, T.; Nogi, M.; Sugahara, T.; Nagao, S.; Koga, H.; He, P.; Suganuma, K. Silver nanowire electrodes: conductivity improvement without post-treatment and application in capacitive pressure sensors. *Nano-micro letters* **2015,** *7* (1), 51-58.
(249) Kang, S.; Kim, T.; Cho, S.; Lee, Y.; Choe, A.; Walker, B.; Ko, S.-J.; Kim, J. Y.; Ko, H. Capillary printing of highly aligned silver nanowire transparent electrodes for high-performance optoelectronic devices. *Nano letters* **2015,** *15* (12), 7933-7942.
(250) Xu, Y.; Ge, D.; Calderon-Ortiz, G. A.; Exarhos, A. L.; Bretz, C.; Alsayed, A.; Kurz, D.; Kikkawa, J. M.; Dreyfus, R.; Yang, S.; Yodh, A. G. Highly conductive and transparent coatings from flow-aligned silver nanowires with large electrical and optical anisotropy. *Nanoscale* **2020,** *12* (11), 6438-6448.
(251) Takemoto, A.; Araki, T.; Noda, Y.; Uemura, T.; Yoshimoto, S.; Abbel, R.; Rentrop, C.; van den Brand, J.; Sekitani, T. Fine printing method of silver nanowire electrodes with alignment and accumulation. *Nanotechnology* **2019,** *30* (37), 37LT03.
(252) Cho, S.; Kang, S.; Pandya, A.; Shanker, R.; Khan, Z.; Lee, Y.; Park, J.; Craig, S. L.; Ko, H. Large-Area Cross-Aligned Silver Nanowire Electrodes for Flexible, Transparent, and Force-Sensitive Mechanochromic Touch Screens. *ACS nano* **2017,** *11* (4), 4346.
(253) Dong, J.; Abukhdeir, N. M.; Goldthorpe, I. A. Simple assembly of long nanowires through substrate stretching. *Nanotechnology* **2015,** *26* (48), 485302.
(254) Chen, Y.-R.; Hong, C.-C.; Liou, T.-M.; Hwang, K. C.; Guo, T.-F. Roller-Induced Bundling of Long Silver Nanowire Networks for Strong Interfacial Adhesion, Highly Flexible, Transparent Conductive Electrodes. *Scientific Reports* **2017,** *7* (1), 16662.
(255) Yang, B.; Liu, G.; Han, S.; Cao, W.; Chen, H.; Lu, J.; Shieh, H. D. Hybrid Effect of Crossed Alignment and Multi-Stacking Structure on the Percolation Behavior of Silver Nanowire Networks. *Journal of Display Technology* **2015,** *11* (7), 625-629.
(256) Huang, Q.; Zhu, Y. Gravure Printing of Water-based Silver Nanowire ink on

Plastic Substrate for Flexible Electronics. *Scientific Reports* **2018,** *8* (1), 15167.
(257) Al-Milaji, K. N.; Huang, Q.; Li, Z.; Ng, T. N.; Zhao, H. Direct embedment and alignment of silver nanowires by inkjet printing for stretchable conductors. *ACS Applied Electronic Materials* **2020,** *2* (10), 3289-3298.
(258) Wang, J.-C.; Chang, M.-W.; Ahmad, Z.; Li, J.-S. Fabrication of patterned polymer-antibiotic composite fibers via electrohydrodynamic (EHD) printing. *Journal of Drug Delivery Science Technology* **2016,** *35*, 114-123.
(259) Li, X.; Kim, K.; Oh, H.; Moon, H. C.; Nam, S.; Kim, S. H. Cone-jet printing of aligned silver nanowire/poly (ethylene oxide) composite electrodes for organic thin-film transistors. *Organic Electronics* **2019,** *69*, 190-199.
(260) Tao, A.; Kim, F.; Hess, C.; Goldberger, J.; He, R.; Sun, Y.; Xia, Y.; Yang, P. Langmuir− Blodgett silver nanowire monolayers for molecular sensing using surface-enhanced Raman spectroscopy. *Nano letters* **2003,** *3* (9), 1229-1233.
(261) Bian, R.; Meng, L.; Zhang, M.; Chen, L.; Liu, H. Aligning one-dimensional nanomaterials by solution processes. *ACS omega* **2019,** *4* (1), 1816-1823.
(262) Tao, A. R.; Huang, J.; Yang, P. Langmuir− Blodgettry of nanocrystals and nanowires. *Accounts of chemical research* **2008,** *41* (12), 1662-1673.
(263) Zhu, R.; Lai, Y.; Nguyen, V.; Yang, R. Scalable alignment and transfer of nanowires in a spinning Langmuir film. *Nanoscale* **2014,** *6* (20), 11976-11980.
(264) Duan, S.-k.; Niu, Q.-l.; Wei, J.-f.; He, J.-b.; Yin, Y.-a.; Zhang, Y. Water-bath assisted convective assembly of aligned silver nanowire films for transparent electrodes. *Phys Chem Chem Phys* **2015,** *17* (12), 8106-8112.
(265) Shi, L.-f.; Liu, J.-z.; Yang, J.-h.; Cai, L.-f.; Shi, L.-y.; Qiu, H.-x. Langmuir-Blodgett assembly of transparent graphene oxide-silver microwire hybrid films with an antibacterial property. *New Carbon Materials* **2017,** *32* (4), 344-351.
(266) Choi, J. H.; Shin, M. G.; Jung, Y.; Kim, D. H.; Ko, J. S. Fabrication and Performance Evaluation of Highly Sensitive Flexible Strain Sensors with Aligned Silver Nanowires. *Micromachines* **2020,** *11* (2).
(267) Pu, D.; Zhou, W.; Li, Y.; Chen, J.; Chen, J.; Zhang, H.; Mi, B.; Wang, L.; Ma, Y. Order-enhanced silver nanowire networks fabricated by two-step dip-coating as polymer solar cell electrodes. *RSC Advances* **2015,** *5* (122), 100725-100729.
(268) Shin, M. G.; Choi, C. J.; Jung, Y.; Choi, J. H.; Ko, J. S. Alignment of silver nanowires using heat-assisted dip-coating method. *AIP Advances* **2020,** *10*, 035101.
(269) Wang, M. C.; Zhang, X.; Majidi, E.; Nedelec, K.; Gates, B. D. Electrokinetic assembly of selenium and silver nanowires into macroscopic fibers. *ACS nano* **2010,** *4* (5), 2607-2614.
(270) Farain, K.; Esfandiar, A.; Moshfegh, A. Z. Shooting at the nanoscale: Collection and acceleration of nanowires with an external electric field. *Applied Physics Letters* **2019,** *114*, 013102.
(271) Farain, K.; Esfandiar, A.; Moshfegh, A. Z. Universal rotation of nanowires in static uniform electric fields in viscous dielectric liquids. *Applied Physics Letters* **2018,** *113* (6).
(272) Cao, Y.; Liu, W. G.; Sun, J.-L.; Han, Y.; Zhang, J.; Liu, S.; Sun, H.; Guo, J. In *A technique for controlling the alignment of silver nanowires with an electric field*, 2006.

(273) Wang, X.; Chen, K.; Liu, L.; Xiang, N.; Ni, Z. Dielectrophoresis-based multi-step nanowire assembly on a flexible superstrate. *Nanotechnology* **2018,** *29* (2), 025301.
(274) Arenas-Guerrero, P.; Delgado Á, V.; Ahualli, S.; Jiménez, M. L. Polymer-induced orientation of nanowires under electric fields. *J. Colloid Interface Sci.* **2021,** *591*, 58-66.
(275) Ma, J.; Wang, K.; Zhan, M. Growth mechanism and electrical and magnetic properties of Ag–Fe3O4 core–shell nanowires. *ACS applied materials & interfaces* **2015,** *7* (29), 16027-16039.
(276) Li, N.; Huang, G.-W.; Shen, X.-J.; Xiao, H.-M.; Fu, S.-Y. Controllable fabrication and magnetic-field assisted alignment of Fe 3 O 4-coated Ag nanowires via a facile co-precipitation method. *Journal of Materials Chemistry C* **2013,** *1* (32), 4879-4884.
(277) Li, N.; Huang, G.-W.; Xiao, H.-M.; Fu, S.-Y. Preparation of aligned Fe3O4@Ag-nanowire/poly(vinyl alcohol) nanocomposite films via a low magnetic field. *Composites Part A: Applied Science and Manufacturing* **2015,** *77*, 87-95.
(278) Trotsenko, O.; Tokarev, A.; Gruzd, A.; Enright, T.; Minko, S. Magnetic field assisted assembly of highly ordered percolated nanostructures and their application for transparent conductive thin films. *Nanoscale* **2015,** *7* (16), 7155-7161.
(279) He, L.; Tjong, S.-C. Electrical behavior and positive temperature coefficient effect of graphene/polyvinylidene fluoride composites containing silver nanowires. *Nanoscale research letters* **2014,** *9* (1), 1-8.
(280) Hwang, B.; An, Y.; Lee, H.; Lee, E.; Becker, S.; Kim, Y.-H.; Kim, H. Highly flexible and transparent Ag nanowire electrode encapsulated with ultra-thin Al 2 O 3: thermal, ambient, and mechanical stabilities. *Scientific reports* **2017,** *7* (1), 1-7.
(281) Choo, D. C.; Kim, T. W. Degradation mechanisms of silver nanowire electrodes under ultraviolet irradiation and heat treatment. *Scientific Reports* **2017,** *7* (1), 1-12.
(282) Giusti, G.; Langley, D.; Lagrange, M.; Collins, R.; Jiménez, C.; Bréchet, Y.; Bellet, D. Thermal annealing effects on silver nanowire networks. *International journal of nanotechnology* **2014,** *11* (9-1011), 785-795.
(283) Cui, Z.; Poblete, F. R.; Zhu, Y. Tailoring the Temperature Coefficient of Resistance of Silver Nanowire Nanocomposites and their Application as Stretchable Temperature Sensors. *ACS Applied Materials & Interfaces* **2019,** *11* (19), 17836-17842.
(284) Bardet, L.; Papanastasiou, D. T.; Crivello, C.; Akbari, M.; Resende, J.; Sekkat, A.; Sanchez-Velasquez, C.; Rapenne, L.; Jiménez, C.; Muñoz-Rojas, D.; Denneulin, A.; Bellet, D. Silver Nanowire Networks: Ways to Enhance Their Physical Properties and Stability. *Nanomaterials* **2021,** *11* (11), 2785.
(285) Langley, D.; Lagrange, M.; Giusti, G.; Jiménez, C.; Bréchet, Y.; Nguyen, N. D.; Bellet, D. Metallic nanowire networks: effects of thermal annealing on electrical resistance. *Nanoscale* **2014,** *6* (22), 13535-13543.
(286) Lagrange, M.; Langley, D.; Giusti, G.; Jiménez, C.; Bréchet, Y.; Bellet, D. Optimization of silver nanowire-based transparent electrodes: effects of density, size and thermal annealing. *Nanoscale* **2015,** *7* (41), 17410-17423.
(287) Vafaei, A.; Hu, A.; Goldthorpe, I. A. Joining of individual silver nanowires via electrical current. *Nano-Micro Letters* **2014,** *6* (4), 293-300.
(288) Woo, J. S.; Han, J. T.; Jung, S.; Jang, J. I.; Kim, H. Y.; Jeong, H. J.; Jeong, S. Y.;

Baeg, K.-J.; Lee, G.-W. Electrically Robust Metal Nanowire Network Formation by In-Situ Interconnection with Single-Walled Carbon Nanotubes. *Scientific Reports* **2014,** *4* (1), 4804.
(289) Khaligh, H. H.; Xu, L.; Khosropour, A.; Madeira, A.; Romano, M.; Pradére, C.; Tréguer-Delapierre, M.; Servant, L.; Pope, M. A.; Goldthorpe, I. A. The Joule heating problem in silver nanowire transparent electrodes. *Nanotechnology* **2017,** *28* (42), 425703.
(290) Song, T.-B.; Chen, Y.; Chung, C.-H.; Yang, Y.; Bob, B.; Duan, H.-S.; Li, G.; Tu, K.-N.; Huang, Y.; Yang, Y. Nanoscale Joule Heating and Electromigration Enhanced Ripening of Silver Nanowire Contacts. *ACS Nano* **2014,** *8* (3), 2804-2811.
(291) Seong, B.; Chae, I.; Lee, H.; Nguyen, V. D.; Byun, D. Spontaneous self-welding of silver nanowire networks. *Physical Chemistry Chemical Physics* **2015,** *17* (12), 7629-7633.
(292) Kim, J.; Nam, Y. S.; Song, M. H.; Park, H. W. Large pulsed electron beam welded percolation networks of silver nanowires for transparent and flexible electrodes. *ACS Applied Materials & Interfaces* **2016,** *8* (32), 20938-20945.
(293) Hong, C.-H.; Oh, S. K.; Kim, T. K.; Cha, Y.-J.; Kwak, J. S.; Shin, J.-H.; Ju, B.-K.; Cheong, W.-S. Electron beam irradiated silver nanowires for a highly transparent heater. *Scientific reports* **2015,** *5*, 17716.
(294) Ding, Y.; Cui, Y.; Liu, X.; Liu, G.; Shan, F. Welded silver nanowire networks as high-performance transparent conductive electrodes: Welding techniques and device applications. *Applied Materials Today* **2020,** *20*, 100634.
(295) Liang, X.; Zhao, T.; Jiang, W.; Yu, X.; Hu, Y.; Zhu, P.; Zheng, H.; Sun, R.; Wong, C.-P. Highly transparent triboelectric nanogenerator utilizing in-situ chemically welded silver nanowire network as electrode for mechanical energy harvesting and body motion monitoring. *Nano Energy* **2019,** *59*, 508-516.
(296) Kang, H.; Kim, Y.; Cheon, S.; Yi, G.-R.; Cho, J. H. Halide Welding for Silver Nanowire Network Electrode. *ACS Applied Materials & Interfaces* **2017,** *9* (36), 30779-30785.
(297) Chen, S.-P.; Liao, Y.-C. Highly stretchable and conductive silver nanowire thin films formed by soldering nanomesh junctions. *Phys. Chem. Chem. Phys.* **2014,** *16* (37), 19856-19860.
(298) Hui, Z.; Liu, Y.; Guo, W.; Li, L.; Mu, N.; Jin, C.; Zhu, Y.; Peng, P. Chemical sintering of direct-written silver nanowire flexible electrodes under room temperature. *Nanotechnology* **2017,** *28* (28), 285703.
(299) Shen, Y.; Yao, R.-H. Improvement of the Conductivity of Silver Nanowire Film by Adding Silver Nano-Particles. *Chinese Physics Letters* **2016,** *33* (3), 037801.
(300) Lin, S. C.; Chang, C. W.; Liao, Y. C. Welding Silver Nanowire Junctions for Transparent Conducting Films by a Rapid Electroplating Method. *Journal of nanoscience and nanotechnology* **2018,** *18* (1), 251-255.
(301) Kang, H.; Kim, J. S.; Choi, S.-R.; Kim, Y.-H.; Kim, D. H.; Kim, J.-G.; Lee, T.-W.; Cho, J. H. Electroplated core–shell nanowire network electrodes for highly efficient organic light-emitting diodes. *Nano Convergence* **2022,** *9* (1), 1.
(302) Wang, S.; Tian, Y.; Hang, C.; Wang, C. Cohesively enhanced electrical

conductivity and thermal stability of silver nanowire networks by nickel ion bridge joining. *Scientific Reports* **2018,** *8* (1), 5260.
(303) Chu, X.; Wang, K.; Tao, J.; Li, S.; Ji, S.; Ye, C. Tackling the Stability Issues of Silver Nanowire Transparent Conductive Films through FeCl3 Dilute Solution Treatment. *Nanomaterials* **2019,** *9* (4), 533.
(304) Yang, S. B.; Choi, H.; Lee, D. S.; Choi, C. G.; Choi, S. Y.; Kim, I. D. Improved optical sintering efficiency at the contacts of silver nanowires encapsulated by a graphene layer. *Small* **2015,** *11* (11), 1293-1300.
(305) Park, J. H.; Hwang, G. T.; Kim, S.; Seo, J.; Park, H. J.; Yu, K.; Kim, T. S.; Lee, K. J. Flash-induced self-limited plasmonic welding of silver nanowire network for transparent flexible energy harvester. *Advanced Materials* **2017,** *29* (5), 1603473.
(306) Liu, G.-S.; Wang, T.; Wang, Y.; Zheng, H.; Chen, Y.; Zeng, Z.; Chen, L.; Chen, Y.; Yang, B.-R.; Luo, Y.; Chen, Z. One-step plasmonic welding and photolithographic patterning of silver nanowire network by UV-programable surface atom diffusion. *Nano Research* **2021**.
(307) Hu, Y.; Liang, C.; Sun, X.; Zheng, J.; Duan, J.; Zhuang, X. Enhancement of the Conductivity and Uniformity of Silver Nanowire Flexible Transparent Conductive Films by Femtosecond Laser-Induced Nanowelding. *Nanomaterials (Basel)* **2019,** *9* (5).
(308) Chung, W.-H., Kim, Sang-Ho, and Kim, Hak-Sung. *Welding of Silver Nanowire Networks via Flash White Light and UV-C Irradiation for Highly Conductive and Reliable Transparent Electrodes*, Scientific Reports: 2016; Vol. 6, p 32086.
(309) Liang, X.; Lu, J.; Zhao, T.; Yu, X.; Jiang, Q.; Hu, Y.; Zhu, P.; Sun, R.; Wong, C. Facile and Efficient Welding of Silver Nanowires Based on UVa Induced Nanoscale Photothermal Process for RolŒ t□ Roll Manufacturing of Higˆ Performance Transparent Conducting Films. *Advanced Materials Interfaces* **2018,** *6*, 1801635.
(310) Chung, W.-H.; Jang, Y.-R.; Hwang, Y.-T.; Kim, S.-H.; Kim, H.-S. The surface plasmonic welding of silver nanowires via intense pulsed light irradiation combined with NIR for flexible transparent conductive films. *Nanoscale* **2020,** *12* (34), 17725-17737.
(311) Jang, Y.-R.; Chung, W.-H.; Hwang, Y.-T.; Hwang, H.-J.; Kim, S.-H.; Kim, H.-S. Selective wavelength plasmonic flash light welding of silver nanowires for transparent electrodes with high conductivity. *ACS applied materials & interfaces* **2018,** *10* (28), 24099-24107.
(312) Jiu, J., Nogi, M., Sugahara, T., *et al.* Strongly adhesive and flexible transparent silver nanowire conductive films fabricated with a high-intensity pulsed light technique. *Journal of Materials Chemistry* **2012,** *22*, 23561.
(313) Jiu, J.; Sugahara, T.; Nogi, M.; Araki, T.; Suganuma, K.; Uchida, H.; Shinozaki, K. High-intensity pulse light sintering of silver nanowire transparent films on polymer substrates: the effect of the thermal properties of substrates on the performance of silver films. *Nanoscale* **2013,** *5* (23), 11820-8.
(314) Stapleton, A. J.; Afre, R. A.; Ellis, A. V.; Shapter, J. G.; Andersson, G. G.; Quinton, J. S.; Lewis, D. A. Highly conductive interwoven carbon nanotube and silver nanowire transparent electrodes. *Science and technology of advanced materials* **2013,** *14* (3), 035004.

(315) Goak, J. C.; Kim, T. Y.; Kim, D. U.; Chang, K. S.; Lee, C. S.; Lee, N. Stable heating performance of carbon nanotube/silver nanowire transparent heaters. *Applied Surface Science* **2020,** *510*, 145445.
(316) Liu, B.-T.; Kuo, H.-L. Graphene/silver nanowire sandwich structures for transparent conductive films. *Carbon* **2013,** *63*, 390-396.
(317) Lee, D.; Lee, H.; Ahn, Y.; Lee, Y. High-performance flexible transparent conductive film based on graphene/AgNW/graphene sandwich structure. *Carbon* **2015,** *81*, 439-446.
(318) Lee, J.; Woo, J. Y.; Kim, J. T.; Lee, B. Y.; Han, C.-S. Synergistically Enhanced Stability of Highly Flexible Silver Nanowire/Carbon Nanotube Hybrid Transparent Electrodes by Plasmonic Welding. *ACS Applied Materials & Interfaces* **2014,** *6* (14), 10974-10980.
(319) Hwang, Y.; Hwang, Y. H.; Choi, K. W.; Lee, S.; Kim, S.; Park, S. J.; Ju, B.-K. Highly stabilized flexible transparent capacitive photodetector based on silver nanowire/graphene hybrid electrodes. *Scientific Reports* **2021,** *11* (1), 10499.
(320) Khan, A.; Nguyen, V. H.; Muñoz-Rojas, D.; Aghazadehchors, S.; Jiménez, C.; Nguyen, N. D.; Bellet, D. Stability enhancement of silver nanowire networks with conformal ZnO coatings deposited by atmospheric pressure spatial atomic layer deposition. *ACS applied materials & interfaces* **2018,** *10* (22), 19208-19217.
(321) Xu, Q.; Shen, W.; Huang, Q.; Yang, Y.; Tan, R.; Zhu, K.; Dai, N.; Song, W. Flexible transparent conductive films on PET substrates with an AZO/AgNW/AZO sandwich structure. *Journal of Materials Chemistry C* **2014,** *2* (19), 3750-3755.
(322) You, S.; Park, Y. S.; Choi, H. W.; Kim, K. H. Fabrication of Ag nanowire and Al-doped ZnO hybrid transparent electrodes. *Japanese Journal of Applied Physics* **2015,** *55* (1S), 01AE14.
(323) Chen, X.; Xu, G.; Zeng, G.; Gu, H.; Chen, H.; Xu, H.; Yao, H.; Li, Y.; Hou, J.; Li, Y. Realizing Ultrahigh Mechanical Flexibility and> 15% Efficiency of Flexible Organic Solar Cells via a "Welding" Flexible Transparent Electrode. *Advanced Materials* **2020,** *32* (14), 1908478.
(324) Wang, R.; Cai, P.; Xu, W.; Tan, R.; Shen, W.; Wang, Z.; Chen, G.; Huang, J.; Fang, X.; Song, W. Highly flexible and transparent film heaters based on colorless polyimide substrate with a GZO/AgNW/GZO sandwich structure. *Journal of Materials Science: Materials in Electronics* **2020,** *31* (6), 4743-4751.
(325) Nam, S.; Song, M.; Kim, D.-H.; Cho, B.; Lee, H. M.; Kwon, J.-D.; Park, S.-G.; Nam, K.-S.; Jeong, Y.; Kwon, S.-H.; Park, Y. C.; Jin, S.-H.; Kang, J.-W.; Jo, S.; Kim, C. S. Ultrasmooth, extremely deformable and shape recoverable Ag nanowire embedded transparent electrode. *Scientific Reports* **2014,** *4* (1), 4788.
(326) Song, M.; Park, J. H.; Kim, C. S.; Kim, D.-H.; Kang, Y.-C.; Jin, S.-H.; Jin, W.-Y.; Kang, J.-W. Highly flexible and transparent conducting silver nanowire/ZnO composite film for organic solar cells. *Nano Research* **2014,** *7* (9), 1370-1379.
(327) Go, M.; Hwang, B.; Lim, S. Highly reliable mulberry paper (Hanji)-based electrode with printed silver nanowire/zinc oxide hybrid for soft electronics. *Materials and Manufacturing Processes* **2019,** *34*, 1605 - 1611.
(328) Song, T.-B.; Rim, Y. S.; Liu, F.; Bob, B.; Ye, S.; Hsieh, Y.-T.; Yang, Y. Highly

robust silver nanowire network for transparent electrode. *ACS applied materials & interfaces* **2015,** *7* (44), 24601-24607.
(329) Giesz, P.; Mackiewicz, E.; Grobelny, J.; Celichowski, G.; Cieślak, M. Multifunctional hybrid functionalization of cellulose fabrics with AgNWs and TiO2. *Carbohydrate polymers* **2017,** *177*, 397-405.
(330) Chen, T. Y.; Fan, C. M.; Wu, J. Y.; Lin, T. L. Hybrid Silver Nanowire/Titanium Oxides Nanocomposites as Anode for Dye-Sensitized Solar Cell Application. *Journal of the Chinese Chemical Society* **2009,** *56* (6), 1244-1249.
(331) Sohn, H.; Kim, S.; Shin, W.; Lee, J. M.; Lee, H.; Yun, D.-J.; Moon, K.-S.; Han, I. T.; Kwak, C.; Hwang, S.-J. Novel flexible transparent conductive films with enhanced chemical and electromechanical sustainability: TiO2 nanosheet–Ag nanowire hybrid. *ACS applied materials & interfaces* **2018,** *10* (3), 2688-2700.
(332) Cheng, J.; Li, Y.; Plissonneau, M.; Li, J.; Li, J.; Chen, R.; Tang, Z.; Pautrot-d'Alençon, L.; He, T.; Tréguer-Delapierre, M.; Delville, M.-H. Plasmon-induced hot electron transfer in AgNW@TiO(2)@AuNPs nanostructures. *Scientific reports* **2018,** *8* (1), 14136-14136.
(333) Huang, Y.; Tian, Y.; Hang, C.; Liu, Y.; Wang, S.; Qi, M.; Zhang, H.; Peng, Q. TiO2-Coated Core–Shell Ag Nanowire Networks for Robust and Washable Flexible Transparent Electrodes. *ACS Applied Nano Materials* **2019,** *2* (4), 2456-2466.
(334) Ahn, Y.; Jeong, Y.; Lee, Y. Improved thermal oxidation stability of solution-processable silver nanowire transparent electrode by reduced graphene oxide. *ACS applied materials & interfaces* **2012,** *4* (12), 6410-6414.
(335) Li, L.; Li, W.; Jiu, J.; Suganuma, K. Efficient assembly of high-performance reduced graphene oxide/silver nanowire transparent conductive film based on in situ light-induced reduction technology. *Applied Surface Science* **2018,** *459*, 732-740.
(336) Liu, H. S.; Pan, B. C.; Liou, G. S. Highly transparent AgNW/PDMS stretchable electrodes for elastomeric electrochromic devices. *Nanoscale* **2017,** *9* (7), 2633-2639.
(337) Zhang, W.; Chen, X.; Zhang, G.; Wang, S.; Zhu, S.; Wu, X.; Wang, Y.; Wang, Q.; Hu, C. Conducting polymer/silver nanowires stacking composite films for high-performance electrochromic devices. *Solar Energy Materials and Solar Cells* **2019,** *200*, 109919.
(338) Moreno, I.; Navascues, N.; Arruebo, M.; Irusta, S.; Santamaria, J. Facile preparation of transparent and conductive polymer films based on silver nanowire/polycarbonate nanocomposites. *Nanotechnology* **2013,** *24* (27), 275603.
(339) Yao, S.; Ren, P.; Song, R.; Liu, Y.; Huang, Q.; Dong, J.; O'Connor, B. T.; Zhu, Y. Nanomaterial-enabled flexible and stretchable sensing systems: processing, integration, and applications. *Advanced Materials* **2020,** *32* (15), 1902343.
(340) Yao, S.; Swetha, P.; Zhu, Y. Nanomaterial-enabled wearable sensors for healthcare. *Advanced healthcare materials* **2018,** *7* (1), 1700889.
(341) Tan, D.; Jiang, C.; Li, Q.; Bi, S.; Song, J. Silver nanowire networks with preparations and applications: A review. *Journal of Materials Science: Materials in Electronics* **2020**, 1-28.
(342) Huang, Q.; Zhu, Y. Printing conductive nanomaterials for flexible and stretchable electronics: A review of materials, processes, and applications. *Advanced Materials*

Technologies **2019,** *4* (5), 1800546.
(343) Kim, T.; Kim, Y. W.; Lee, H. S.; Kim, H.; Yang, W. S.; Suh, K. S. Uniformly interconnected silver-nanowire networks for transparent film heaters. *Advanced Functional Materials* **2013,** *23* (10), 1250-1255.
(344) Amjadi, M.; Pichitpajongkit, A.; Lee, S.; Ryu, S.; Park, I. Highly Stretchable and Sensitive Strain Sensor Based on Silver Nanowire–Elastomer Nanocomposite. *ACS Nano* **2014,** *8* (5), 5154-5163.
(345) Kim, Y.; Ryu, T. I.; Ok, K.-H.; Kwak, M.-G.; Park, S.; Park, N.-G.; Han, C. J.; Kim, B. S.; Ko, M. J.; Son, H. J.; Kim, J.-W. Transparent Electronics: Inverted Layer-By-Layer Fabrication of an Ultraflexible and Transparent Ag Nanowire/Conductive Polymer Composite Electrode for Use in High-Performance Organic Solar Cells. *Advanced Functional Materials* **2015,** *25* (29), 4743-4743.
(346) Kim, S.; Hwang, B. Ag nanowire electrode with patterned dry film photoresist insulator for flexible organic light-emitting diode with various designs. *Materials & Design* **2018,** *160*, 572-577.
(347) Nair, N. M.; Khanra, I.; Ray, D.; Swaminathan, P. Silver Nanowire-Based Printable Electrothermochromic Ink for Flexible Touch-Display Applications. *ACS Applied Materials & Interfaces* **2021,** *13* (29), 34550-34560.
(348) Jeong, W.; Lee, S.; Yoo, S.; Park, S.; Choi, H.; Bae, J.; Lee, Y.; Woo, K.; Choi, J.-H.; Lee, S. A Hierarchical Metal Nanowire Network Structure for Durable, Cost-Effective, Stretchable, and Breathable Electronics. *ACS Applied Materials & Interfaces* **2021,** *13* (50), 60425-60432.
(349) Madaria, A. R.; Kumar, A.; Zhou, C. Large scale, highly conductive and patterned transparent films of silver nanowires on arbitrary substrates and their application in touch screens. *Nanotechnology* **2011,** *22* (24), 245201.
(350) Gao, W.; Emaminejad, S.; Nyein, H. Y. Y.; Challa, S.; Chen, K.; Peck, A.; Fahad, H. M.; Ota, H.; Shiraki, H.; Kiriya, D. Fully integrated wearable sensor arrays for multiplexed in situ perspiration analysis. *Nature* **2016,** *529* (7587), 509-514.
(351) Lee, D. J.; Oh, Y.; Hong, J.-M.; Park, Y. W.; Ju, B.-K. Light sintering of ultra-smooth and robust silver nanowire networks embedded in poly(vinyl-butyral) for flexible OLED. *Scientific Reports* **2018,** *8* (1), 14170.
(352) Kim, K. K.; Ha, I.; Won, P.; Seo, D.-G.; Cho, K.-J.; Ko, S. H. Transparent wearable three-dimensional touch by self-generated multiscale structure. *Nature communications* **2019,** *10* (1), 1-8.
(353) Lee, J.-M.; Kim, Y.-H.; Kim, H.-K.; Kim, H.-J.; Hong, C.-H. Effect of AlOx protection layer on AgNWs for flexible transparent heater. *Scientific Reports* **2020,** *10* (1), 4592.
(354) You, B.; Han, C. J.; Kim, Y.; Ju, B.-K.; Kim, J.-W. A wearable piezocapacitive pressure sensor with a single layer of silver nanowire-based elastomeric composite electrodes. *Journal of Materials Chemistry A* **2016,** *4* (27), 10435-10443.
(355) Huang, H.; Cai, C. J.; Yeow, B. S.; Ouyang, J.; Ren, H. Highly Stretchable and Kirigami-Structured Strain Sensors with Long Silver Nanowires of High Aspect Ratio. *MACHINES* **2021,** *9* (9), 186.
(356) Park, S. B.; Han, J. W.; Kim, J. H.; Wibowo, A. F.; Prameswati, A.; Park, J.; Lee,

J.; Moon, M.-W.; Kim, M.-S.; Kim, Y. H. Multifunctional Stretchable Organic–Inorganic Hybrid Electronics with Transparent Conductive Silver Nanowire/Biopolymer Hybrid Films. *Advanced Optical Materials* **2021,** *9* (14), 2002041.
(357) Chen, L.; Chen, G.; Bi, L.; Yang, Z.; Wu, Z.; Huang, M.; Bao, J.; Wang, W.; Ye, C.; Pan, J.; Peng, Y.; Ye, C. A highly sensitive strain sensor with a sandwich structure composed of two silver nanoparticles layers and one silver nanowires layer for human motion detection. *Nanotechnology* **2021,** *32* (37).
(358) Zhu, Y.; Deng, Y.; Yi, P.; Peng, L.; Lai, X.; Lin, Z. Flexible Transparent Electrodes Based on Silver Nanowires: Material Synthesis, Fabrication, Performance, and Applications. *Advanced Materials Technologies* **2019,** *4* (10), 1900413.
(359) Joo, Y.; Byun, J.; Seong, N.; Ha, J.; Kim, H.; Kim, S.; Kim, T.; Im, H.; Kim, D.; Hong, Y. Silver nanowire-embedded PDMS with a multiscale structure for a highly sensitive and robust flexible pressure sensor. *Nanoscale* **2015,** *7* (14), 6208-6215.
(360) Shuai, X.; Zhu, P.; Zeng, W.; Hu, Y.; Liang, X.; Zhang, Y.; Sun, R.; Wong, C.-p. Highly Sensitive Flexible Pressure Sensor Based on Silver Nanowires-Embedded Polydimethylsiloxane Electrode with Microarray Structure. *ACS Applied Materials & Interfaces* **2017,** *9* (31), 26314-26324.
(361) Quan, Y.; Wei, X.; Xiao, L.; Wu, T.; Pang, H.; Liu, T.; Huang, W.; Wu, S.; Li, S.; Chen, Z. Highly sensitive and stable flexible pressure sensors with micro-structured electrodes. *Journal of Alloys and Compounds* **2017,** *699*, 824-831.
(362) Yongyun, M.; Bing, J.; Ge, C.; Changxiang, H.; Bingpu, Z.; Yanqing, T. *Robust and Wearable Pressure Sensor Assembled from AgNW-Coated PDMS Micropillar Sheets with High Sensitivity and Wide Detection Range*, 2019.
(363) Lee, J.-G.; Lee, J.-H.; An, S.; Kim, D.-Y.; Kim, T.-G.; Al-Deyab, S. S.; Yarin, A. L.; Yoon, S. S. Highly flexible, stretchable, wearable, patternable and transparent heaters on complex 3D surfaces formed from supersonically sprayed silver nanowires. *Journal of Materials Chemistry A* **2017,** *5* (14), 6677-6685.
(364) Du, Z.; Chen, Z.; Xu, J.; Zheng, D.; Zou, H.; Liu, J.; Wang, M. A facile approach to prepare a flexible and durable electrically driven cotton fabric-based heater. *Journal of Industrial Textiles* **2020**, 1528083720965678.
(365) Park, J.; Han, D.; Choi, S.; Kim, Y.; Kwak, J. Flexible transparent film heaters using a ternary composite of silver nanowire, conducting polymer, and conductive oxide. *RSC advances* **2019,** *9* (10), 5731-5737.
(366) Veeramuthu, L.; Chen, B.-Y.; Tsai, C.-Y.; Liang, F.-C.; Venkatesan, M.; Jiang, D.-H.; Chen, C.-W.; Cai, X.; Kuo, C.-C. Novel stretchable thermochromic transparent heaters designed for smart window defroster applications by spray coating silver nanowire. *RSC Advances* **2019,** *9* (61), 35786-35796.
(367) Kwon, J.; Suh, Y. D.; Lee, J.; Lee, P.; Han, S.; Hong, S.; Yeo, J.; Lee, H.; Ko, S. H. Recent progress in silver nanowire based flexible/wearable optoelectronics. *Journal of Materials Chemistry C* **2018,** *6* (28), 7445-7461.
(368) Lan, W.; Chen, Y.; Yang, Z.; Han, W.; Zhou, J.; Zhang, Y.; Wang, J.; Tang, G.; Wei, Y.; Dou, W.; Su, Q.; Xie, E. Ultraflexible Transparent Film Heater Made of Ag Nanowire/PVA Composite for Rapid-Response Thermotherapy Pads. *ACS Appl Mater*

Interfaces **2017,** *9* (7), 6644-6651.
(369) Langley, D.; Giusti, G.; Mayousse, C.; Celle, C.; Bellet, D.; Simonato, J.-P. Flexible transparent conductive materials based on silver nanowire networks: a review. *Nanotechnology* **2013,** *24* (45), 452001.
(370) Chen, S.; Guan, Y.; Li, Y.; Yan, X.; Ni, H.; Li, L. A water-based silver nanowire ink for large-scale flexible transparent conductive films and touch screens. *Journal of Materials Chemistry C* **2017,** *5* (9), 2404-2414.
(371) Lee, G.; Lee, S. G.; Chung, Y.; Bae, G. Y.; Lee, S.; Ryu, S.; Cho, K. Omnidirectionally and highly stretchable conductive electrodes based on noncoplanar zigzag mesh silver nanowire arrays. *Advanced Electronic Materials* **2016,** *2* (8), 1600158.
(372) Ditte, K.; Perez, J.; Chae, S.; Hambsch, M.; Al-Hussein, M.; Komber, H.; Formanek, P.; Mannsfeld, S. C. B.; Fery, A.; Kiriy, A.; Lissel, F. Ultrasoft and High-Mobility Block Copolymers for Skin-Compatible Electronics. *Advanced Materials* **2021,** *33* (4), 8.
(373) Kuzmanovic, M.; Delva, L.; Cardon, L.; Ragaert, K. Relationship between the Processing, Structure, and Properties of Microfibrillar Composites. *Advanced Materials* **2020,** *32* (52), 29.
(374) Marina, S.; Kaufmann, N. P.; Karki, A.; Gutierrez-Meza, E.; Gutierrez-Fernandez, E.; Vollbrecht, J.; Solano, E.; Walker, B.; Bannock, J. H.; de Mello, J.; Silva, C.; Nguyen, T. Q.; Cangialosi, D.; Stingelin, N.; Martin, J. The Importance of Quantifying the Composition of the Amorphous Intermixed Phase in Organic Solar Cells. *Advanced Materials* **2020,** *32* (47), 7.
(375) Sun, C.; Pan, F.; Bin, H.; Zhang, J.; Xue, L.; Qiu, B.; Wei, Z.; Zhang, Z.-G.; Li, Y. A low cost and high performance polymer donor material for polymer solar cells. *Nature Communications* **2018,** *9* (1), 743.
(376) Xia, Y. L.; He, Y.; Zhang, F. H.; Liu, Y. J.; Leng, J. S. A Review of Shape Memory Polymers and Composites: Mechanisms, Materials, and Applications. *Advanced Materials* **2021,** *33* (6), 33.
(377) Yang, Y.; Zhao, G. J.; Cheng, X.; Deng, H.; Fu, Q. Stretchable and Healable Conductive Elastomer Based on PEDOT:PSS/Natural Rubber for Self-Powered Temperature and Strain Sensing. *Acs Applied Materials & Interfaces* **2021,** *13* (12), 14612-14624.
(378) Qiu, H. Y.; Gapeeva, A.; Holken, I.; Kaps, S.; Adelung, R.; Baum, M. J. Polydimethylsiloxane Microdomains Formation at the Polythiourethane/Air Interface and Its Influence on Barnacle Release. *Acs Applied Materials & Interfaces* **2021,** *13* (3), 4545-4552.
(379) Li, Y.; Arnold, W.; Thapa, A.; Jasinski, J. B.; Sumanasekera, G.; Sunkara, M.; Druffel, T.; Wang, H. Stable and Flexible Sulfide Composite Electrolyte for High-Performance Solid-State Lithium Batteries. *Acs Applied Materials & Interfaces* **2020,** *12* (38), 42653-42659.
(380) Alsewailem, F. D. Low-Temperature Synthesis Method for the Fabrication of Efficient Polymer-Blend Systems. *Journal of Materials Research and Technology* **2021,** *13*, 1098-1102.

(381) Yang, H.; Wu, Y.; Zou, Y.; Dong, Y.; Yuan, J.; Cui, C.; Li, Y. A new polymer donor for efficient polymer solar cells: simultaneously realizing high short-circuit current density and transparency. *Journal of Materials Chemistry A* **2018,** *6* (30), 14700-14708.
(382) Benten, H.; Mori, D.; Ohkita, H.; Ito, S. Recent research progress of polymer donor/polymer acceptor blend solar cells. *Journal of Materials Chemistry A* **2016,** *4* (15), 5340-5365.
(383) Cui, C.; Li, Y. High-performance conjugated polymer donor materials for polymer solar cells with narrow-bandgap nonfullerene acceptors. *Energy & Environmental Science* **2019,** *12* (11), 3225-3246.
(384) Xu, X.; Feng, K.; Lee, Y. W.; Woo, H. Y.; Zhang, G.; Peng, Q. Subtle Polymer Donor and Molecular Acceptor Design Enable Efficient Polymer Solar Cells with a Very Small Energy Loss. *Advanced Functional Materials* **2020,** *30* (9), 1907570.
(385) Wang, Z.; Wang, C.; Gan, Q.; Cao, Y.; Yuan, H.; Hua, D. Donor–Acceptor-Type Conjugated Polymer-Based Multicolored Drug Carriers with Tunable Aggregation-Induced Emission Behavior for Self-Illuminating Cancer Therapy. *ACS Applied Materials & Interfaces* **2019,** *11* (45), 41853-41861.
(386) Sung, Y. K.; Kim, S. W. Recent advances in polymeric drug delivery systems. *Biomaterials Research* **2020,** *24* (1), 12.
(387) Macha, I. J.; Ben-Nissan, B.; Vilchevskaya, E. N.; Morozova, A. S.; Abali, B. E.; Müller, W. H.; Rickert, W. Drug Delivery From Polymer-Based Nanopharmaceuticals-An Experimental Study Complemented by Simulations of Selected Diffusion Processes. *Frontiers in bioengineering and biotechnology* **2019,** *7*, 37.
(388) Liechty, W. B.; Kryscio, D. R.; Slaughter, B. V.; Peppas, N. A. Polymers for drug delivery systems. *Annu Rev Chem Biomol Eng* **2010,** *1*, 149-173.
(389) Shamsuddoha, M.; Islam, M. M.; Aravinthan, T.; Manalo, A.; Lau, K.-t. Effectiveness of using fibre-reinforced polymer composites for underwater steel pipeline repairs. *Composite Structures* **2013,** *100*, 40-54.
(390) Benyahia, H.; Tarfaoui, M.; El Moumen, A.; Ouinas, D.; Hassoon, O. H. Mechanical properties of offshoring polymer composite pipes at various temperatures. *Composites Part B: Engineering* **2018,** *152*, 231-240.
(391) Kim, D. C.; Shim, H. J.; Lee, W.; Koo, J. H.; Kim, D. H. Material-Based Approaches for the Fabrication of Stretchable Electronics. *Advanced Materials* **2020,** *32* (15), 29.
(392) Yao, B.; Hong, W.; Chen, T. W.; Han, Z. B.; Xu, X. W.; Hu, R. C.; Hao, J. Y.; Li, C. H.; Li, H.; Perini, S. E.; Lanagan, M. T.; Zhang, S. L.; Wang, Q.; Wang, H. Highly Stretchable Polymer Composite with Strain-Enhanced Electromagnetic Interference Shielding Effectiveness. *Advanced Materials* **2020,** *32* (14), 7.
(393) Krisnadi, F.; Nguyen, L. L.; Ankit; Ma, J.; Kulkarni, M. R.; Mathews, N.; Dickey, M. D. Directed Assembly of Liquid Metal-Elastomer Conductors for Stretchable and Self-Healing Electronics. *Advanced Materials* **2020,** *32* (30), 10.
(394) Polgar, L. M.; Fallani, F.; Cuijpers, J.; Raffa, P.; Broekhuis, A. A.; van Duin, M.; Picchioni, F. Water-swellable elastomers: synthesis, properties and applications. *Reviews in Chemical Engineering* **2019,** *35* (1), 45-72.
(395) Oyama, Y.; Hiejima, Y.; Nitta, K.-h. Swelling behavior of butyl and chloroprene

rubber composites with poly(sodium acrylate) showing high water uptake. *Journal of Applied Polymer Science* **2020,** *137* (14), 48535.
(396) Thomas, A. G.; Muniandy, K. Absorption and desorption of water in rubbers. *Polymer* **1987,** *28* (3), 408-415.
(397) Manaila, E.; Craciun, G.; Ighigeanu, D. Water Absorption Kinetics in Natural Rubber Composites Reinforced with Natural Fibers Processed by Electron Beam Irradiation. *Polymers (Basel)* **2020,** *12* (11), 2437.
(398) Trakuldee, J.; Boonkerd, K. Effect of filler water absorption on water swelling properties of natural rubber. *IOP Conference Series: Materials Science and Engineering* **2017,** *223*, 012007.
(399) Sugiman, S.; Salman, S.; Maryudi, M. Effects of volume fraction on water uptake and tensile properties of epoxy filled with inorganic fillers having different reactivity to water. *Materials Today Communications* **2020,** *24*, 101360.
(400) Eiler, J.; Simonsen, S. B.; Hansen, D.; Bingöl, B.; Hansen, K.; Thormann, E. Water transport in polymer composites through swelling-induced networks of hydrogel particles. *Soft Matter* **2020,** *16* (35), 8254-8261.
(401) Fedors, R. F. Osmotic effects in water absorption by polymers. *Polymer* **1980,** *21* (2), 207-212.
(402) Lee, S.; Song, Y.; Ko, Y.; Ko, Y.; Ko, J.; Kwon, C. H.; Huh, J.; Kim, S. W.; Yeom, B.; Cho, J. A Metal-Like Conductive Elastomer with a Hierarchical Wrinkled Structure. *Advanced materials (Deerfield Beach, Fla.)* **2020,** *32* (7), e1906460.
(403) Gao, N.; Zhang, X.; Liao, S.; Jia, H.; Wang, Y. Polymer Swelling Induced Conductive Wrinkles for an Ultrasensitive Pressure Sensor. *ACS Macro Letters* **2016,** *5* (7), 823-827.
(404) Zhao, J.; Dehbari, N.; Han, W.; Huang, L.; Tang, Y. Electrospun multi-scale hybrid nanofiber/net with enhanced water swelling ability in rubber composites. *Materials & Design* **2015,** *86*, 14-21.
(405) Kappert, E. J.; Raaijmakers, M. J. T.; Tempelman, K.; Cuperus, F. P.; Ogieglo, W.; Benes, N. E. Swelling of 9 polymers commonly employed for solvent-resistant nanofiltration membranes: A comprehensive dataset. *Journal of Membrane Science* **2019,** *569*, 177-199.
(406) Raim, V.; Srebnik, S. Simulation of osmotic pressure across an amorphous semipermeable membrane. *J. Membr. Sci.* **2018,** *563*, 183-190.
(407) Yao, S.; Ren, P.; Song, R.; Liu, Y.; Huang, Q.; Dong, J.; O'Connor, B. T.; Zhu, Y. Nanomaterial-Enabled Flexible and Stretchable Sensing Systems: Processing, Integration, and Applications. *Advanced materials (Deerfield Beach, Fla.)* **2020,** *32* (15), e1902343.
(408) Huang, S.; Liu, Y.; Zhao, Y.; Ren, Z.; Guo, C. F. Flexible Electronics: Stretchable Electrodes and Their Future. **2018**.
(409) Trung, T. Q.; Lee, N. E. Recent Progress on Stretchable Electronic Devices with Intrinsically Stretchable Components. *Advanced materials (Deerfield Beach, Fla.)* **2017,** *29* (3).
(410) Wang, X.; Sun, H.; Yue, X.; Yu, Y.; Zheng, G.; Dai, K.; Liu, C.; Shen, C. A highly stretchable carbon nanotubes/thermoplastic polyurethane fiber-shaped strain sensor

with porous structure for human motion monitoring. *Composites Science and Technology* **2018,** *168*, 126-132.
(411) Pu, J.-H.; Zhao, X.; Zha, X.-J.; Li, W.-D.; Ke, K.; Bao, R.-Y.; Liu, Z.-Y.; Yang, M.-B.; Yang, W. A strain localization directed crack control strategy for designing MXene-based customizable sensitivity and sensing range strain sensors for full-range human motion monitoring. *Nano Energy* **2020,** *74*, 104814.
(412) Trung, T. Q.; Lee, N. E. Flexible and stretchable physical sensor integrated platforms for wearable human-activity monitoringand personal healthcare. *Advanced materials* **2016,** *28* (22), 4338-4372.
(413) Xie, R.; Hou, S.; Chen, Y.; Zhang, K.; Zou, B.; Liu, Y.; Liang, J.; Guo, S.; Li, H.; Zheng, B. Leather-Based Strain Sensor with Hierarchical Structure for Motion Monitoring. *Advanced Materials Technologies* **2019,** *4* (10), 1900442.
(414) Yue, X.; Jia, Y.; Wang, X.; Zhou, K.; Zhai, W.; Zheng, G.; Dai, K.; Mi, L.; Liu, C.; Shen, C. Highly stretchable and durable fiber-shaped strain sensor with porous core-sheath structure for human motion monitoring. *Composites Science and Technology* **2020,** *189*, 108038.
(415) Hang, C.-Z.; Zhao, X.-F.; Xi, S.-Y.; Shang, Y.-H.; Yuan, K.-P.; Yang, F.; Wang, Q.-G.; Wang, J.-C.; Zhang, D. W.; Lu, H.-L. Highly stretchable and self-healing strain sensors for motion detection in wireless human-machine interface. *Nano Energy* **2020,** *76*, 105064.
(416) Wu, Y.; Karakurt, I.; Beker, L.; Kubota, Y.; Xu, R.; Ho, K. Y.; Zhao, S.; Zhong, J.; Zhang, M.; Wang, X. Piezoresistive stretchable strain sensors with human machine interface demonstrations. *Sensors and Actuators A: Physical* **2018,** *279*, 46-52.
(417) Chen, S.; Lou, Z.; Chen, D.; Jiang, K.; Shen, G. Polymer-Enhanced Highly Stretchable Conductive Fiber Strain Sensor Used for Electronic Data Gloves. *Advanced Materials Technologies* **2016,** *1* (7), 1600136.
(418) Xie, M.; Zhu, M.; Yang, Z.; Okada, S.; Kawamura, S. Flexible self-powered multifunctional sensor for stiffness-tunable soft robotic gripper by multimaterial 3D printing. *Nano Energy* **2021,** *79*, 105438.
(419) Devaraj, H.; Schober, R.; Picard, M.; Teo, M. Y.; Lo, C.-Y.; Gan, W. C.; Aw, K. C. Highly elastic and flexible multi-layered carbon black/elastomer composite based capacitive sensor arrays for soft robotics. *Measurement: Sensors* **2019,** *2-4*, 100004.
(420) Xue, P.; Chen, C.; Diao, D. Ultra-sensitive flexible strain sensor based on graphene nanocrystallite carbon film with wrinkle structures. *Carbon* **2019,** *147*, 227-235.
(421) Yang, Y.; Luo, C.; Jia, J.; Sun, Y.; Fu, Q.; Pan, C. A Wrinkled Ag/CNTs-PDMS Composite Film for a High-Performance Flexible Sensor and Its Applications in Human-Body Single Monitoring. *Nanomaterials (Basel)* **2019,** *9* (6), 850.
(422) Yuan, Z.; Pei, Z.; Shahbaz, M.; Zhang, Q.; Zhuo, K.; Zhao, C.; Zhang, W.; Ma, X.; Sang, S. Wrinkle Structured Network of Silver-Coated Carbon Nanotubes for Wearable Sensors. *Nanoscale Research Letters* **2019,** *14* (1), 356.
(423) Tolvanen, J.; Hannu, J.; Jantunen, H. Stretchable and Washable Strain Sensor Based on Cracking Structure for Human Motion Monitoring. *Scientific Reports* **2018,** *8* (1), 13241.

(424) Xin, Y.; Zhou, J.; Tao, R.; Xu, X.; Lubineau, G. Making a Bilateral Compression/Tension Sensor by Pre-Stretching Open-Crack Networks in Carbon Nanotube Papers. *ACS Applied Materials & Interfaces* **2018,** *10* (39), 33507-33515.
(425) Liang, F.-C.; Chang, Y.-W.; Kuo, C.-C.; Cho, C.-J.; Jiang, D.-H.; Jhuang, F.-C.; Rwei, S.-P.; Borsali, R. A mechanically robust silver nanowire–polydimethylsiloxane electrode based on facile transfer printing techniques for wearable displays. *Nanoscale* **2019,** *11* (4), 1520-1530.
(426) Zhang, Y.; Kou, K.; Ji, T.; Huang, Z.; Zhang, S.; Zhang, S.; Wu, G. Preparation of Ionic Liquid-Coated Graphene Nanosheets/PTFE Nanocomposite for Stretchable, Flexible Conductor via a Pre-Stretch Processing. *Nanomaterials (Basel, Switzerland)* **2019,** *10* (1), 40.
(427) Liu, C.; Cai, J.; Li, X.; Zhang, W.; Zhang, D. Flexible and tunable electromagnetic meta-atom based on silver nanowire networks. *Materials & Design* **2019,** *181*, 107982.
(428) Bae, J. S.; Lee, Y.; Li, J.; Liang, J.; Chen, D.; Pei, Q.; Lee, S. The Feasibility of Healable Electronics and Mechanical Behavior of Silver Nanowire (AgNW)/Healable Polymer Composite. *Advanced materials and technologies* **2018,** *3*, 1700364.
(429) Kim, D.; Park, S.-J.; Jeon, S.-B.; Seol, M.-L.; Choi, Y.-K. A Triboelectric Sponge Fabricated from a Cube Sugar Template by 3D Soft Lithography for Superhydrophobicity and Elasticity. *Advanced Electronic Materials* **2016,** *2* (4), 1500331.
(430) Wan, Y.; Qin, N.; Wang, Y.; Zhao, Q.; Wang, Q.; Yuan, P.; Wen, Q.; Wei, H.; Zhang, X.; Ma, N. Sugar-templated conductive polyurethane-polypyrrole sponges for wide-range force sensing. *Chemical Engineering Journal* **2020,** *383*, 123103.
(431) Cao, L.; Huang, Q.; Cui, J.; Lin, H.; Li, W.; Lin, Z.; Zhang, P. Rapid and Facile Synthesis of High-Performance Silver Nanowires by A Halide-Mediated, Modified Polyol Method for Transparent Conductive Films. *Nanomaterials (Basel)* **2020,** *10* (6), 1139.
(432) Chen, G.; Yan, L.; Wan, X.; Zhang, Q.; Wang, Q. In Situ Synthesis of Silver Nanoparticles on Cellulose Fibers Using D-Glucuronic Acid and Its Antibacterial Application. *Materials (Basel, Switzerland)* **2019,** *12* (19), 3101.
(433) Chen, J.; Wang, Q.; Luan, M.; Mo, J.; Yan, Y.; Li, X. Polydopamine as reinforcement in the coating of nano-silver on polyurethane surface: Performance and mechanisms. *Progress in Organic Coatings* **2019,** *137*, 105288.
(434) Jung, Y.; Jung, K.; Park, B.; Choi, J.; Kim, D.; Park, J.; Ko, J.; Cho, H. Wearable piezoresistive strain sensor based on graphene-coated three-dimensional micro-porous PDMS sponge. *Micro and Nano Systems Letters* **2019,** *7* (1), 1-9.
(435) Hassan, G.; Khan, M. U.; Bae, J.; Shuja, A. Inkjet printed self-healable strain sensor based on graphene and magnetic iron oxide nano-composite on engineered polyurethane substrate. *Scientific reports* **2020,** *10* (1), 1-12.
(436) Bhattacharjee, M.; Soni, M.; Escobedo, P.; Dahiya, R. PEDOT: PSS Microchannel-Based Highly Sensitive Stretchable Strain Sensor. *Advanced Electronic Materials* **2020,** *6* (8), 2000445.
(437) Kim, Y.; Zhu, J.; Yeom, B.; Di Prima, M.; Su, X.; Kim, J. G.; Yoo, S. J.; Uher, C.; Kotov, N. A. Stretchable nanoparticle conductors with self-organized conductive

pathways. *Nature* **2013,** *500* (7460), 59-63.
(438) Chen, S.; Wei, Y.; Yuan, X.; Lin, Y.; Liu, L. A highly stretchable strain sensor based on a graphene/silver nanoparticle synergic conductive network and a sandwich structure. *Journal of Materials Chemistry C* **2016,** *4* (19), 4304-4311.
(439) Xiao, S.; Zhou, X.; Deng, H.; Fu, Q. Preparation of elastic conductor with high stretchability and stable conductivity under strain via pre-stretching and spraying approach. *Composites Communications* **2021,** *24*, 100641.
(440) Chu, Z.; Jiao, W.; Li, J.; Guo, H.; Zheng, Y.; Wang, R.; He, X. A novel wrinkle-gradient strain sensor with anti-water interference and high sensing performance. *Chemical Engineering Journal* **2021,** *421*, 129873.
(441) Li, R.; Song, C. The influence of hydroxyl groups on friction of graphene at atomic scale. *Crystals* **2018,** *8* (4), 167.
(442) Gonzalez-Martinez, E.; Saem, S.; Beganovic, N. E.; Moran-Mirabal, J. Fabrication of microstructured electrodes via electroless metal deposition onto polydopamine-coated polystyrene substrates and thermal shrinking. *Nano Select* **2021**.
(443) Su, Y.; Zhao, Y.; Zhang, H.; Feng, X.; Shi, L.; Fang, J. Polydopamine functionalized transparent conductive cellulose nanopaper with long-term durability. *J. Mater. Chem. C.* **2017,** *5* (3), 573-581.
(444) Yu, Z.; Gao, Y.; Di, X.; Luo, H. Cotton modified with silver-nanowires/polydopamine for a wearable thermal management device. *RSC Adv.* **2016,** *6* (72), 67771-67777.
(445) Sanbhal, N.; Saitaer, X.; Peerzada, M.; Habboush, A.; Wang, F.; Wang, L. One-step surface functionalized hydrophilic polypropylene meshes for hernia repair using bio-inspired polydopamine. *Fibers* **2019,** *7* (1), 6.
(446) Bhattacharya, P.; Gohil, S.; Mazher, J.; Ghosh, S.; Ayyub, P. Universal, geometry-driven hydrophobic behaviour of bare metal nanowire clusters. *Nanotechnology* **2008,** *19* (7), 075709.
(447) Yang, Y.; Qi, P.; Ding, Y.; Maitz, M. F.; Yang, Z.; Tu, Q.; Xiong, K.; Leng, Y.; Huang, N. A biocompatible and functional adhesive amine-rich coating based on dopamine polymerization. *J. Mater. Chem. B* **2015,** *3* (1), 72-81.
(448) Kang, H.; Kim, Y.; Cheon, S.; Yi, G.-R.; Cho, J. H. Halide welding for silver nanowire network electrode. *ACS Appl. Mater. Interfaces* **2017,** *9* (36), 30779-30785.
(449) Han, S.; Liu, C.; Xu, H.; Yao, D.; Yan, K.; Zheng, H.; Chen, H.-J.; Gui, X.; Chu, S.; Liu, C. Multiscale nanowire-microfluidic hybrid strain sensors with high sensitivity and stretchability. *npj Flexible Electronics* **2018,** *2* (1), 1-10.
(450) Huang, G.-W.; Xiao, H.-M.; Fu, S.-Y. Wearable electronics of silver-nanowire/poly (dimethylsiloxane) nanocomposite for smart clothing. *Scientific reports* **2015,** *5* (1), 1-9.
(451) Yao, S.; Yang, J.; Poblete, F. R.; Hu, X.; Zhu, Y.; interfaces. Multifunctional electronic textiles using silver nanowire composites. *ACS Applied Materials & Interfaces* **2019,** *11* (34), 31028-31037.
(452) Feng, X.; Meitl, M. A.; Bowen, A. M.; Huang, Y.; Nuzzo, R. G.; Rogers, J. A. Competing fracture in kinetically controlled transfer printing. *Langmuir* **2007,** *23* (25), 12555-12560.

(453) Wang, Y.; Chen, Z.; Mei, D.; Zhu, L.; Wang, S.; Fu, X. Highly sensitive and flexible tactile sensor with truncated pyramid-shaped porous graphene/silicone rubber composites for human motion detection. *Composites Science and Technology* **2022,** *217*, 109078.
(454) Ma, L.; Lei, X.; Li, S.; Guo, S.; Yuan, J.; Li, X.; Cheng, G. J.; Liu, F. A 3D flexible piezoresistive sensor based on surface-filled graphene nanosheets conductive layer. *Sensors and Actuators A: Physical* **2021,** *332*, 113144.
(455) Shi, Z.; Li, A.; Zhang, C.; Zhang, Y.-F. Reduced graphene oxide coated polyurethane composite foams as flexible strain sensors for large deformation. *Materials Science and Engineering: B* **2021,** *272*, 115360.
(456) Song, P.; Wang, G.; Zhang, Y. Preparation and performance of graphene/carbon black silicone rubber composites used for highly sensitive and flexible strain sensors. *Sensors and Actuators A: Physical* **2021,** *323*, 112659.
(457) Mao, R.; Yao, W.; Qadir, A.; Chen, W.; Gao, W.; Xu, Y.; Hu, H. 3-D graphene aerogel sphere-based flexible sensors for healthcare applications. *Sensors and Actuators A: Physical* **2020,** *312*, 112144.
(458) Wang, Y.; Gao, G.; Ren, X. Graphene assisted ion-conductive hydrogel with super sensitivity for strain sensor. *Polymer* **2021,** *215*, 123340.
(459) Cheng, L.; Feng, J. Facile fabrication of stretchable and compressible strain sensors by coating and integrating low-cost melamine foam scaffolds with reduced graphene oxide and poly (styrene-b-ethylene-butylene-b-styrene). *Chemical Engineering Journal* **2020,** *398*, 125429.
(460) Singh, K.; Sharma, S.; Gupta, M.; Tripathi, C. C. Fabrication of serpentine and I structured graphene-CNT based highly sensitive and flexible strain sensors. *Microelectronic Engineering* **2021,** *250*, 111631.
(461) Zhang, M.; Wang, C.; Wang, H.; Jian, M.; Hao, X.; Zhang, Y. Carbonized cotton fabric for high-performance wearable strain sensors. *Advanced Functional Materials* **2017,** *27* (2), 1604795.
(462) Wang, X.; Sparkman, J.; Gou, J. Strain sensing of printed carbon nanotube sensors on polyurethane substrate with spray deposition modeling. *Composites Communications* **2017,** *3*, 1-6.
(463) Liu, Q.; Chen, J.; Li, Y.; Shi, G. High-Performance Strain Sensors with Fish-Scale-Like Graphene-Sensing Layers for Full-Range Detection of Human Motions. *ACS Nano* **2016,** *10* (8), 7901-7906.
(464) Yang, Z.; Wang, D.-Y.; Pang, Y.; Li, Y.-X.; Wang, Q.; Zhang, T.-Y.; Wang, J.-B.; Liu, X.; Yang, Y.-Y.; Jian, J.-M.; Jian, M.-Q.; Zhang, Y.-Y.; Yang, Y.; Ren, T.-L. Simultaneously Detecting Subtle and Intensive Human Motions Based on a Silver Nanoparticles Bridged Graphene Strain Sensor. *ACS Applied Materials & Interfaces* **2018,** *10* (4), 3948-3954.
(465) Sun, Q.; Seung, W.; Kim, B. J.; Seo, S.; Kim, S.-W.; Cho, J. H. Active Matrix Electronic Skin Strain Sensor Based on Piezopotential-Powered Graphene Transistors. *Advanced Materials* **2015,** *27* (22), 3411-3417.
(466) Liu, P.; Liu, J.; Zhu, X.; Wu, C.; Liu, Y.; Pan, W.; Zhao, J.; Guo, X.; Liu, C.; Huang, Y.; Song, A. A highly adhesive flexible strain sensor based on ultra-violet

adhesive filled by graphene and carbon black for wearable monitoring. *Composites Science and Technology* **2019,** *182*, 107771.
(467) Darabi, M. A.; Khosrozadeh, A.; Wang, Q.; Xing, M. Gum Sensor: A Stretchable, Wearable, and Foldable Sensor Based on Carbon Nanotube/Chewing Gum Membrane. *ACS Applied Materials & Interfaces* **2015,** *7* (47), 26195-26205.
(468) Xiao, W.; Wang, L.; Li, B.; Li, Y.; Wang, Y.; Luo, J.; Huang, X.; Xie, A.; Gao, J. Interface-engineered reduced graphene oxide assembly on nanofiber surface for high performance strain and temperature sensing. *J. Colloid Interface Sci.* **2022,** *608*, 931-941.
(469) Chun, S.; Choi, Y.; Park, W. All-graphene strain sensor on soft substrate. *Carbon* **2017,** *116*, 753-759.
(470) Park, J. J.; Hyun, W. J.; Mun, S. C.; Park, Y. T.; Park, O. O. Highly Stretchable and Wearable Graphene Strain Sensors with Controllable Sensitivity for Human Motion Monitoring. *ACS Applied Materials & Interfaces* **2015,** *7* (11), 6317-6324.
(471) Li, C.; Cui, Y.-L.; Tian, G.-L.; Shu, Y.; Wang, X.-F.; Tian, H.; Yang, Y.; Wei, F.; Ren, T.-L. Flexible CNT-array double helices Strain Sensor with high stretchability for Motion Capture. *Scientific Reports* **2015,** *5* (1), 15554.
(472) Reghat, M.; Mirabedini, A.; Tan, A. M.; Weizman, Y.; Middendorf, P.; Bjekovic, R.; Hyde, L.; Antiohos, D.; Hameed, N.; Fuss, F. K.; Fox, B. Graphene as a piezo-resistive coating to enable strain monitoring in glass fiber composites. *Composites Science and Technology* **2021,** *211*, 108842.
(473) Duan, S.-k.; Niu, Q.-l.; Wei, J.-f.; He, J.-b.; Yin, Y.-a.; Zhang, Y. Water-bath assisted convective assembly of aligned silver nanowire films for transparent electrodes. *Physical Chemistry Chemical Physics* **2015,** *17* (12), 8106-8112.
(474) Xiong, J.; Li, S.; Ciou, J.-H.; Chen, J.; Gao, D.; Wang, J.; Lee, P. S. A Tailorable Spray-Assembly Strategy of Silver Nanowires-Bundle Mesh for Transferable High-Performance Transparent Conductor. *Advanced Functional Materials* **2021,** *31* (1), 2006120.
(475) Liu, J.-W.; Wang, J.-L.; Huang, W.-R.; Yu, L.; Ren, X.-F.; Wen, W.-C.; Yu, S.-H. Ordering Ag nanowire arrays by a glass capillary: A portable, reusable and durable SERS substrate. *Scientific reports* **2012,** *2* (1), 1-7.
(476) Chen, C.; Hao, J.; Zhu, L.; Yao, Y.; Meng, X.; Weimer, W.; Wang, Q. K. Direct two-phase interfacial self-assembly of aligned silver nanowire films for surface enhanced Raman scattering applications. *Journal of Materials Chemistry A* **2013,** *1* (43), 13496-13501.
(477) Tao, A.; Kim, F.; Hess, C.; Goldberger, J.; He, R.; Sun, Y.; Xia, Y.; Yang, P. Langmuir−Blodgett Silver Nanowire Monolayers for Molecular Sensing Using Surface-Enhanced Raman Spectroscopy. *Nano Letters* **2003,** *3* (9), 1229-1233.
(478) Park, B.; Bae, I.-G.; Huh, Y. H. Aligned silver nanowire-based transparent electrodes for engineering polarisation-selective optoelectronics. *Scientific Reports* **2016,** *6* (1), 1-9.
(479) Shin, M.; Choi, C.; Jung, Y.; Choi, J.; Ko, J. Alignment of silver nanowires using heat-assisted dip-coating method. *AIP Advances* **2020,** *10* (3), 035101.
(480) Qiu, J.; Wang, X.; Ma, Y.; Yu, Z.; Li, T. Stretchable transparent conductive films

based on Ag nanowires for flexible circuits and tension sensors. *ACS Applied Nano Materials* **2021,** *4* (4), 3760-3766.
(481) Zhang, S.; Liu, H.; Yang, S.; Shi, X.; Zhang, D.; Shan, C.; Mi, L.; Liu, C.; Shen, C.; Guo, Z. Ultrasensitive and highly compressible piezoresistive sensor based on polyurethane sponge coated with a cracked cellulose nanofibril/silver nanowire layer. *ACS Applied Materials & Interfaces* **2019,** *11* (11), 10922-10932.
(482) Jing, M.-x.; Han, C.; Li, M.; Shen, X.-q. High performance of carbon nanotubes/silver nanowires-PET hybrid flexible transparent conductive films via facile pressing-transfer technique. *Nanoscale research letters* **2014,** *9* (1), 1-7.
(483) Sun, J.; Zhou, W.; Yang, H.; Zhen, X.; Ma, L.; Williams, D.; Sun, X.; Lang, M.-F. Highly transparent and flexible circuits through patterning silver nanowires into microfluidic channels. *Chem. Commun.* **2018,** *54* (39), 4923-4926.
(484) Yang, B.-R.; Cao, W.; Liu, G.-S.; Chen, H.-J.; Noh, Y.-Y.; Minari, T.; Hsiao, H.-C.; Lee, C.-Y.; Shieh, H.-P. D.; Liu, C. Microchannel Wetting for Controllable Patterning and Alignment of Silver Nanowire with High Resolution. *ACS Applied Materials & Interfaces* **2015,** *7* (38), 21433-21441.
(485) Yao, S.; Yang, J.; Poblete, F. R.; Hu, X.; Zhu, Y. Multifunctional electronic textiles using silver nanowire composites. *ACS Applied Materials & Interfaces* **2019,** *11* (34), 31028-31037.
(486) Huang, Q.; Shen, W.; Fang, X.; Chen, G.; Yang, Y.; Huang, J.; Tan, R.; Song, W. Highly thermostable, flexible, transparent, and conductive films on polyimide substrate with an AZO/AgNW/AZO structure. *ACS Applied Materials & Interfaces* **2015,** *7* (7), 4299-4305.

Appendix A: Supporting Information

Elastomer/sugar film swelling over long-term soaking; Fourier transform infrared spectroscopy (FTIR) characterization; Surface Wettability Characterization; Surface Morphology of pure Ecoflex elastomers; Characterization of AgNPs; Mechanical properties of the elastomer films; Electrical performance of the pure Ecoflex elastomer films with AgNPs under stretching; Morphology of the wrinkled conductors after cyclic stretching/releasing; Hand motion detection by the conductive elastomer film sensor; Viscosity of the pure Ecoflex elastomer and the Ecoflex/sugar hybrid; Complex pattern printed with the elastomer/sugar composite; Gauge factor of the 3D printed lattice sensor at different strains; Resistance of the 3D printed lattice sensor responding to large arm bending angles.

Published review paper “Advances in constructing silver nanomaterials-based conductive pathways for flexible and stretchable electronics” is based on Chapter 2. Published research papers “Highly conductive silicone elastomers via environment-friendly swelling and in-situ synthesis of silver nanoparticles” “Water-induced polymer swelling and its application in soft electronics” “Silver nanowire-based stretchable strain sensors with hierarchical wrinkled structures” are based on Chapter 3 and 4. Published research papers “3D printing of antibacterial polymer devices based on nitric oxide release from embedded s-nitrosothiol crystals” is based on Chapter 7.2.1.

Curriculum Vitae

Yuanhang Yang
Department of Mechanical& Nuclear Engineering, Virginia Commonwealth University, VA, USA.
Tel: 1 (804) 2988154
E-mail: yangy38@vcu.edu

EDUCATION

- Ph.D. candidate, Mechanical and Nuclear Engineering, Virginia Commonwealth University, VA, USA, 01/2019~present.
- M.S., Mechanical Engineering, Beijing Institute of Petrochemical Technology, Beijing, China, 09/2015~06/2018.

  Joint training, Materials Science and Engineering, Tsinghua University, Beijing, China, 06/2016~06/2018.

  Research scholar, Mechanical Engineering, Villanova University, PA, USA, 01/2017~06/2017.
- B.Sc., Mechanical Engineering, Qingdao University, Qingdao, China, 09/2011~07/2015.

RESEARCH EXPERIENCE

- Research Orientation:

  1. Investigating soft electronics with hierarchical wrinkled structure via 3D printing technology and water-induced polymer swelling.
  2. Designing flexible electrodes with desirable complex pattern by transferring conductive layer into soft substrates in a 3D printing process.
  3. Fabricating Micro-arc oxidation coating on Aluminum-based materials to enhance the anti-corrosion performance.
  4. Exploring novel strategies to promote the corrosion resistance of chromium oxide films.
- Publications:

  1. **Yuanhang Yang**, Yunhang Ling, Yanhong Gu, Zhengjun Zhang. Comparisons of air and water oxidation on the passive properties of chromium, *Solid Thin Film*, in revision, 2022.

  2. **Yuanhang Yang**, Shun Duan, Hong Zhao. Advances in constructing silver nanomaterials-based conductive pathways for flexible and stretchable electronics, *Nanoscale*, accepted, 2022.

  3. **Yuanhang Yang**, Shun Duan, Weijun Xiao, Hong Zhao. Silver nanowire-based stretchable strain sensors with hierarchical wrinkled structures, *Sensor and Actuators: A. Physical,* 2022, 343, 113653.

  4. **Yuanhang Yang**, Hong Zhao. Water-induced polymer swelling and its

application in soft electronics, *Applied Surface Science*, 2022, 577(1), 151895.

5. Wuwei Li[#], **Yuanhang Yang#**, Christopher J. Ehrhardt, Nastassja Lewinski, David Gascoyne, Gary Lucas, Hong Zhao, Xuewei Wang. 3D printing of antibacterial polymer devices based on nitric oxide release from embedded s-nitrosothiol crystals, *ACS Applied Bio Materials*, 2021, 4(10), 7653-7662. (Co-first author)

6. **Yuanhang Yang**, Shun Duan, and Hong Zhao. Highly conductive silicone elastomers via environment-friendly swelling and in-situ synthesis of silver nanoparticles, *Advanced Materials Interfaces*, 2021, 8(9), 2100137.

7. **Yuanhang Yang**, Gang Feng, Yanhong Gu, *et al.* Analysis on corrosion of aluminum-based micro-arc oxidation coating, *Anti-Corrosion Methods and Materials*, 2021, 68(5), 404-412.

8. **Yuanhang Yang**, Yanhong Gu, and Jian Liang, *et al.* A proposal for modified galvanic corrosion model: Investigating effects of micro-arc oxidation on Al alloy, *Surface Review and Letters*, 2019, 26(2), 1850147.

9. **Yuanhang Yang**, Yanhong Gu, and Lei Zhang, *et al.* Influence of MAO treatment on the galvanic corrosion between aluminum alloy and 316L steel, *Journal of Material Engineering and Performance*, 2017, 26, 6099-6106.

10. **Yuanhang Yang**, Juntie Che, and Yanhong Gu, *et al.* Study about Combined Protection of 316L Stainless Steel Welding, *Journal of Beijing Institute of Petrochemical technology*, 2017, 25(1), 30-35.

11. **Yuanhang Yang**, Yanhong Gu, and Juntie Che, *et al.* Study on micro-cell corrosion mechanism of welding area of 316L stainless steel, *Materials Protection*, 2017, 50(4), 10-14.

12. **Yuanhang Yang**, Juntie Che, and Yanhong Gu, *et al.* Influence of the Welding Technology to 316J1L Stainless Steel in Seawater, *Journal of Beijing Institute of Petrochemical Technology*, 2016, 24(4), 25-30.

◆ Patent Applications:

1. Xuewei Wang, Hong Zhao, Yuanhang Yang, Wuwei Li, Nitric Oxide-Releasing 3D-Printing Compositions and Uses Thereof, Patent Application 17207991, filed to USPTO on March 22nd, 2021 (currently pending).

2. Yanhong Gu, Xiaoyu Yang, Huijuan Ma, Yuanhang Yang, *et al.* Preparation method of magnesium alloy surface coating and magnesium alloy [P]. Beijing: CN106191963A, 2016.12.07.

◆ Conference Presentations:

1. Yang, Y., Duan, S., Zhao, H., Highly Conductive Silicone Elastomers via Water-Induced Swelling and In Situ Synthesis of Silver Nanoparticles, *the 95th ACS Colloid and Surface Science Symposium*, June 14-16, 2021.

2. Yang, Y., Zhao, H., An Ultra-Sensitive Strain Sensor Based on A Dopamine-Modified Complex 3D Printed Structure, *the 7th Virginia Soft Matter Workshop*, Sept. 7, 2019, University of Virginia, VA.

3. Yang, Y., Ling, Y., Gu, Y., *et al.*, Effect of nitridation on the surface structure and hydrogen adsorption characteristic of iron nickel based stainless steel, *the 2nd International Conference on Applied Surface Science*, June 12-15, 2017.

4. Yang, Y., Gu, Y., Cathodic protection of 316L steel using MAO coated Aluminum Anode, *the 4th International Corrosion Engineering Conference*, Aug. 1, 2016.

Professional Skills

- Experimental Skills: Operation of Scanning Electrical Microscope (SEM), Laser Scanning Microscope (LSM), Optical Microscope (OM), Scanning Electrochemical Microscopy (SECM), Rheometer, Extrusion-based 3D printing, Energy Dispersive Spectrometer (EDS), X-ray Diffractometer (XRD), Raman Spectrometer, Electrochemical workstation, Scanning Vibration Electrode Techniques (SVET), Scanning Kelvin Probe (SKP), Localized Electrochemical Impedance System (LEIS), Multi-channel Galvanic Corrosion tester, Hardness tester, Optical Tensiometers, etc.
- Software Skills: Proficient in using Jade5, ZMAN, and XPSPEAK, Adobe Photoshop CS6, Microsoft Visio, Adobe Illustrator, Origin, CoreIDRAWX6, Endnote, 3D Max, Keysight Bench-Vue, King-Draw, Adobe Photoshop CS6, Microsoft Visio 2010, Adobe Illustrator, Origin 9.0, CorelDRAWX6, Endnote 7, and C++, etc.

Honors and Awards

1. VCU Graduate School Dissertation Assistantship for spring& summer, 2022.
2. Excellent graduate student Award in Institute, 2018.
3. Outstanding Dissertation Award in Institute, 2018.
4. Excellent volunteer Award in student community, May 2017.
5. Enterprise Practice Scholarship, 2017.
6. Outstanding Graduate Cadres, 2016~2017.
7. Graduate Petroleum Equipment Innovation Design Competition Award, 2016.
8. Top Ten Students Award Nomination of Institute, May 2016.
9. Mechanical Engineer Qualification Certification, May 2016.
10. Graduate Academic Scholarships, 2016.
11. International Training Scholarship, March 2016.
12. Table Tennis Competition Award of Institute, 2015.
13. Graduate Freshman Scholarship, 2015.